Impact of Increased DFIG
Wind Penetration
on Power Systems and Markets

Final Project Report

Power Systems Engineering Research Center

*Empowering Minds to Engineer
the Future Electric Energy System
Since 1996*

Impact of Increased DFIG Wind Penetration on Power Systems and Markets

Final Project Report

Project Team

Vijay Vittal, Project Leader, Arizona State University

James McCalley, Iowa State University

V. Ajjarapu, Iowa State University

Uday V. Shanbhag, Univ. of Illinois at Urbana-Champaign

October 2009

Information about this project

Vijay Vittal
Ira A. Fulton Chair Professor
Department of Electrical Engineering
Arizona State University
PO Box 875706
Tempe, AZ 85287-5706
Tel: 480-965-1879
Fax: 480-965-0745
Email: vijay.vittal@asu.edu

Power Systems Engineering Research Center

The Power Systems Engineering Research Center (PSERC) is a multi-university Center conducting research on challenges facing the electric power industry and educating the next generation of power engineers. More information about PSERC can be found at the Center's website: http://www.pserc.org.

For additional information, contact:

Notice Concerning Copyright Material

Acknowledgements

Executive Summary

This project examines the impact of increased penetration of doubly fed induction generator (DFIG) based wind generation on power system dynamic performance and hence reliability. DFIG wind turbines have controls that effectively isolate the inertia from the grid. In addition, large wind farms are typically connected to the grid at lower voltage levels resulting in higher fault currents. As a result, with the increase in penetration of wind generation, transient stability, the overall frequency response, regulation, voltage response, fault ride-through capability, and load following capability may be affected. This project analyzes the impact of increased wind penetration under two different scenarios: a) Increased wind penetration with concomitant displacement of aged conventional generation and b) Increased wind penetration without any decrease in existing conventional generation and determine conditions and conditions under which the increased wind penetration will result in violation of reliability criteria. The important aspects (such as low voltage ride through (LVRT), dynamic reactive compensation as per the requirements of FERC standards) are also studied. The effects of increased wind penetration on frequency stability are analyzed and solutions to mitigate the resulting problems are explored.

When the reliability criteria are violated due to the increased penetration of wind turbines, the impact of this reduced level of reliability on market operation is also examined. The analysis models the reliability impacts of wind-power and determines the impact on market mechanisms, such as day-ahead reserves on such concerns. The study focuses on markets characterized by i) energy, reserves and capacity bidding, and ii) market settlement. In addition, technical solutions to maintain the requisite reliability standards are examined and the impact of these solutions on market mechanisms are analyzed.

In this report, each aspect of impact of increased DFIG penetration on 1) small-signal and transient stability, 2) frequency stability, 3) voltage response, and 4) market operation is studied in detail and presented as a separate part. An overview of the work accomplished in each part is presented below:

Part I. Impact of Increased DFIG Penetration on Small-Signal and Transient Stability (work done at Arizona State University)

Growing environmental concerns and attempts to reduce dependency on fossil fuel resources are bringing renewable energy resources to the mainstream of the electric power sector. Among the various renewable resources, wind power is assumed to have the most favorable technical and economical prospects. When deployed in small scale, as was done traditionally, the impact of wind turbine generators (WTGs) on power system stability is minimal. In contrast, when the penetration level increases, the dynamic performance of the power system can be affected.

Among the several wind generation technologies, variable speed wind turbines utilizing doubly fed induction generators (DFIGs) are gaining prominence in the power industry. As the performance is largely determined by the converter and the associated

controls, a DFIG is an asynchronous generator. Since DFIGs are asynchronous machines, they primarily have four mechanisms by which they can affect the damping of electromechanical modes (since they themselves do not participate in the modes):

1. Displacing synchronous machines thereby affecting the modes

2. Impacting major path flows thereby affecting the synchronizing forces

3. Displacing synchronous machines that have power system stabilizers

4. DFIG controls interacting with the damping torque on nearby large synchronous generators.

This part of the report addresses the first two mechanisms listed above. Following a large disturbance, the restoring mechanisms that bring the affected generators back to synchronism are related to the interaction between the synchronizing forces and the inertia of the generators in the system. In the case of a DFIG, however, the inertia of the turbine is effectively decoupled from the system. The power electronic converter at the heart of the DFIG controls the performance and acts as an interface between the machine and the grid. With conventional control, rotor currents are always controlled to extract maximum energy from the wind. Hence, with the increased penetration of DFIG based wind farms, the effective inertia of the system will be reduced and system reliability following large disturbances could be significantly affected.

In order to examine the impact on small signal stability a systematic approach to pin point the impact of increased penetration of DFIGs on electromechanical modes of oscillation using eigenvalue sensitivity to inertia is developed. In evaluating the sensitivity of specific modes of oscillation with respect to inertia, the DFIGs are replaced by conventional round rotor synchronous machines with the same MVA rating. The sensitivity analysis is performed only for the system where all the generators are synchronous machines. The sensitivity analysis identifies electromechanical modes of oscillations that are detrimentally and beneficially impacted by increased DFIG penetration. The method inherently accounts for the insertion point of the DFIGs in the network. The results of the sensitivity analysis are then confirmed using exact eigenvalue analysis performed by including the DFIGs in the base case and in the increased wind penetration case. Three specific cases of transient stability are also examined. In this analysis the modes observed in small signal analysis are excited by placing specific faults at buses close to the generators having the largest participation factors in the oscillatory modes identified. Transient stability behavior in terms of sufficient system damping and rotor angle stability is analyzed.

For the system operating conditions considered, the analysis conducted indicates that it is possible to identify a certain inter-area mode which is detrimentally affected by the increased DFIG penetration. Moreover, using the concept of participation factors, the specific mode can be excited in time domain.

The system is found to have both beneficial and detrimental impact with the increased penetration of DFIG. Both of these situations observed by sensitivity analysis for small signal stability are also observed in nonlinear time domain analysis by considering corresponding fault scenarios in time domain.

The sensitivity of the real part of the eigenvalue with respect to inertia evaluated for a system where the DFIGs at their planned insertion points in the network are replaced by equivalent round rotor synchronous machines provides a good metric to evaluate the impact due to increased DFIG penetration on system dynamic performance. Both detrimental and beneficial impacts of increased DFIG penetration can be identified. The eigenvalue sensitivity analysis together with the detailed eigenvalue analysis carried out for each of the cases considered is also substantiated by the results obtained from time domain simulation.

Part II. Impact of Increased DFIG Penetration on Frequency Response and Stability (work done at Iowa State University)

Wind energy, being non-dispatchable, has different operational characteristics than conventional energy sources. Additionally high levels of wind penetration create issues of power system control and interconnection issues. In this work we focus on MW-frequency control issues, system attributes, the grid problems introduced due to those attributes, and possible solutions to address them. The ultimate objective is to provide an approach for identifying the right combination of solutions for a given power system with a given projection regarding wind penetration levels. To do so, we need to establish the performance impact of each solution on each problem and we need to estimate cost per unit for each solution. The overall problem is an optimization problem of a combinatorial nature. The challenge is to ensure, at a particular wind penetration level, minimum cost and, at the same time, maximum impact sets of solution. Although this is the ultimate goal of our work, the objective in this project was to understand the impact of high wind penetration on transient frequency dip and on regulation/reserve requirements.

A 2008 case for the U.S. Eastern Interconnection was analyzed to assess transient frequency behavior under different wind penetration levels. The installed capacity for the system was 541 GW. Two very severe (and highly unlikely) contingencies of 2.9 GW and 10.16 GW outages were studied. Assuming conventional generation is displaced, and assuming DFIGs are not provided with inertial emulation, DFIG wind generation will cause deterioration in transient frequency performance. The frequency dips in both cases were found to be small and of little concern in terms of tripping underfrequency load shedding or of tripping generator protection, even when wind penetration was increased to 8% of total Eastern Interconnection capacity. This would also be the case for wind penetration levels significantly higher than 8% due to the fact that even a 10 GW outage does not create significant transient frequency dips, owing to the very large size of the Eastern Interconnection. This would not be the case for the Western or Texas Interconnections. It should be recognized, however, that islanded conditions would necessarily magnify the detrimental effect of DFIG penetration on transient frequency performance. In addition, it is expected that high DFIG penetration will cause degraded performance in terms of control performance standards CPS1 and CPS2, but this issue was not studied in this project.

We also examined wind effects on and ability to provide regulation. A statistical study was performed to determine the impact of wind addition on the generation portfolio and ramping requirements in a control area with a given load distribution and in different time frames (i.e., ten-minute and one-hour). Different solutions to reduce the impact of wind on MW variability were considered.

Our investigations conclude that generator controls can alleviate the problems of transient frequency dip and regulation. Inertial emulation is a good and necessary idea, although attention should be paid to the overall cost of replicating this control on so many turbines, assuming wind penetration increases to the 300 GW level in the nation. The cost of distributed control must be considered for using wind to provide regulation; however, the very real cost of spilling wind should also be considered.

Part III. Impact of increased DFIG penetration on voltage response and stability (work done at Iowa State University)

Assessing the reactive power capability of a DFIG machine is essential to analyze the effect of high penetration of DFIG wind parks on voltage response and stability. DFIG machines have sensitive power electronic devices which are sensitive to high voltages and currents. Control enhancements have been developed to fully utilize the reactive power capability of the machine and the power electronic converters. These control enhancements include grid-side reactive power boost which allows the grid-side power converter to inject reactive power into the grid when the rotor is short circuited with a crowbar to protect the rotor-side converter. The enhancements also include retrip prevention and DC overvoltage prevention which protect the power electronics and allow maximum utilization of reactive power.

The reactive capability curve is developed for a 1.5 MW machine and scaled up to represent the reactive capability of a wind park. The reactive capability of a wind park at low wind levels can become a significant reactive power source. Since there is no control on the real power output of a wind farm, the additional reactive capability at low wind output can significantly enhance the voltage performance of the system. The operation of a DFIG wind park with a new voltage controller is compared with two reactive power strategies. In one strategy the capability curve is utilized and in the second strategy with +/- 0.95 power factor restriction is used. With the restricted power factor operation, the available reactive power decreases with decreasing wind output whereas while employing the capability curve, the available reactive power increases with reducing wind levels. The two strategies are compared for both static and dynamic performance, and an improved performance over the entire range of wind speed from cut in to full potential is observed. From static analysis, a greater power transfer margin and lower system losses are obtained using the capability curve. The additional benefits are more significant at lower wind speeds. In the dynamic analysis, the capability curve provides a better post fault voltage profile, and, at lower wind speeds, the additional reactive capability can prevent transient instability.

At the plant level, the Irish grid code maintains a requirement that, during a fault, the wind park must provide the maximum possible amount of reactive current without violating generator limits. By modifying this rationale to include the capability curve, a revised U.S. grid code could implicitly define the exact injection to be commanded at the point of interconnection for a given operational point. A policy revision mandating wind park owners to submit plant capability curves to system operators may lend itself to not only economic dispatch improvements, but also to increased stability during voltage emergencies. The additional enhancement in voltage performance is obtained at no additional cost. The presence of the additional reactive capacity in high penetration scenarios is crucial to enhancing system performance.

The final section of Part 3 deals with the impact of wind variability on voltage security assessment. Electricity generated from wind power can be highly variable with several different time scales: hourly, daily, and seasonal periods. This variability can lead to increased regulation costs and operating reserves. Wind variations in the small time frame (~seconds) is very small (~0.1%) for a large wind park. Thus, static tools can be used to assess impact of wind variation.

Traditional P-V curves assume that generation is dispatchable and voltage stability of the test power system with respect to load variation. Wind energy is an intermittent resource, hence, it cannot be assumed to be dispatchable. Thus, the traditional PV curves are unable to capture the stability margin for an integrated system which has high wind penetration. Thus, a new tool that would incorporate wind variability is required for assessing long term voltage stability of power systems with high levels of wind generation.

The developed tool calculates sets of PV curves plotted along parallel planes, thus giving a three dimensional voltage secure region of operation. The tool calculates the most restrictive contingency at each wind level and obtains the PV curve for that contingency. Different redispatch strategies are also utilized to compensate for wind gusts and loss of wind. The developed tool was used to study the impact of wind variability on two test systems. One system was the 23-bus PSS/E test system and the second system considered in the Eastern Interconnection.

The results indicate that the redispatch strategy has an important impact on the transfer margin of a system. The most severe contingencies in a system depend on the level of wind generation. Also, the maximum power transfer need not be at either minimum or maximum wind but could be at an intermediary wind level.

Part IV: Impact of increased DFIG penetration on market mechanisms (work done at the University of Illinois at Urbana-Champaign)

Increased penetration of wind-based resources into the generation mix is expected to have a distinct impact on the functioning of power markets. As electricity markets gravitate towards a regime where renewables, such as windpower, are an integral part of a firm's generation mix, multiple questions persist in terms of how market mechanisms should evolve to contend with the challenges arising from uncertainty and intermittency. As part of the work done at the University of Illinois at Urbana-Champaign, we develop a flexible methodology for modeling strategic behavior in markets where firms may have wind-based generation. Importantly, we introduce a risk-based mechanism that charges firms when their bids have a large exposure to risk. Unlike the more standard deviation cost metric, this is an ex-ante measure and possesses the benefit that it can be computed prior to the clearing of the real-time market. Introducing this risk measure results in a rather challenging game-theoretic problem that is well beyond the reach of existing analytical and computational tools. Yet, it is this class of models that can provide us with insights on both existing and improved market designs. Accordingly, our research effort concentrated on the developing a modeling framework that can accommodate a host of complexities, ranging from capturing uncertainty and risk preferences in the setting of a two-settlement forward-spot market.

We consider the strategic behavior of firms in an imperfectly competitive networked electricity market under uncertainty. Firms in such a setting are assumed to have access to first and second period (recourse) decisions while minimizing a mean-risk objective. Motivated by the risk exposure arising from market participants with uncertain generation assets, agents are exposed to the risk of capacity shortfall in the real-time market through a conditional value-at-risk (CVaR) measure. Unfortunately, there is little available by way of existence theory or convergent schemes for this class of problems. In other words it remains unclear if equilibria can be expected to exist and if they do, whether they can be computed efficiently. Our main contribution in this part of the research is showing that in a broad class of games arising in these settings, Nash equilibria are expected to exist. Furthermore, a perturbed game is seen to admit a unique equilibrium. Note that these results do not directly follow directly from known results on games and represent an important step in understanding strategic behavior in large networked engineering-economic systems.

Clearly, any effort to draw policy insights requires computing these equilibria in networks of a practical size. The challenge in such a computation lies in the sheer size of the problems and the coupling through the shared constraints. In particular, every firm in the game is faced by the challenge of optimizing over what is possibly a massive network. Furthermore, the firm's problem has to be cognizant of uncertainty in available capacity (such as arising from wind power), amongst others leading to a growth in complexity arising from scenario-based modeling. Finally, any computation requires one to aggregate all the firm problems, suggesting that a large number of firms would make solvability difficult at best. As part of our research, we constructed an algorithm that scales slowly in effort with respect to growth in problem size. This scalability is crucial being able to solve problems of meaningful sizes and represents an important building block as we make efforts to integrate renewables into our portfolio. Our scheme is naturally distributed across agents while the firm problems are solved via a scalable cutting-plane method. A key contribution of our work is the provision of theoretical convergence guarantees and error bounds. Preliminary numerical tests suggest that the algorithm scales slowly in all three sources of complexity (network size, number of scenarios and number of firms). We see this work as extremely important in terms of efficiently solving a broad class of game-theoretic problems that are complicated by risk and uncertainty.

Finally, we derive some insights using a 53-node model of the Belgian network. Here, we allow a set of generators, some with a significant proportion of wind assets, to compete in the forward and spot-market in the face of uncertainty. Every firm intends to maximize expected profit over both periods while reducing his risk of capacity shortfall. For generators with highly predictable availability, this risk is largely zero; for wind-based generators that bid aggressively, this risk can be significant. Our models provide several insights for market design. For instance, we observe that higher levels of risk-aversion lead to lower participation in the forward markets while higher level of wind penetration.

PART 1

Impact of Increased DFIG Penetration on Small-Signal and Transient Stability

Vijay Vittal

Arizona State University

Information about this project

Vijay Vittal
Ira A. Fulton Chair Professor
Department of Electrical Engineering
Arizona State University
PO Box 875706
Tempe, AZ 85287-5706
Tel: 480-965-1879
Fax: 480-965-0745
Email: vijay.vittal@asu.edu

Power Systems Engineering Research Center

The Power Systems Engineering Research Center (PSERC) is a multi-university Center conducting research on challenges facing the electric power industry and educating the next generation of power engineers. More information about PSERC can be found at the Center's website: http://www.pserc.org.

For additional information, contact:

Notice Concerning Copyright Material

Table of Contents

i

List of Figures

ii

List of Tables

Glossary

A	state or plant matrix
A_r	area swept by the rotor blades
B	input matrix
C	output matrix
Cp	power coefficient
D	feed forward matrix
DFIG	doubly fed induction generator
f	frequency of oscillation
GE	General Electric
GENROU	round rotor generator model
GWEC	global wind energy council
H	inertia constant (s)
K_b	fixed constant
P	mechanical power extracted from the wind
p_{ji}	participation factor of the jth variable in the ith mode
P_m	mechanical power delivered by the generator
P_R	power delivered to the rotor
P_S	power delivered by the stator
PSAT	power flow and short circuit analysis tool
SSAT	small signal analysis tool
TSAT	transient security assessment tool
v_i	right eigenvector
v_w	wind speed
w_i	left eigenvector
WTG	wind turbine generator
δ_{max}	maximum angle separation of two generators
ζ	damping ratio
η	transient stability index
θ	blade pitch angle
λ	ratio of the rotor blade tip speed and wind speed
ρ	air density
ω	rotational speed of the turbine

1. Introduction

1.1 Background

Growing environmental concerns and attempts to reduce dependency on fossil fuel resources are bringing renewable resources to the mainstream of the electric power sector. Among the various renewable resources, wind power is assumed to have the most favorable technical and economical prospects [1]. When deployed in small scale, as was done traditionally, the impact of wind turbine generators (WTGs) on power system stability is minimal. In contrast, when the penetration level increases, the dynamic performance of the power system can be affected.

Several countries are taking steps to develop large-scale wind markets. According to news released by global wind energy council (GWEC) [2], year 2008 was another record year with more than 27 GW of new installations, bringing the world's total wind installed capacity to over 120 GW. The United States surpassed Germany to become the number one market in wind power reaching total installed wind power capacity to over 25.17 GW. Following in rank are Germany, Spain and China with installed capacities of 23.9 GW, 16.75 GW and 12.21 GW respectively.

The WTGs in a wind farm are distributed within the farm, but the total output of the farm normally connects to the bulk power system at a single substation, in a fashion similar to conventional central-station generation [3]. The increased number of wind farms brings large amount of asynchronous generators in the system. As the dynamics of asynchronous machines are different from those of synchronous machines, the grid could face technical challenges. With the large penetration of wind power, the stability of the grid could be seriously impacted [4,5].

There are many different generator types for wind-power applications in use today. Among those, variable speed wind turbines utilizing doubly fed induction generators (DFIGs) are gaining prominence in the power industry. As the performance is largely determined by the converter and the associated controls, a DFIG is an asynchronous generator. Since DFIGs are asynchronous machines, they primarily only have four mechanisms by which they can affect the damping of electromechanical modes (since they themselves do not participate in the modes):

1. Displacing synchronous machines thereby affecting the modes
2. Impacting major path flows thereby affecting the synchronizing forces
3. Displacing synchronous machines that have power system stabilizers
4. DFIG controls interacting with the damping torque on nearby large synchronous generators

This work addresses the first two mechanisms listed above.

Following a large disturbance, the restoring mechanisms that bring the affected generators back to synchronism, are related to the interaction between the synchronizing forces and the inertia of the generators in the system. In the case of a DFIG, however, the inertia of the turbine is effectively decoupled from the system. The power electronic converter at the heart of the DFIG controls the performance and acts as an interface

between the machine and the grid. With conventional control, rotor currents are always controlled to extract maximum energy from the wind. Hence, with the increased penetration of DFIG based wind farms, the effective inertia of the system will be reduced and system reliability following large disturbances could be significantly affected.

Several research efforts have been devoted to address the challenges raised by the proliferation of wind power. According to [6], the DFIG equipped with four-quadrant ac-to-ac converter increases the transient stability margin of electric grids compared to the fixed speed wind systems based on squirrel-cage generators. Reference [7] advocates that the DFIG equipped with power electronics converters and fault ride through capability will have no adverse effect on the stability of a weak grid. Reference [8] focuses on the operational mode of variable speed wind turbines that could enhance the transient stability of the nearby conventional generators. The effect of wind farms on the modes of oscillation of a two-area, four-generator power system has been analyzed in [9]. Reference [10] advocates that the generator types used in wind turbines do not take part in power system oscillations. Rather, the penetration of wind power will have a damping effect due to reduction in the size of synchronous generators that engage in power system oscillations. Reference [11] advocates that increased wind power penetration is accompanied by congestion at weak interconnection lines that leads to reduced damping.

This work presents a systematic approach based on eigenvalue sensitivity to examine the effect of penetration of DFIGs on a large system. The approach involves detailed analysis of a fairly large system using commercial grade software. The analysis of the critical modes of oscillation is further extended to observe whether or not the system is transiently stable when the particular mode is excited due to a large disturbance.

1.2 Overview of the Problem

The electric power industry is embracing several renewable technologies with the aim of reducing dependency on fossil fuel based technologies for electric power generation. These energy conversion technologies are normally based on asynchronous generation which is coupled to the grid via power electronic converters. When deployed in small scale, as was done traditionally, the impact of these renewable based generations on power system stability is minimal. In contrast, when the penetration level increases, the dynamic behavior of the power system gets affected. Moreover, penetration of power electronic based variable speed wind turbine generator such as DFIG shows marked impact on stability of the system. These large wind farms are connected to the grid at lower voltage levels, which results in higher fault currents. As a result, with the increase in penetration of wind generation, transient stability and overall frequency response may be affected. Given this premise, the present study encompasses the study of the grid impact of DFIG wind farms. The impact study is carried out by perturbing the system with short circuit faults and applying disturbances at various locations in the system.

The restoring forces that bring the affected generators back to synchronism, following the large disturbance, are related to the interaction between the synchronizing power coefficient and the total system inertia. In the case of DFIG, however, the inertia of the turbine is effectively decoupled from the system. With the penetration of DFIG based wind farms, the effective inertia of the system will be reduced. With the inertia decreasing due to the penetration of DFIG based wind farms and the possibility of large

impacts due to larger fault currents, system reliability following large disturbances could be significantly affected.

Although the generator technologies used in wind turbines do not engage in power system oscillations [12], the changes in operational structure due to the placement of wind farms can impact the oscillations. Wind farms are normally located far from major load centers. This constitutes power transfer over longer distances and might involve power flow through congested lines. The scenario might lead to significant change in generation profile and power flow, consequently, affecting the small signal stability of the system. In this framework, the objectives of the proposed work are outlined in the following section.

1.3 Report Organization

The part of the report is organized into seven sections. Section 2 presents an overview of various technologies with regard to wind turbine generators. Section 3 presents underlying modeling concept of DFIG technology. Section 4 discusses the impacts associated with the penetration of DFIGs on power system stability. Section 5 details the approach developed to analyze the impact of increased penetration of DFIGs on small signal and transient stability. Section 6 presents the simulation results and discussion with regard to the small signal and transient stability. Conclusions drawn from the analysis are presented in Section 7.

2. Wind Turbine Generator Technologies

There are many different generator types for wind power applications in use today. The main distinction can be made between fixed speed and variable speed wind generator types.

2.1 Fixed speed wind turbine generator

In the early stage of wind power development, most wind farms were equipped with fixed speed wind turbines and induction generators. A fixed speed wind generator is usually equipped with a squirrel cage induction generator whose speed variations are limited. Power can only be controlled through pitch angle variations. Because the efficiency of wind turbines depends on the tip-speed ratio, the power of a fixed speed wind generator varies directly with the wind speed [13]. Since induction machines have no reactive power control capabilities, fixed or variable power factor correction systems are usually required for compensating the reactive power demand of the generator. Figure 2.1 shows the schematic diagram of the fixed speed induction machine.
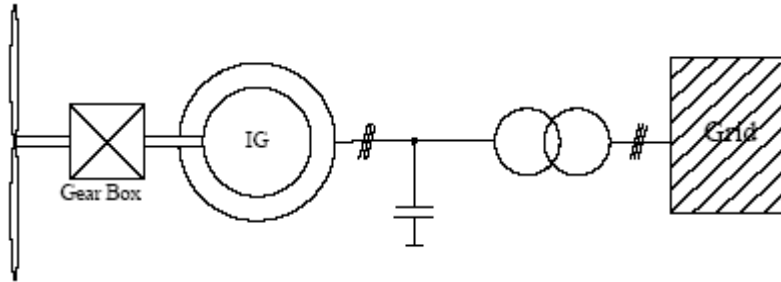
Figure 2.1 Fixed speed induction machine [13]

2.2 Variable speed wind turbine generator

Several technologies and historical applications of variable speed wind generator have been discussed in [14]. Variable speed concepts allow operating the wind turbine at the optimum tip-speed ratio and hence at the optimum power coefficient for a wide wind speed range. The two most widely used variable speed wind generator concepts are the DFIG and the converter driven synchronous generator [13].

2.2.1 Doubly fed induction generator wind turbine

Due to advantages such as high energy efficiency and controllability, the variable speed wind turbine using DFIG is getting more attention. DFIG is basically a standard, wound rotor induction generator with a voltage source converter connected to the slip-rings of the rotor. The stator winding is coupled directly to the grid and the rotor winding is connected to power converter as shown in Figure 2.2.

The converter system enables two way transfer of power. The grid side converter provides a dc supply to the rotor side converter that produces a variable frequency three phase supply to generator rotor via slip rings. The variable voltage into the rotor at slip frequency enables variable speed operation. Manipulation of the rotor voltage permits the control of the generator operating conditions.

In case of low wind speeds, the drop in rotor speed may lead the generator into a sub-synchronous operating mode. During this mode, DFIG rotor absorbs power from the grid. On the other hand during high wind speed, the DFIG wind turbine running at super synchronous speed will deliver power from the rotor through the converters to the network. Hence, the rotational speed of the DFIG determines whether the power is delivered to the grid through the stator only or through the stator and rotor [15]. Power delivered by the rotor and stator is given by [16]:

$$P_R = sP_S \qquad\qquad ((3.1)$$

$$P_G = (1 \pm s)P_S \qquad\qquad ((3.2)$$

where, P_G is the mechanical power delivered by the generator, P_S is the power delivered by the stator, P_R is the power delivered to the rotor.

However, under all operating situations, the frequency of rotor supply is controlled so that under steady conditions, the combined speed of the rotor plus the rotational speed of the rotor flux vector matches that of the synchronously rotating stator flux vector fixed by the network frequency [17]. Hence, the power could be supplied to the grid through the stator in all three the modes of operation, namely, sub synchronous, synchronous and super synchronous modes. This provides DFIG a unique feature beyond the conventional induction generator as the latter can deliver power to the grid during super synchronous speed only.
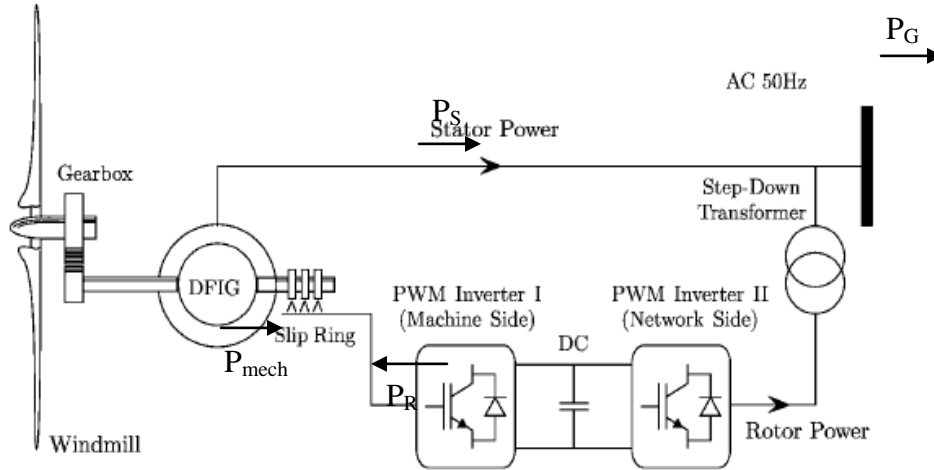
Figure 2.2 Doubly fed induction generator [18]

2.2.2 Converter driven synchronous generator

This category of wind turbines uses a synchronous generator that can either be an electrically excited synchronous generator or a permanent magnet machine. To enable variable-speed operation, the synchronous generator is connected to the network through a variable frequency converter, which completely decouples the generator from the network. The electrical frequency of the generator may vary as the wind speed changes, while the network frequency remains unchanged. The rating of the power converter in

this wind turbine corresponds to the rated power of the generator plus losses. The schematic of the converter driven synchronous generator is as shown in Figure 2.3
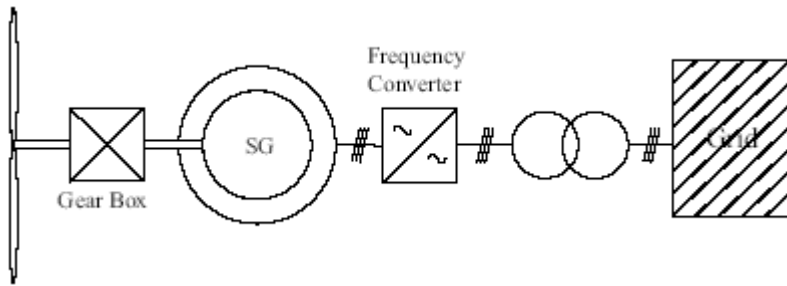
Figure 2.3 Converter driven synchronous generator [13]

3. Modeling of DFIG

For power system stability studies, modeling of a DFIG should be considered for steady state analysis as well as for large disturbance dynamic analysis [19].

3.1 Modeling for steady state analysis

For power flow analysis, the fixed speed WTG is modeled as a negative load and integrated into the system as a PQ bus. The model is assumed to have constant reactive power (Q) equal to the amount being absorbed at the real power (P) level being studied. This should be accompanied by modeling of shunt capacitors for the WTG reactive consumption. For DFIG and full converter units that have voltage source converters, the units may be modeled as a PV bus with appropriate VAR limits. This is because both these types of units have the capability to generate reactive power.

Although the wind turbines are distributed within the wind farms, the bulk power from wind farms is connected to the grid at a single substation similar to the central generation plants. The aggregated model is applicable when the purpose is to observe the influence on power network rather than within the wind farm. The modeling of a GE WTG represented by a single model, with a simplified representation of the collector system is shown in Figure 3.1 below [19].
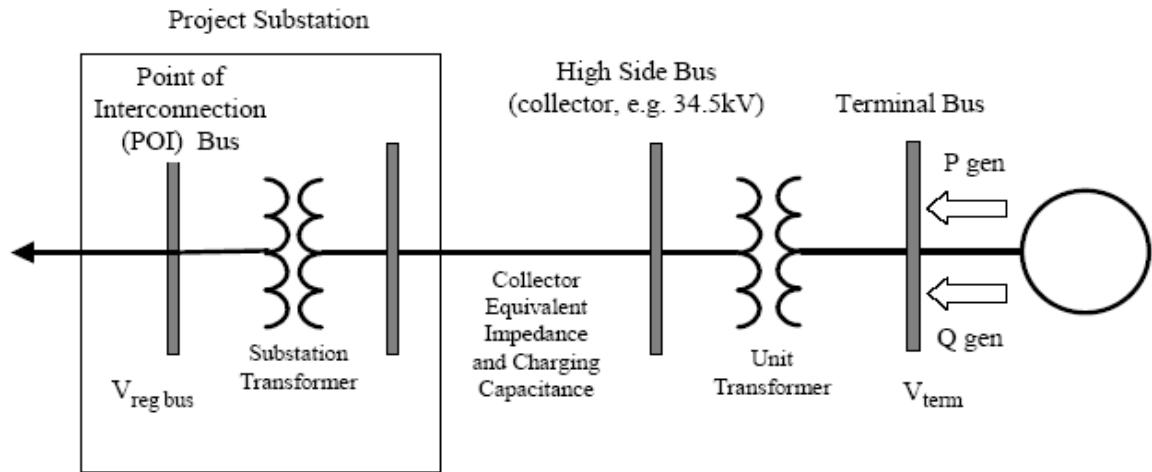
Figure 3.1 Power flow model of wind farm [19]

3.2 Modeling for dynamic analysis

The power flow provides initial conditions for dynamic simulation. For power system dynamic simulations, the wind farm is modeled as a single equivalent machine as shown in Figure 3.1. The assumption is reasonable when the purpose is to observe the effect of penetration on the external network rather than within the wind farm [20**Error! Bookmark not defined.**]. Apparently, a complete model of wind farm with large number of wind turbines will increase the computational burden. A number of components contribute to the dynamic behavior of a DFIG. These are [21],

- Turbine Aerodynamics

- Turbine mechanical control (i.e. pitch control)

- Shaft dynamics

- Generator electrical characteristics

- Electrical controls (such as converter controls, switching of shunt capacitor banks etc.)

- Protection relay settings.

Figure 3.2 shows the overall component of a WTG model.
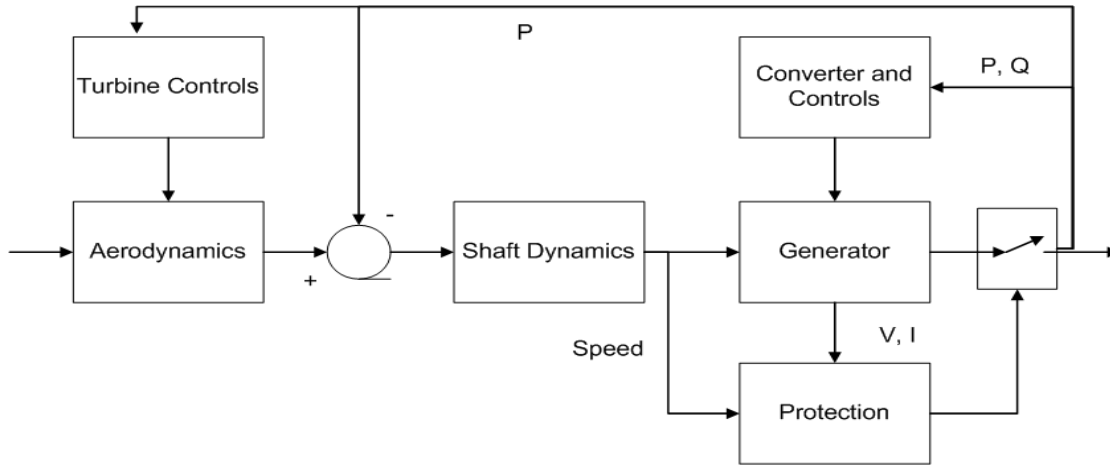
Figure 3.2 Components of a WTG model [21]

Although the parameters for the aerodynamics, turbine controls and protection systems for the various types of WTG might be different from one manufacturer to the other, the model structure will essentially be similar. In the case of stall controlled units, there is no turbine blade pitch control. For constant speed units, blade pitch will be used to regulate power instead of speed on variable-speed units. The shaft dynamics may be modeled as a single equivalent mass or as two masses where one mass represents rotor/turbine blades and the second represents the electrical generator [21].

3.3 DFIG control models

The DFIG wind turbine control usually consists of two parts, namely, the mechanical control to govern the wind turbine blade pitch angle and the electrical control on the power converter. The power converter usually includes the power control, the rotor side current control, dc link dynamics and the grid side current control. The two controls should work in harmony in order to achieve the overall objective of the DFIG.

3.4 Wind generator model

Three controllers are required to provide controls for frequency/active power, voltage/reactive power, and pitch angle/mechanical power [22]. The output of these three controllers would be the input to the end block of DFIG which is essentially the wind

generator model. Each controller has one reference value. The operating condition of the generator in the power flow is used to initialize the model and the outputs from the model are the current injections into the network at the generator bus. The pitch angle/mechanical power controller output (mechanical power) is used to solve the induction generator swing equation [22].

3.4.1 Mechanical power computation model

The purpose of this block is to compute the mechanical power of a DFIG model for a given pitch angle and wind speed. This model signifies the aerodynamics block in Figure 3.2. The wind turbine mechanical power can be calculated from the energy contained in the wind as follows [19],

$$P = \frac{\rho}{2} A_r v_w^3 C_p(\lambda, \theta) \tag{4.1}$$

where, P is the mechanical power extracted from the wind, ρ is the air density, A_r is the area swept by the rotor blades, v_w is the wind speed, C_p is the power coefficient, λ is the ratio of the rotor blade tip speed and wind speed, θ is the blade pitch angle. The tip speed ratio can be calculated as [19],

$$\lambda = K_b = \frac{\omega}{v_w} \tag{4.2}$$

where, ω is the rotational speed of the turbine, K_b is a fixed constant.

3.4.2 Turbine control model

The turbine control model is used to control the blade pitch angle in response to the wind speed. When the available wind power is above equipment rating, blades are pitched to limit the mechanical power delivered to the shaft to the equipment rating (1 pu). When available wind power is less than rated, blades are set at minimum pitch to maximize the mechanical power. The turbine control model sends a power order signal to the electrical control, requesting that the converter deliver this power to the grid.

The overall DFIG model comprising of the details of each control blocks together with the parameter values that have been used for the present study is shown in Figure 3.3.

9

Figure 3.3 DFIG Model [22]

10

4. Impacts on Power System Operation and Stability

Power system stability is the property of a power system that ensures the stable operating equilibrium under normal conditions and restores an acceptable state of equilibrium when the system is subjected to a disturbance [27]. The ability of the network to cope with these disturbances and to restore the normal operating condition is addressed by stability studies. In order for satisfactory system operation, synchronous machines that represents a major portion of electrical power generation should remain in synchronism. One of the major factors governing the stability is the dynamics of generator rotor angles and power-angle relationships [27].

In an interconnected system, the ability to restore equilibrium between electromagnetic torque and mechanical torque is determined by the rotor angle stability of each synchronous machine. With the increased number of wind farms in operation, the system experiences change in dynamic characteristics. The change in dynamics can be attributed to the introduction of asynchronous machines for power generation. Furthermore, the characteristics associated with exploitation of wind energy and components used for power conversion also contribute to change in system dynamics.

Following a perturbation, the change in electromagnetic torque of the synchronous machine can be explained by two torque components, namely, synchronizing torque component and damping torque component. System stability depends on the existence of both components of torque for each of the synchronous machines [23]. Insufficient synchronizing torque results in non-oscillatory instability whereas insufficient damping torque results in oscillatory instability. In order to simplify the analysis of stability problems, the rotor angle stability is further categorized into transient stability and small signal stability. These categories in response to the penetration of wind power are discussed in the following sections.

4.1 Transient stability

Transient stability is the ability of a power system to maintain synchronism when subjected to a severe disturbance. The severe network disturbances include equipment outages, load changes or faults that result in large excursion of generator rotor angles. The resulting system response is influenced by the nonlinear power angle relationship. Transient stability depends on both the initial operating state of the system and the severity of the disturbance. Instability is usually due to insufficient synchronizing torque and results in aperiodic angular separation. The time frame of interest in transient stability studies is usually 3 to 5 seconds following the disturbance. The duration may extend up to 10-20 seconds for a very large system with dominant inter-area swings [23].

In a synchronous machine, if during a network disturbance the electrical torque falls below the mechanical torque, the rotor will accelerate causing the increase in rotor speed and angular position of the rotor flux vector. Since the increase in rotor angle results in an increase in the generator load torque, a mechanism exists to increase the electrical torque so as to match the mechanical torque. In case of DFIG, generator load disturbances also give rise to variations in the speed and the position of the rotor. However, due to the asynchronous operation involved, the position of the rotor flux vector is not dependent on the physical position of the rotor and the synchronizing torque angle characteristic does

not exist [17]. Proper control mechanism can reduce the impact of disturbance prominent due to increased DFIG penetration. The wind farms may be controlled in such a way that the dynamic characteristics depicted by DFIG in the network mimic those of conventional synchronous generator [5,17].

Traditionally, the protection systems of wind turbines were designed to disconnect the units whenever a grid fault was detected. However, with the increasing integration of wind power, new system requirements have demanded the wind turbines to ride through the temporary faults. This has resulted in more emphasis on transient stability performance, power oscillations and system damping. As discussed earlier, the transient stability of a system with wind turbines also depends on factors such as fault conditions and network parameters. Wind speed, however, is assumed to be constant in transient stability simulation involving wind turbines. The mechanical power and mechanical torque, on the other hand, is not constant as it depends on wind speed as well as the generator speed [24].

Several recent papers have revealed that transient stability of the system is enhanced when variable speed wind turbines using DFIG are integrated into the system instead of fixed-speed turbines. However, a major drawback of using grid-connected power electronic converter based DFIGs, is their sensitivity to grid disturbances. Faults in the system may result in rush of active power from the rotor terminals towards the converter. The power tends to flow from the rotor side converter to the grid side converter through the capacitor linking the two converters. Due to the low voltages at machine terminals, the grid side converter is limited in its ability to transfer this extra power to the grid. Consequently, charging on the capacitor increases leading to high voltage across its terminals [6,25]. In order to avoid further damages, a circuit known as a crowbar is used to protect the converter. The crowbar short circuits the generator rotor through a resistance and provides a safe route to the high transient currents when the rotor current exceeds certain protection limits [26]. With the crowbar, the machine behaves like a conventional induction generator.

4.2 Small signal stability

Small signal stability is defined as the ability of the power system to maintain synchronism when subjected to small disturbances [27]. The disturbance is regarded as small if the equations describing the system response can be linearized for the purpose of analysis. The small signal stability problem normally occurs due to insufficient damping torque which results in rotor oscillations of increasing amplitude [27]. The following general equations can be used to describe the dynamics of the power system,

$$\dot{x} = f(x, u, t) \tag{(5.1)}$$

$$y = g(x, u). \tag{(5.2)}$$

For small signal stability analysis, the nonlinear equations of the dynamic power system are first linearized around a specific operating point. The resulting set of linear differential equations describes the dynamic behavior of the power system subject to a small disturbance around this operating point. The linearized equation is of the form,

$$\Delta \dot{x}_i = \frac{\partial f_i}{\partial x_1} \Delta x_1 + \cdots + \frac{\partial f_i}{\partial x_n} \Delta x_n + \frac{\partial f_i}{\partial u_1} \Delta u_1 + \cdots + \frac{\partial f_i}{\partial u_r} \Delta u_r \qquad ((5.3)$$

$$\Delta y_j = \frac{\partial g_j}{\partial x_1} \Delta x_1 + \cdots + \frac{\partial g_j}{\partial x_n} \Delta x_n + \frac{\partial g_j}{\partial u_1} \Delta u_1 + \cdots + \frac{\partial g_j}{\partial u_r} \Delta u_r. \qquad ((5.4)$$

The linearized equation can be written in the form,

$$\Delta \dot{x} = A \Delta x + B \Delta u \qquad ((5.5)$$

$$\Delta y = C \Delta x + D \Delta u \qquad ((5.6)$$

where, A, B, C and D are known as state or plant matrix, input matrix, output matrix and feed forward matrix respectively.

The state equation in the frequency domain can be obtained by performing the Laplace transform of the above equation as follows,

$$s\Delta x(s) - \Delta x(0) = A\Delta x(s) + B\Delta u(s) \qquad ((5.7)$$

$$\Delta y(s) = C\Delta x(s) + D\Delta u(s) \qquad ((5.8)$$

$$(sI - A)\Delta x(s) = \Delta x(0) + B\Delta u(s). \qquad ((5.9)$$

Equation 5.9 is defined as the characteristic equation of matrix A. The values of s which satisfy the characteristic equation are known as the eigenvalues of matrix A. Matrix A consists of the partial derivatives of the function f with respect to the state variables. The eigenvalues of matrix A, thus exhibit important information about the system response to small perturbations and thus characterize the stability of the system [27]. The change in design and operating condition of the power system is reflected in the eigenvalues of the system state matrix.

The time dependent characteristic of a mode corresponding to an eigenvalue λ is given by $e^{\lambda t}$. A real positive eigenvalue determines an exponentially increasing behavior while a negative real eigenvalue represents a decaying mode. A complex eigenvalue with positive real part results in an increasing oscillatory behavior and one with a negative real part results in damped oscillation. The real component of the eigenvalue gives the damping and the imaginary component gives the frequency of oscillation. The frequency of oscillation (f) and damping ratio (ζ) of a complex eigenvalue ($\lambda = \sigma + j\omega$) can be represented as,

$$f = \frac{\omega}{2\pi} \qquad (5.10)$$

$$\zeta = \frac{-\sigma}{\sqrt{\omega^2 + \sigma^2}}. \qquad (5.11)$$

The damping ratio determines the rate of decay of the amplitude of the oscillation. An eigenvalue of the state matrix A and the associated right eigenvector (v_i) and left eigenvector (w_i) are defined as,

$$A v_i = v_i \lambda_i \qquad (5.12)$$

13

$$w_i^T A = \lambda_i w_i^T. \tag{5.13}$$

The component of right eigenvector measure the relative activity of each variable in the ith mode and the component of left eigenvector weight the initial condition of the ith mode. The participation factor of the jth variable in the ith mode is defined as the product of the jth component of the right and left eigenvectors corresponding to the ith mode,

$$p_{ji} = w_{ji} v_{ji}. \tag{5.14}$$

The effect of the system parameters on the overall system dynamics can be examined by evaluating the sensitivity of the eigenvalues with respect to variations in system parameters [28]. In large power systems, the small-signal stability problem can be either local or global in nature. Power system oscillations are usually in the range between 0.1 and 2 Hz depending on the number of generators involved. Local oscillations lie in the upper part of the range and consist of the oscillation of a single generator or a group of generators against the rest of the system [29]. Stability (damping) of these oscillations depends on the strength of the transmission system as seen by the power plant, generator excitation control systems and plant output [27]. In contrast inter area oscillations are in the lower part of the frequency range and comprise the oscillations among the group of generators. Load characteristics, in particular, have a major effect on the stability of inter area modes [27]. The time frame of interest in small signal stability studies is of the order of 10-20 seconds following a disturbance [23].

The variable speed design consisting of power electronics converter imparts paramount effect on dynamic performance of the DFIG. The dynamic characteristics of variable speed wind turbines are completely governed by the power electronic converter. The converter decouples the turbine from the grid by not only controlling the rotor speed and electrical power, but also damping out any rotor speed oscillations that may occur within the WTG. On the other hand, the control action of DFIG might as well affect the damping torque on the nearby large synchronous generators.

As the penetration level increases, the replacement of synchronous machines by these asynchronous machines having entirely different dynamics does affect the system modes of oscillations. The system dynamics becomes even more diverse when the displaced synchronous machines have power system stabilizers. Wind farms are generally located far from major load centers. This constitutes power transfer over longer distances and might involve power flow through congested lines. The scenario might lead to significant change in generation profile and power flow, consequently, affecting the small signal stability of the system.

4.3 Frequency control and inertia

In any power system, frequency is controlled by balancing the power generation against load demand on a second-by-second basis. There is a need for continuous adjustment of generator output as the load demand varies. At the same time, the system should be able to respond to occasional larger mismatches in generation and load caused, for example, by the tripping of a large generator or a large load.

In the event of a sudden failure in generation or connection of a large load, the system frequency may drop below its continuously controlled limit. The system frequency drops at a rate initially determined by power imbalance and inertia of the system. Thus when the power system frequency suddenly decreases, the system tries to meet the electrical power deficit by the energy stored in rotating mass of the system. This is due to the coupling between the power system frequency and the electromagnetic torque of the generators and is known as the "natural" inertial response of the generators.

The inertia of wind turbines is comparable to that of conventional synchronous generators. In fixed speed wind turbine systems with uncontrolled squirrel cage rotors, this inertia of the turbine is automatically available as the frequency of the grid tends to decrease following a fault or loss of generation/transmission line, the speed of the turbine reduces correspondingly, and part of stored energy is fed in to the distribution system through the induction generator. However, in the case of DFIG units, their dynamic performance as seen by the grid is completely governed by the power electronic converters that control them. With the conventional control, where rotor currents are always controlled to extract maximum energy from the wind by varying the rotor speed, the inertia of the turbine is effectively decoupled from the system. With the penetration of DFIG based wind farms, the effective inertia of the system will be reduced. With the inertia decreasing due to a large number of DFIG wind turbines in operation, system reliability following large disturbances could be significantly affected.

5. Proposed Approach

The work encompasses the study of increased penetration of wind turbine generators on the small signal and transient stability of the system. The power flow solution provides the initial operating condition for dynamic simulation of the power system. The dynamic simulation includes transient stability study and small signal stability study.

5.1 Small signal stability

The basis of this study lies on the premise that with the penetration of DFIG based wind farms the effective inertia of the system will be reduced. In this regard, a first step proposed towards studying the system behavior with increased DFIG penetration is to identify how the small signal stability behavior changes with the change in inertia. The approach is intended to evaluate eigenvalue sensitivity with respect to generator inertia. The eigenvalue sensitivity with respect to inertia can be expressed as [30],

$$\frac{\partial \lambda_i}{\partial H_j} = \frac{w_i \frac{\partial A}{\partial H_j} v_i^T}{w_i^T v_i} \tag{5.1}$$

where, H_j is the inertia of jth conventional synchronous generator, λ_i is the ith eigenvalue, w_i and v_i is the left and right eigenvector corresponding to i^{th} eigenvalue respectively.

The eigenvalue of the state matrix A and the associated right eigenvector (v_i) and left eigenvector (w_i) are defined as,

$$A v_i = \lambda_i v_i \tag{5.2}$$

$$w_i^T A = \lambda_i w_i^T \tag{5.3}$$

The eigenvalue sensitivity had been addressed as early as the 1960s [31]. However, the key to the proposed analysis is to examine the sensitivity with respect to inertia and identify which modes are affected in a detrimental fashion and which modes are benefitted by the increased DFIG penetration. The following steps are adopted while evaluating the system response with respect to small disturbances:

- Replace all the DFIGs with conventional synchronous generators of the same MVA rating which will represent the base case operating scenario for the assessment.

- Perform eigenvalue analysis in the frequency range: 0.1 to 2 Hz and damping ratio below 2.5%.

- Evaluate the sensitivity of the eigenvalues with respect to inertia (H_j) of each wind farm represented as a conventional synchronous machine which is aimed at observing the effect of generator inertia on dynamic performance.

- Perform eigenvalue analysis for the case after introducing the existing as well as planned DFIG wind farms in the system.

5.2 Transient Stability

The machine rotor angle measured with respect to a synchronously rotating reference is considered as one of the parameters to test stability of the system. The severity of a contingency and the trajectory of a system following a disturbance can be assessed by evaluating the transient stability index (*TSI*). The *TSI* is obtained from the transient security assessment tool (TSAT) which calculates the index based on angle margin algorithm as follows [22],

$$TSI = \frac{360 - \delta_{max}}{360 + \delta_{max}} \times 100 \qquad -100 < TSI < 100 \tag{5.4}$$

where, δ_{max} is the maximum angle separation of any two generators in the system at the same time in the post-fault response. *TSI* > 0 and *TSI* ≤ 0 correspond to stable and unstable conditions respectively.

The objective of transient stability analysis here is to examine if the modes identified in the small signal stability analysis can be excited by the large disturbance and analyze the transient stability performance. Each of the critical modes obtained in the small signal stability study is scrutinized in time domain.

6. Simulation Results and Discussion

The simulation results carried out for the two different study objectives, namely, small signal stability and transient stability are detailed. With the objective of observing the system response for small and large disturbances, the same base case operating scenario is considered for small signal stability and transient stability study cases.

6.1 System Description

The study is carried out on a large system having over 22000 buses, 3104 generators with a total generation of 580,611 MW. All the modeling details provided within the base set of data are retained and represented in the analysis. Within this large system, the study area with a large increase of wind penetration has a total installed capacity of 4730.91MW. The analysis performed is based on the information provided with regard to the existing and planned increases in wind penetration. A total of 14 wind farms with a total installed capacity of 1460 MW are modeled as DFIGs. This information is used to set up the change cases from the base case provided. The objective is to systematically analyze the impact on system dynamic performance given a large system and the planned penetration of DFIG wind generation.

The system has transmission voltage levels ranging from 34.5 kV, 69 kV, 161 kV to 345 kV. WTGs are connected at distribution voltage level of 575 V, 600 V, 690 V and 25 kV. The DFIG model used throughout the work is based on the model developed in [19]. The study is conducted using the package DSA^{Tools} developed by Powertech Labs Inc. This includes power flow and short circuit analysis tool (PSAT), transient security assessment tool (TSAT) and small signal analysis tool (SSAT). All new wind farms are represented using the GE 1.5 MW DFIG model available in TSAT.

6.2 Scenario Description

Four different cases are analyzed. The description of each case is provided below:

- Case A constitutes the case wherein all the existing DFIGs in the study area in the original base case are replaced by conventional round rotor synchronous machines (GENROU) of equivalent MVA rating.

- The original base case provided with existing DFIGs in the system is referred to as Case B.

- Case C constitutes the case wherein the penetration of DFIG based WTGs in the study area is increased by 915 MW. The load in the study area is increased by 2% (predicted load growth) and rest of the generation increase is exported to a designated nearby area.

- Case D constitutes the case wherein the DFIG wind farms with the increased wind penetration are replaced by GENROU of corresponding MVA rating. Thus, in Case D the GENROU machines representing the WTGs are of higher MVA rating than in Case A.

The export of increased power from the study area is aimed at keeping the total system power generation constant. This implies that the power export from the study area to the

neighboring area is implemented by the concomitant reduction in the generated power in the neighboring area by the same amount.

6.3 Small Signal Stability Analysis

6.3.1 Sensitivity analysis with respect to inertia

The sensitivity analysis with respect to inertia is only conducted for Case A where all machines in the system are represented by conventional synchronous generators. The sensitivity of a given mode with respect to inertia of each wind farm replaced by a conventional synchronous generator is obtained. The sensitivity is evaluated by computing a pair of modes, one of them with the value of inertia in the base case and the other with a "perturbed" value. When computing the mode in the perturbed case, the inertia is increased by 0.5%. The computation is performed using an available feature in SSAT. This feature allows for the evaluation of sensitivity with respect to a wide range of parameters. In this analysis inertia was chosen to be the sensitivity parameter. The analysis inherently accounts for the insertion points of the wind farms in the system.

The analysis is carried out only for Case A, for all modes in a range of frequencies from 0.1Hz to 2Hz. As the stability of a mode is determined by the real part of eigenvalue, the sensitivity of the real part is examined and the mode which has the largest real part sensitivity to change in inertia is identified. Among the several modes of oscillation analyzed, the result of sensitivity analysis associated with the mode having significant detrimental real part sensitivity, in comparison to the real part of the eigenvalue is shown in Table 6.1.

Table 6.1 Dominant Mode with Detrimental Effect on Damping

Real Part (1/s)	Imaginary Part (rad/s)	Frequency (Hz)	Damping Ratio (%)
-0.0643	3.5177	0.5599	1.83

The corresponding sensitivity values for the real part of this mode with respect to each of the 14 wind farm generators replaced by conventional synchronous machines of the same MVA rating are shown in Table 6.2.

The real part sensitivities all having negative values as shown in Table 6.2 reveal that with the decrease in inertia at these locations, the eigenvalue will move towards the positive right half plane making the system less stable. Participation factor analysis for this mode shows that altogether 26 machines participate in the mode. Participation factors corresponding to each machine are shown in Figure 6.1.

Table 6.2 Eigen Value Sensitivity corresponding to the Dominant Mode
with Detrimental Effect on Damping

No.	Generator Bus #	Base Value of Inertia (s)	Sensitivity of Real Part (1/s^2)
1	32672	2.627	-0.0777
2	32644	5.7334	-0.0355
3	32702	3	-0.0679
4	32723	5.548	-0.0367
5	49045	5.2	-0.0383
6	49050	4.6	-0.0444
7	49075	4.2	-0.0475
8	52001	5.2039	-0.0389
9	55612	3.46	-0.0581
10	55678	4.3	-0.0467
11	55881	4	-0.0506
12	55891	4.418	-0.0466
13	55890	5.43	-0.037
14	55889	5.43	-0.0374
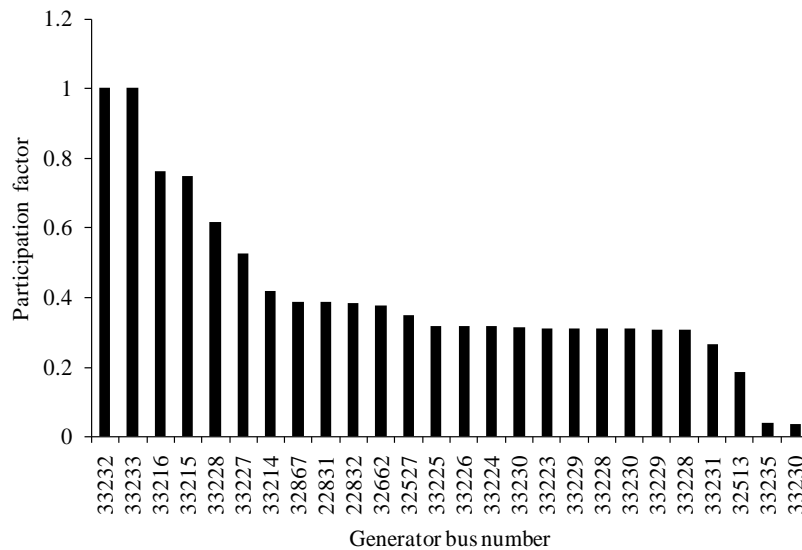
Figure 6.1 Participation factor corresponding to the generator speed state for the
dominant mode with detrimental effect on damping

The next step in the analysis is to observe if the penetration of DFIGs has beneficial
impact in terms of damping power system oscillations. The sensitivity with respect to
inertia is examined for positive real part sensitivity. This identifies the mode where the
increased penetration of DFIGs in the system results in shifting the eigenvalues of the
system state matrix towards the negative half plane. Among the several modes of

oscillation analyzed, the result of sensitivity analysis associated with the mode having the largest positive real part sensitivity is shown in Table 6.3.

Table 6.3 Dominant Mode with Beneficial Effect on Damping

Real Part (1/s)	Imaginary Part (rad/s)	Frequency (Hz)	Damping Ratio (%)
-0.0651	2.8291	0.4503	2.3

The corresponding real part sensitivity values for each of the 14 wind farm generators represented by conventional synchronous machines are shown in Table 6.4. The real part sensitivities are all positive in sign indicating that with the decrease in inertia at each of these locations the mode will move further into the left half plane making the system more stable. The participation factor analysis shows that 34 machines participate in this mode. The participation factors corresponding to each machine are shown in Figure 6.2.

Table 6.4 Eigen Value Sensitivity corresponding to the Dominant Mode
with Beneficial Effect on Damping

| No.	Generator Bus #	Base Value of Inertia(s)	Sensitivity of Real Part (1/s^2)
1	32672	2.627	0.0169
2	32644	5.7334	0.0078
3	32702	3	0.015
4	32723	5.548	0.008
5	49045	5.2	0.0075
6	49050	4.6	0.0092
7	49075	4.2	0.0104
8	52001	5.2039	0.0079
9	55612	3.46	0.0125
10	55678	4.3	0.0098
11	55881	4	0.0107
12	55891	4.418	0.0095
13	55890	5.43	0.0082
14	55889	5.43	0.008

Figure 6.2 Participation factor corresponding to the generator speed state for the dominant mode with beneficial effect on damping

6.3.2 Eigenvalue Analysis with DFIG penetration

Detailed eigenvalue analysis is conducted for Cases A to D in the frequency range of 0.1 Hz to 2 Hz to substantiate the results of the sensitivity analysis.

Table 6.5 shows the result of eigenvalue analysis corresponding to the mode listed in Table 6.1 which has detrimental impact with increased DFIG penetration. The critical mode is observed in all the four cases. The frequency of the mode is relatively unchanged. It is observed that the damping ratio associated with the mode is reduced from 1.83% in Case A to 1.16% in Case B. The damping ratio has further reduced to 0.68% in the Case C. However, in Case D with DFIGs replaced by conventional machines the damping ratio is improved to 1.22%. The change in damping ratio due the increased penetration of DFIGs accurately reflects the trend indicated by sensitivity analysis. In Cases B and C where the inertia is reduced due to the inclusions of DFIGs the damping has dropped. In Cases A and D where the machines are represented as conventional synchronous machines of equivalent rating, the damping is higher. The increased flow into the neighboring area does not affect this mode whereas the change in inertia significantly affects the damping of this mode.

Table 6.5 Result Summary for Cases A, B, C and D for Dominant Mode
with Detrimental Effect on Damping

Case	Real	Imaginary	Frequency (Hz)	Damping Ratio (%)	Dominant Machine
A	-0.0643	3.5177	0.5599	1.83	33232
B	-0.0412	3.5516	0.5653	1.16	33232
C	-0.0239	3.5238	0.5608	0.68	33232
D	-0.0427	3.4948	0.5562	1.22	33232

A total number of 28 dominant machines participate in the mode of oscillation in Case A. In Case B, the number of machines participating in the mode increases to 32. In Case C the number of machines participating in the mode further increased to 33. However, the number of machines participating in the mode of oscillation for Case D is 27.

Due to the space limitations the entire list of generators participating in all these modes is not shown here. Nevertheless, this analysis indicates a trend that with the increased penetration of DFIGs in the system, more machines are affected and they participate in the mode of oscillation.

In the course of the modal analysis in the frequency range considered, another mode, which is not observed in Case A and Case B is observed only in Cases C and D and is found to have low damping. The results corresponding to this mode are shown in Table 6.6. It appears that this mode manifests largely as a result of the increased exports to the neighboring area. The machines participating in the mode shown in Table 6.6 with their corresponding participation factor are shown in Figure 6.3.

Table 6.6 Result Summary between Cases C and D for Dominant Mode with Detrimental Effect on Damping with Increased Exports

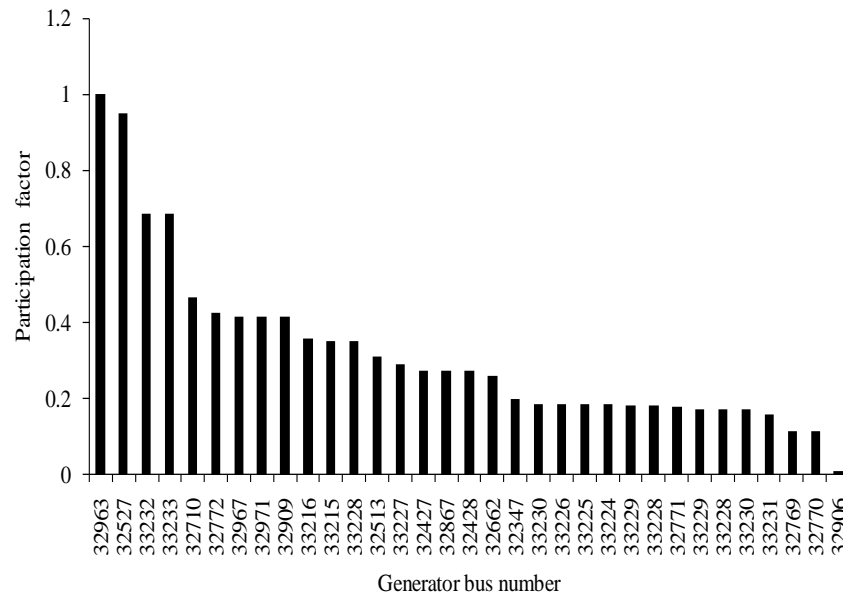| Case	Real	Imaginary	Frequency (Hz)	Damping Ratio (%)	Dominant Machine
C	-0.0663	3.9097	0.6223	1.7	32963
D	-0.0304	3.7911	0.6034	0.8	32963

Figure 6.3 Participation factor corresponding to the generator speed state for the dominant mode with increased exports

The eigenvalue analysis carried out for the mode with beneficial eigenvalue sensitivity is shown in Table 6.7. The damping ratio associated with the mode having a beneficial

impact has increased from 2.3% in the Case A to 2.55% in the Case B. It is also observed that the damping ratio has further improved to 2.68% in the Case C. However, in Case D with DFIGs replaced by conventional machines the damping ratio is reduced to 2.02%. These results again reflect the trend in damping change identified by the sensitivity analysis and also show the small change in damping as reflected by the sensitivity values in comparison to the mode which was detrimentally affected by the change in inertia.

Table 6.7 Result Summary for Cases A, B, C and D for the Dominant Mode with Beneficial Effect on Damping

Case	Real	Imaginary	Frequency (Hz)	Damping Ratio (%)	Dominant Machine
A	-0.0651	2.8291	0.4503	2.3	42037
B	-0.0725	2.8399	0.452	2.55	33216
C	-0.0756	2.8189	0.4486	2.68	42037
D	-0.0566	2.805	0.4464	2.02	42037

These results reveal that the eigenvalue sensitivity with respect to inertia provides an effective measure of evaluating the impact of DFIG penetration on the system dynamic performance. The detailed eigenvalue analysis carried out for each of the four cases is found to substantiate the results obtained from sensitivity analysis. The proposed method is found to be valid for identifying both the beneficial as well as the detrimental impact due to increased DFIG penetration.

6.4 Transient Stability Analysis

In conducting the transient stability analysis, the objective is to examine if the modes with low damping observed in the small signal analysis could be excited by a large disturbance. In order to identify the disturbance location which will excite the specific mode, the network structure around the machines with the largest participation factors in the specific mode is examined. Simulations are conducted for various three phase faults at several buses followed by outage of the line connected to the faulted bus. The fault is cleared at a suitable time depending on the bus voltage level.

6.4.1 Fault scenario 1 - Detrimental impact on system performance

The bus structure near the generator 33232 which has the largest participation factor (see Figure 6.1) in the mode detrimentally affected by the penetration of DFIGs (see Table 6.1) is shown in Figure 6.4. The objective here is to observe if a large disturbance near generator 33232 will excite the mode shown in Table 6.1. A three phase fault is applied at bus 33283 which is a 230 kV bus and is cleared after 5 cycles. The fault is cleared followed by the clearing of the line connecting the buses 33283 and 33282.
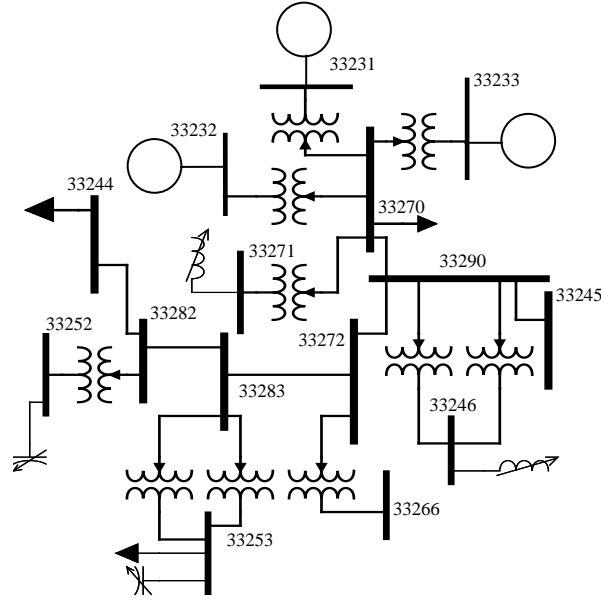
Figure 6.4 Single line diagram showing the bus structure near a generator
with highest participation

As the dominant mode considered from small signal analysis corresponds to the speed
state of the machines, the generator speed is observed in time domain. Figure 6.5 shows
the generator speed corresponding to the generator 32527 which is one of the machines
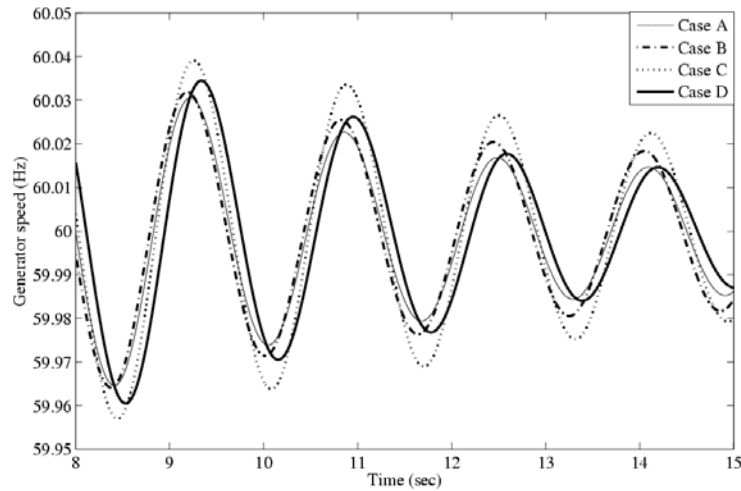participating in the mode as shown in Figure 6.1.

Figure 6.5 Bus 32527 generator speed for Cases A, B, C and D

Observing the oscillation corresponding to the last swing of Figure 6.5, the least amount
of damping is found in Case C which is followed by Case B and Case D. The damping is
found to be the highest in Case A. The damping behavior observed in time domain
corresponds exactly to the damping ratio provided by the eigenvalue analysis in Table

25

6.5. This fault scenario is thus found to have detrimental impact on system performance with respect to increased wind penetration.

6.4.2 Fault scenario 2 - Examine low damping mode with increased export

The bus structure near the generator at bus 32963 is shown in Figure 6.6.
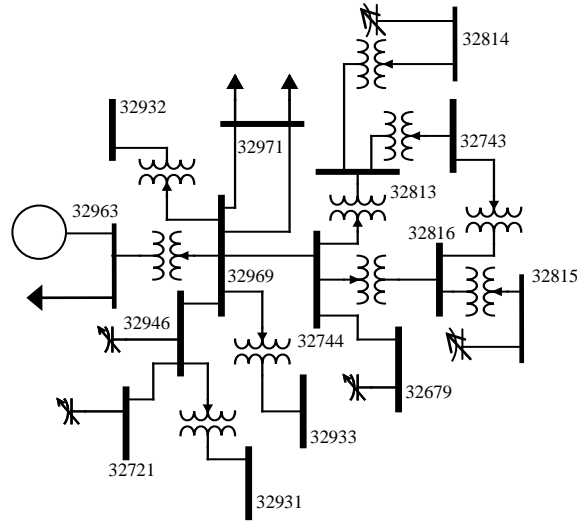

Figure 6.6 Single line diagram showing the bus structure near the generator 32963 with high participation

This is the generator which has the largest participation factor (see Figure 6.3) in the mode given in Table 6.6. The objective here is to observe if a large disturbance near generator 32963 will excite the mode shown in Table 6.6 and reflect the result obtained from small signal stability. A three phase fault is applied at bus 32946 which is at 345 kV. The fault is cleared after 4.5 cycles followed by clearing the line connecting the buses 32969 and 32946.

The time domain simulation is carried out to observe the effect of increased DFIG penetration on the system. The relative rotor angle plots for the Cases B and C are shown in Figure 6.7 – Figure 6.9. The machines represented in these plots are the dominant machines shown in Figure 6.3.
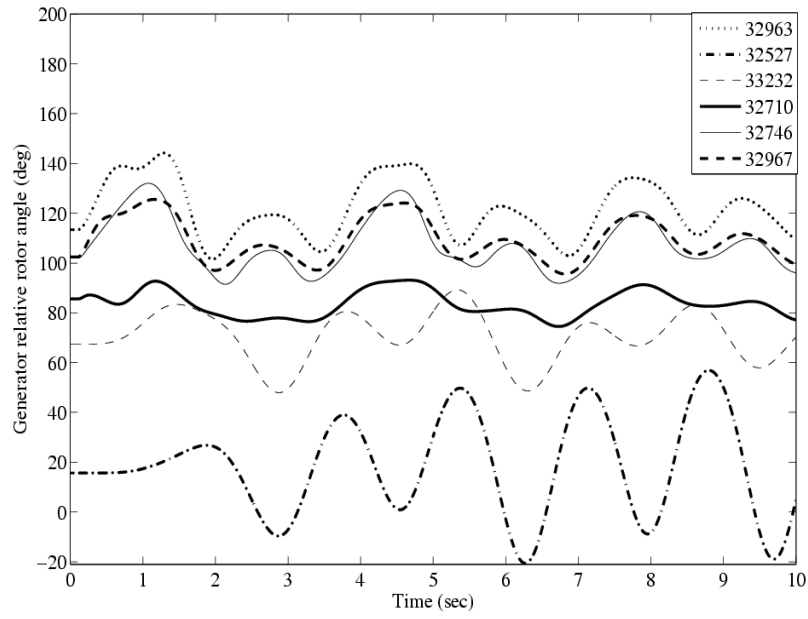
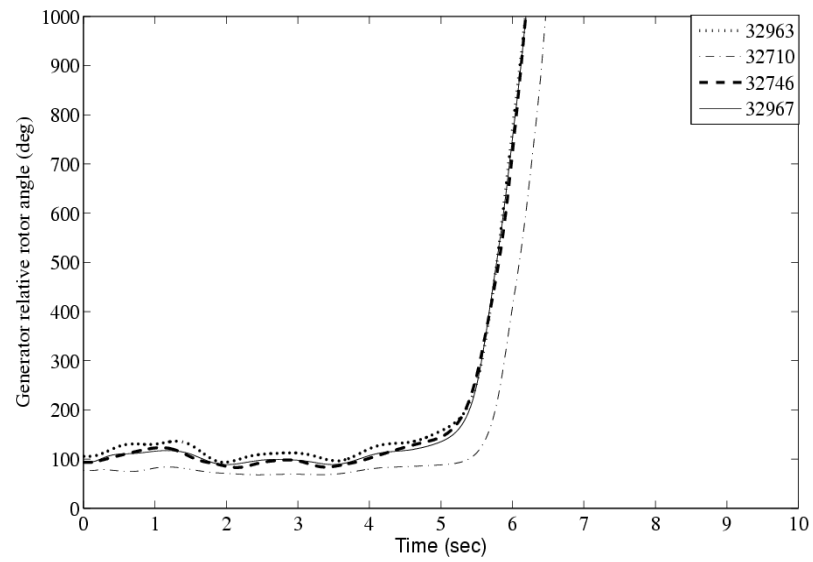Figure 6.7 Generator relative rotor angle for Case B

Figure 6.8 Generator relative rotor angle for machines accelerating in Case C
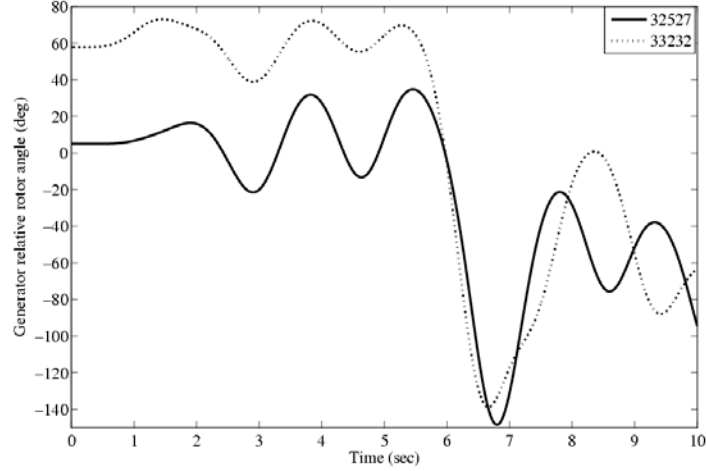
27

Figure 6.9 Generator relative rotor angle for machines decelerating in Case C

The system is found to be transiently secure in Case B whereas it is found to be transiently insecure in Case C. The machines swinging apart in Case C as a result of the fault can be segregated into accelerating and decelerating groups. The machines that accelerate are shown in Figure 6.8 and the machines that decelerate are shown in Figure 6.9. The result of the disturbance is a large inter area phenomenon as predicted by the small signal analysis shown in Table 6.6.

6.4.3 Fault scenario 3 - Beneficial impact on system performance

Following the same procedure adopted for the other two cases for exciting the required mode following a fault, a three phase fault is applied at a 230 kV bus 33270 as shown in Figure 6.4 and is cleared after 6.6cycles. The fault clearance is followed by clearing the line connecting the buses 33270 and 33290. As the dominant mode considered for small signal analysis corresponds to the speed state of the machines, the generator speeds are observed in time domain. Figure 6.10 shows the generator speed corresponding to the generator 33216 which is one of the machines participating in the mode as shown in Figure 6.2.
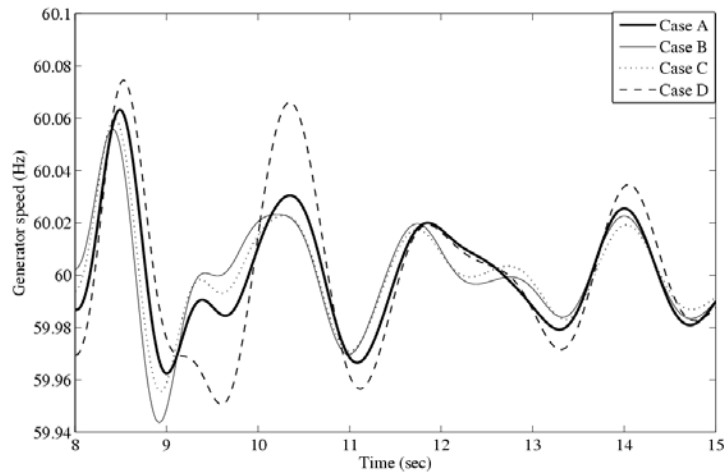

Figure 6.10 Bus 33216 generator speed for Cases A, B, C and D

28

The results show that the system is transiently stable for all the four cases and confirms the mode damping ratio results depicted in Table 6.7. The damping in the plots for Cases A-C is very close to each other and accurately reflects the damping ratio results shown in Table 6.7. For Case D the damping is markedly lower and verifies that the higher inertia case will have the lower damping. The oscillation damping is increased with the increase in DFIG penetration. This fault scenario is thus found to have a beneficial impact with respect to increased wind penetration. The analysis clearly indicates that the results obtained from sensitivity analysis and from eigenvalue analysis are confirmed by exciting the mode in time domain.

7. Conclusions

In this work, the impact of increased penetration of DFIG based WTGs on small signal stability and transient stability is examined for a large system. In order to examine the impact on small signal stability, a systematic approach to pin point the impact of increased penetration of DFIGs on electromechanical modes of oscillation using eigenvalue sensitivity to inertia is developed. In evaluating the sensitivity of specific modes of oscillation with respect to inertia, the DFIGs are replaced by conventional round rotor synchronous machines with the same MVA rating. The sensitivity analysis is performed only for the system where all the generators are synchronous machines. The sensitivity analysis identifies electromechanical modes of oscillations that are detrimentally and beneficially impacted by increased DFIG penetration. The method inherently accounts for the insertion point of the DFIGs in the network. The results of the sensitivity analysis are then confirmed using exact eigenvalue analysis performed by including the DFIGs in the base case and in the increased wind penetration case. Three specific cases of transient stability are also examined. In this analysis the modes observed in small signal analysis are excited by placing specific faults at buses close to the generators having the largest participation factors in the oscillatory modes identified. Transient stability behavior in terms of sufficient system damping and rotor angle stability is analyzed.

For the system operating conditions considered, the analysis conducted indicates that it is possible to identify a certain inter-area mode which is detrimentally affected by the increased DFIG penetration. Moreover, using the concept of participation factors, the specific mode can be excited in time domain.

The system is found to have both beneficial and detrimental impact with the increased penetration of DFIG. Both of these situations observed by sensitivity analysis for small signal stability are also observed in nonlinear time domain analysis by considering corresponding fault scenarios in time domain.

The sensitivity of the real part of the eigenvalue with respect to inertia evaluated for a system where the DFIGs at their planned insertion points in the network are replaced by equivalent round rotor synchronous machines provides a good metric to evaluate the impact due to increased DFIG penetration on system dynamic performance. Both detrimental and beneficial impacts of increased DFIG penetration can be identified. The eigenvalue sensitivity analysis together with the detailed eigenvalue analysis carried out for each of the four cases considered is also substantiated by the results obtained from time domain simulation.

8. Work in Progress

The next phase of the work aims to design the supplementary control strategy for the DFIG power converters such that the effective inertia contributed by these wind generators to the system is increased. The main issue with the DFIG is not the low inertia, the wind turbines do have significant amount of kinetic energy stored in the rotating mass of turbine blades. It is possible for the DFIG to supply the effect of inertia to the system, as is done by the synchronous machines, if a proper mechanism is developed to exploit the segregated inertia. Hence, the mathematical model is being developed to extract the kinetic energy stored in the rotating mass of the turbine. Accordingly, the control blocks will be developed and the output signal from the inertia control block is added to the torque set point of the existing DFIG model.

In order to observe the effectiveness of the additional control, load change will be simulated with and without the inertia control block. The power supplied by the DFIG with supplementary inertia block is expected to increase when the load is increased in the system. The additional power delivered by the DFIG (governed by turbine inertia) should be accompanied by the subsequent drop in DFIG rotor speed.

References

[1]   S. Heier, "Grid Integration of Wind Energy Conversion Systems," John Wiley & Sons Ltd., Chichester, England, 2006.

[2]   GWEC News Release: "Wind is a global power source," Available online:

http://www.gwec.net/index.php?id=13

[3]   N. Miller and Z. Ye, "Report on Distributed Generation Penetration Study," National Renewable Energy Laboratory, August 2003. Available online: www.nrel.gov/docs/fy03osti/34715.pdf

[4]   M. P. Palsson, T. Toftevaag, K. Uhlen and J. O. G. Tande, "Control Concepts to Enable Increased Wind Power Penetration," in Proc. IEEE Power Engineering Society General Meeting, 2003

[5]   H. Holttinen, P. Meibom, C. Ensslin, L. Hofmann, J. McCann, J. Pierik, J. O. Tande, E. Hagstrøm, A. Estanqueiro, H. Amaris, L. Söder, G. Strbac and B. Parsons, "Design and Operation of Power Systems with Large Amounts of Wind Power, IEA collaboration", Nordic Wind Power Conference, 22-23 May, 2006, Espoo, Finland. Available online:

http://www.ieawind.org/AnnexXXV/PDF/NordicWindConference.pdf

[6]   M. V. A. Nunes, J. A. P. Lopes, H. H. Zurn, U. H. Bezerra, and R. G. Almeida "Influence of the Variable-Speed Wind Generators in Transient Stability Margin of the Conventional Generators Integrated in Electrical Grids," *IEEE Trans. on Energy Conversion*, vol. 19, no. 4, pp. 692-701, Dec. 2004.

[7]   E. Muljadi, C. P. Butterfield, B. Parsons and A. Ellis, "Effect of Variable Speed Wind Turbine Generator on Stability of a Weak Grid," *IEEE Trans. on Power Systems*, vol. 22, no. 1, pp. 29-35, Mar. 2008.

[8]   N. R. Ullah and T. Thiringer, "Effect of Operational Modes of a Wind Farm on the Transient Stability of Nearby Generators and on Power Oscillations: a Nordic Grid Study," *Wind Energy*, vol. 11, pp. 63-73, Sept. 2007.

[9]   J. J. Sanchez Gasca, N. W. Miller and W. W. Price, "A Modal Analysis of a Two-Area System with Significant Wind Power Penetration," in *Proc. 2004 IEEE PES Power Systems Conference and Exposition*.

[10]   J. G. Slootweg and W. L. Kling, "The Impact of Large Scale Wind Power Generation on Power System Oscillations," *Electric Power Systems Research*, vol. 67, no., pp. 9-20, 2003.

[11]   A. Mendonca and J. A. P. Lopes, "Impact of Large Scale Wind Power Integration on Small Signal Stability," in *Proc. 2005 International Conference on Future Power Systems*.

[12]   J. G. Slootweg and W. L. Kling, "The Impact of Large Scale Wind Power Generation on Power System Oscillations," Electric Power Systems Research, Vol. 67, No., pp. 9-20, 2003.

[13]   M. Poller and S. Achilles, "Aggregated Wind Park Models for Analyzing Power System Dynamics," in Proc. 4th International Workshop on Large-Scale Integration of Wind Power and Transmission Networks for Offshore Wind Farms, Billund, Denmark, 2003.

[14]   P.W. Carlin, A.S. Laxson and E.B. Muljadi "The History and State of the Art of Variable-Speed Wind Turbine Technology,"Technical Report, NREL, 2001. Available online: http://www.nrel.gov/docs/fy01osti/28607.pdf

[15]   L. Holdsworth, X.G. Wu, J.B. Ekanayake and N. Jenkins, "Comparison of Fixed Speed and Doubly-Fed Induction Wind Turbines during Power System Disturbances," in Proc. IEE Generation, Transmission and Distribution, May 2003.

[16]   J. Usaola and P. Ledesma, "Dynamic Incidence of Wind Turbines in Networks with High Wind Penetration," in Proc. IEEE Power Engineering Society Summer Meeting, 2001.

[17]   F. M. Hughes, O. A. Lara, N. Jenkins and G. Strbac, "Control of DFIG-Based Wind Generation for Power Network Support," IEEE Transactions on Power Systems, Vol. 20, No. 4, pp. 1958-1966, November 2005.

[18]   Y. Lei, A. Mullane, G. Lightbody, and R. Yacamini, "Modeling of the Wind Turbine with a Doubly Fed Induction Generator for Grid Integration Studies," IEEE Transactions on Energy Conversion, Vol. 21, No. 1, pp. 257-264, March 2006.

[19]   GE Energy, "Modeling of GE Wind Turbine-Generators for Grid Studies," version 3.4b, Mar. 2005.

[20]   R. D. Fernandez, R. J. Mantz and P. E. Battaiotto, "Impact of wind farms on power system - an Eigen Value Analysis Approach," Renewable Energy, Vol. 32, pp. 1676-1688, 2007

[21]   CIGRE Technical Brochure on "Modeling and Dynamic Behavior of Wind Generation as it Relates to Power System Control and Dynamic Performance," Working Group 01, Advisory Group 6, Study Committee C4, Draft Report, August 2006.

[22]   Powertech Labs Inc., DSA Tools model manual, Version 7.1.

[23]   P. Kundur, J. Paserba, V. Ajjarapu, G. Andersson, A. Bose, C. Canizares, N. Hatziargyriou, D. Hill, A. Stankovic, C. Taylor, T. V. Custem and V. Vittal, "Definition and Classification of Power System Stability," IEEE Transactions on Power Systems, Vol. 19, No. 2, pp. 1387-1401, May 2004.

[24]   M. Kayikci and J. V. Milanovic, "Assessing Transient Response of DFIG-Based Wind Plants-The Influence of Model Simplifications and Parameters," IEEE Transactions on Power Systems, Vol. 23, No. 2, pp. 545-554, May 2008.

[25]   R. J. Koessler, S. Pillutla, L. H. Trinh and D. L. Dickmander, "Integration of Large Wind Farms into Utility Grids (Part 1 – Modeling of DFIG)," Available online:

http://library.abb.com/global/scot/scot221.nsf/veritydisplay/01ac651ffcec1227c1256fda0 03b4d6d/$File/WindPanelPaperPart1.pdf

[26]   A. D. Hansena and G. Michalke, "Fault Ride-Through Capability of DFIG Wind Turbines," Renewable Energy, Vol. 32, No. 9, July 2007.

[27]   P. Kundur, *Power System Stability and Control*, New York, McGraw Hill Inc., 1994.

[28]   J. Ma, Z. Y. Dong and P. Zhang, "Eigenvalue Sensitivity Analysis or Dynamic Power System," in Proc. International Conference on Power System Technology, 2006.

[29]   L. Rouco, "Eigenvalue-based Methods for Analysis and Control of Power System Oscillations," in Proc. IEE Colloquium on Power Dynamics Stabilization, February 1998.

[30]   T. Smed, "Feasible Eigenvalue Sensitivity for Large Power Systems," IEEE Trans. on Power Systems, vol. 8, no. 2, pp. 555-561, May 1993.

[31]   J.E. Van Ness, J.M. Boyle, and F.P. Imad, "Sensitivities of Large Multiple-Loop Control Systems", IEEE Trans. on Automatic Control, vol. AC-10, pp. 308-315, 1965.

Project Publications

1. Durga Gautam and Vijay Vittal, "Impact of Increased Penetration of DFIG based Wind Turbine Generators on Transient and Small Signal Stability of Power Systems," *IEEE Transactions on Power Systems*, Vol. 24, No. 3, pp. 1426-1434, Aug 2009.
2. Durga Gautam and Vijay Vittal, "Impact of DFIG based Wind Turbine Generators on Transient and Small Signal Stability of Power Systems," Paper # PESGM2009-000483 *IEEE Power and Energy Society General meeting*, Calgary, July 2009.

PART 2

Impact of Increased DFIG Penetration
on Transient Frequency Response and Regulation

James McCalley, Iowa State University

(with Siddhartha Kr. Khaitan, Ph. D and Shuyang Zhang)

Information about this project

James McCalley
Harpole Professor in Electrical Engineering
Department of Electrical and Computer Engineering
Iowa State University
1115 Coover Hall
Ames IA 50011
Phone: 515-294-4844
Email: jdm@iastate.edu

Power Systems Engineering Research Center

The Power Systems Engineering Research Center (PSERC) is a multi-university Center conducting research on challenges facing the electric power industry and educating the next generation of power engineers. More information about PSERC can be found at the Center's website: http://www.pserc.org.

Table of Contents

List of Tables

List of Figures

1. Introduction

1.1 Introduction

Wind turbines have different operational characteristics relative to the traditional forms of generating electric energy. This is due to the fact that the primary energy source, wind, is not controllable. This fact alone results in wind plants being viewed as non-dispatchable, implying it is not possible to *a-priori* specify what the power output of a wind plant should be.

This decrease in plant controllability is a key motivator behind use of technologies other than standard synchronous machines, since torque and rotational speed cannot be simultaneously maintained constant. In addition, it creates issues regarding system power control that must be addressed for high levels of wind penetration. We have focused on the MW-control issues in this part of the project with emphasis on transient frequency and regulation control issues. However, there are other interconnection and control issues. An overview of these issues is provided in the next section.-

1.2 Overview of interconnection & control issues

A list of interconnection and control issues related to wind plant operation within grids is as follows [1]:
- MW-frequency control:
  - Transient frequency disturbances
  - Regulation
  - Load following
  - Scheduling
- Reactive control and voltage issues:
  - Transient voltage response & low-voltage ride-through
  - Voltage regulation
- Protection issues:
  - Disconnection for faults
  - Coordination with reclosing
- Power quality
  - DC injection
  - Flicker
  - Harmonics
- Other issues:
  - Grounding requirements
  - Synchronization
  - Islanded operation

Many of these issues are addressed by standards and codes, such as those specified by IEEE 1547, the National Electric Code, Underwriters Laboratory [1], the North American Electric Reliability Corporation, and requirements specified by regional transmission organizations and individual companies.

Of these, MW-frequency control and MVAR-voltage control issues have been challenging. Since the MVAR-voltage control issue is addressed in Part 3 of this report, here we will focus on the MW-frequency control issue.

Fig. 1 below compactly summarizes the MW-Hz issues related to wind. The rows in the figure identify wind related attributes and corresponding grid problems caused by each attribute. The columns represent possible solutions to alleviate the grid problems. The ultimate objective is to provide an approach for identifying the right combination of solutions for a given power system with a given projection regarding wind penetration levels. To do so, we need to establish performance impacts of each solution on each problem, and we need to estimate cost per unit for each solution. The figure below gives an idea of the relative cost /MW for proposed solutions. However it is a rich area of further research to identify the right solution for a particular situation which is economical, feasible, effective and fast. It also depends on the level at which the solutions are sought; for example, the solution strategy at the ISO level may differ from the solution strategy at the wind plant level.

Wind energy attrbute	Grid prblem caused by wind attrbute	Solutions													
		DFIG Control			Inc. reserves		Storage		Load Cntrl		Stoch-astic Unit Cmmt prgrm	Dec fore-cast error	Wind plant remote trip (SPS)	HVDC control	Geo-diversity of wind
		Inrtial emu-lation	Freq reg via pitch+ cnvrtr	Fast rmping	Spnng /10 min	1 hour	Fast	Slow	Fast	Slow					
		Estimated relative costs/MW of solution technology (to be refined)													
		5	5	6	10	10	9	9	9	9	4	4	6	10	10
Decreased inertia	Transient frequency dips, CPS2 perfrmance	√					√		√					√	
Increased 1 min MW variability	CPS2 perfrmance		√		√		√		√					√	√
Increased 10 min MW variability	CPS1, CPS2 perfrmance		√	√	√			√		√		√		√	√
Increased 1 hr MW variability	Balancing market perfrmance					√		√		√	√	√		√	√
Increased day-ahead MW variability	Day-ahead market perfrmance					√		√		√	√	√		√	√
Increased transmission loading	Increased need for transmssion			√									√	√	
Low, variable capacity factor	More planning uncertainty							√		√		√			√

Fig. 1 MW-Freq (Hz) Spectrum of Wind Related Issues

1.3 Time-frames for MW-frequency control

As indicated in the last section, the MW-frequency control issue can be divided into:
- Transient frequency disturbances
- Regulation (or load-frequency control)
- Load following
- Scheduling

Transient frequency occurs in a time frame of seconds, regulation occurs in a time frame of seconds-to-minutes, load following in a time frame of minutes to hours, and scheduling in a time frame of hours to a day. Reference [2] provides a good overview differentiating between regulation and load following. It states: "The key distinction between load following and regulation is the time period over which these fluctuations occur. Regulation responds to rapid load fluctuations (on the order of one minute) and load following responds to slower changes (on the order of five to thirty minutes)."

Mechanisms by which these issues are addressed are:
- Transient response: Inertia and governor
- Regulation: Governor and AGC
- Load following: AGC and economic dispatch

Transient response is discussed in the Chapter 2 and regulation and load following are discussed in Chapter 3.

2. Grid Operation and Coordination with Wind - Transient Frequency Response

Fig. 2 illustrates the transient frequency response for a 50 Hz system. From the figure we note that the frequency declines from t=1.5 to about t=1.5+2.75 seconds. This frequency decline is due to the fact that the loss of generation has caused a generation deficit, and so generators decelerate, utilizing some of their inertial energy to compensate for the generation deficit. Then the frequency recovers during the time period from about t=4.25 seconds to about t=9 seconds. This recovery is primarily due to the effect of governor control (also, underfrequency load shedding plays a role). At the end of the simulation period, the frequency has reached a steady-state, but it is not back to 50 Hz. This steady-state frequency deviation is intentional on the part of the governor control and ensures that different governors do not constantly make adjustments against each other. The resulting steady-state error will be zeroed by the actions of the automatic generation control (AGC).
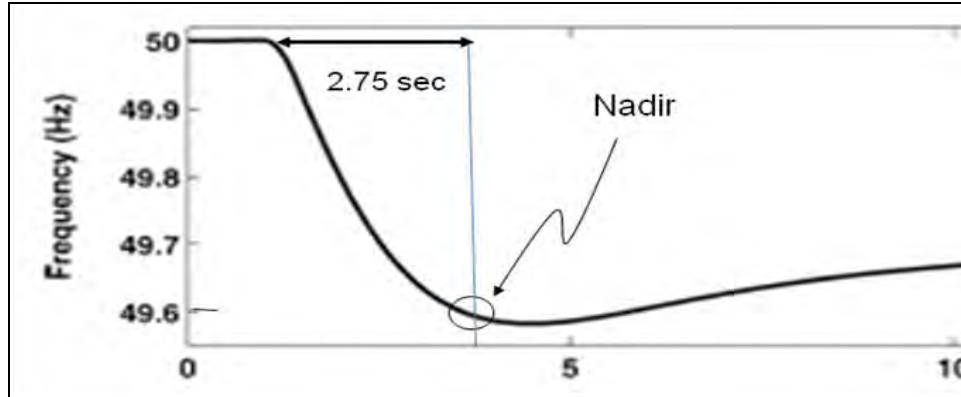
Fig. 2 Illustration of Transient Frequency Response

Here, we desire to explore the significance of transient frequency dip, the nadir (lowest point), occurring at t=2.75 seconds following the disturbance. We are concerned about a low frequency nadir for two physical reasons [3] and third economic reason. The first reason is under-frequency load shedding (UFLS), and the second is due to frequency relays that protect generators and certain kinds of loads. The significance of these problems depends on the size of the system, as we shall see later in the chapter. The third reason is that there are performance requirements regarding frequency dip, and violating those requirements can result in penalties. For example, one region requires that for N-1 contingencies, load bus frequency not drop below 59.6 Hz for >6 cycles, and for N-2 contingencies, load bus frequency not drop below 59.0 Hz for >6 cycles.

We describe the UFLS problem and generation protection in the next sections.

2.1 Underfrequency load shedding (UFLS)

UFLS is used by utilities to protect against severe under-frequency conditions. For a particular frequency nadir, after a contingency, an operational scheme is designed to shed the appropriate load in order to prevent aggravating the frequency drop. The North American Electric Reliability Corporation (NERC) has published the PRC-006 requirement: "Each Regional Reliability Organization shall develop, coordinate, and document an UFLS program". The MRO (Midwest Reliability Organization) has performed an under-frequency load shedding study related to this requirement. Table 1 shows the load to be shed at different frequency set points [4]. If the frequency falls below 59.3 Hz, 6% of the initial load will be shed. The next setting point is 59.1 Hz and so on.

Table 1 UFLS Guidelines [4]

High Speed Load Shedding Block Number	Block Size % of Initial Load	Frequency Set point (HZ)	Relay Time (cy)	Maximum Breaker Time (cy)
1	6	59.3	6	8
2	6	59.1	6	8
3	6	58.9	6	8
4	6	58.7	6	8
5	6	58.4	6	8

However, some systems have higher thresholds. For example, the WECC system in the western US interrupts some load at 59.75 Hz (called "interruptible load"). Although this is allowable under disturbance conditions, it is undesirable. The WECC threshold frequency, below which is unacceptable for credible disturbances, is 59.6 Hz [5].

2.2 Underfrequency effects on generators [6]

Synchronous generators subjected to prolonged periods of underfrequency operation pose a serious threat to the turbines and other auxiliaries along with the generator. Of all turbines, steam turbines are most adversely affected by underfrequency operation.

Damage due to blade resonance is of primary concern. Resonance occurs when the frequency of the vibratory stimuli and the natural frequency of a blade coincides or are close to each other. The steam flow path is not homogeneous due to physical irregularities in the flow path and this produces cyclical force to the blades. At resonance the cyclical forces increases the stress and the damage to the blades is accumulated and

may appear as a crack of some parts in the assembly. Although these cracks may not be catastrophic, they can alter the blade tuning such that resonance could occur near rated speed.

Every turbine blade has numerous natural resonance modes, namely tangential, axial, and torsional. Each mode has a natural frequency that varies with the physical dimensions of the blade. Short blades in the high-pressure and intermediate pressure stages of the turbine can be designed to withstand a resonant condition. However the longer turbine blades associated with the low pressure turbine are prone to damage by prolonged abnormal frequency operation. These blades are protected by tuning their natural resonant frequencies away from rated speed. These blades generally determine the turbine's vulnerability to under frequency operation.

Standards do not specify short time limits for over- or under-frequency operation. The manufacturer of the specific turbine must provide this data. Reference [7] lists the following limitations for one manufacturer's turbines as:
- 1% change, 59.4–60.6Hz, no adverse effect on blade life
- 2% change, 58.8-61.2Hz, potential damage, ~ 90 mins
- 3% change, 58.2-61.8Hz, potential damage, ~10–15 mins
- 4% change, 57.6–62.4Hz, potential damage, ~1 min

Reference [8] states that with a 5% frequency deviation, damage could occur within a few seconds.

Limits vary dramatically among manufacturers, as in Fig. 3, which includes limitation curves from four manufacturers. The shaded regions of Fig. 3 include
- White: Safe for continuous operation
- Light shade: Restricted time operation
- Dark shade: Prohibited operation

A "safe" approach would seem to be to ensure frequency remains in the band 59.5→60.05 Hz.
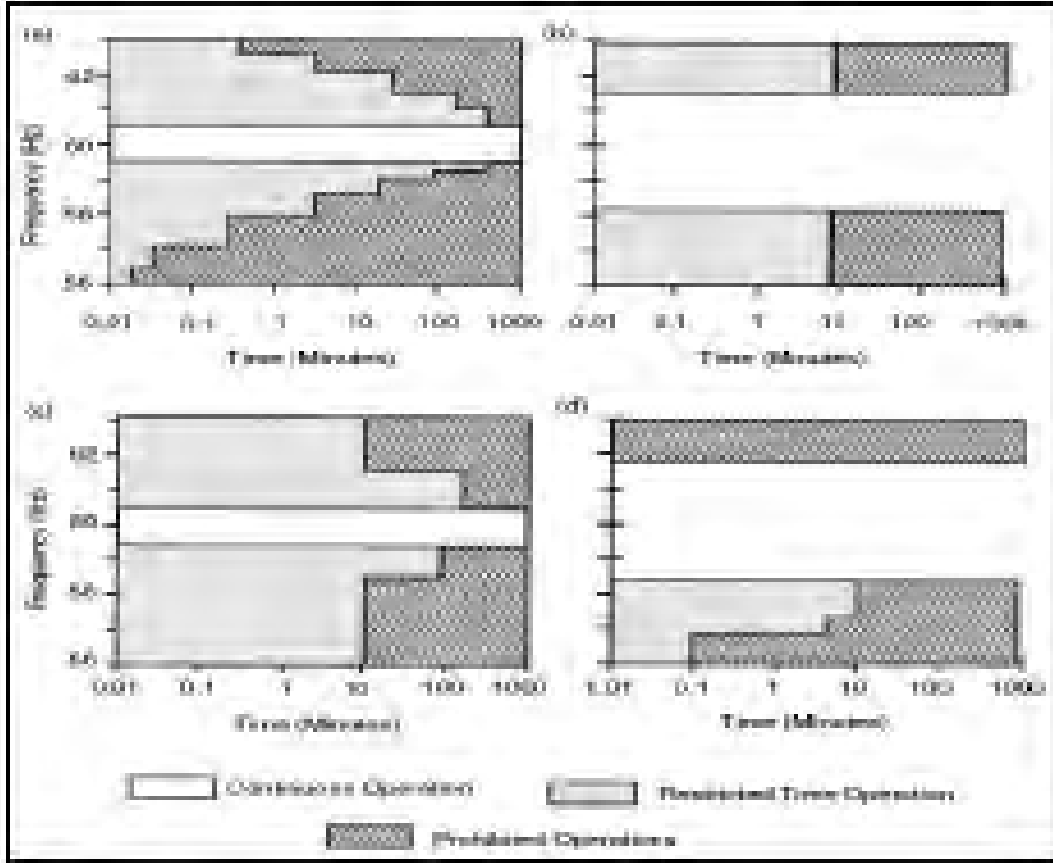
Fig. 3 Frequency Limitation Curves from Different Manufacturers [8]

Protective settings should be such as to coordinate with the automatic load shedding on the system and at the same time provides protection for each band of the manufacturer's withstand characteristics.

The backup protection employs a multilevel underfrequency tripping scheme. A separate time delayed underfrequency function is required for each band on the manufacturer's limit curve. The timers are set near the maximum allowable time for the band they protect. This strategy aims at maximizing the availability of large units during system disturbances, thus enhancing the power system's ability to ride through such disturbances.

2.3 Inertial effects on transient frequency response

Reference [9] provides a basis for understanding the effects of a generation-load imbalance on a power system comprised of synchronous machines. Consider that the power system experiences a load increase (or equivalently, a generation decrease) of ΔP_L at t=0, located at bus k. Then, at $t=0^+$, each generator i will compensate according to its proximity to the change, as captured by the synchronizing power coefficient P_{Sik} between units i and k, according to

7

$$\Delta P_{ei} = \frac{(-P_{Sik})(-\Delta P_L)}{\sum_{j=1}^{n} P_{Skj}} = \frac{P_{Sik}}{\sum_{j=1}^{n} P_{Skj}} \Delta P_L \qquad (2.1)$$

where $P_{Sik} = \left. \dfrac{\partial P_{ik}}{\partial \delta_{ik}} \right|_{\delta_{ik0}}$.

Equation (2.1) is derived for a multi-machine power system model where each synchronous generator is modeled with classical machine models, loads are modeled as constant impedance, the network is reduced to generator internal nodes, and mechanical power into the machine is assumed constant.

In such a case, the linearized swing equation for machine i (ignoring damping) is:

$$\frac{2H_i}{\omega_{Re}} \frac{d^2 \Delta \delta_i}{dt^2} = -\Delta P_{ei} \qquad (2.2)$$

For a load change ΔP_{Lk}, at $t=0^+$, we substitute eq. (2.1) into the right-hand-side of (2.2), we obtain:

$$\frac{2H_i}{\omega_{Re}} \frac{d^2 \Delta \delta_i}{dt^2} = -\frac{P_{Sik}}{\sum_{j=1}^{n} P_{Skj}} \Delta P_L \qquad (2.3)$$

Bring H_i over to the right-hand-side and rearrange to get:

$$\frac{2}{\omega_{Re}} \frac{d^2 \Delta \delta_i}{dt^2} = -\left[\frac{P_{Sik}}{H_i} \right] \frac{\Delta P_L}{\sum_{j=1}^{n} P_{Skj}} \qquad (2.4)$$

For $\Delta P_L > 0$, each machine will decelerate but at different rates, according to P_{Sik}/H_i.

Now rewrite eq. (2.3) with H_i inside the differentiation, use $\Delta \omega_i$ instead of $\Delta \delta_i$, write it for all generators 1,…,n, then add them up. All H_i must be given on a common base for this step.

$$\frac{2}{\omega_{\mathrm{Re}}}\frac{dH_1\Delta\omega_1}{dt} = -\frac{P_{S1k}}{\sum\limits_{j=1}^{n}P_{Skj}}\Delta P_L$$

$$\vdots$$

$$+\frac{2}{\omega_{\mathrm{Re}}}\frac{dH_n\Delta\omega_n}{dt} = -\frac{P_{Snk}}{\sum\limits_{j=1}^{n}P_{Skj}} \tag{2.5a}$$

$$\frac{2}{\omega_{\mathrm{Re}}}\sum_{i=1}^{n}\frac{dH_i\Delta\omega_i}{dt} = -\frac{\sum\limits_{i=1}^{n}P_{Sik}}{\sum\limits_{j=1}^{n}P_{Skj}}\Delta P_L = -\Delta P_L \tag{2.5b}$$

Now define the "inertial center" of the system, in terms of angle and speed, as
- The weighted average of the angles:

$$\overline{\delta} \equiv \frac{\sum\limits_{i=1}^{n}H_i\delta_i}{\sum\limits_{i=1}^{n}H_i} \quad \text{or} \quad \overline{\Delta\delta} \equiv \frac{\sum\limits_{i=1}^{n}H_i\Delta\delta_i}{\sum\limits_{i=1}^{n}H_i} \tag{2.6}$$

- The weighted average of the speeds:

$$\overline{\omega} \equiv \frac{\sum\limits_{i=1}^{n}H_i\omega_i}{\sum\limits_{i=1}^{n}H_i} \quad \text{or} \quad \overline{\Delta\omega} \equiv \frac{\sum\limits_{i=1}^{n}H_i\Delta\omega_i}{\sum\limits_{i=1}^{n}H_i} \tag{2.7}$$

Differentiating $\overline{\Delta\omega}$ with respect to time, we get:

$$\frac{d\overline{\Delta\omega}}{dt} \equiv \frac{\sum\limits_{i=1}^{n}\dfrac{d\left(H_i\Delta\omega_i\right)}{dt}}{\sum\limits_{i=1}^{n}H_i} \tag{2.8}$$

Solve for the numerator on the right-hand-side, to get:

$$\sum_{i=1}^{n}\frac{d\left(H_i\Delta\omega_i\right)}{dt} = \left[\sum_{i=1}^{n}H_i\right]\left[\frac{d\overline{\Delta\omega}}{dt}\right] \tag{2.9}$$

Now substitute eq. (2.9) into eq. (2.5) to get:

$$\frac{2}{\omega_{\text{Re}}}\left[\sum_{i=1}^{n}H_i\right]\left[\frac{d\overline{\Delta\omega}}{dt}\right] = -\Delta P_L \tag{2.10}$$

Bringing the 2*(summation)/ω_{Re} over to the right-hand-side gives:

$$\frac{d\overline{\Delta\omega}}{dt} = \frac{-\Delta P_L \omega_{\text{Re}}}{2\sum_{i=1}^{n}H_i} \equiv m_\omega \tag{2.11a}$$

Eq. (2.11a) gives the *average deceleration of the system*, m_ω, the initial slope of the frequency deviation plot vs. time. This has also been called the rate of change of frequency (ROCOF) [10]. As stated earlier all H_i (units of seconds) must be given on a common power base for (2.11a) to be correct. In addition -ΔP_L should be in per-unit, also on that same common base, so that -ΔP_L/2 ΣH_i is in pu/sec, and m_ω=-ΔP_L ω_{Re}/2 ΣH_i is in rad/sec/sec. Alternatively,

$$\frac{d\overline{\Delta f}}{dt} = \frac{-\Delta P_L f_{\text{Re}}}{2\sum_{i=1}^{n}H_i} \equiv m_f \tag{2.11b}$$

provides ROCOF in units of Hz/sec.

Consider applying a load increase of ΔP_L at t=0. Assume:
- There is no governor action between time t=0^+, and time t=t_1 (typically, t_1 might be about 1-2 seconds).
- The deceleration of the system is constant from t=0^+ to t=t_1.

The frequency will decline to 60-$m_f t_1$. This is illustrated in Fig. 4 below.
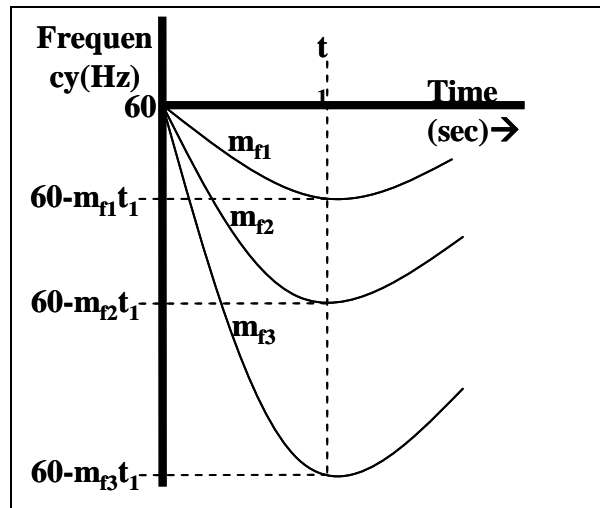

Fig. 4 Frequency Dips as a Function of ROCOF [10]

Inspection of (11) indicates that the only operational parameter term, $\sum_{i=1}^{n} H_i$, the denominator, can cause the system to behave with characteristic of m_{f3}, instead of m_{f2} or m_{f1}, for a given ΔP_L, Thus, we observe that as the total system inertia decreases, the initial slope increases, and a given load change ΔP_L causes a greater frequency decline. This is an important concept in regards to understanding the effect of wind on transient frequency response.

2.4 Effect of system size

From (2.11b), we have seen that m_f, the average deceleration of the system, i.e., the rate of change of frequency (ROCOF), at the moment of the generation imbalance, depends on the total inertia for the entire interconnected system. The "larger" (more inertia) of the system, the smaller m_f will be, and the less severe will be the frequency dip. Small "isolated" systems such as those on islands experience very severe problems in this way. Large system under islanding condition can also experience similar problem. For example, in 2000, the island of Crete had only 532 MW of conventional generation [11]. One plant has capacity of 132 MW. Consider loss of this 132 MW plant when the capacity is 532 MW. Then remaining capacity is 532-132=400 MW. If we assume that all plants comprising that 400 MW have inertia constant (on their own base) of 3 seconds, then the total inertia following loss of the 132 MW plant, on a 100 MVA base, is

$$\sum_{i=1}^{n} H_i = \frac{400*3}{100} = 12$$

Then, for ΔP_L=132/100=1.32 pu, and assuming the nominal frequency is 50 Hz, ROCOF is given by

$$m_f = \frac{d\overline{\Delta f}}{dt} = \frac{-\Delta P_L f_{Re}}{2\sum_{i=1}^{n} H_i} \equiv \frac{-1.32(50)}{2*12} = -2.75 Hz/\sec$$

If we assume t_1=2 seconds, then Δf= -2.75*2=-5.5 Hz, so that the nadir would be 50-5.5=44.5Hz! For a 60 Hz system, then m_f=-3.3Hz/sec, Δf=-3.3*2=-6.6 Hz, so that the nadir would be 60-6.6=53.4 Hz.

Next, we consider the example of Ireland. Reference [10] reports on frequency issues for Ireland. The authors performed analysis on the 2010 Irish system for which the peak load (occurs in winter) is inferred to be about 7245 MW. The largest credible outage would result in loss of 422 MW. We assume a 15% reserve margin is required, so that the total spinning capacity is 8332 MW. Let's consider this 422 MW outage, meaning the remaining generation would be 8332-422=7910 MW.

The inertia of the Irish generators is likely to be higher than that of the Crete units, so we will assume all remaining units have inertia of 6 seconds on their own base. Then the total inertia following loss of the 422 MW plant, on a 100 MVA base, is

$$\sum_{i=1}^{n} H_i = \frac{7910*6}{100} = 475$$

Then, for ΔP_L=422/100=4.32, and assuming the nominal frequency is 50 Hz, ROCOF is given by

$$m_f = \frac{d\overline{\Delta f}}{dt} = \frac{-\Delta P_L f_{\text{Re}}}{2\sum_{i=1}^{n} H_i} \equiv \frac{-4.32(50)}{2*475} = -0.227 Hz/\sec$$

Assuming t_1=2.75 seconds, thenΔf= -0.227*2.75=-0.624 Hz, so that the nadir is 50-0.624=49.38Hz. Fig. 5 [10] illustrates simulated response for this disturbance.
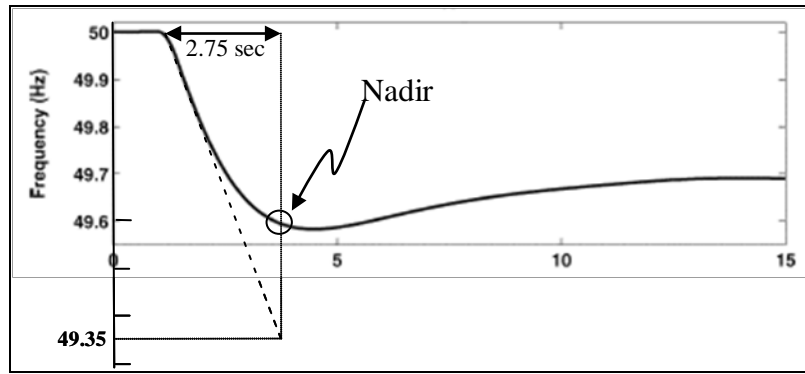
Fig. 5 Transient Frequency Response for the Ireland System [10]

The computed nadir (49.38 Hz) is almost exactly the same as the frequency dip that would be observed if the ROCOF at t=0+ were constant over the entire 2.75 sec (49.35 Hz). The fact that the actual nadir, at about 49.6 Hz is higher is due to two influences:
- Governors have some influence in the simulation that is not accounted for in the calculation.
- Some portion of the load is modeled with frequency sensitivity in the simulation, and this effect is not accounted for in the calculation.

Reference [12] reports on frequency issues for the US Eastern Interconnection, conducted as a part of this project. A 2008 case was analyzed for which installed capacity was 541 GW. Two outages were studied, as illustrated in Fig. 6. The large black dot in northern Florida indicates a 2.9 GW plant dropped for outage 1. All black dots represent generation totaling about 10.18 GW as below, for outage 2.

Florida: 2.9GW+1.272GW+2.390GW=6.552GW
Potomac Electric Power Co (Wash D.C.): 1.295GW

Maryland: 1.164GW
Tennessee: 1.150GW

The blue dot is where the frequency was monitored.
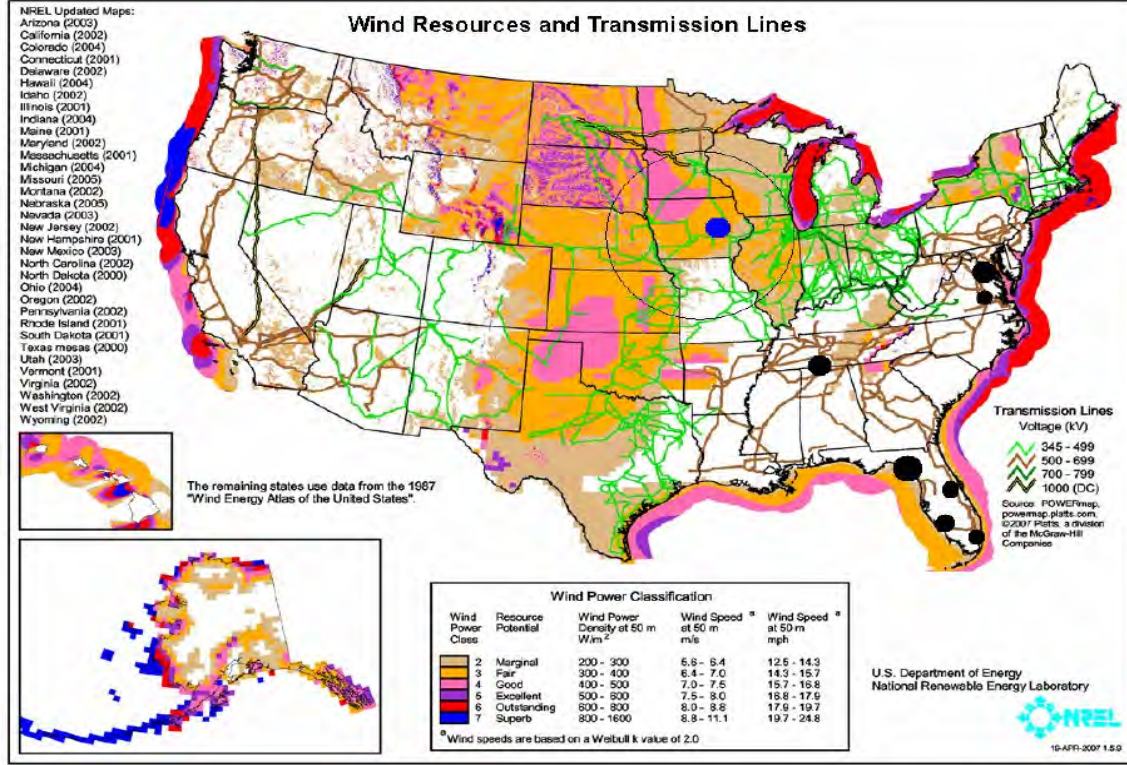
Fig. 6 Contingency Location for the U.S. Eastern Interconnection System [12]

With a 2.9 GW outage, the remaining generation is 541-2.9=538.1 GW. We assume the inertia of the generators is 6 seconds on their own base. Then the total inertia following loss of the 2.9 GW plant, on a 100 MVA base, is

$$\sum_{i=1}^{n} H_i = \frac{538100 * 6}{100} = 32286$$

Then, for ΔP_L=2900/100=29, and with nominal frequency of 60 Hz, ROCOF is given by

$$m_f = \frac{d\overline{\Delta f}}{dt} = \frac{-\Delta P_L f_{Re}}{2\sum_{i=1}^{n} H_i} \equiv \frac{-29(60)}{2*32286} = -0.0269 Hz/\sec$$

Assuming t_1=2.5 seconds, then Δf= -0.0269*2.5=-0.0673 Hz, so that the nadir is 60-0.0673=59.9327Hz. Fig. 7 (pink curve) illustrates simulated response for this disturbance.

13
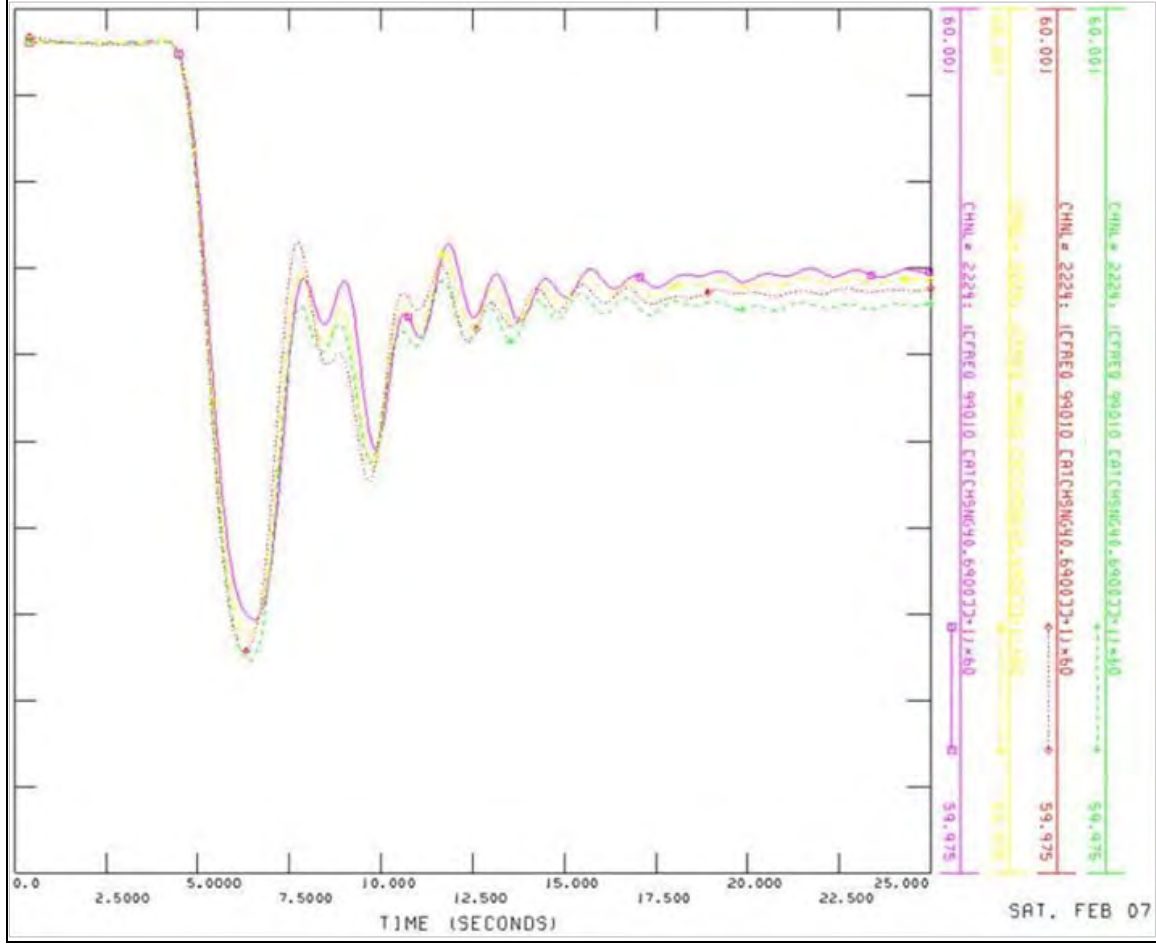
Fig. 7 Frequency Response for 2.9 GW Contingency

With a 10.16 GW outage, the remaining generation is 541-10.16=530.84 GW. We assume the inertia of the generators is 6 seconds on their own base. Then the total inertia following loss of the 10.16 GW generation, on a 100 MVA base, is

$$\sum_{i=1}^{n} H_i = \frac{530840 * 6}{100} = 31850$$

Then, for ΔP_L=10160/100=101.60, and with nominal frequency of 60 Hz, ROCOF is given by

$$m_f = \frac{d\overline{\Delta f}}{dt} = \frac{-\Delta P_L f_{\mathrm{Re}}}{2\sum_{i=1}^{n} H_i} \equiv \frac{-101.60(60)}{2*31850} = -0.0957 Hz/\sec$$

Assuming t_1=2.2 seconds, then Δf= -0.0957*2.2=-0.2105 Hz, so that the nadir is 60-0.2105=59.79Hz. Fig. 8 illustrates simulated response for this disturbance.

14

Fig. 8 Frequency Response for 10.16 GW Contingency
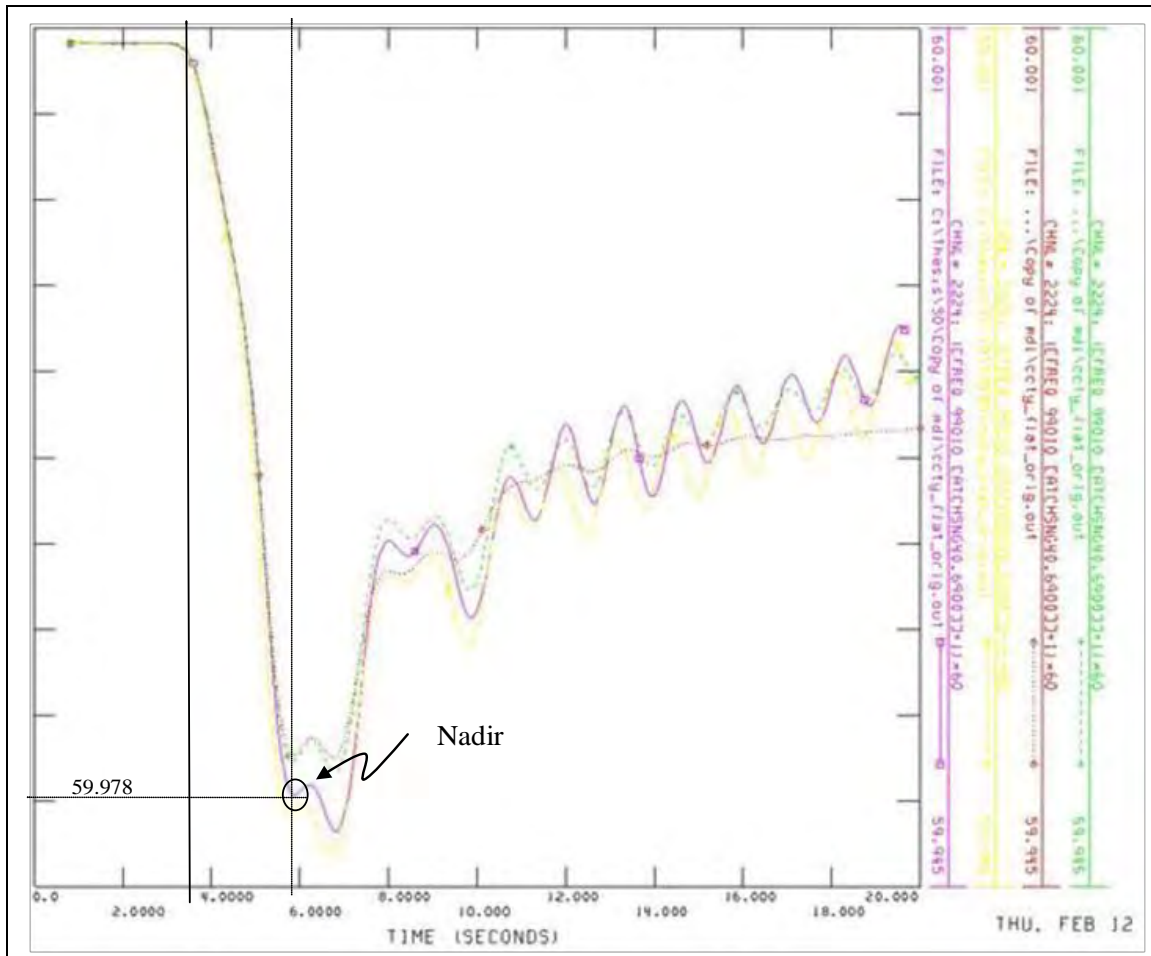
The frequency dips of Fig. 7 and Fig. 8 are small and of little concern in terms of tripping underfrequency load shedding or of tripping generator protection. The amount of generation tripped is very large, and it is unlikely the eastern interconnection will see generation trips larger than 10 GW. The reason for this excellent frequency stability is the very large size of the system.

The following plot in Fig. 9 shows the simulation result of the frequency nadir in the unit decommitment scenario with increased (2%, 4% and 8%) wind penetration levels after a 2.9 GW generator is tripped. The x-axis is time, and the y-axis is the frequency response.
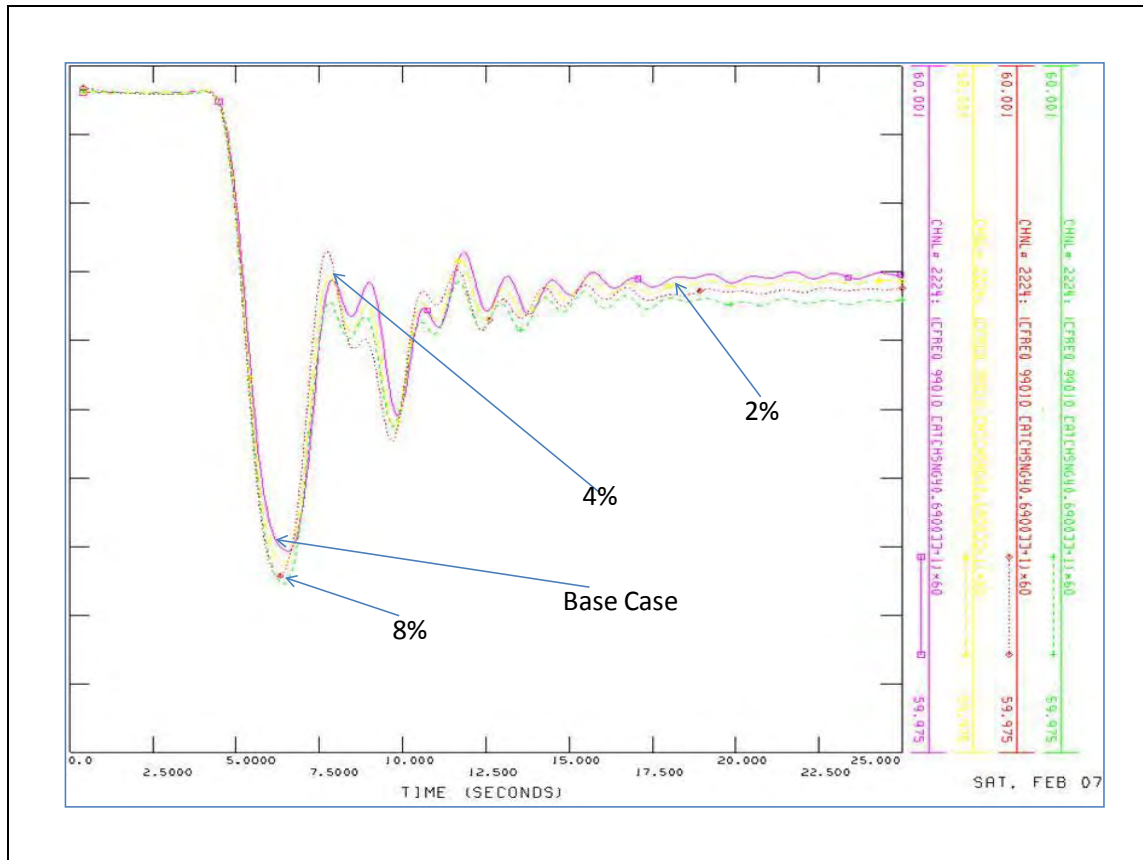
Fig. 9 Frequency Nadir After Worst Contingency for Unit Decommitment Scenario at Different Wind Penetration Levels

In Fig. 9 above, the scale of the y axis is from 59.975 HZ to 60.001 HZ, and the wind penetrations are labeled. It is clear that the frequency response is degrading with the increase of wind penetration levels. Yet, that wind penetration up to 8% of the eastern interconnection does not represent a significant problem for transient freq dip as long as the system remains intact.

Despite the very small frequency dips, even for extremely large outages, there are two reasons why frequency stability is still of concern within the eastern interconnection. The first is that during *islanding conditions*, the frequency stability is determined by the size of each island, not by the size of the entire interconnection. Islanding occurs very rarely, but frequency stability is of high significance when it does. During such events, the inertia of the island can be significantly lower than the entire interconnection, and generation-load imbalance can also be large, resulting in a large m_f, according to (2.11a) and (2.11b).

The second reason why frequency stability is still of concern within the eastern interconnection has to do with **C**ontrol **P**erformance **S**tandards CPS1 and CPS2. These are two performance metrics associated with load frequency control. These measures depend on area control error (ACE), given for control area *i* as

$$ACE_i = \Delta P_i + \beta \Delta f \tag{2.12}$$

$$\Delta P_i = AP_i - SP_i \tag{2.13}$$

where AP_i and SP_i are actual and scheduled exports, respectively.

CPS1 and CPS2 are defined as follows
- CPS1: It measures ACE variability, a measure of short-term error between load and generation [13]. It is an average of a function combining ACE and interconnection frequency error from schedule [14]. It measures control performance by comparing how well a control area's ACE performs in conjunction with the frequency error of the interconnection. It is given by

$$CPS1 = (2 - CF) \times 100\% \tag{2.14a}$$

$$CF = \frac{ControlParameter_{12-Month}}{(\varepsilon_1)^2} \tag{2.14b}$$

$$ControlParameter = \frac{ACE_{minute}}{-10B} \times \Delta F_{minute} \tag{2.14c}$$

where
  - CF is the compliance factor, the ratio of the 12 month average control parameter divided by the square of the frequency target ε_1.
  - ε_1 is the maximum acceptable steady-state frequency deviation – it is 0.018 Hz=18 mHz in the eastern interconnection.
  - The control parameter, a "MW-Hz," indicates the extent to which the control area is contributing to or hindering correction of the interconnection frequency error.,

If ACE is positive, the control area will be increasing its generation, and if ACE is negative, the control area will be decreasing its generation. If ΔF is positive, then the overall interconnection needs to decrease its generation, and if ΔF is negative, then the overall interconnection needs to increase its generation. Therefore if the sign of the product ACEΔF is positive, then the control area is hindering the needed frequency correction, and if the sign of the product ACEΔF is negative, then the control area is contributing to the needed frequency correction.
  - A CPS1 score of 200% is perfect (actual measured frequency equals scheduled frequency over any 1-minute period)
  - The minimum passing long-term (12-month rolling average) score for CPS1 is 100%
- CPS2: The ten-minute average ACE.

Reference [15] provides a good description of CPS1 and CPS2.

In summary, from [16], "CPS1 measures the relationship between the control area's ACE and its interconnection frequency on a one-minute average basis. CPS1 values are

recorded every minute, but the metric is evaluated and reported annually. NERC sets minimum CPS1 requirements that each control area must exceed each year. CPS2 is a monthly performance standard that sets control-area-specific limits on the maximum average ACE for every 10-minute period." The underlying issue here is that control area operators are penalized if they do not maintain CPS. The ability to maintain these standards is decreased as inertia decreases.

2.4.1   Impact of wind on transient frequency response

There are 4 types of wind turbines deployed today.
- Type 1: The self-excited induction generator (SEIG) or squirrel cage induction generator. It is fixed speed.
- Type 2: The wound-rotor induction generator, operationally, is much like type 1, with the exception that its wound-rotor enables a limited amount of speed control via variation of a resistance in series with the rotor circuit.
- Type 3: The double-fed induction generator (DFIG) has the stator windings directly connected to the grid while the rotor windings are connected via slip rings to a converter which connects to the grid. The DFIG is a variable speed machine.
- Type 4: The direct-connected machine has its stator windings connected to a full-power converter which connects to the grid. The generator can either be a synchronous or induction machine.

Fig. 10 illustrates all four types [17]. As far as transient frequency response is concerned, type 2 is similar to type 1. Reference [18] also provides a useful illustration of types 1, 3, and 4. Type 4 is not as commonly used as the others, so we focus further discussion on the type 1 fixed-speed machine and the type 3 variable-speed machine.
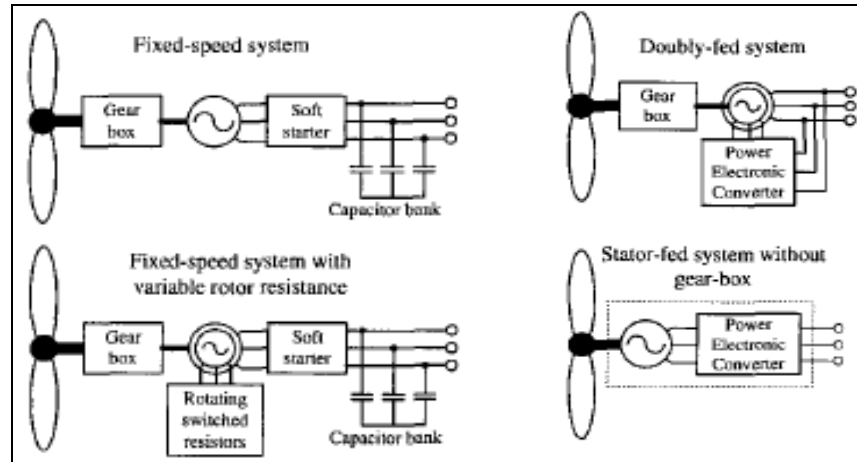

Fig. 10 Types of Wind Turbines [17]

Referring back to (2.11b) and (2.5a) we know that the transient frequency decline is reduced by contribution of each machine's inertial energy (2.11b).

$$\frac{d\overline{\Delta f}}{dt} = \frac{-\Delta P_L f_{\mathrm{Re}}}{2\sum\limits_{i=1}^{n} H_i} \equiv m_f \tag{2.11b}$$

Also by (2.5a), a machine contributes inertial energy if it decelerates in response to a frequency drop according to the following equation of motion:

$$\frac{2}{\omega_{\mathrm{Re}}} \frac{dH_i \Delta\omega_i}{dt} = -\frac{P_{Sik}}{\sum\limits_{j=1}^{n} P_{Sij}} \Delta P_L \tag{2.5a}$$

Therefore, a machine that decelerates in response to a frequency drop contributes inertial energy and acts to arrest frequency decline. A machine that does not decelerate in response to a frequency drop does not contribute inertial energy and does not act to arrest frequency decline.

The operation of type 1 (fixed speed) and type 3 (DFIG) are investigated next to determine whether they contribute inertial energy to the power system or not.

2.4.1.1 *Frequency response: fixed-speed machines*

Type I turbines are simple induction machines. They operate at fixed slip for any given power level, so they can only operate over a relatively small speed range. One way to think about this is to consider the steady-state torque expression for an induction machine, given by

$$T = \frac{3V_{th}^2 R_2'}{\left(s\omega_s\right)\left[\left(R_{th} + \dfrac{R_2'}{s}\right)^2 + \left(X_{th} + X_2'\right)^2\right]} \tag{2.12}$$

From (2.12), we see torque is a function of slip, s, given by

$$\mathrm{s} = \frac{\left(\omega_s - \omega_m\right)}{\omega_s} \tag{2.13}$$

where ω_s is synchronous speed, ω_m is the rotor speed.

The plot of T vs. s is given in Fig. 11 [19]. For stable operation, the electrical torque, to counter the mechanical torque, should increase as the machine speed (driven by the wind) increases. Fig. 11 shows stable operation to be between s=0 and about s=-12%. In reality, these units operate in a tighter slip range, typically within a 2% band - *almost* fixed speed; as a result, they are called fixed-speed machines.
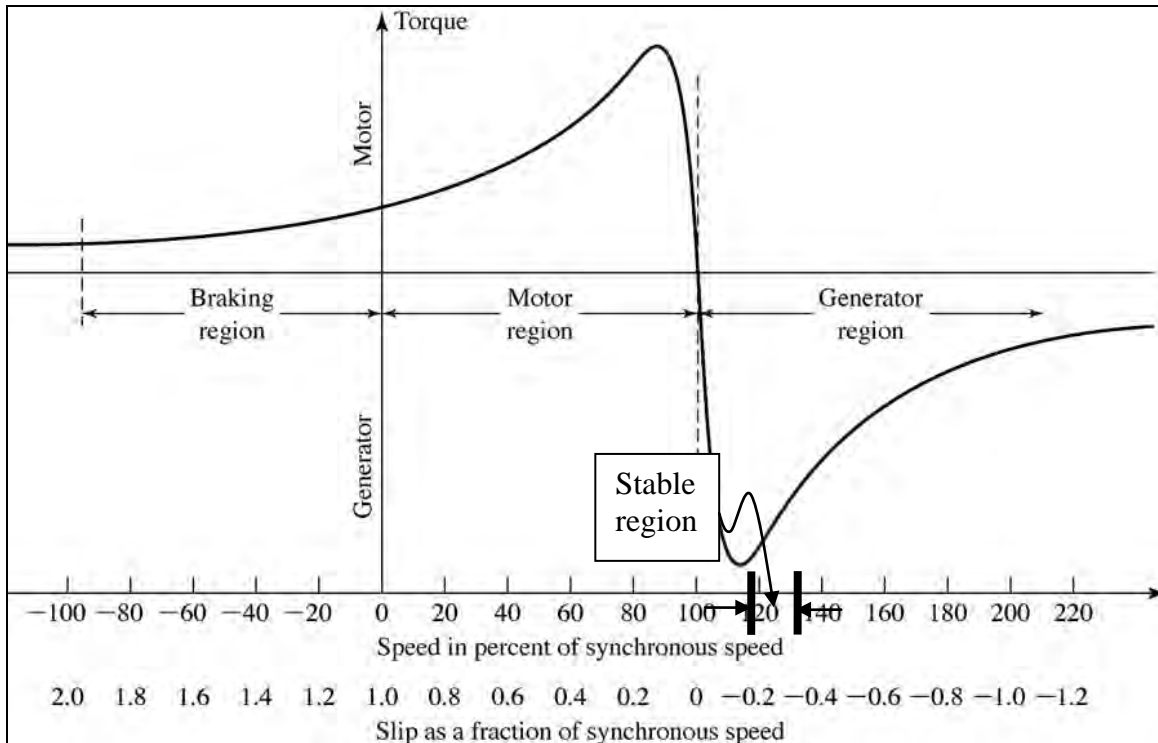
Fig. 11 Torque vs. Slip (Speed) [19]

Fig. 12 [20] illustrates how induction generator rated or nominal slip tends to reduce with generator power rating, with the larger units being designed to operate with lower slips. This is a result of the fact that induction generator efficiency improves as slip decreases, and efficiency becomes more important for larger machines. The point is, here, that for grid-size machines, nominal slip is in the 0-2% range.
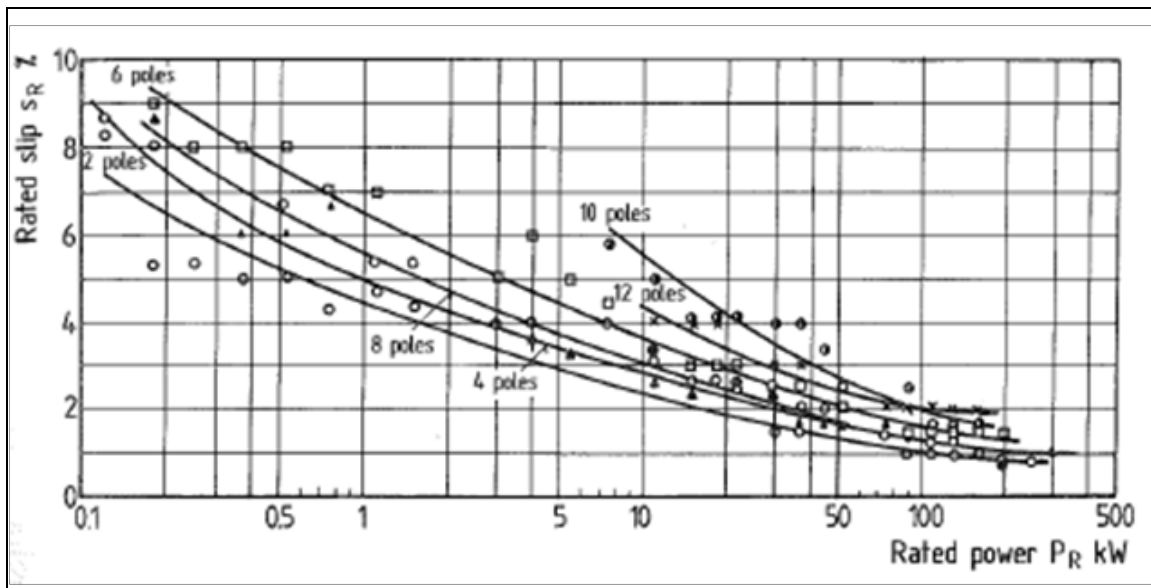
Fig. 12 Slip vs. Rated Power [20]

20

When the wind speed changes the fixed-speed machine, because of the induction generator characteristic, per Fig. 11, it will resist increase in rotor speed by increasing its electromechanical torque, effectively converting the higher wind speed to a higher power output.

Because of the steepness of the speed-torque relation, fixed speed machines have the undesirable characteristic of providing power injection into the grid that is as variable as the wind speed itself; they tend to surge power into the grid during wind gusts.

Consider now what happens to a fixed-speed machine when the network frequency changes due to, for example, loss of a generator somewhere in the system that causes a power imbalance. From (2.12) and (2.13), we see that

$$ T = \frac{3 V_{th}^{2} R_2'}{\left(s \omega_s \right) \left[\left(R_{th} + \frac{R_2'}{s} \right)^2 + \left(X_{th} + X_2' \right)^2 \right]} \tag{2.12} $$

where slip is given by (2.13),

$$ s = \frac{\left(\omega_s - \omega_m \right)}{\omega_s} = 1 - \frac{\omega_m}{\omega_s} \tag{2.13} $$

if the frequency changes from ω_s to $k\omega_s$, with 0<k<1, then the slip will also change from (2.13) to

$$ s_{new} = \frac{\left(\omega_s - \omega_m \right)}{\omega_s} = 1 - \frac{\omega_m}{k\omega_s} \tag{2.14} $$

and (2.12) will change to

$$ T = \frac{3 V_{th}^{2} R_2'}{\left(1 - \frac{\omega_m}{k\omega_s} \right) k\omega_s \left[\left(R_{th} + \frac{R_2'}{1 - \frac{\omega_m}{k\omega_s}} \right)^2 + \left(X_{th} + X_2' \right)^2 \right]} \tag{2.15} $$

where we have replaced ω_s by $k\omega_s$ and s=1- ω_m/ω_s by s_{new}=1- $\omega_m/k\omega_s$.

The torque-speed characteristic for an induction generator for f=60 Hz and for f=98% of 60Hz (58.8 Hz) are provided in Fig. 13. We assume a -2% slip for the 60 Hz case, so that the mechanical rotor speed will be $\omega_m = \omega_s(1-s) = 125.664(1--.02) = 128.18 \quad rad/\sec$ The vertical line corresponding to this mechanical speed is drawn in the plot of Fig. 13.
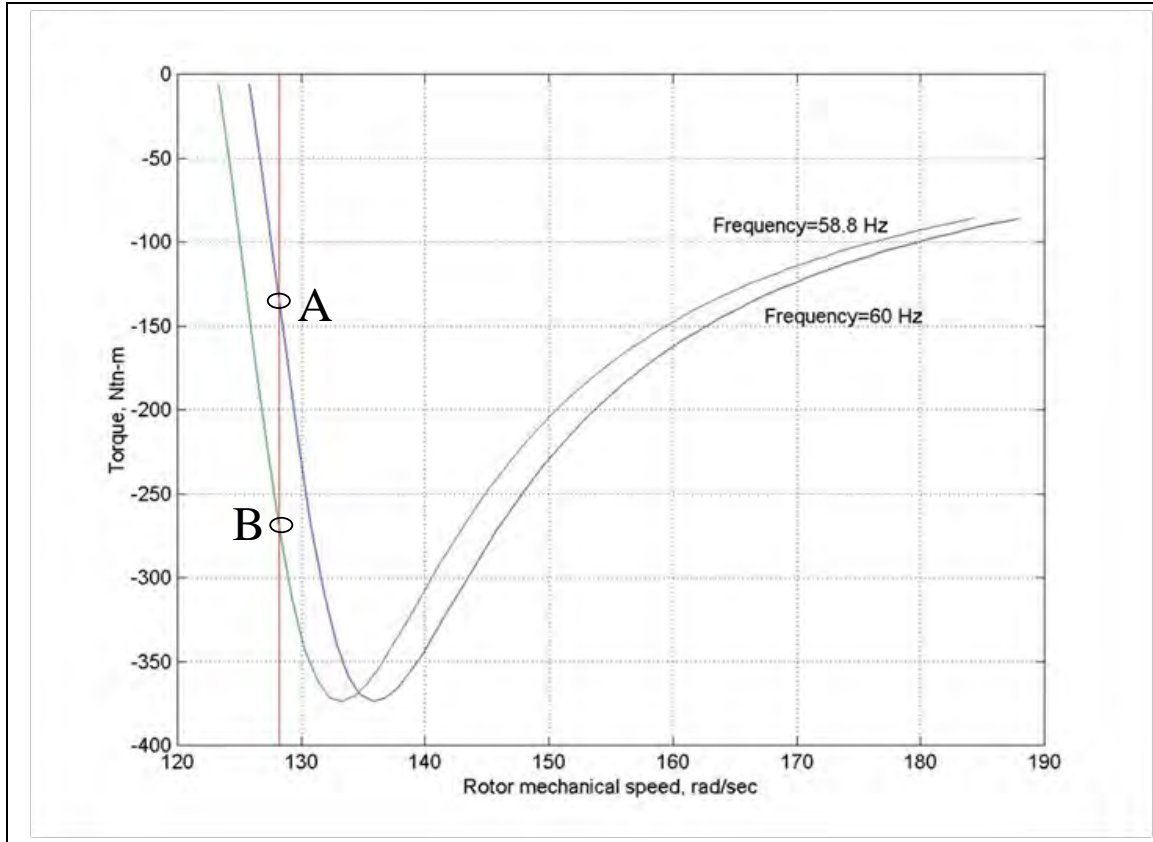
Fig. 13 Torque vs. Speed

Assume that the wind speed does not change over the short time period (a few seconds) when the network experiences the frequency drop. Then the mechanical power into the machine also does not change during this time, and the rotor speed, driven by the turbine, will remain fairly constant.

Under these conditions, Fig. 13 indicates that the electric torque provided by the generator will increase significantly, moving from point A on the 60Hz curve to point B on the 58.8 Hz curve. The generator torque, and corresponding power, has almost doubled. With the electrical torque so much greater than the mechanical torque, the machine decelerates, releasing stored energy into the system.

The rotational inertia of the fixed speed wind turbine is effectively "seen" by the external system, although its effect is tempered by the fact that the slip does dynamically change during disturbances. Although there is no "governor" to adjust the wind turbine output in response to changes in external power system frequency, the machine will passively provide some frequency restoration due to its rotational inertia.

2.4.1.2 *Frequency response: DFIGs*

To understand transient frequency response of a DFIG, we will first summarize the DFIG standard control systems. There are 3 main functional systems that are controlled in a

wind turbine: rotor yawing (ability to follow wind direction), speed-power control (including reactive power), and operational sequence[1] [20]. Our interest is the speed-power control, and we will briefly review the essentials of this system. This section is adapted largely from [20].

Fig. 14 compares a DFIG wind turbine to a typical steam-driven turbine-generator set (lines from "control" box indicate control capability, not feedback). The steam turbine has 3 types of control available to it: fuel input, steam valve, and generator field, with the first 2 related to speed-power control and the 3rd one related to MVAR-voltage control. In the case of the steam-turbine, the fuel supply controls the input mechanical power, and the steam-valve controls the output mechanical power.
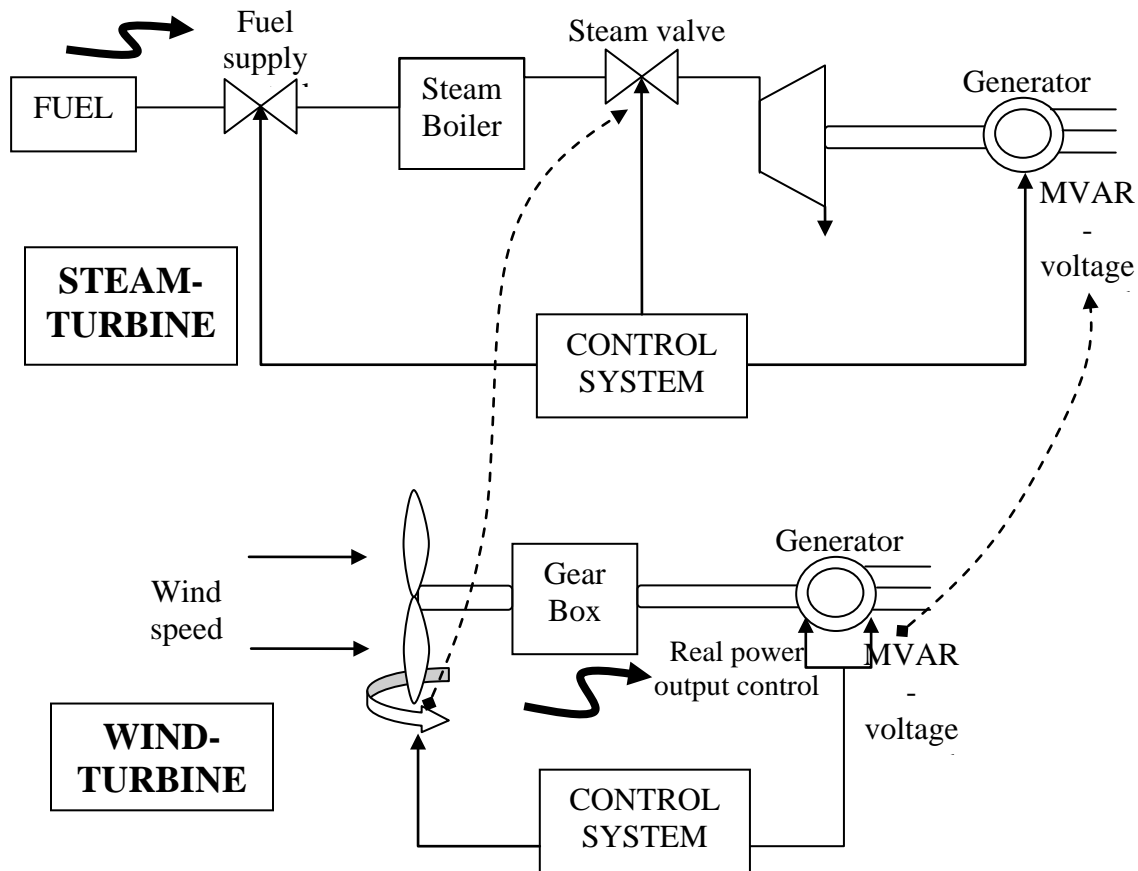
Fig. 14 Steam and Wind Turbines [20]

---

[1] Operational sequence is addressed by the sequence controller, which, from Erich Hau's excellent text, "receives external inputs according to the operating conditions and, above all, the wind conditions and the operator's intentions. This information will determine the setpoint values for the control system. The sequence controller monitors operating conditions and functional sequences and makes decisions concerning the mode of operation on the basis of logical deductions. As a rule, it is implemented in a programmable process computer with an associated data acquisition system."

The wind turbine also has three forms of control, although there are similarities, there are also significant differences. One similarity is the MVAR-voltage control capability; although this control is accomplished in a different manner, the ultimate effect is quite similar. This control capability in each machine is connected via a dashed line on the right-hand-side of Fig. 14.

The wind turbine can also control the output mechanical power applied to the generator through pitching the blades. Therefore we see that pitching the blades is analogous to steam flow control in a steam turbine. This control capability in each machine is connected via a dashed line in the middle portion of Fig. 14.

Whereas the steam turbine has the additional power control capability at the fuel input (indicated by a dark snaked arrow at the top of Fig. 14), which the wind turbine does not have, the wind turbine has power control capability at the generator output (indicated by a dark snaked arrow at the bottom of Fig. 14), which the steam turbine does not have. Control of the generator power output is performed via control of the d-axis component of the rotor current.

The ability to control mechanical power into the generator using pitch control and generator power output using rotor current control enables avoidance of mismatch between mechanical power in and electrical power out and, therefore, also avoidance of rotor deceleration under network frequency decline. This means DFIGs contribute no inertial energy under underfrequency conditions.

As long as DFIGs are merely added to historical generation commitment schedules, this feature is not problematic. But as soon as DFIGs begin to displace conventional generators in the generation commitment schedules, the denominator of (2.11b) will decrease, and as a consequence, the ROCOF will increase.

$$
\frac{d\overline{\Delta f}}{dt} = \frac{-\Delta P_L f_{\mathrm{Re}}}{2\sum\limits_{i=1}^{n} H_i} \equiv m_f
$$
(2.11b)

This results in lower (greater) transient frequency dips under large-scale generation outages, as indicated in reference [21], which compares, for a test system, four different DFIG:FSM splits of a 15.6% wind-turbine penetration level: 50:50, 60:40, 70:30, and 100:0.

One can observe a similar trend for the US Eastern Interconnection in Fig, 15, where an 8% penetration level is compared under
- Pink: Base Case
- Yellow: Unit De-Commitment
- Red: Load Increasing
- Green: Generation Decreasing without De-Commitment

24
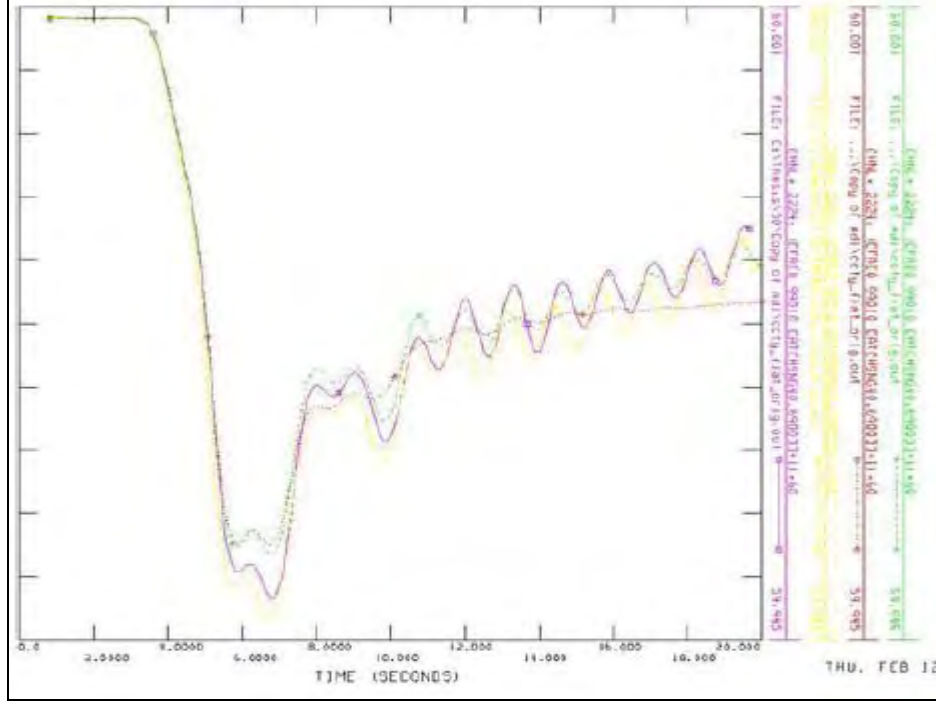
Fig. 15 Frequency Response for Different Scenarios for U.S. Eastern Connection

Although we did not study the impact of decreased inertia on CPS1 and CPS2 in this work, we think it highly likely that it causes significantly degraded performance with respect to these two metrics.

Several European grid operators have imposed requirements on wind plants in regards to frequency contributions, including the Nordic countries [22, 23]. North American interconnections have so far not imposed requirements on wind farms in regards to frequency contributions, with the exception of Hydro-Quebec.

Hydro Quebec requires that wind farms be able to contribute to reduce large (>0.5 Hz), short-term (< 10 sec) frequency deviation [24]. The Hydro-Quebec requirement states [25], "The frequency control system must reduce large, short-term frequency deviations at least as much as does the inertial response of a conventional generator whose inertia (H) equals 3.5 sec."

2.4.2 Adding transient frequency control to DFIGs

The power which can be extracted from the wind by the wind turbine rotor, P_m, is less than the power in the wind, P_{wind}, and this concept is captured by the relation

$$P_m = C_p P_{wind} \tag{2.16}$$

where C_p is the power coefficient and depends on the tip speed ratio, λ. The tip speed ratio is the ratio of the rotor tip velocity and the wind speed, V_{wind}, given by [26]

$$\lambda = \frac{\omega_r R}{V_{wind}} \tag{2.17}$$

25

where ω_r is the angular velocity of the rotor and R is its radius, so that the product gives the speed at the "tip."

The dependence of C_p on λ is illustrated in Fig. 16, where it is clear that there is a value of λ for which C_p is maximum. This is the most desirable operating point. Therefore for a certain wind velocity, we desire to ensure that the tip-speed ratio is λ_{opt} in order to maximize the power extracted from the wind.
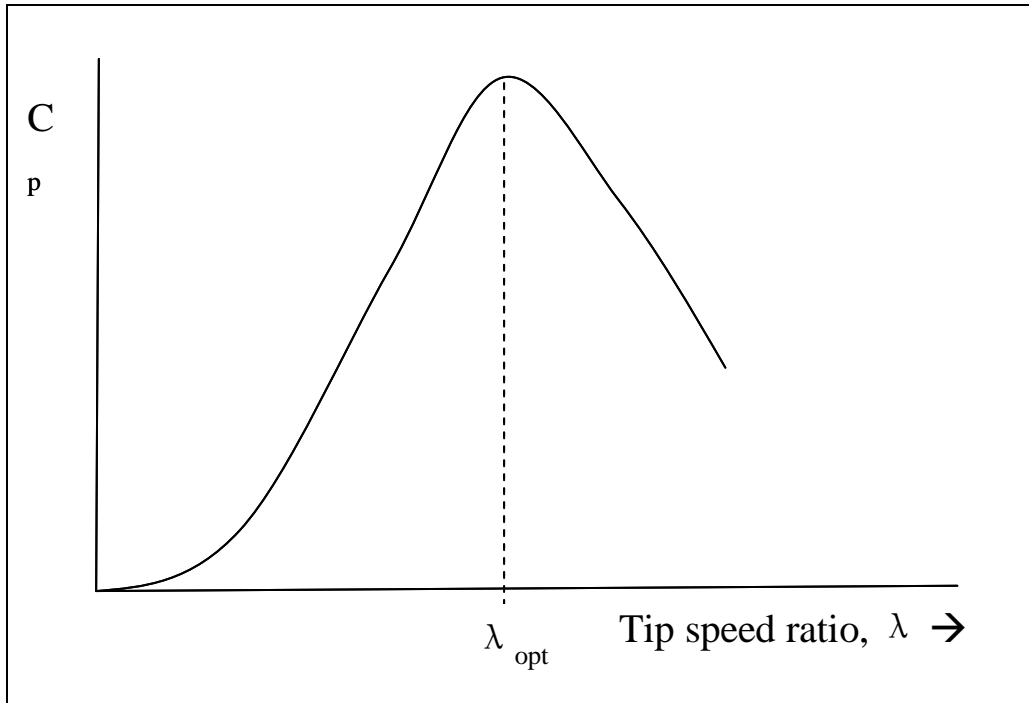
Fig. 16 C_p vs.λ [26]

Fig. 17a [27] illustrates this same notion, but instead of plotting C_p against λ, generator torque is plotted against generator speed for different wind speeds. For a given wind speed, the curve identifies optimal generator torque and speed.
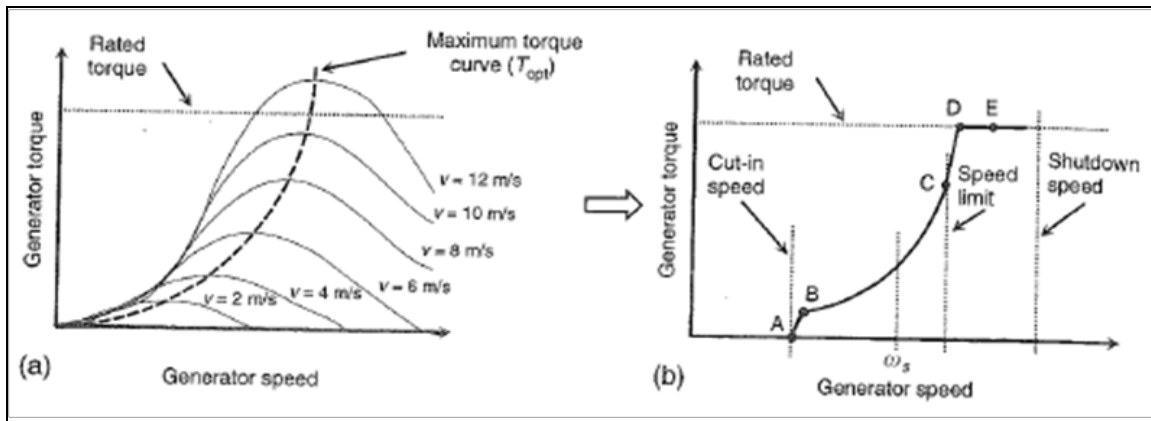
Fig. 17 Generator Torque vs. Generator Speed for Different Wind Speeds [27]

In Fig. 17a, a dotted curve is drawn through the points of maximum torque. This curve is very useful for control, in that we can be sure that as long as we are operating at a point on this curve, we are guaranteed to be operating the wind turbine at maximum efficiency. Therefore this curve, redrawn in Fig. 17b, dictates how the machine should be controlled in terms of torque and speed. The torque-speed control loop for a DFIG wind turbine is shown in a Fig. 18 [26].
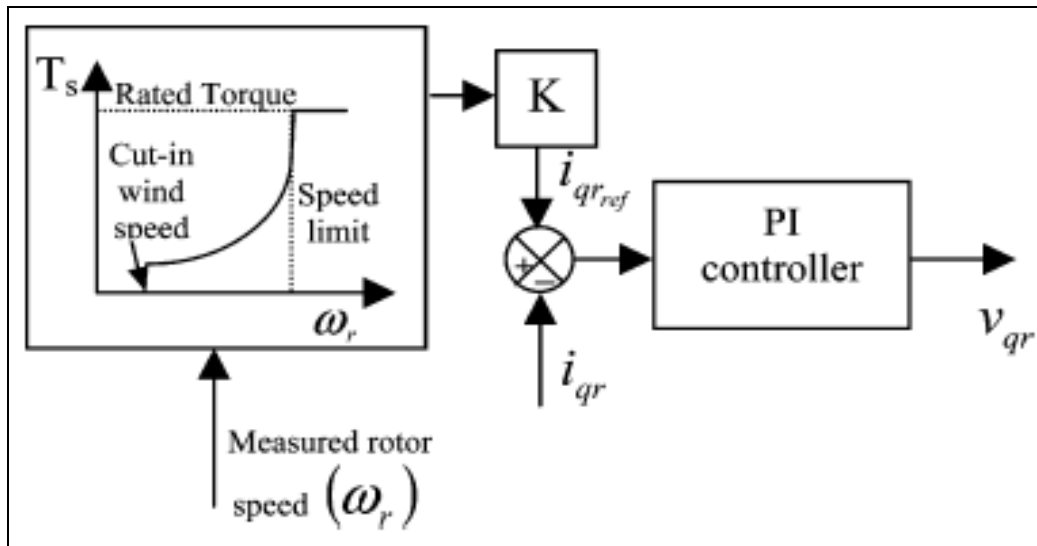
Fig. 18 Torque Control Loop [26]

This is how almost all DFIG's operating today in North America were designed, and it is the primary reason why we do not obtain inertial response from DFIGs for transient frequency performance. It is possible to provide supplementary control, however. Such control is illustrated in Fig. 19.
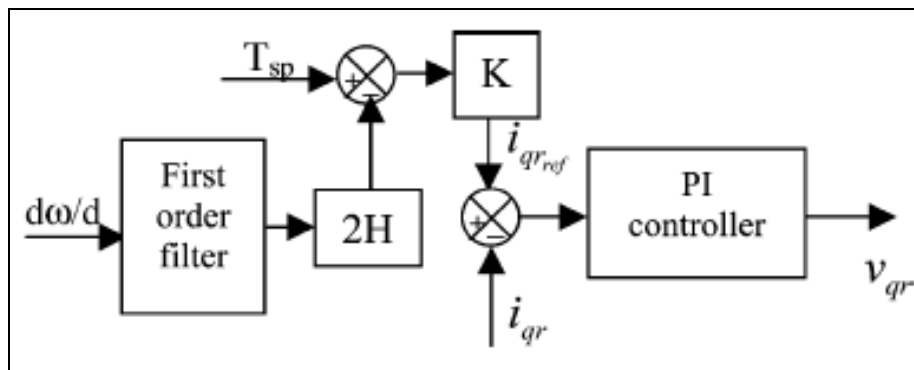
Fig. 19 Torque Control Loop with Supplementary Control [26]

Comparison between Fig. 18 and Fig. 19 shows that in Fig. 19 we have added a signal dω/dt scaled by 2H. This provides the control necessary to provide inertial response for transient frequency performance.

3. Grid Operation and Coordination with Wind - Regulation

3.1 Introduction

In this chapter, the need for regulation is presented. We have stated in Chapter 2 that regulation occurs in the time frame of about 1 minute. Fig. 20 [28] illustrates the time frame relative to the initial transient period (Chapter 2) and the later load following and scheduling time periods. This picture provides a very good view on:

- Relation between inertial response (kinetic energy), primary reserves, and secondary reserves, and
- Effect of load frequency sensitivity
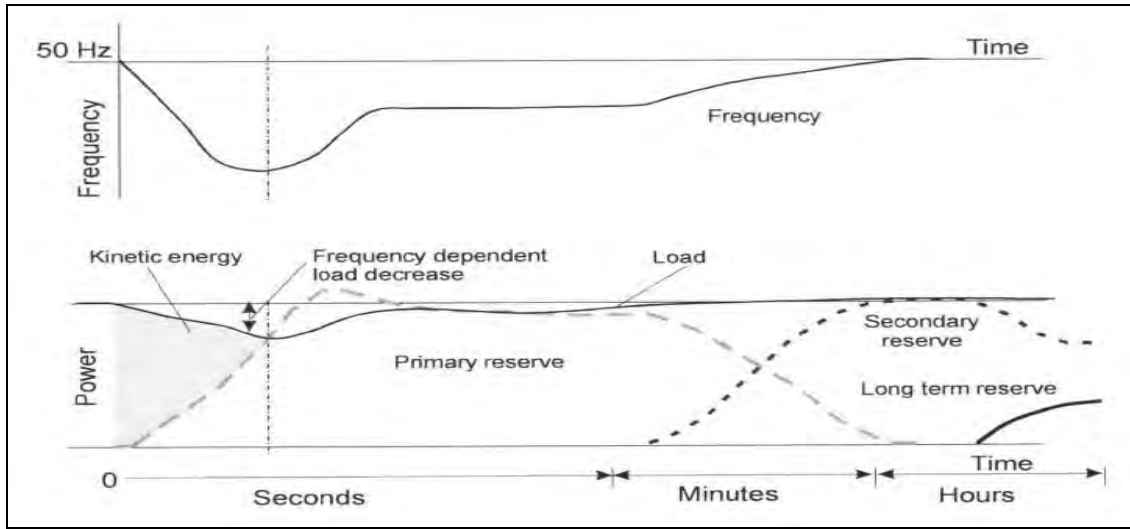
Fig. 20 Time Frame for MW-Frequency Response [28]

Our focus is on primary frequency control. Fig. 20 uses the term "primary reserves" to capture the power operations requirement that there must be generation interconnected at any given moment having spinning reserve (difference between capacity and existing generation level) sufficient to compensate for credible events which cause load-generation imbalance.

The North American Electric Reliability Corporation (NERC) states in [29], "As a minimum, the Balancing Authority or Reserve Sharing Group shall carry at least enough Contingency Reserve to cover the most severe single contingency. All Balancing Authorities and Reserve Sharing Groups shall review, no less frequently than annually, their probable contingencies to determine their prospective most severe single contingencies."

We will see most existing wind turbines today do not have control capability necessary to provide regulation. But perhaps even more significant is the variability associated with wind, i.e., wind not only does not help regulate, it contributes to a need for more regulation.

28

3.2 Variability of wind power

There are two important ways to understand the variability in wind power: temporally and spatially.

3.2.1 Temporal variability

Clearly wind speed varies with time, so that the wind speed for turbine k at time t_1, $v_k(t_1)$, will generally differ from the wind speed for turbine k at time t_2, $v_k(t_2)$, where $t_2 > t_1$. For fixed speed machines, because the mechanical power into a turbine depends on the wind speed, and because electric power out of the wind generator depends on the mechanical power in to the turbine, variations in wind speed from t_1 to t_2 cause variations in electric power out of the wind generator.

Double-fed induction generators (DFIGs) also produce power that varies with wind speed, although the torque-speed controller provides that this variability is less volatile than fixed-speed machines. For a single turbine, this variability depends on three features: (1) time interval; (2) location; (3) terrain.

3.2.1.1 Time interval

Variability in wind plant output tends to increase with time interval, that is, 12 hour variation tends to be larger than 4 hour, which tends to be larger than 1 hour, etc. Reference [30] illustrates this tendency for the Midwestern US via distributions for 1-hour, 4-hour, and 12-hour intervals; it also provides a similar distribution for Germany. Reference [30] illustrates this tendency for a number of other regions around the world by showing maximum increase and decrease for 10-15 minute intervals, 1 hour intervals, 4 hour intervals, and 12 hour intervals.

Perhaps the most severe kind of variation occurs during extreme weather events where turbines can be shut down to avoid rotor overspeed in high wind conditions. A wind farm can go from near-full output to near-zero output when a severe storm passes through the area. Examples of such occurrences are described below [30]:

1. Denmark: 2000 MW (83% of capacity) decrease in 6 hours or 12 MW (0.5% of capacity) in a minute on 8th January, 2005.
2. North Germany: over 4000 MW (58% of capacity) decrease within 10 hours, extreme negative ramp rate of 16 MW/min (0.2% of capacity) on 24th December, 2004.
3. Ireland: 63 MW in 15 mins (approx 12% of capacity at the time), 144 MW in 1 hour (approx 29% of capacity) and 338 MW in 12 hours (approx 68% of capacity).
4. Portugal: 700 MW (60% of capacity) decrease in 8 hours on 1st June, 2006.
5. Spain: Large ramp rates recorded for about 11 GW of wind power: 800 MW (7%) increase in 45 minutes (ramp rate of 1067 MW/h, 9% of capacity), and 1000 MW (9%) decrease in 1 hour and 45 minutes (ramp rate -570 MW/h, 5% of capacity). Generated wind power between 25 MW and 8375 MW have occurred (0.2%-72% of capacity).

6. Texas, US: loss of 1550 MW of wind capacity at the rate of approximately 600 MW/hr over a 2½ hour period on February 24, 2007.

3.2.1.2 Location and terrain

There are two major attributes to wind power variability by time interval: location (latitude of the site on the globe) and terrain. Reference [31] states the following: "In medium continental latitudes, the wind fluctuates greatly as the low-pressure regions move through. In these regions, the mean wind speed is higher in winter than in the summer months. The proximity of water and of land areas also has a considerable influence. For example, higher wind speeds can occur in summer in mountain passes or in river valleys close to the coast because the cool sea air flows into the warmer land regions due to thermal effects. A particularly spectacular example are the regions of the passes in the coastal mountains in California through to the lower lying desert-like hot land areas in California and Arizona."

3.2.2 Spatial variability

Reference [30] provides 24 hour plots of normalized power output from (a) a single turbine in the region; (b) a group of turbines in the same wind plant within the region; and (c) all turbines in the region (in this case, the "region" was the country of Germany). In these plots, one observes that the variability of the single turbine, as a percentage of capacity, is significantly greater than the variability of the wind plant, which is in turn significantly greater than the variability of the region. We refer to this effect as "geographical smoothing" where the variability of a larger region, as a percentage of the capacity, is typically less than that of smaller portion of the same region.

This tendency may also be observed via Fig. 21 below [28]. This is a *duration curve*, which provides the number of hours on the horizontal axis for which the wind power production exceeds the percent capacity on the vertical axis. Observations regarding this curve follow:
- The single turbine reaches or exceeds 100% of its capacity for perhaps 100 hours per year, the area called "Denmark West" has a maximum power production of only about 90% throughout the year, and the overall Nordic system has maximum power production of only about 80%.
- At the other extreme, the single turbine output exceeds 0 for about 7200 hours per year, leaving 8760-7200=1560 hours it is at 0. The area wind output rarely goes to 0, and the system wind output never does.
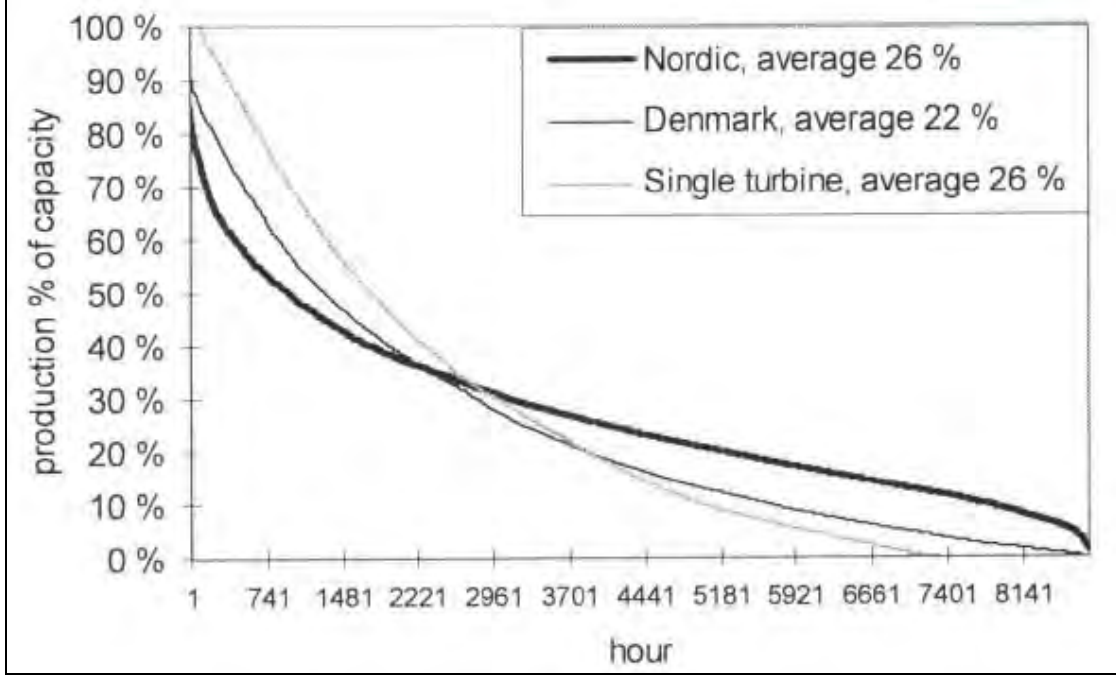
Fig. 21 Duration Curve [28]

Another interesting way to look at wind production variability combines both temporal and spatial effects. To understand this approach, we define the correlation coefficient for two time series x and y as

$$r_{xy} = \frac{\sum_{i=1}^{N}(x_i - \mu_x)(y_i - \mu_y)}{N\sqrt{\sum_{i=1}^{N}(x_i - \mu_x)^2}\sqrt{\sum_{i=1}^{N}(y_i - \mu_y)^2}} = \frac{\sum_{i=1}^{N}(x_i - \mu_x)(y_i - \mu_y)}{N\sigma_x\sigma_y} \qquad (3.1)$$

where N is the number of points in the time series, and μ_x, μ_y and σ_x, σ_y are the means and standard deviations, respectively, of the two time series. The correlation coefficient indicates how well two time series, x and y in this case, follow each other. It will be near 1.0 if the two time series follow each other very well, it will be 0 if they do not follow each other at all, and it will be near -1 if increases in one occur with decreases in another.

Consider taking minute-by-minute measurements for wind turbine power production at a large number of locations within a 600 km radius. There will be many different distances between each location. We assume that we have such measurements over an extended period of time, say 3 years.

We then compute sequential (consecutive) averages of time intervals T for each location. Then compute a T-interval average at t=0, t=T, t=2T, t=3T,…. For example, we may choose T=5 minutes, so we obtain, at each location x1, x2, x3,… a time series of sequential 5 minute averages. We can then compute the correlation coefficient between time series at each pair of locations. The computed correlation coefficient can then be

plotted against the distance between each pair of locations. This can be done for various values of T, e.g., T=5 min intervals, T=30 min intervals, T=1 hr intervals, and so on.

Fig. 22 [32] illustrates the resulting plot where it is clear that for 5 minute intervals, there is almost no correlation for locations separated by more than about 20 km. This is because wind gusts tend to occur for only a relatively small region. This suggests that even small regions will experience geographical smoothing at 5 min intervals.
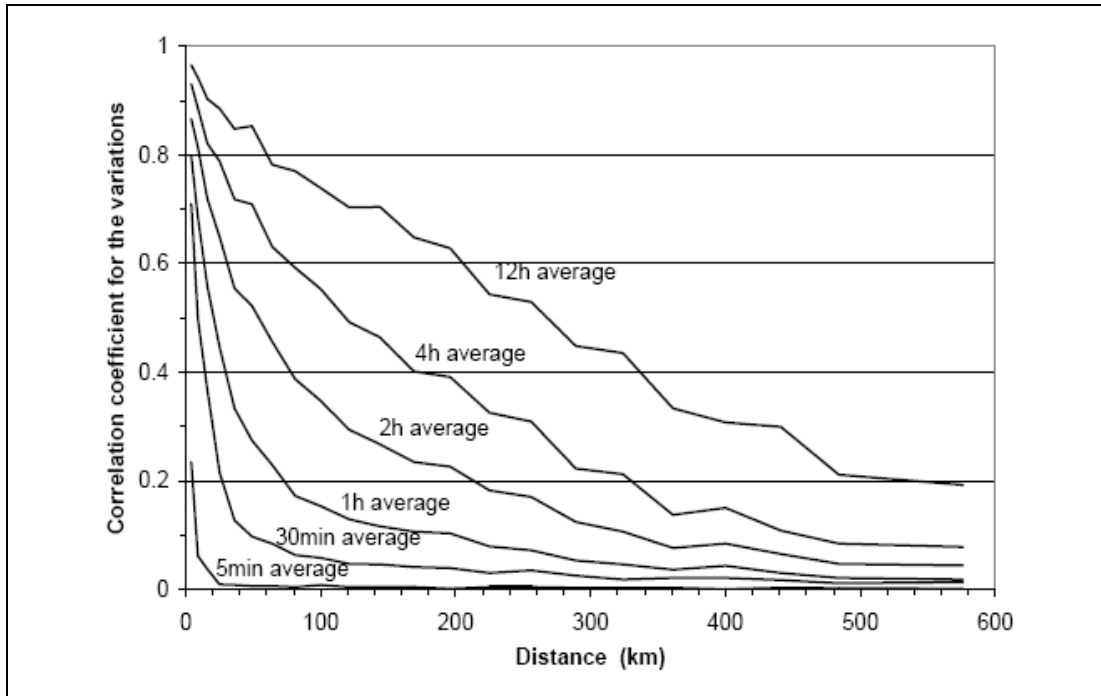
Fig. 22 Correlation vs.Distance [32]

At the other extreme, for 12 hour intervals, Fig. 22 indicates that wind power production is correlated even for very large regions, since these averages are closely linked to overall weather patterns that can be similar for very large regions.

Fig. 23 [33] shows another way to view smoothing, where clearly the variability of the 1 farm, given as a percentage of its capacity, is significantly greater than that of the entire region of Western Denmark.
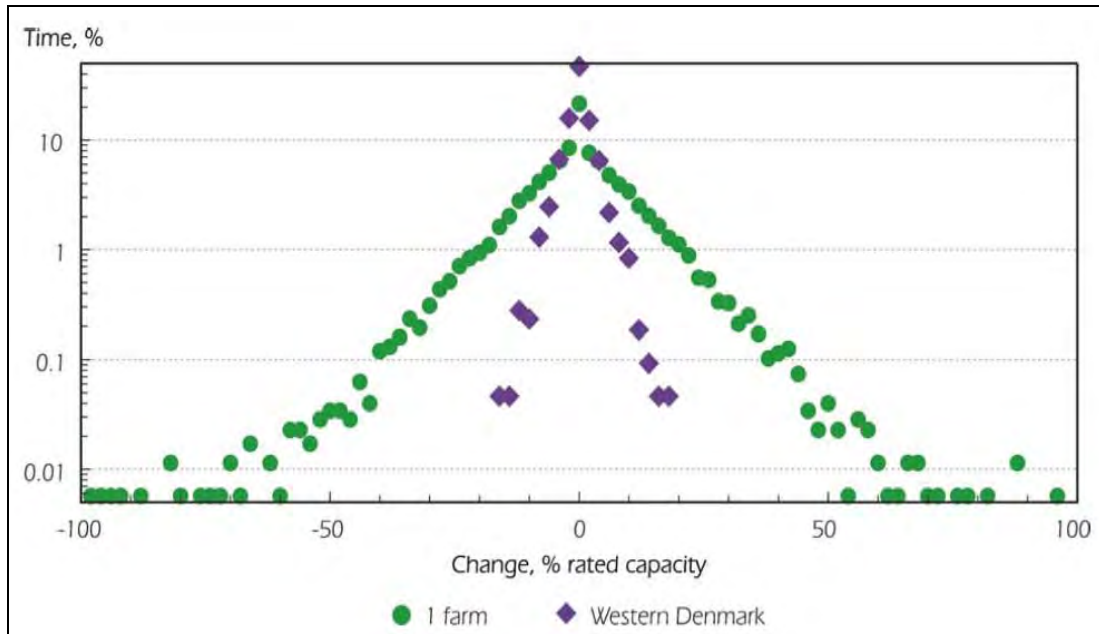
Fig. 23 Smoothing for Western Denmark [33]

If data used to develop Fig. 23 is captured for a large number of wind farms and regions, the standard deviation may be computed for each farm or region. This standard deviation may then be plotted against the approximate diameter of the farm's or region's geographical area. Fig. 24 [30] shows such a plot, where the variations were taken hourly. It is clear that hourly variation, as measured by standard deviation, decreases with the wind farm's or region's diameter.
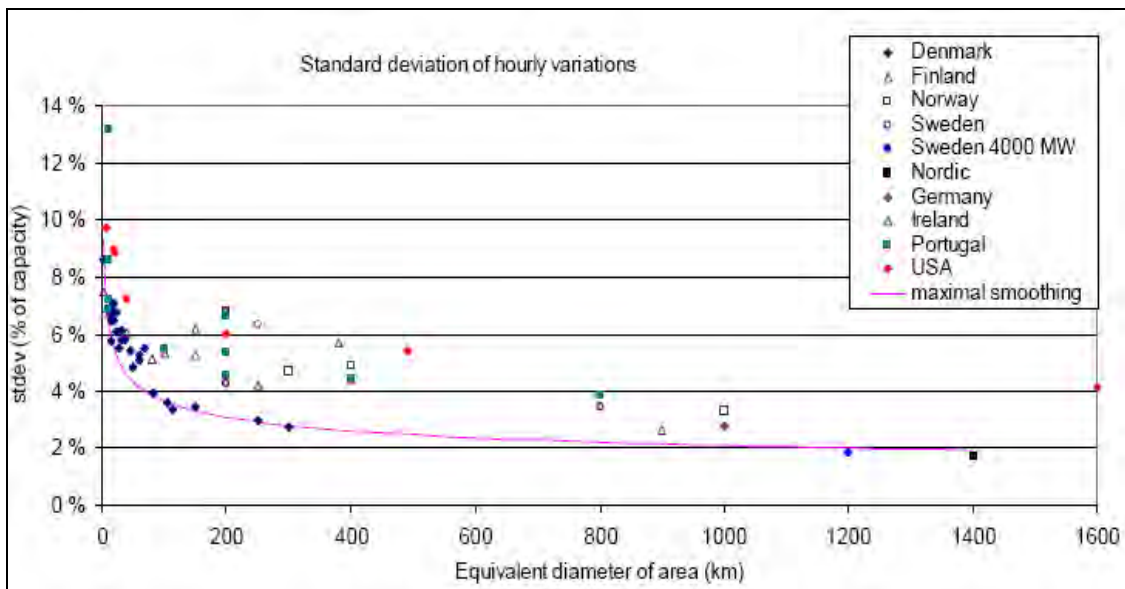
Fig. 24 Standard Deviation vs. Diameter [30]

Reference [32] makes the following comment about geographical smoothing: "How large is the smoothing effect? It becomes more noticeable if there are a large number of turbines spread over a larger area. The smoothing effect of a specified area has an upper limit. There will be a saturation in the amount of variation; that is, where an increase in the number of turbines will not decrease the (relative) variations in the total wind power production of the area. Beyond that point, the smoothing effect can be increased only if the area covered becomes larger. And there is a limit to that effect, too. The examples we use are from comparatively uniform areas. If wind power production is spread over areas with different weather patterns (coasts, mountains and desert), the smoothing effect will probably be stronger."

3.3 Variability of net demand

The load varies from minute to minute and from hour to hour. A control area's portfolio of conventional generation is designed to meet that load variability. This is done by ensuring there are enough generators that are on governor control, and that there are enough generators having ramp rates sufficient to meet the largest likely load ramp. Typical ramp rates for different kinds of units are listed below (given as a percentage of capacity):

- Diesel engines 40 %/min
- Industrial GT 20 %/min
- GT Combined Cycle 5 -10 %/min
- Steam turbine plants 1- 5 %/min
- Nuclear plants 1- 5 %/min

For example, one utility states that in their generation portfolio [34], "Coal units typically have ramp rates that are in the range of 1% to 1.5% of their nameplate rating per minute between minimum load and maximum load set points. Coal unit minimum load set-points range from 20% to 50% of nameplate, depending on the design of the air quality control system being used. For example, a 500 MW coal plant may have a minimum load of 100 MW and would be able to ramp up at the rate of 5 MW per minute. In addition, it can take a day or more to bring a coal plant up to full load from a cold start condition. Natural gas-fired combustion turbines, on the other hand, can normally be at full load from a cold start in 10 to 30 minutes (which results in an effective ramp rate of 3.3% to 10% of their nameplate rating per minute)."

Without wind generation, one selects a generation portfolio to satisfy load variability. Fig. 25, and Fig. 26, show 1 hr, and 10 min load variability for a particular control area.
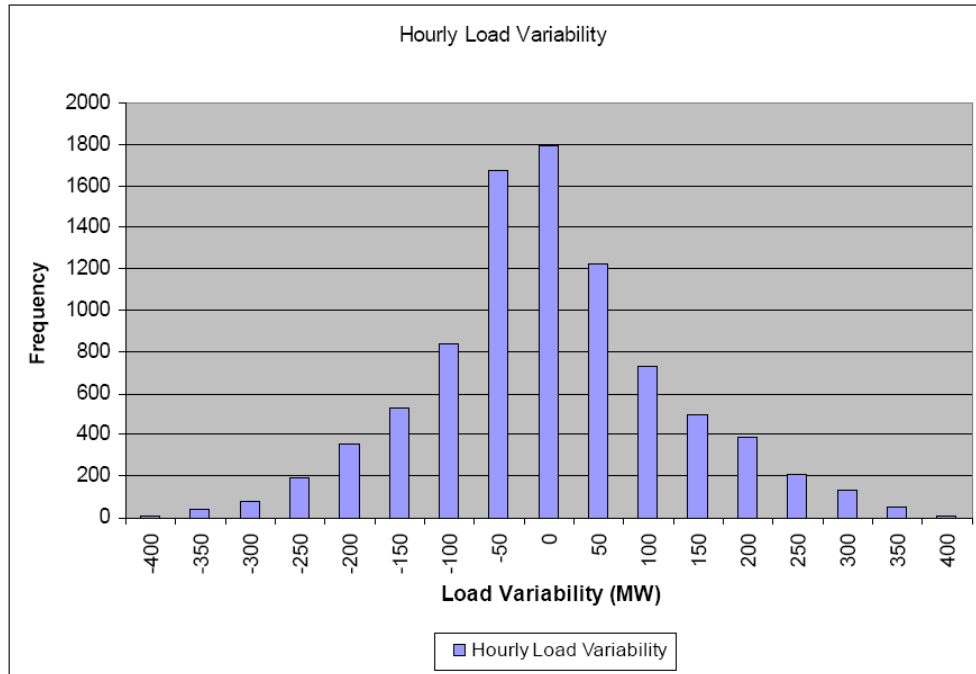
Fig. 25 Hourly Load Variability
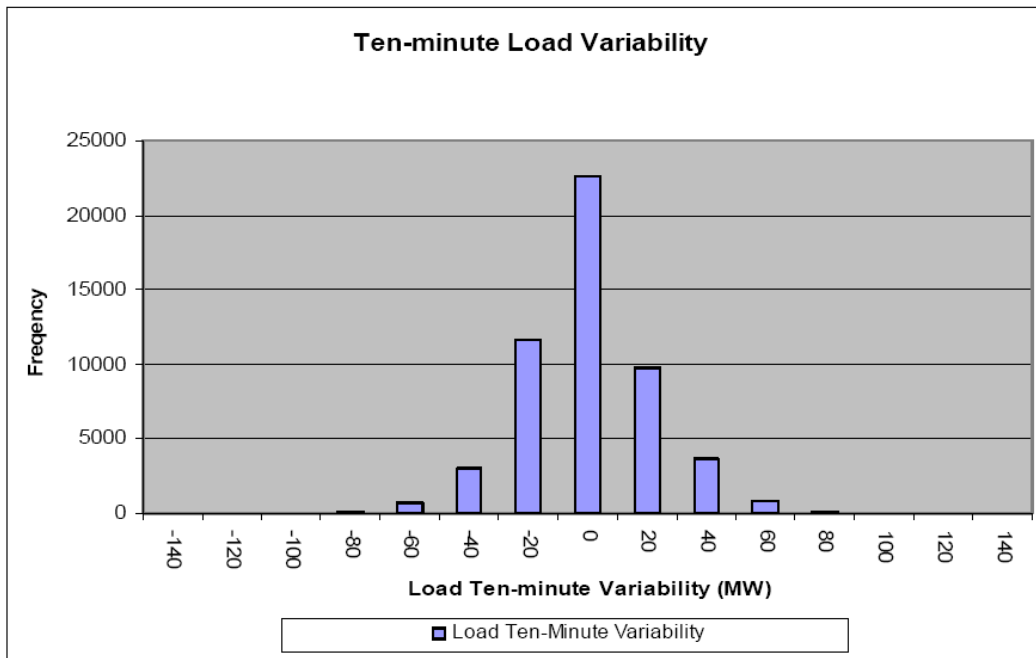
Fig. 26 10-Minutes Load Variability

These plots show that the particular control area responsible for balancing this load must have capability to ramp 400 MW in one hour (6.7 MW/min), and 80 MW in 10 minutes (8 MW/min), in order to meet all MW variations seen in the system. The question arises: what happens to these requirements if wind is added to the generation portfolio?

Fig. 27, and Fig. 28, show variability of a certain amount of wind generation in this control area.
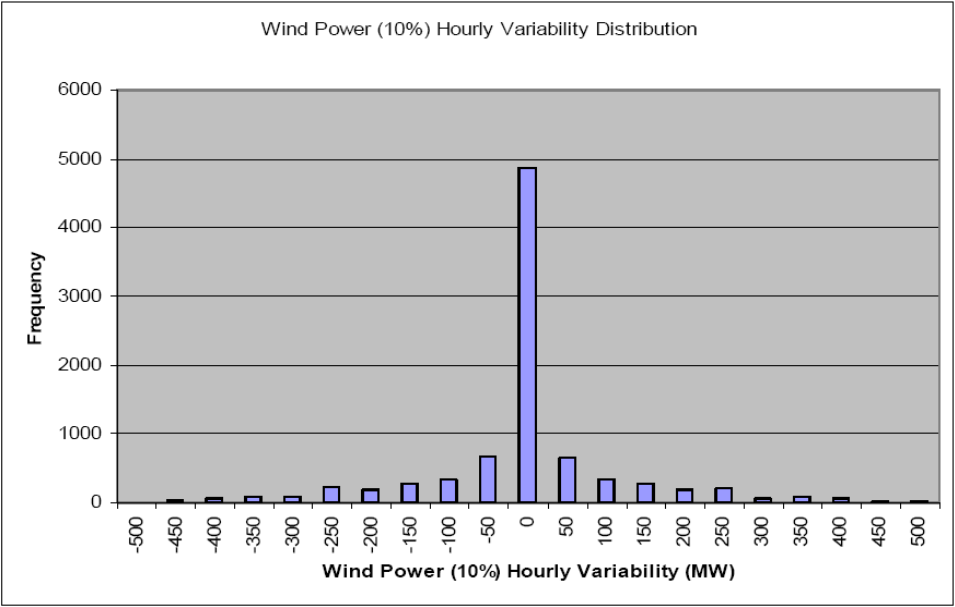
Fig. 27 Hourly Wind Variability
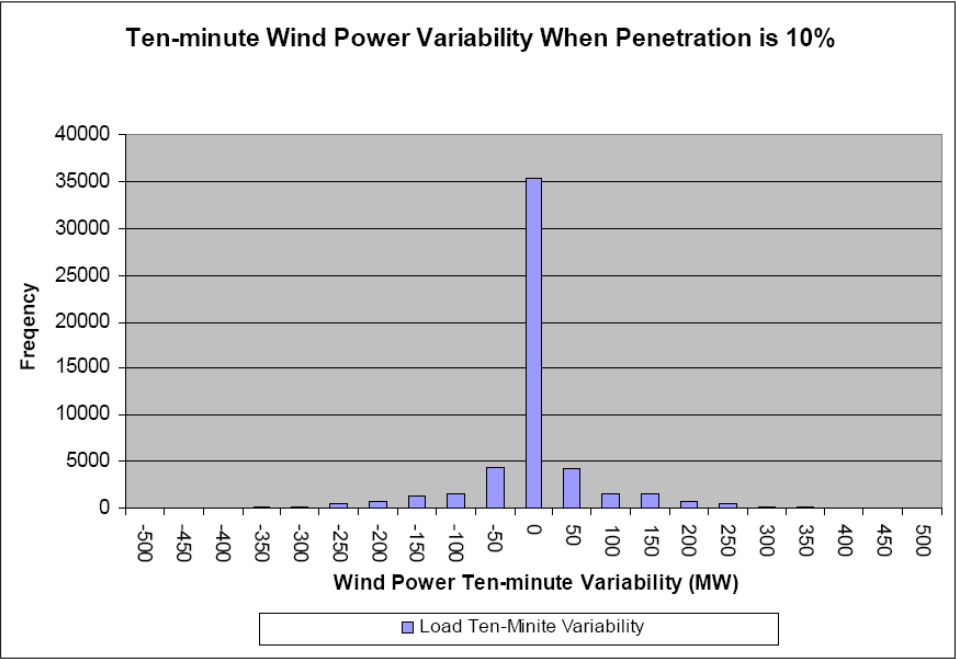
Fig. 28 10-Minutes Wind Variability

Statistically, the question of adding wind to the load can be stated as: "Given two random variables x (load) and y (wind power) for which we know the distributions $f_x(x)$ and $f_Y(y)$, respectively, how do we obtain the distribution of the net-load random variable z=x-y, $f_z(z)$?"

If these random variables are *independent*, then for the means, we have $\mu_z=\mu_x-\mu_y$, and for the variances, we have $\sigma_z^2 = \sigma_x^2+\sigma_y^2$. The impact on the means is of little interest since the means of variability, for both load and wind, will be ~0. On the other hand, the impact on the variance is of great interest, since it implies the distribution of the difference will always be wider than either individual distribution. Therefore we expect that when wind generation is added to a system, the maximum MW variation seen in the control area will increase.

We can manually create the distribution for net-load as follows. For each time interval, subtract the wind power from the load to yield the net-load. Then compute variability from each interval to the next. Application of this approach results in the distributions of net-load for 1 hour and 10 minute intervals, as shown in Fig. 29 and Fig. 30.

For ease of comparison, Fig. 29 and Fig. 30, also show the distribution of only load. Table 2 summarizes for each interval the standard deviation, σ, and the maximum variation, corresponding to load only and net-load.
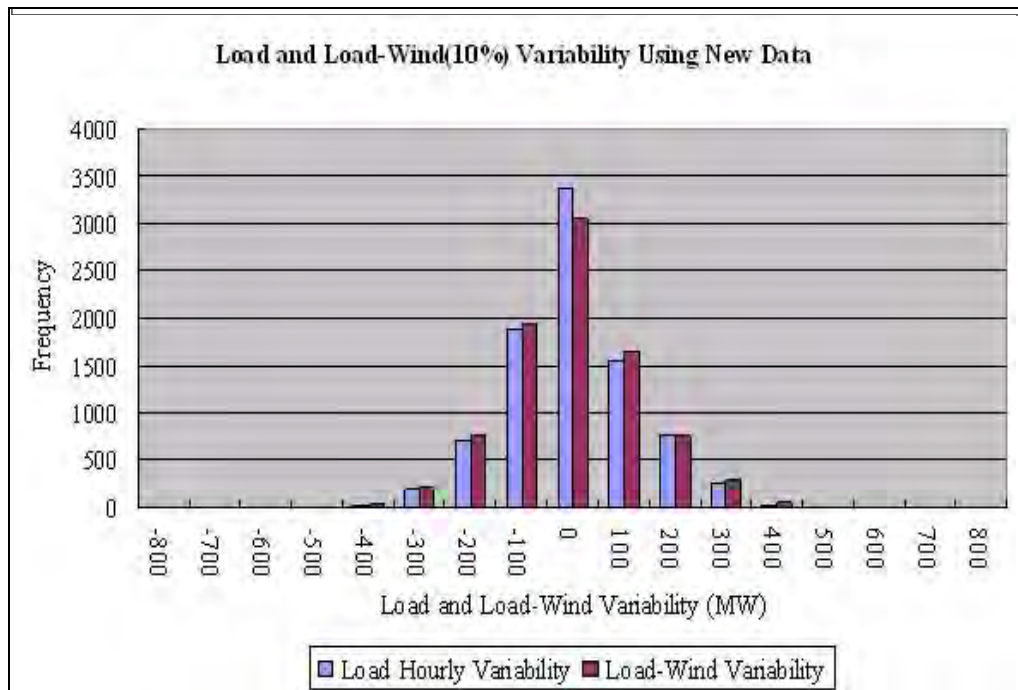
Fig. 29 Hourly Load and net-Load Variability
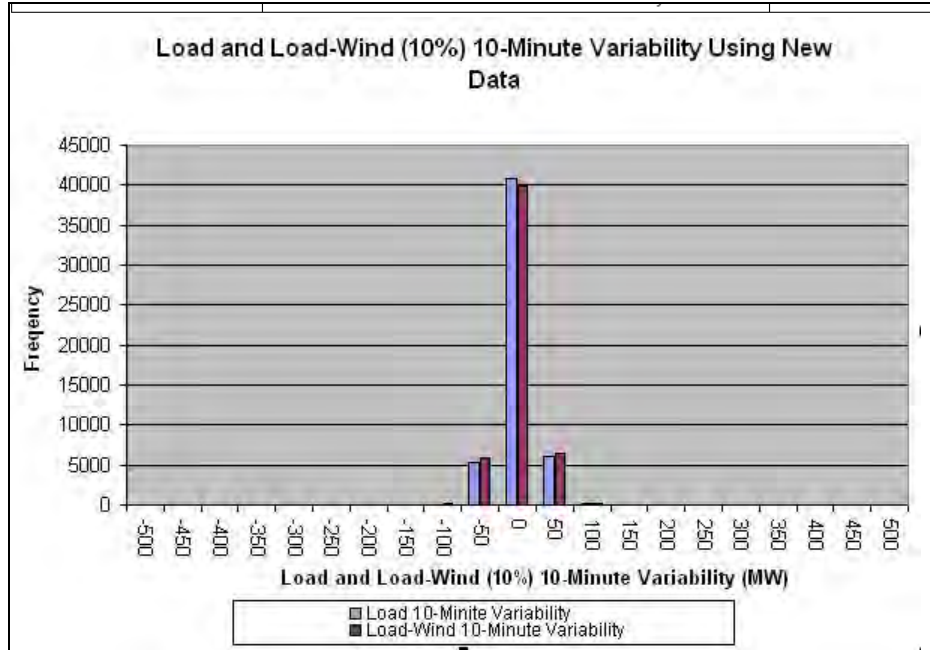
Fig. 30 10-minutes Load and net-Load Variability

Table 2 Standard Deviation and Maximum Variation for Load and Net Load for Different Time Frame

	1 hour		10 min	
	σ	max	σ	max
Load (MW)	123	400	22	135
Net load (MW)	130	499	23.6	158

It is important to understand when, during the day, the high-MW variability instances occur. To understand this issue, one needs to realize that most control area operators will provide more reserve during times of high load variability, for example, during morning rise and evening fall. Therefore, if the high net-load variability instances occur during times of high load variability, then the amount of additional reserves necessary to handle it will be relatively small. On the other hand, if the high net-load variability instances occur during times of low load variability, then the amount of additional reserves will be relatively large. For example, wind could create a need for 25% reserves on top of what is otherwise a 15% mid-afternoon requirement, or it could create a need for 25% reserves on top of what is otherwise a 20% morning requirement. The first case would require an additional 10% during the afternoon, whereas the second case would require an additional 5% during the morning. Although the two reserve requirements are the same, it is possible that supplying the 25% in the afternoon would have to be met with more expensive generation.

3.4 Limiting wind ramp rates

Fig. 1 summarizes ways to address the effect of wind on increased MW variability, and these ways include increasing control of wind generation. One such control is limiting wind ramp rates.

Reference [35, pg. 168-169] addresses limiting ramp rates as follows: "When the turbines are operational, the positive ramp rate can be controlled easily by adjusting the rotor pitch angle. This operation can be implemented independently for each turbine or coordinated across the entire wind farm. In contrast, the output of stall-controlled (passive) wind turbines cannot be readily controlled. The German maximum ramping rate specification is 10 percent of turbine rating per minute, while in Ireland two settings are specified – ramp rate per minute and ramp rate over 10 minutes. The one-minute ramp rate is set currently at 8 per cent of registered capacity per minute (not less than 1 MW/minute and not higher than 12 MW/minute) while the 10 minute ramp rate is 4 per cent of registered capacity per minute (not less than 1 MW/minute and not higher than 6 MW/minute). In Great Britain, the ramping requirements are defined by the size of the wind farm – no limit for wind farms up to 300 MW capacity, 50 MW/minute between 300 and 1000 MW capacity, and 40 MW/minute beyond 1000 MW in size. With sufficient notice the ramp rate should be adjustable by the TSO, with increasing wind penetration. In Ireland, for example, both settings (per minute and per 10 minutes) should be independently variable over the range 1-30 MW/minute. In Energinet (Denmark), the ramp rate should be adjustable within the range of 10-100 per cent turbine rating per minute."

3.5 Primary frequency control: conventional generation

It is useful to understand the primary frequency control function for conventional generation in order to appreciate the corresponding controls on a wind turbine. A conventional synchronous generator, for both steam-turbines and hydro turbines, can control the mechanical power seen by the generator in response to either a change in set-point, ΔP_C, or in response to change in frequency $\Delta\omega$. The dynamics of this feedback control system are derived in [36, 37], the conclusion of which is provided in (3.2) below:

$$\Delta\hat{P}_M = \frac{\Delta\hat{P}_C}{(1+T_T s)(1+T_G s)} - \frac{1}{(1+T_T s)(1+T_G s)}\frac{\Delta\hat{\omega}}{R}$$

(3.2)

where T_T is the time constant of the turbine, and T_G is the time constant of the speed-governor, and the circumflex above the three variables indicates these are given in the Laplace domain. Therefore, in the steady state the above equation becomes

$$\Delta P_M = \Delta P_C - \frac{\Delta\omega}{R}$$

(3.3)

In eq. (3.3), ΔP_M, ΔP_C, and $\Delta\omega$ are steady-state values of the time-domain variables. The frequency change expressed by $\Delta\omega$ in eq. (3.3) is the frequency deviation at the end of the simulation. The ΔP_M in eq. (3.3), is **not** the amount of generation that was outaged, but rather the amount of generation increased at a certain generator in response to the generation outage. In other words, the primary governing control will operate (in response to some frequency deviation caused by a load-generation imbalance) to change

the generation level by ΔP_M and leave a steady-state frequency deviation of $\Delta \omega$. Although we have not developed relations for ω, P_M, and P_C (but rather $\Delta\omega$, ΔP_M, and ΔP_C), we assume that the local behavior as characterized by eq. (3.3) can be extrapolated to a larger domain, so that a plot of P_M vs. ω for a certain setting of $P_C=P_{C1}$ is as in Fig. 31.
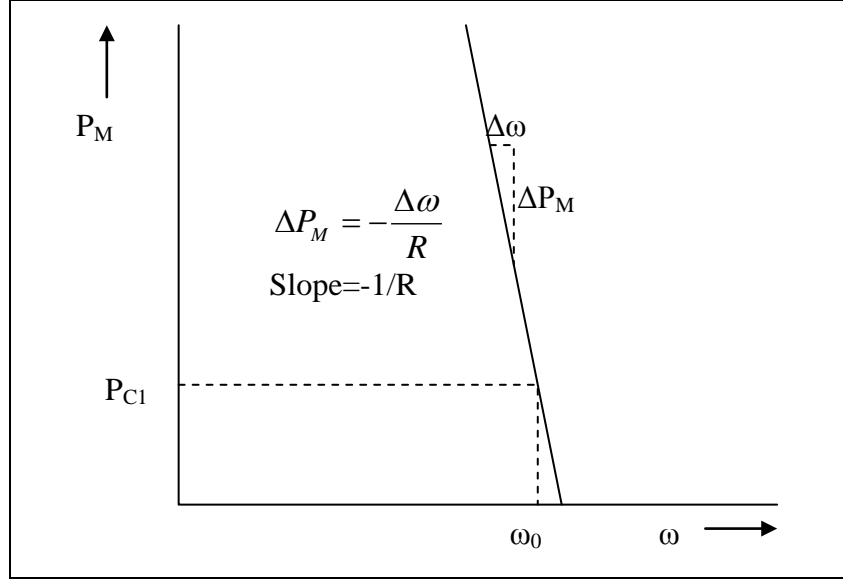
Fig. 31 PM vs.ω

It is assumed in Fig. 31 that the adjustment to the generator set point, designated by $P_C=P_{C1}$, is done by the AGC control system which results in $\omega=\omega_0$. The plot, therefore, provides an indication of what happens to the mechanical power P_M, and the frequency ω, following a disturbance from this pre-disturbance condition for which $P_M=P_{C1}$ and $\omega=\omega_0$.

It is clear from Fig. 31 that the "local" behavior is characterized by $\Delta P_M = -\dfrac{\Delta\omega}{R}$.

The R constant is called the regulation constant or the droop setting. When power is specified in units of MW and frequency in units of rad/sec, then R has units of rad/sec/MW. When both power and frequency are specified in pu, then R is dimensionless and relates fractional changes in ω to fractional changes in P_M. In North America, most governors are set with $R_{pu}=0.05$, i.e., if a disturbance occurs which causes a 5% decrease in steady-state frequency (from 60 to 57 Hz), the corresponding change in unit output will be 1 pu (100%).

Now we consider a general multimachine system having K generators. From eq. (3.3), for a load change of ΔP MW, the ith generator will respond according to:

$$R_{pui} = -\frac{\Delta f / 60}{\Delta P_{Mi}/S_{Ri}} \Rightarrow \Delta P_{Mi} = \frac{-S_{Ri}}{R_{pui}}\frac{\Delta f}{60} \qquad (3.4)$$

The total change in generation will equal ΔP, so:

$$\Delta P = -\left[\frac{S_{R1}}{R_{1pu}} + ... + \frac{S_{RK}}{R_{Kpu}}\right]\frac{\Delta f}{60} \tag{3.5}$$

Solving for Δf results in

$$\frac{\Delta f}{60} = \frac{-\Delta P}{\left[\dfrac{S_{R1}}{R_{1pu}} + ... + \dfrac{S_{RK}}{R_{Kpu}}\right]} \tag{3.6}$$

Substitute eq. (3.6) back into eq. (3.3) to get:

$$\Delta P_{Mi} = \frac{-S_{Ri}}{R_{pui}}\frac{\Delta f}{60} = \frac{S_{Ri}}{R_{pui}}\frac{\Delta P}{\left[\dfrac{S_{R1}}{R_{1pu}} + ... + \dfrac{S_{RK}}{R_{Kpu}}\right]} \tag{3.7}$$

If all units have the same per-unit droop constant, i.e., $R_{pui} = R_{1pu} = ... = R_{Kpu}$, then eq. (3.7) becomes:

$$\Delta P_{Mi} = \frac{-S_{Ri}}{R_{pui}}\frac{\Delta f}{60} = \frac{S_{Ri}\Delta P}{\left[S_{R1} + ... + S_{RK}\right]} \tag{3.8}$$

which shows that units "pick up" in proportion to their MVA ratings. This is a nice feature of how power systems with conventional generation operate to share in performing the primary control function, each generator picks up their "share" according to their size. Larger generators pick up more than smaller generators. But all contribute.

3.6 Primary frequency control: wind generation

Most wind turbines operating in the world today do not employ primary frequency control. However, this is because there have been no requirements to do so, not because it is not possible to do so.

3.6.1   Frequency control requirements for wind

A brief review of the websites from TSOs (in Europe), reliability councils (i.e., NERC and regional organizations) and ISOs (in North America) suggest that there are no requirements regarding use of primary frequency control in wind turbines. Representative examples include [38] which indicates neither Turkey, Norway, or Germany require wind turbines to participate in providing primary reserves, and [39] which indicates neither British Columbia Transmission Company (BCTC), Manitoba Hydro, Hydro Quebec, or Alberta Electric System Operator (AESO) requires frequency regulation capability.

There do appear to be some requirements for having *capability* to provide frequency control. For example, the 2007 Nordic Grid Code [40], which specifies grid requirements for transmission system operators in Denmark, Finland, Iceland, Norway and Sweden, states, pg. 173, "Automatic control of the wind turbine active production as a function of the system frequency must be *possible*." Likewise, reference [39] indicates that with respect to frequency regulation capability,

- BCTC will specify "on a site by site basis,"

- Hydro Quebec requires that wind turbines be "designed so that they can be equipped with a frequency control system (WTG >10 MW)"
- Manitoba Hydro "reserves the right for future wind generators"

Clearly, neither the Europeans nor the Canadians are *requiring* frequency control. The problem has been recognized by a recent publication of the North American Electric Reliability Corporation [41] (April 2009), where it says (pg. 63), "Interconnection procedures and standards should be enhanced to address voltage and frequency ride-through, reactive and real power control, frequency and inertial response and must be applied in a consistent manner to all generation technologies."

Some areas have already initiated action. For example, a recent (Feb 2009) ERCOT white paper [42] suggested the following language for standardization: "Wind generators need to assist in frequency control for ERCOT. One of the problems that has occurred has been a rapid increase in system frequency as wind generation has increased. Implementation of the nodal software addresses the main, root cause of this problem. However, as wind generation becomes a bigger percentage of the on line generation, wind generation will have to contribute to automatic frequency control. Wind generator control systems can provide an automatic response to frequency that is similar to governor response on steam turbine generators. The following draft protocol/operating guide concept is proposed for all new wind generators: All WGRs with signed interconnect agreements dated after March 1, 2009 shall have an automatic response to frequency deviations. …"

3.6.2 Frequency control wind by blade pitching

Fig. 14 illustrates the capability of all modern (equipped with blade-pitch control) wind turbines to control blade pitch, indicating it is equivalent to steam-flow control in a conventional steam turbine. It follows, then, that just as primary frequency control is accomplished through steam-valve control in steam turbines, primary frequency control can be accomplished through blade pitch control in wind turbines.

It should be recognized that blade pitch control has two main purposes for which it was developed:
- To maximize energy extraction from the wind.
- To protect the turbine under high wind conditions.

Fig. 32 shows the performance coefficient curves for the GE SLE 1.5 MW wind turbine. In this plot, $C_p = P_m/P_{wind}$, λ is the tip speed ratio, and θ is equivalent to the blade pitch angle [43].
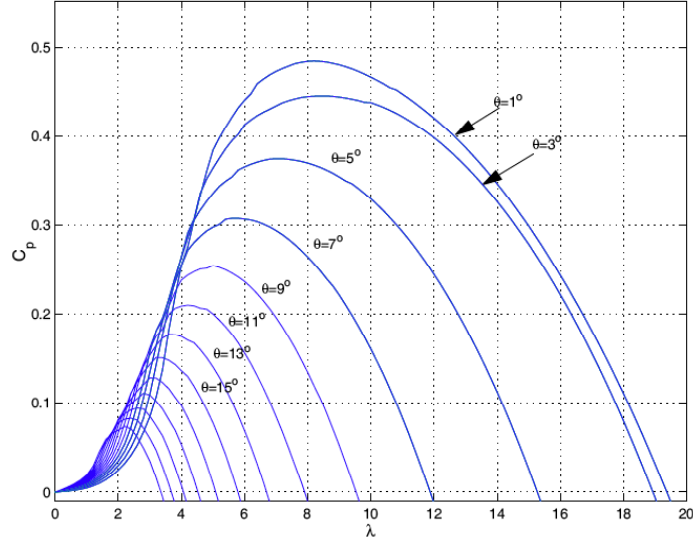
Fig. 32 Performance Coefficient curves [43]

Equation (3.9) relates mechanical power extracted from the wind to the performance coefficient.

$$P_{Mech} = \frac{1}{2} \cdot \rho_{air} \cdot A \cdot v_{wind}^3 \cdot C_p(\lambda, \theta) \qquad (3.9)$$

where ρ_{air} is air density, A is cross-sectional area swept by the blades, v_{wind} is the wind velocity, and

$$\lambda = \frac{\omega_r R}{V_{wind}} \qquad (3.10)$$

Therefore, for a given wind speed, we maximize power output by controlling either ω_r (rotor speed) and thus tip speed λ, or pitch angle θ, or both ω_r and θ. In fixed-speed machines, it is not possible to control ω_r, therefore the only option is to control θ. For DFIGs, both are used. The other purpose for control of θ is to protect the machine; when wind speeds exceed a known "safe" level (typically 20-25 m/sec, or 45-56 mph), the pitch controller will feather the blades to reduce the torque on them to a level where they can be parked.

A wind turbine's pitch controller uses advanced computer-based schemes to ensure the rotor blades pitch exactly the amount required. This control scheme will normally pitch the blades a few degrees every time the wind changes to keep the rotor blades at the optimum angle and maximize output for all wind speeds. The same control mechanism could be used to provide primary frequency control such that:
*   A fall in frequency (demand exceeds generation) causes a decrease in pitch angle and hence an increase in electrical output;

- An increase in frequency (generation exceeds demand) causes an increase in pitch angle and a decrease in electrical output.

3.6.3   Frequency control wind by rotor speed control

As we have seen, we may utilize rotor current control through the rotor-side converter to emulate an inertial response. The corresponding block diagram is seen in Fig. 19.
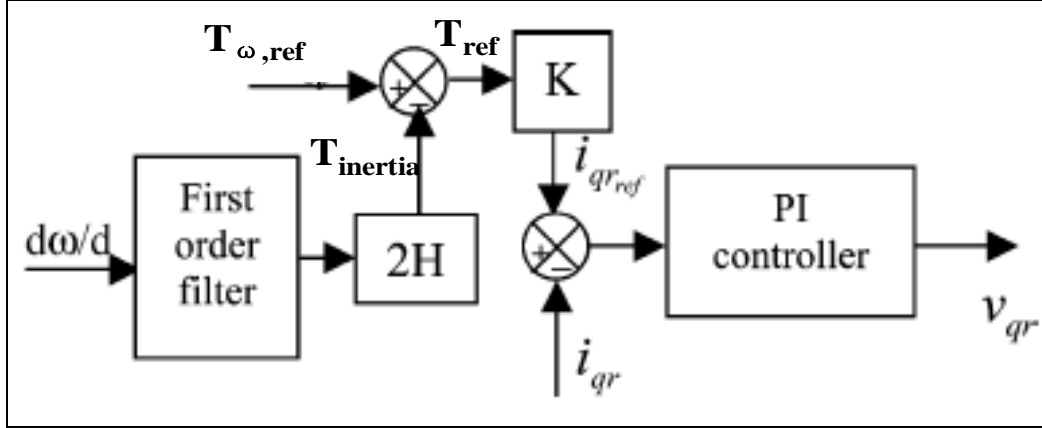
Fig. 33 Rotor Speed Control

Whereas the signal of Fig. 19 is proportional to rate of change of frequency, we may also introduce a signal proportional to frequency deviation from nominal, as indicated in Fig. 34.
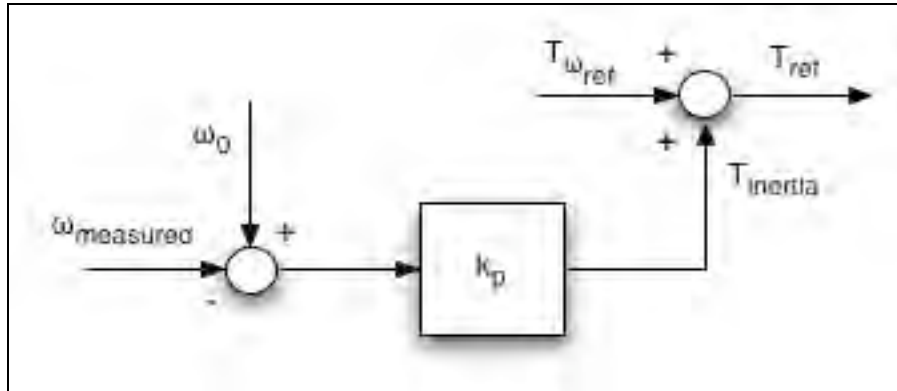
Fig. 34 Rotor Speed Control with Frequency Deviation Signal

Reference [27, p. 183] indicates that whereas this approach, speed control, "may be well suited for continuous, *fine*, frequency regulation, blade pitch control can provide fast acting, *coarse* control both for frequency regulation as well as emergency spinning reserve."

The two forms of control have been studied together in reference [44], where the analysis was done on a design characterized by Fig. 35.
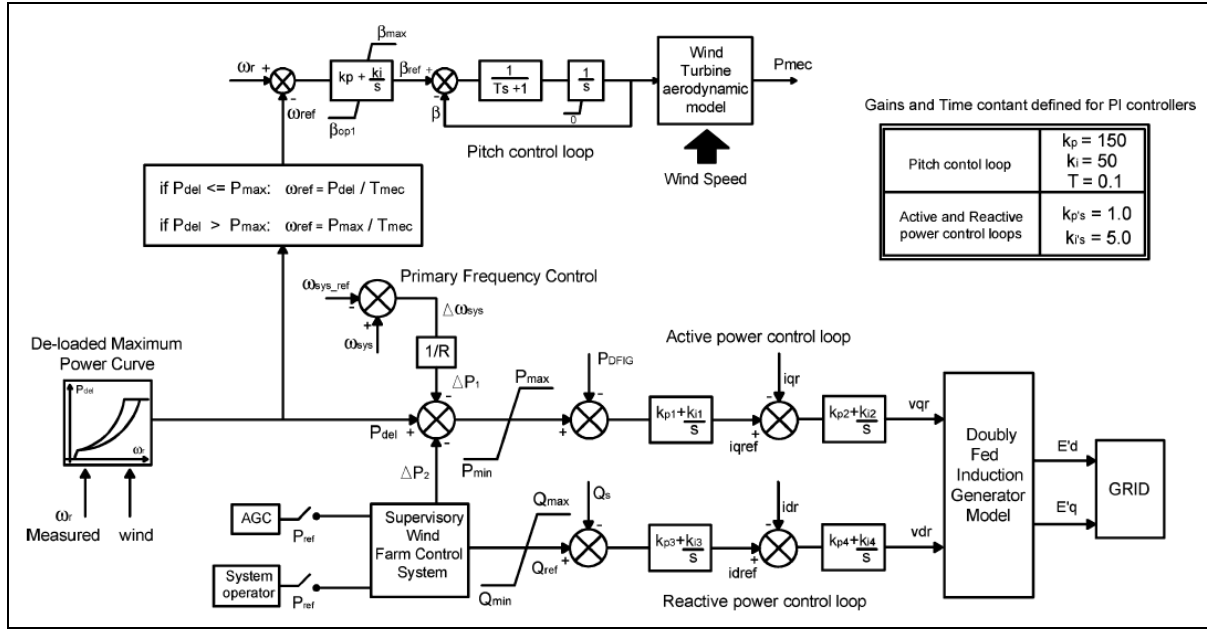
Fig. 35 Two Forms of Control [44]

In addition, it is of interest that there is a 160 MW off-shore wind farm off the coast of Denmark called Horns Rev where these control capabilities have been implemented & tested. Slides on this facility are at [45].

Three additional comments should be made at this point:
- Primary frequency control for over-frequency conditions, which requires generation reduction, can be effectively handled by pitching the blades and thus reducing the power output of the machine. Although this action "spills" wind, it is effective in providing the necessary frequency control.
- Primary frequency control for under-frequency conditions requires some "headroom" so that the wind turbine can increase its power output. This means that it must be operating below its maximum power production capability on a continuous basis. This also implies a "spilling" of wind. Primary frequency control for wind turbines has been referred to as "delta control" since its ability to respond to under-frequency requires a "delta" between the actual production level and the available production capability.
- Another important function that is achievable by pitch control is ramp rate limitation.

The two forms of control, ramp-rate limitation, and delta, are illustrated in Fig. 36 for the Horns Rev facility [45].
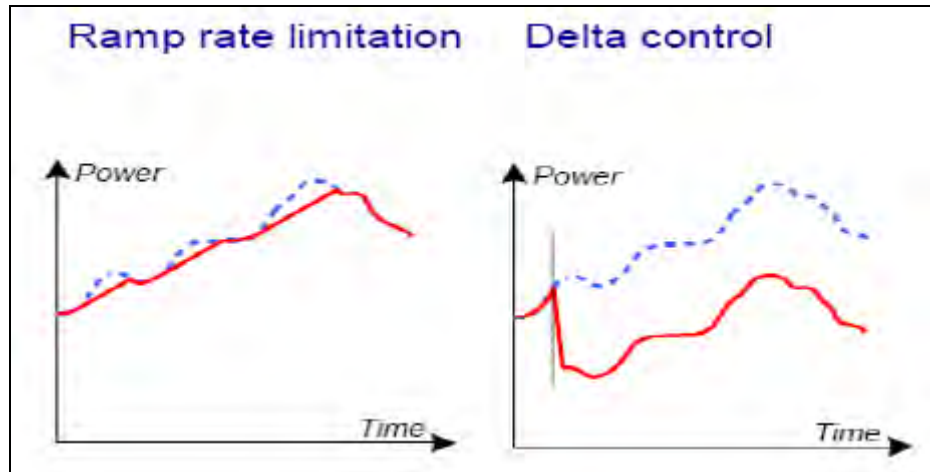
Fig. 36 Controls for Horns Rev Facility [45]

It is controversial whether wind turbines should "spill" wind in order to provide frequency control, in contrast to using all wind and relying on some other means (e.g., conventional generation or storage) to provide the frequency control. The answer to this question is certainly related to what wind penetration levels the industry/society will ultimately implement.

4. Conclusion

Based on our results from the previous chapters we can draw the following conclusions:

1. Generator controls (governor control, ramping control and inertial control) can alleviate the problems of transient frequency dip and regulation.

2. Inertial emulation is a good and necessary idea, although attention should be paid to the overall cost of replicating this control on so many turbines, assuming national wind penetration increases to the 300GW level (or more).

3. The cost of distributed control should also be considered for using wind to provide regulation; however, the very real cost of spilling wind should also be considered.

4. It could be that regulation needs will be cheaper if they are applied in bulk, centrally, rather than in a distributed fashion using wind. Use of storage is probably a good example in that building a few large storage facilities within an interconnection is probably much more cost-efficient than replicating large number of small storage facilities at every wind park.

As stated in the first chapter, it is quite challenging to ensure, at a particular wind penetration level (probably high wind penetration), minimum cost (economic feasibility) and at the same time maximum impact sets of solution. This is an optimization problem and ultimate goal. We will continue further in this direction in future efforts.

[1] B. Kroposki, T. Basso, R. Deblasio, and N. Friedman, "Interconnection of Alternative Energy Sources with the Grid," in "Integration of Alternative Sources of Energy," edited by F. Farret and M. Simoes, Wiley-Interscience, 2006.

[2] E. Hirst and B. Kirby, "Separating and measuring the regulation and load-following ancillary services," Utilities Policy 8, 1999, pp. 75–81.

[3] Prabha Kundur, Power System Stability and Control, McGraw-Hill Professional, January 1, 1994.

[4] Charles Lawrence, Richa Singhal, Eric Ruskamp, "MRO Under frequency Load Shedding Study", available online: http://www.midwestreliability.org/04_standards/drafting_teams/ufls/BarryFrancisPresentation081024.pdf.

[5] WSCC Reliability Subcommittee, "Supporting Document for Reliability Criteria for Transmission System Planning," 1994, available at www.wecc.biz/documents/library/RS/August_1994_Supporting_Document_for_Reliability_Criteria_for_Transmission_System_Planning.pdf

[6] S. Khaitan, "On-line cascading event tracking and avoidance decision support tool," PhD Dissertation, Iowa State University, 2008.

[7] F. Baily, H. Bardwick, and R. Fenton, "Operating and maintaining steam turbine generators–Operating at off-normal conditions, Power, August 1976, The McGraw-Hill Companies.

[8] J. Berdy, P. Brown, and L. Goff, "Protection of Steam Turbine Generators During Abnormal Frequency Conditions," General Electric Company, Schenectady, New York.

[9] P. Anderson and A. Fouad, "Power system control and stability," Iowa State University Press, 1977.

[10] G. lalor, A. Mullane, and M. O'Malley, "Frequency control and wind turbine technologies," IEEE Trans. On Power Systems, Vol. 20, No. 4, Nov. 2005.

[11] N. Hatziargyriou, G. Contaxis, M. Papadopoulos, B. Papadias, M. Matos, J. Pecas Lopes, E. Nogaret, G. Kariniotakis, J. Halliday, G. Dutton, P. Dokopoulos, A. Bakirtzis, A. Androutsos, J. Stefanakis, A. Gigantidou, "Operation and control of island systems-the Crete case," IEEE Power Engineering Society Winter Meeting, Volume 2, 23-27 Jan. 2000, pp. 1053 -1056.

[12] S. Zhang, "Two Approaches to Study Wind Integration: Transient Simulation and Statistical Method," MS Thesis, Iowa State University, 2009.

[13] M. Shahidehpour, Hatim Yamin, and Zuyi Li, "Market Operations in Electric Power Systems," Wiley, 2002.

[14] N. Jaleeli and L. VanSlyck, "NERC's New Control Performance Standards," IEEE Transactions on Power Systems, Vol. 14, No. 3, August 1999.

[15] M. Terbrueggen, "Control Performance Standards," a NERC Operators Training Document."

[16] B. Kirby, M. Milligan, Y. Makarov, D. Hawkins, K. Jackson, H. Shiu "California Renewables Portfolio Standard Renewable Generation Integration Cost Analysis, Phase I: One Year Analysis Of Existing Resources, Results And Recommendations, Final Report," Dec. 10, 2003, available at http://www.consultkirby.com/files/RPS_Int_Cost_PhaseI_Final.pdf.

[17] T. Thiringer, A. Petersson and T. Petru, "Grid Disturbance Response of Wind Turbines Equipped with Induction Generator and Doubly-Fed Induction Generator," 2003.

[18] A. Mullane and M. O'Malley, "Modifying the Inertial Response of Power-Converter Based Wind Turbine Generators," Power Electronics, Machines and Drives, 2006. The 3rd IET International Conference on Mar. 2006 Page(s):121 – 126.

[19] E. Muljadi, presentation notes, Spring 2007, University of Colorado.

[20] E. Hau, "Wind Turbines: Fundamentals, Technologies, Application, Economics," 2nd edition, Springer, 2006.

[21] E. Vittal, A. Keane, and M. O'Malley, "Varying Penetration Ratios of Wind Turbine Technologies for Voltage and Frequency Stability," 20-24 July, 1-6, 2008.

[22] "Wind Turbines Connected to Grids with Voltages above 100 kV – Technical Regulation for the Properties and the Regulation of Wind Turbines, Elkraft System and Eltra Regulation, Draft version TF 3.2.5, Dec., 2004.

[23] "Nordic Grid Code 2007 (Nordic Collection of Rules), Nordel. Tech. Rep., Jan 2004, updated 2007.

48

[24] N. Ullah, T. Thiringer, and D. Karlsson, "Temporary Primary Frequency Control Support by Variable Speed Wind Turbines – Potential and Applications," IEEE Transactions on Power Systems, Vol. 23, No. 2, May 2008.

[25] "Technical Requirements for the Connection of Generation Facilities to the Hydro-Quebec Transmission System: Supplementary Requirements for Wind Generation," Hydro=Quebec, Tech. Rep., May 2003, revised 2005.

[26] J. Ekanayake, L. Holdsworth, and N. Jenkins, "Control of DFIG Wind Turbines," Proc. Instl Electr. Eng., Power Eng., vol. 17, no. 1, pp. 28-32, Feb 2003.

[27] B. Fox, D. Flynn, L. Bryans, N. Jenkins, D. Milborrow, M. O'Malley, R> Watson, and O. Anaya-Lara, "Wind Power Integration: Connection and system operational aspects," Institution of engineering and technology, 2007.

[28] H. Holttinen, "The impact of large-scale power production on the Nordic electricity system," VTT Publications 554, PhD Dissertation, Helsinki University of Technology, 2004.

[29] NERC Standard BAL-002-0 — Disturbance Control Performance, Effective data, April 1, 2005.

[30] Task 25 of the International Energy Agency (IEA), "Design and operation of power systems with large amounts of wind power: State-of-the-art report," available at www.vtt.fi/inf/pdf/workingpapers/2007/W82.pdf.

[31] E. Hau, "Wind Turbines: Fundamentals, Technologies, Application, Economics," 2nd edition, Springer, 2006.

[32] H. Holttinen and Ritva Hirvonen, "Power System Requirements for Wind Power," in "Wind Power in Power Systems," editor, T. Ackermann, Wiley, 2005.

[33] International Energy Agency,"VARIABILITY OFWIND POWER AND OTHER RENEWABLES: Management options and strategies," June 2005, at http://www.iea.org/textbase/papers/2005/variability.pdf.

[34]www.xcelenergy.com/COMPANY/ABOUT_ENERGY_AND_RATES/RESOURCE%20AND%20RENEWABLE%20ENERGY%20PLANS/Pages/2007_Minnesota_Resource_Plan.aspx

[35] B. Fox, D. Flynn, L. Bryans, N. Jenkins, D. Milborrow, M. O'Malley, R> Watson, and O. Anaya-Lara, "Wind Power Integration: Connection and system operational aspects," Institution of engineering and technology, 2007.

[36] J. McCalley, EE 457 class notes, http://www.ee.iastate.edu/~jdm/EE457/AGC1.doc.

[37] J. McCalley, EE 457 class notes, http://www.ee.iastate.edu/~jdm/EE457/AGC2.doc.

[38] Bora Alboyaci, Bahtiyar Dursun, "Grid Connection Requirements for Wind Turbine Systems in selected Countries - Comparison to Turkey," Electrical Power Quality & Utilization Magazine, Volume 3, Issue 2, June 2008, available at http://www.scribd.com/doc/2428245/Grid-Connection-Requirements-for-Wind-Turbine-Systems-in-some-Countries-Comparison-to-Turkey.

[39] "Wind Generation Interconnection Requirements," Technical Workshop, November 7, 2007, available at www.bctc.com/NR/rdonlyres/13465E96-E02C-47C2-B634-F3BCC715D602/0/November7WindInterconnectionWorkshop.pdf.

[40] "2007 Nordic Grid Code," available at http://www.nordel.org/content/Default.asp?PageID=218.

[41] North American Electric Reliability Corporation, "Special Report: Accommodating High Levels of Variable Generation," April 2009, available at http://www.nerc.com/files/IVGTF_Report_041609.pdf.

[42] Draft White Paper, "Wind Generation White Paper: Governor Response Requirement," Feb, 2009, available at www.ercot.com/content/meetings/ros/keydocs/2009/0331/WIND_GENERATION_GOVERNOR_RESPONSE_REQUIREMENT_draft.doc.

[43] W.W. Price, J.J. Sanchez-Gasca, "Simplified Wind Turbine Generator Aerodynamic Models for Transient Stability Studies," IEEE Power Systems Conference and Exhibition, 2006.

[44] Rogério G. de Almeida and J. A. Peças Lopes, "Participation of Doubly Fed Induction Wind Generators in System Frequency Regulation," IEEE TRANSACTIONS ON POWER SYSTEMS, VOL. 22, NO. 3, AUGUST 2007.

[45] http://www.univ-lehavre.fr/recherche/greah/documents/ecpe/sorensen.pdf.

PART 3

Impact of Increased DFIG Penetration
on Voltage Response and Stability

Project Team

Venkataramana Ajjarapu
Ryan J Konopinski
Pradip Vijayan
Subhadarshi Sarkar
Iowa State University

Information about this project

For information about this project contact:

Venkataramana Ajjarapu
Department of Electrical and Computer Engineering
Iowa State University
Ames, IA 50010
Tel: 515-294-7687
Fax: 515-294-4263
Email: vajjarap@iastate.edu

Power Systems Engineering Research Center

The Power Systems Engineering Research Center (PSERC) is a multi-university Center conducting research on challenges facing the electric power industry and educating the next generation of power engineers. More information about PSERC can be found at the Center's website: http://www.pserc.org.

For additional information, contact:

Power Systems Engineering Research Center
Arizona State University
577 Engineering Research Center
Tempe, Arizona 85287-5706
Phone: 480-965-1643
Fax: 480-965-0745

Notice Concerning Copyright Material

Table of Contents

Table of Figures

List of Tables

1. Introduction

1.1 Background

The fluctuating global fuel prices, concerns with the depleting fossil fuel reserves and concerns relating to climate change has resulted in an increasing focus on renewable sources to satisfy rising global energy requirements. Amongst the available renewable sources of energy wind and hydro are the most feasible for utility scale power generation. With a majority of the hydro reserves around the world reaching the maximum capacity in terms of available power there is an increasing shift towards wind power generation to satisfy the need of a clean renwable source [1], [2]. The year 2008 was a record year for wind generation in the United States with a total increase of 8,360 MW which is 50% of the total wind capacity at the end of 2007 [3]. Wind energy accounted for 42% of the total new capacity added. In 2008, the United States overtook Germany to become the country with the largest installed wind power capacity in the world. The total wind power capacity of the United States is at 25,170 MW[4].

Federal policy in the form of production tax credits and state regulations in the form of renewable portfolio standards (RPS) [5] have contributed to encouraging the development of wind generation in the United States [6]. Over 25 states have accepted RPS by requiring a substantial contribution from renewables to their power generation portfolio [7].

1.2 Wind Generation Technologies

There are two major classifications amongst wind generation units fixed speed generation and variable speed generation [8]. The fixed speed generators have a design speed for which they have maximum efficiency whereas for other speeds their efficiency is lower. But variable speed generators have the Maximum power tracking capability that extracts maximum available power out of the wind at different speeds thereby resulting in more efficient systems. Also the variable speed generators reduce mechanical stresses on the turbine thus increasing the lifetime of the turbine. It also helps damp out oscillations in torques more efficiently. Thus variable speed generators are more commonly installed.

Amongst the variable speed generators there are two major kinds, synchronous generators with direct power electronic converters and doubly fed induction generators with rotor side power electronic converters. Both have the above mentioned advantages of variable speed generators but the power electronic ratings of the two machines are different. In a doubly fed induction generator the power electronic converter has a rating of about 30% of the machine rating whereas for the synchronous generator the rating of the power electronic converter is the same as machine rating thereby resulting in higher costs. Thus DFIGs are the preferred choice for installation.

1.3 Doubly Fed Induction Generators

1.3.1 Basic Operation

The Doubly Fed Induction Machine set up for wind generation as shown in figure 2[9], consists of a wind turbine that is connected via a gear train to the rotor shaft of the induction generator. The rotor terminals of the induction machine are connected to the four-quadrant power electronic converter capable of both supplying real/reactive power from the grid to the rotor as well as supply power from the rotor to the grid [5]. The converter consists of two separate converters with different functions, the generator side converter and the grid side converter. The generator side converter controls the real and reactive power output of the machine and the grid side converter maintains the DC link voltage at its set point. These converters are controlled respectively by the Generator side controller and the Grid side controller. The DFIG also has a wind turbine control that maximizes the power output from the turbine via pitch control and sends this computed maximum power output $P_{grid}^{conv,ref}$ to the converter.

The power electronic converter is connected to the grid via a transformer that steps up the voltage to the grid. The stator side of the induction generator is also connected to the grid via a step up transformer. The point of interconnection with the grid is the point used to measure the active and reactive power output of the wind farm. In case the system reliability requires that additional reactive power be injected a STATCOM may be connected at this point of interconnection.
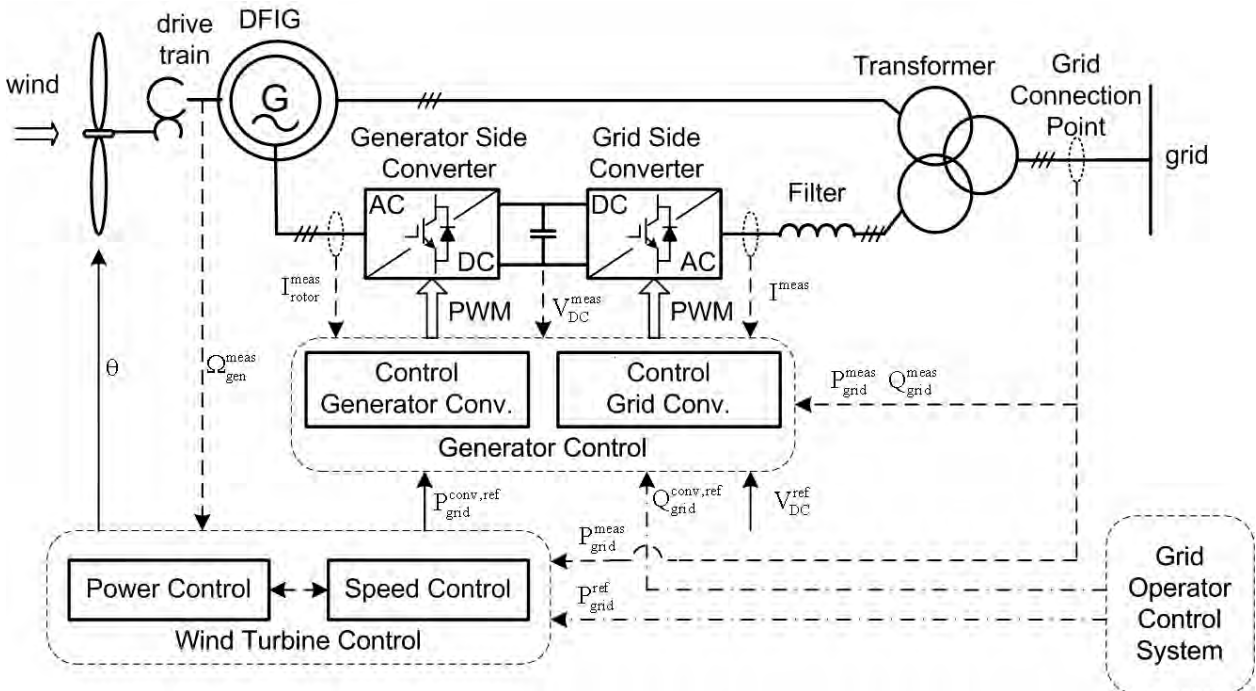
Figure 1.1 Schematic of a Doubly Fed Induction Generator

2

The doubly fed Induction generator consists of a three phase induction generator with three phase windings on the rotor. The rotor is connected to a converter which supplies power to the rotor via the slip rings. The power electronic converter is capable of handling power flow in both directions which permits the DFIG to operate at both sub synchronous and super synchronous speeds. The DFIG produces controlled voltage V_1 at grid frequency f_1 at the stator and variable voltage V_2 is provided at the rotor at variable frequency f_2. The frequency of the rotor depends on the angular velocity of the rotor which in turn depends on the wind speed. Let f_r be the electrical frequency of revolution of the rotor. The following relation holds between the various frequencies:

$$f_r = f_1 \pm f_2 \qquad \qquad 1.1$$

The positive sign above is for the super synchronous operation where rotor speed exceeds rated speed and negative sign is for sub synchronous operation when rotor speed is less than rated speed. At super synchronous speed the phase sequence of the rotor currents is the same as the stator and power is supplied from the rotor to the grid. In the sub synchronous operation power is drawn by the rotor from the grid and the phase sequence of rotor currents is opposite to the phase sequence of the stator currents.

The steady state operation of the DFIG is only restricted by the converter ratings of the rotor side converter. The maximum power rating of the rotor side converter (P_{max}) is generally 25%-30% of the Induction machine ratings. Thus if the converter is operated such that all magnetizing power is provided by the stator, the maximum rotor power supplied/absorbed is P_{max}, and the maximum/minimum slip for operation is given by

$$s_{max} = {P_{max}}/{P_{rated}} \qquad \qquad 1.2$$

Where P_{rated} is the rated power output of the DFIG. This means that the DFIG can provide an operating range of 75% to 125% of the rated wind speed. Also the pitch control with maximum power tracking allows the DFIG to produce maximum power at different wind speeds thus increasing overall efficiency of the unit.

The space phasor equivalent circuit of a DFIG is given below:
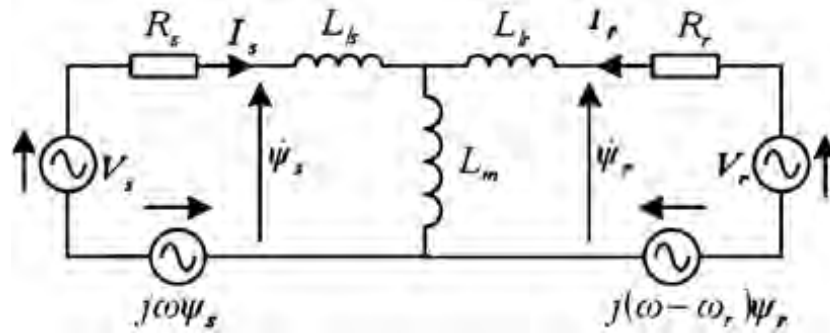
Figure 1.2 Space Phasor Equivalent Circuit

Considering a synchronously rotating reference frame with $= \omega_1$, and converting to time domain, we obtain the following equations:

3

$$I_s R_s + V_s = -\frac{d}{dt}\Psi_s - j\omega\,\Psi_s \qquad\qquad 1.3$$

$$I_r R_r + V_r = -\frac{d}{dt}\Psi_r - j(\omega - \omega_r)\,\Psi_r \qquad\qquad 1.4$$

1.3.2 Control of Generator Side Converter

Now the stator flux is more or less constant and thus we assume that the stator flux is constant. We also assume that saturation does not occur. Also stator resistance is negligible and hence we assume stator resistance is zero. Now we select the d-q axis such that the stator flux Ψ_s is along the d axis. There for $\Psi_q = 0$. Also since we assume that Ψ_d is constant $\frac{d}{dt}\Psi_d = 0$. Now using these values in the stator equation of (3) we obtain:

$$V_d = 0 \qquad\qquad 1.5$$

$$V_q = -\omega_1\,\Psi_d \qquad\qquad 1.6$$

Now, rearranging the stator flux equation to obtain I_s in terms of the other values we obtain:

$$I_s = \Psi_s - \frac{L_m}{L_s}\,I_r \qquad\qquad 1.7$$

where $L_s = L_{sl} + L_m$

Now power delivered at stator is given by:

$$S_s = V_s * I_s \qquad\qquad 1.8$$

Thus,

$$P_s = \frac{3}{2}(V_d I_d + V_q I_q) = \frac{3}{2}V_q I_q = \frac{3}{2}\omega_1\Psi_d\frac{L_m}{L_s}I_{qr} \qquad\qquad 1.9$$

$$Q_s = \frac{3}{2}(V_d I_q - V_q I_d) = -\frac{3}{2}V_q I_d = \frac{3}{2}\omega_1\,\Psi_d\left(\Psi_d - \frac{L_m}{L_s}I_{dr}\right) \qquad 1.10$$

From the above equation we observe that P_s can be controlled by the I_{qr} component and the Q_s component can be controlled by the I_{dr} component assuming the stator flux is constant. Thus we can apply appropriate control to the rotor side converter to obtain the required I_{dr} and I_{qr} for the set point P_s and Q_s values. This is the decoupled control of the active and reactive power in a DFIG.

1.3.3 Control of Grid Side Converter

The objective of the supply side converter is to maintain the DC link voltage at its set point value irrespective of the flow direction of power to the rotor. . The supply side converter maintains the DC link voltage constant irrespective to direction of rotor current and draws a sinusoidal current from the supply. The real power drawn from the supply maintains the DC link voltage at a constant value and this is controlled by the i_{dc} component of the supply current drawn and the i_{qc} component provides the requisite reactive power. For operation in which all reactive power is obtained from the stator side i_{qc} is set to 0. i_{qc} can also be used to set the displacement factor between supply side voltage and current.

1.3.4 Operating Modes of a DFIG

The rotor side converter controls the rotor currents to obtain the required Real and reactive power outputs at the stator side. The real power setting is usually obtained using a maximum power tracking scheme [8]. The reactive power setting can vary depending on the control mode of the DFIG. The two popular control modes are:
1. Power Factor Control
2. Voltage Control

In the power factor control mode the stator real and reactive power are controlled so as to maintain a constant power factor at the point of interconnection. In the voltage control mode the reactive power is controlled to maintain the voltage at the Point of Interconnection to a fixed value. The stator side converter is usually set at unity power factor.

1.4 Overview of Work Done

In the next section some of the controller enhancements that have been incorporated into the Doubly Fed Induction Generator to improve voltage performance is presented. These enhancements better equip the DFIG machines to comply with FERC voltage ride through criteria and maximizing the reactive power availability during a system fault without damaging the machine.

In the following section the reactive capability curve of a DFIG machine is introduced and its impact on steady state operation and dynamic performance is studied. In section 4 the impact of wind variability and associated generation redispatch on power transfer margins is discussed and a new voltage security assessment tool is developed to incorporate wind variability.

2. DFIG Control Enhancements

2.1 Electrical PEC Control Structure

This section provides information regarding the control structure of the power electronic converter and control enhancements to the default model. The control over the power electronic converter is independent on both the rotor and grid side converters. Information regarding details on the control theory behind this can be found in literature [10].

The control structure used in the PowerFactory model is depicted in Figure 2.1. This figure shows three subsection control functions. The "Current" and "Power" subsections were default control loops for the PowerFactory DFIG wind turbine model. The "Protection" subsection control loop was developed as a part of this work and is meant to be a means of protecting the machine.
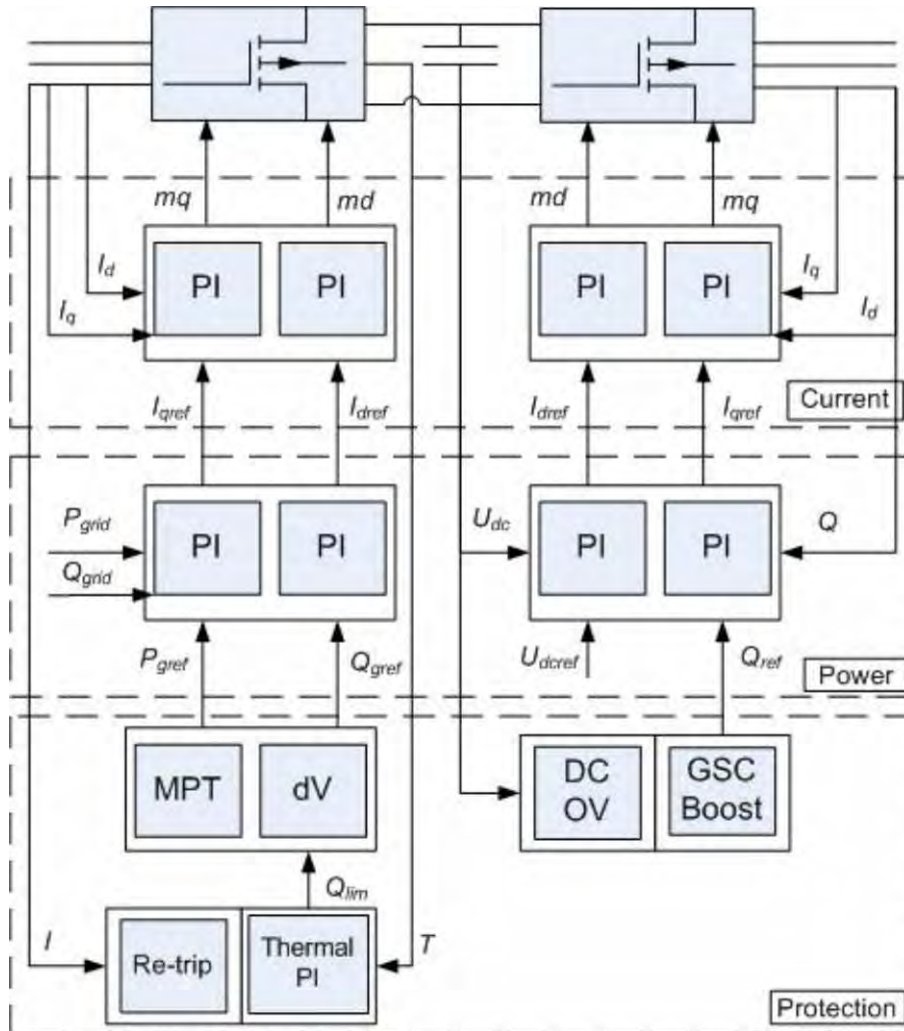
Figure 2.1 DFIG Power Electronic Control Block Diagram

The blocks labeled "DC OV", "GSC Boost", and "Re-trip" will be covered in the following section. DC OV is an overvoltage protection circuit and control logic built into the PEC DC link. The GSC Boost allows for the grid side converter to be utilized to provide reactive power when the RSC circuit is in a protected state. And the Re-trip is another hardware circuit and logic to prevent the default DFIG protection circuit from retriggering in the presence of a severe disturbance

2.2 Controller Development

2.2.1 Section Overview

In this section the development of enhancements made to the DFIG wind turbine control structure will be covered. The control developments are in regards to improvements made to the machine, which increase the likelihood of the plant to contribute to secure operation of the system. In order to test the claimed improvements to the control structure the DFIG wind plant was subject to a severe disturbance as defined by the Federal Energy Regulatory Commission (FERC).

2.2.2 Zero Voltage Ride Through

As mandated by FERC Order 661-A wind-generating plants are to remain online in the presence of severe voltage disturbances for a defined period and voltage profile [11]. This section will address issues regarding the Post-transition Period that takes effect on all newly installed wind generation from January 1, 2008 to present.

The regulations state that wind plants are to remain on-line during three-phase faults with normal clearing times (4-9 cycles) and single line to ground faults with delayed clearing. The post-fault voltage recovery must return to the pre-fault voltage level. The clearing time requirement for a three-phase fault will be determined by the transmission provider and may not have a clearing time greater than 9 cycles (150 ms). In the event that a fault remains greater than the clearing duration or the post-fault voltage does not recover above the determined value, the wind park may disconnect from the transmission system. Wind generating plants must remain connected during such faults with voltage levels down to 0 volts, as measured at the high side of the POI transformer. Figure 2.2 summarizes the fault ride through criteria graphically.

All DFIG control enhancements were tested with a 3-phase short circuit at the high side POI using the test system described in Chapter 5. The following sections elaborate on each control enhancement individually and then draw a comparison between the simulation model before and after the control improvement.

7
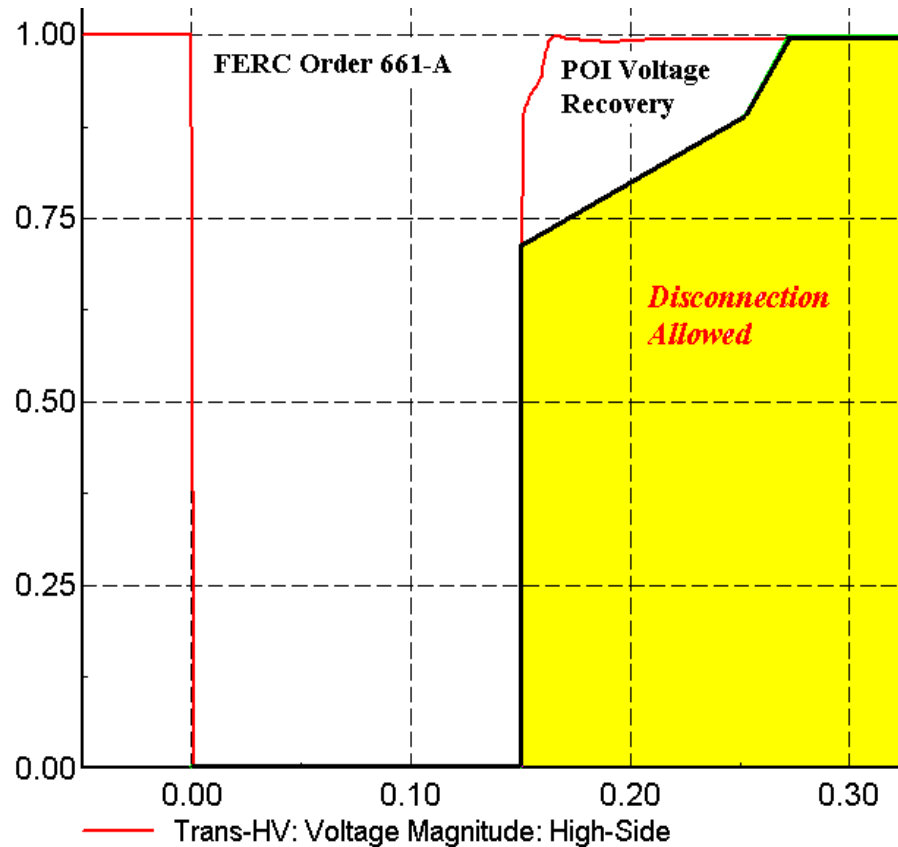
Figure 2.2 FERC Order 661-A (*Black*) vs. POI Bus Voltage (*Red*)

2.2.3 Protection Response of DFIG Wind Turbines

The main problem inherent in a DFIG machine is the current sensitivity of the IGBTs that make up the power electronics converter [12]. These devices may be subject to damage if converter current limitations are exceeded. Since the RSC of the PEC is connected to the rotor via slip rings a crowbar circuit may be short circuited in parallel to the rotor windings as depicted in Figure 2.3.
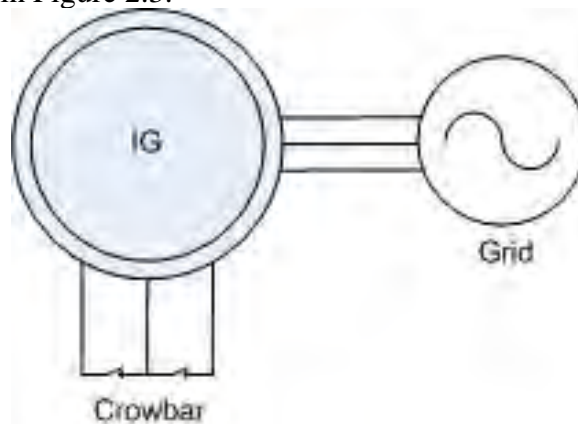
Figure 2.3 DFIG Crowbar Protection Response Schematic

8

This action electrically isolates the RSC from damaging transient currents that may be induced into the rotor winds from the stator side of the machine during a disturbance. Figure 2.4 shows a time dependent simulation of the current through the RSC from pre to post fault. It should be noted that at time 0.0s a short is placed at the high side POI. This action induces large current transients in the RSC just before the RSC protection is triggered. Small transients are observed at 150ms when the protection circuit is cleared and the RSC resynchronizes the machine with the system. The transient currents are thus smaller as the bus voltage has returned to its pre-fault status.
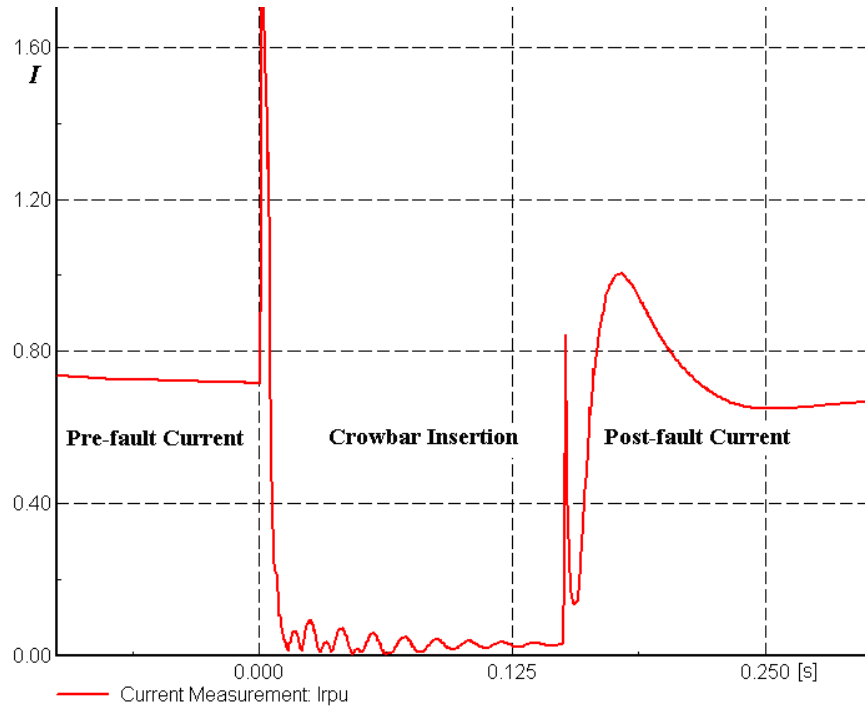
Figure 2.4 Current Flow in Power Electronics during Crowbar Operation

Although this protects the RSC from potentially damaging currents, it unfortunately disables all excitation and power control that is needed for operation of the DFIG. During the protection period the machine effectively is functioning as a traditional induction generator that becomes an inherent reactive power consumer due to the nature of the machine. Thus, control improvements are presented which are used as an aid to overcome some of these shortcomings discussed during fault conditions in the machine.

2.2.4 Grid Side Reactive Power Boosting

During a grid fault where the RSC converter is disconnected from the rotor, as described in the previous section, the machine losses all controllability of real and reactive power. During this protection period the Grid Side Converter may be controlled to provide a reactive power injection as depicted in Figure 2.5. Using this strategy effectively utilizes all components of the PEC system and increases the internal bus voltage within the wind farm collector system.
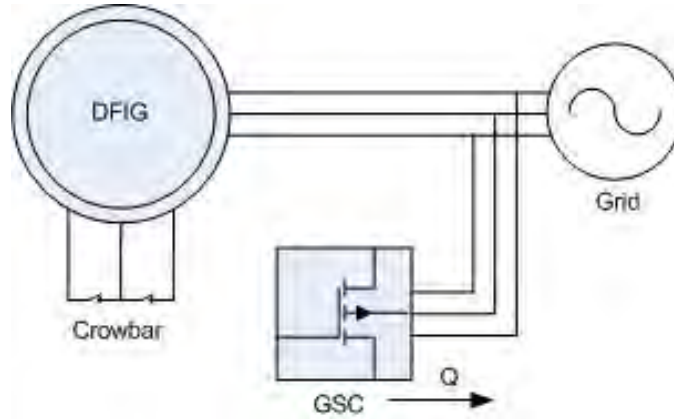
Figure 2.5 Coordinated Converter Control Schematic during Crowbar Operation

During this period the GSC is effectively functioning as a STATCOM device that may inject or consume a dynamic source of reactive power based on the local system needs [12].

Figure 2.6 shows the simulation results where the zero-voltage FERC fault criteria were applied and the DFIG protection system triggered as noticed by the diminished collector system terminal voltage. The upper graph in the figure shows the instantaneous response in the GSC reactive injection with and without the GSC reactive power boosting control strategy.
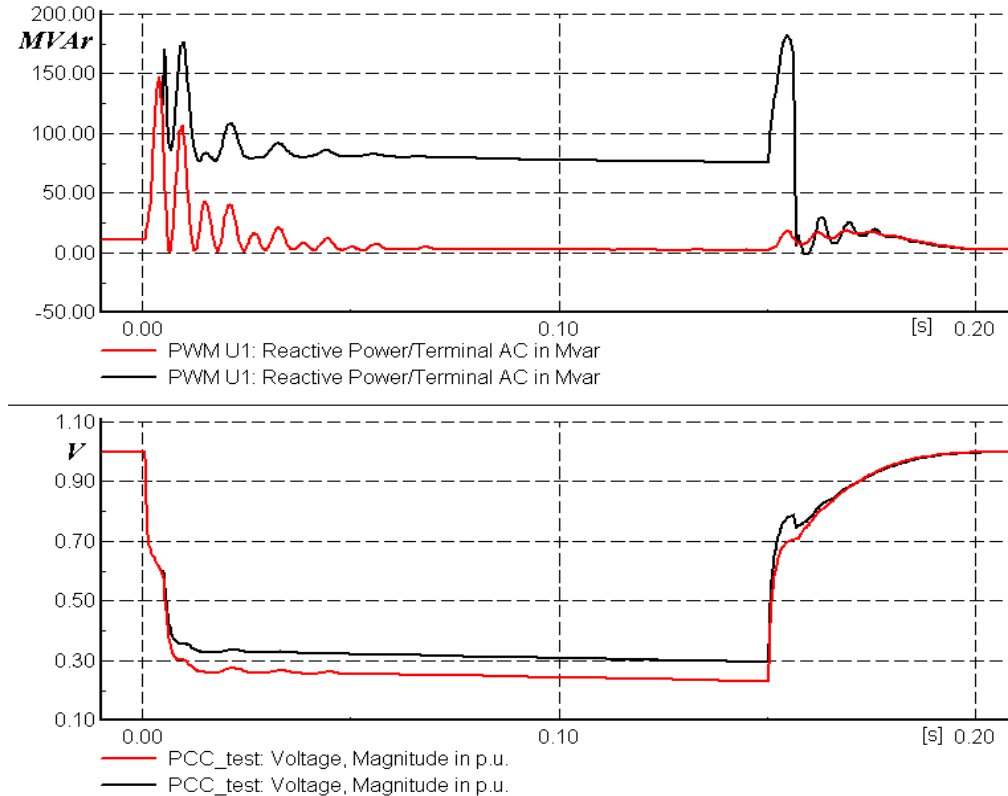
Figure 2.6 Impact of Grid Side Reactive Boosting with (*black*) and without (*red*) Control

10

The redlined simulations are using the default DFIG plant model whereas the black-lined results are after the reactive boosting was added. It can be noted that an approximate increase of 7% in the machine terminal voltage was attributed to the GSC boosting during the short-circuited crowbar protection period.

2.2.5 Crowbar Protection Re-trip Prevention

As noted earlier the natural response of the DFIG protection upon placing and clearing a fault is induced current transients from the stator to rotor. The transient currents upon fault clearing are much less than the fault initiation, but nonetheless still present in the rotor and possibly through the RSC. Under certain conditions the transient current produced during the protection clearing has been shown to re-trigger as displayed in Figure 2.7.
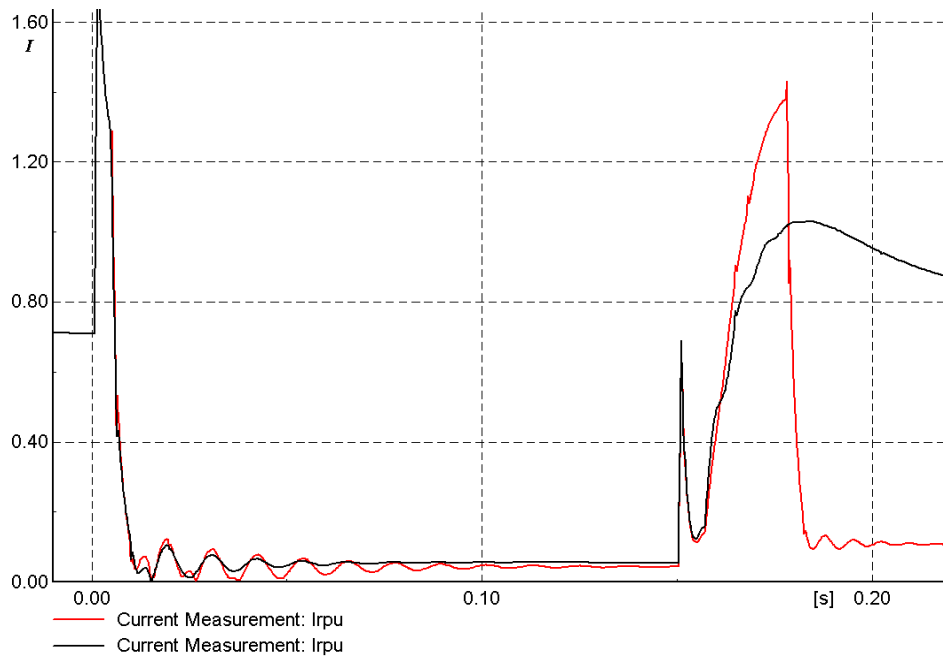
Figure 2.7 PEC Current With and Without Crowbar Re-trip Prevention

The redlined result is the current flow through the RSC before, during, and after the fault without any control modification to the existing DFIG model. If such a scenario were to occur the DFIG plant would remain inoperable for another 150ms until the protection would again resynchronize with the grid. This sustained loss of generation could inevitably repeat itself or have already produced an uncontrolled deterioration to the system during heavily loaded periods.

Either situation may prove devastating; as such the idea of a switched series resistance was mentioned as a potential method to contribute to fault-ride through [13]. Figure 2.8 shows the schematic representation along with the traditionally included crowbar protection. That study concluded that hardware costs would out way the benefit of such investment and was not pursued any further.

11
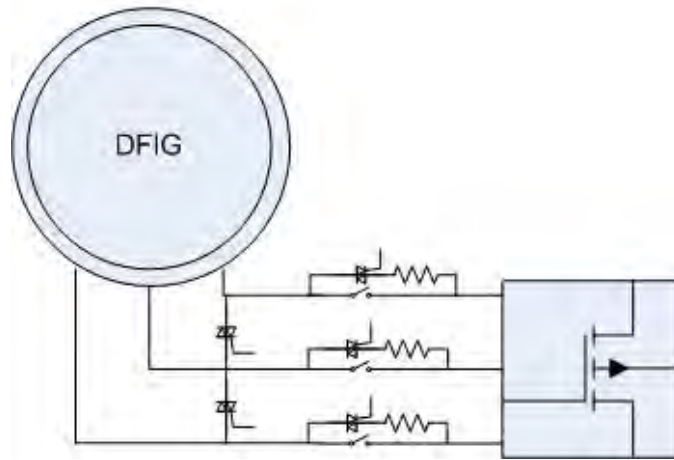
Figure 2.8 Crowbar Re-trip Prevention Implementation

Instead this investigation delves into the possible effectiveness of this implementation while neglecting the cost burden associated with the equipment. A simulation equivalent of the hardware shown in Figure 18 was programmed into the PowerFactory default model and tested with a short circuit at the POI. The positive effect of reducing the transient rotor currents was observed in the previous Figure 2.7. It should be noted that upon re-synchronization at 150ms the RSC rotor current (black line) has a substantially reduced magnitude as compared with the original model. Thus the series crowbar implementation complements the already existing parallel crowbar to prevent the re-trip of the machine protection circuit.

2.2.6 DC Link Capacitor Over Voltage Mitigation

The DC link capacitor in the PEC circuit is integral for bidirectional power flow between the rotor and grid. Proper voltage levels must be maintained at the DC link in order to effectively control the excitation of the machine and to avoid damage to the capacitor. It has been documented that during certain conditions the DC link may encounter a potentially disastrous scenario when the RSC protection is triggered [14]. Figure 2.9 shows the voltage magnitude (red-lie) of the link capacitor when the crowbar triggers due to a 3-phase short at the POI for 150ms. It should be noted that nominal DC link voltage is at 1.3 kV and the transient voltage that occurs produces levels of around 1.9 kV.
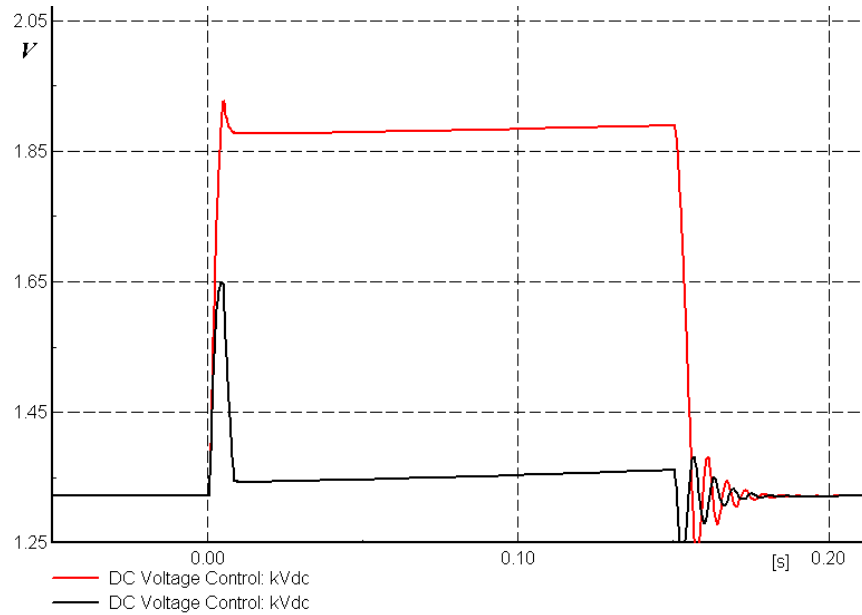
Figure 2.9 DC Link Capacitor Voltage With and Without Chopper Control

This scenario presents itself when the machine is functioning in its sub-synchronous region of operation at high slips. In this regard there is a relatively large amount of energy transfer from the grid through the PEC and to the rotor. When the RSC crowbar trips, the GSC control cannot instantaneously respond which causes overcharging of the capacitor. This situation can be damaging to PEC circuitry. To mitigate such a problem the chopper circuit shown in Figure 2.10 has been implemented as found in literature [14].
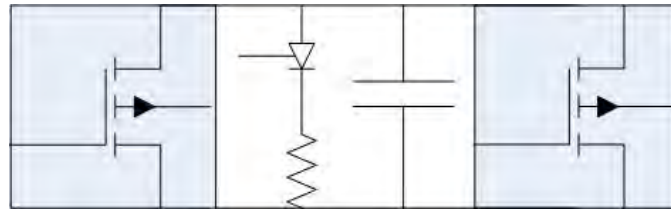
Figure 2.10 DC Link Chopper Circuit Schematic

The control methodology constantly senses the DC link voltage and activates the chopper circuit at a turn on / off thresholds. The voltage level (black-line) in Figure 2.9 shows the reduced voltage transient the results from the implemented chopper hardware and control logic using PowerFactory.

13

3. DFIG Capability Curve and Performance Enhancements

3.1 Capability Curve of a DFIG Machine

It is well known that electro-mechanical machines have inherent limitations that allow for a fixed amount of power production. The operating characteristics of any generator are important for representing a machine's true power capability. The limitations that define a DFIGs electrical power capability are influenced by two factors – the generator and power electronics. Referring to the maximum power tracking characteristic (Appendix 1) it should be noted that only a finite amount of power is able from a given wind speed. Therefore the real power limits are set by the availability of the wind. The maximum reactive capability of the machine is determined by the generator design where the applied currents and voltages set limitations on the stator and rotor. Therefore, the maximum power capability is completely limited by the design of the machine although the back-to-back power converter, which will be addressed in section 2.1.4, defines the actual capability.

A capability curve for a DFIG wind park was formulated using the method followed in [15] with a maximum power tracking characteristic given in Appendix 1. This technique is given for only a single machine, but it is assumed that the power capability of one machine can be scaled up to accurately aggregate the behavior of a DFIG wind park.
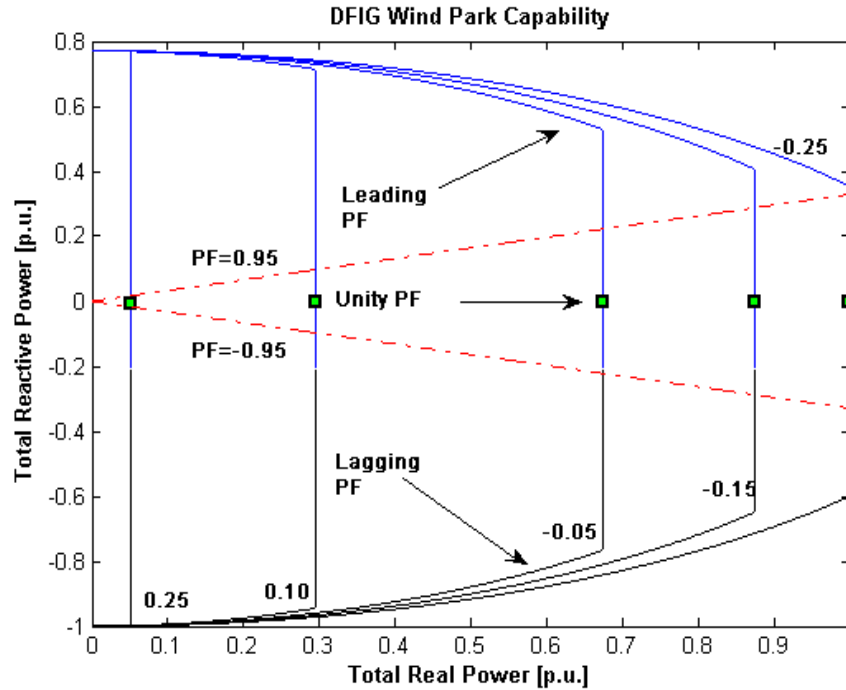
Figure 3.1 DFIG Wind Park Static Power Capability Curve in per units

This is made under the assumption that the DFIG wind park network is not considered such as each machine feeder line and transformer. Additional impedance may be added to the model, which accounts for these simplifications [16].

The plot in figure 3.1 displays the operation of a DFIG within the specified 0.95 leading and 0.95 lagging power factors. Superimposed is the capability curve for the DFIG at different wind speeds corresponding to variable levels of power output. Given in the plot are the capability curves for slips 0.25, 0.1, -0.05, -0.15 and -0.25. This spans the entire spectrum of wind speeds from cut-in speed that corresponds to 0.25 slip to just before cut-out speed that corresponds to -0.25 slip. Thus by utilizing the capability curve in network analysis additional reactive power and hence improved power system performance may be attained over a regulated power factor. It is evident from the figure that at 100% plant output the use of the capability curve does not give much additional reactive support compared to the 0.95 leading operation. In contrast additional reactive consumption may be realized in lagging operation. Wind parks will never continuously operate at 100% output and therefore in the periods of operation below 100% there is significant additional reactive power available that could aid in improved system performance.

3.2 DFIG Wind Park Load Flow Models

For any power system analysis it is important to appropriately model the characteristics of a system device. In the case of DFIG machines and machines that make up the response of a DFIG wind park, models for static analysis are still being developed. The following section will briefly discuss several model representations of DFIG wind plants.

3.2.1 Negative Load Representation

One of the most simplified DFIG wind park representations can be defined by a negative load [17]. During the load flow this representation will inject real power (P) and either leading or lagging reactive power (+/-Q) into the grid. The farm is modeled as a PQ bus. This model assumes that the wind farm operates at a fixed power factor and cannot regulate its reactive output.

3.2.2 Synchronous Machine Representation

A wind park may be modeled as a synchronous generator with either fixed real and reactive power limits or by employing a capability curve. Both models are representative of a PV bus that contains terminal voltage control. The capability curve is the more accurate representation. The only disadvantage of this strategy is that the steady state set points cannot directly be used in dynamic simulations. Therefore, the initial set points must be recomputed for the dynamic DFIG models.

3.2.3 DFIG Representation

Several software manufacturers now appropriately account for DFIG wind park models in load flow studies. Notable are PSS/E [18], [19], PowerFactory [20], and Eurostag [21] simulation software for including models that can automatically be initialized for dynamic analysis. For the strict purpose of steady state analysis, synchronous machine

representation can accurately portray the behavior of a wind plant. As such, employing a DFIG capability curve using a synchronous machine model proves advantageous when studying high levels of wind penetration.

3.3 Wind Park Aggregation

Although models of DFIG turbines have been well studied [22] there is no industry standard and as such each software package may contain its own DFIG model. Moreover since larger scale wind parks will contain upwards of several hundred units, modeling of individual units for power system dynamic studies would result in large simulation times and require greater computation capability. Therefore model simplification and park aggregation is justified in certain power system analysis.

The inclusion of a wind farm into a power system for simulation purposes is often best represented by a condensed model. Aggregation techniques of variable speed wind turbines have been thoroughly discussed and their significance described in [23]. Studies comparing the results between detailed and aggregated models conclude that an aggregated electrical system and non-aggregated mechanical system is an efficient and accurate model for mid and long term simulations [24]. For short-term simulations both electrical and mechanical systems may be aggregated.

For the purpose of dynamic simulation, an aggregated park of approximately 100 DFIG units was modeled in PowerFactory simulation software by DIgSILENT [20]. The park was constructed with a fully aggregated technique that condenses the behavior of each individual turbine's electrical and mechanical models into a single machine model representing both electrical and mechanical characteristics.

3.4 Reactive Capability Validation

The DFIG parks used in this study are 1.5 MW units that contain a power electronic converter rated to 30% of the machine rating (Appendix 2). This assumption is justified by calculating and comparing the required PEC rating necessary to operate between a +/- 0.95 power factor as well as over the entire range of the capability curve in figure 6. The procedure outlined in [25] was followed to compute I_r, V_r, V_{dc}, and S_{conv} corresponding to several operating points given respective active and reactive powers. Rows 1-5 of table 1 detail the converter calculations for several operational points taken from the DFIG capability curve. Row 6 shows the ratings necessary to operate at 0.95 leading power factor at rated output. Observe in figure 6 that at each real power (P) operating point the reactive limitation (Q) of the restricted power factor regulation is less than the capability curve (except near 100% real output). It is apparent in table 1 that as the DFIG active output (P_{tot}) increases likewise does the current magnitude (I_r). Near 50% output the machine reaches its synchronous speed and the voltage applied to the rotor is minimal and therefore the required converter rating is at its lowest. Near 100% output the required rotor current, voltage, and converter ratings are at their highest value. This implies that the leading reactive output (Q_{tot}) determines the converter ratings and size at 100% output. Hence, only the maximum operating point for the power factor regulation was displayed.

Table 3.1 Converter Sizing for Theoretical Reactive Operation

	P_{tot} [p.u.]	Q_{tot} [p.u.]	slip [%]	V_{rotor} [V]	I_{rotor} [A]	$V_{dc\text{-}link}$ [V]	$S_{converter}$ [kVA]
1	0.05	0.80	25.26	244	352	440	258.5
2	0.25	0.72	11.50	108	449	195	146.2
3	0.50	0.63	1.33	8	425	14	10.2
4	0.75	0.49	-9.28	97	428	175	125.4
5	1.00	0.37	-25.14	254	468	460	357.9
6	*1.00*	*0.33*	*-25.14*	*254*	*458*	*460*	*348.6*

The required DC link capacitor voltage based on the stator side voltage is calculated using equation 11 with a maximum modulation index of 0.9. The stator side rated voltage is 575 V and therefore the corresponding DC link voltage is 938 V. From the above table the required $V_{dc\text{-}link}$ from the rotor side voltage is lower compared to that required by the stator side voltage. This implies that no change in the actual DC link capacitor voltage rating is necessary to implement the capability curve. The implemented PEC rating was derived using a margin of safety based on the highest kVA rating from table 1. The DC capacitor voltage was designed from the stator side voltage and rated to 1150 V with the PEC rated at 450 kVA.

It is very important to note that operation of a DFIG with a power factor regulation must produce a Q_{tot} of 0.33 and for the capability curve it must produce 0.37 at rated active power. Comparing I_r and $S_{converter}$ for rows 5 and 6 in table 1 show that only a 2% increase in the ratings is necessary to implement this capability curve over a regulated power factor scheme. Therefore converters installed in operational and newly commissioned DFIG wind farms abiding by the FERC 661-A orders have additional reactive capability that may be utilized. This demonstrates that operating the DFIG within a power factor regulation greatly under-utilizes the machines overall reactive ability.

3.5 Impact of Additional Reactive Power on System Dispatch

3.5.1 Optimal Power Flow Formulation

Optimal power flow (OPF) is a well developed tool and standard procedure in power system planning and operation [23], [24]. As part of this work it is used to study the impact of extended DFIG reactive capability on system operation as compared to regulated power factor operation. The objective of this OPF is to minimize system costs while adhering to operation constraints such as line flow, generation, and bus voltage limitations. The formulation is presented:

Minimize:

$$f(P_{gk}) = \sum_{k=0}^{n} C(P_{gk})$$
 3.1

Subject to:

$$\sum_{k=1}^{n} P_{gk} - \sum_{i=1}^{m} P_{di} - \sum P_{loss\_j} = 0$$
 3.2

$$\sum_{k=0}^{n} Q_{gk} - \sum_{i=0}^{m} Q_{di} - \sum Q_{loss\_j} = 0$$
 3.3

$$P_{gk,min} \leq P_{gk} \leq P_{gk,max}$$
 3.4

$$Q_{gk,min}(P_{gk}) \leq Q_{gk} \leq Q_{gk,max}(P_{gk})$$
 3.5

$$V_{u,min} \leq V_u \leq V_{u,max}$$
 3.6

$$-F_{lim} \leq F_j \leq F_{lim}$$
 3.7

where,

$u \in (1, 2...q), q -$ *total no. of buses*

$j \in (1, 2...p), p -$ *total no. of branches*

$k \in (1, 2...n), n -$ *total no. of generators*

$i \in (1, 2...m), m -$ *total no. of load buses*

Equation 3.1 indicates the total cost of production of power, where $C(P_{gk})$ is the price for P_{gk} units of power from unit k. Q_{gk} is the reactive injection of unit k. The real and reactive demand at bus i is P_{di} and Q_{di} and the real and reactive loss on line j is given by P_{loss_j} and Q_{loss_j}. Equations 3.2 and 3.3 are the power balance equations for real and reactive power. Equations 3.4 and 3.5 are the real and reactive power limits on the generators where the reactive limits are a function of the real power dispatch ($Q_{gk\_min/max}(P_{gk})$). This is done to capture the capability curve / restricted power factor regulations displayed in figure 3.1. The bus voltage constraints (0.95 – 1.05) and the line flow limits (< 1.0 p.u.) are given in equations 3.6 and 3.7. MATPOWER is the software tool used to conduct the OPF analysis [25].

This paper addresses the impact of large scale DFIG wind generation on economic and reliability concerns in a power system. This representation aims to capture the major components of a large scale power system and emulate key system phenomena. The following section will elaborate on the system description.

3.5.2 Power System Description

A sample power network available in the PSS/E software was imported into MATPOWER and PowerFactory for system analysis. The original network consists of 6 conventional machines and 26 buses. The total load was modified to 3035 MW and 1230 MVAr with 305 MW of motor load that has been distributed between buses 3005, 153, 203. Refer to figure 4 for the schematic of the network. Shunt compensation (950 MVAr sum) is located at various buses throughout the system with a large 600 MVAr reactor at bus 151. The transmission voltages range from 230 – 500kV and the line parameters have been modified to reflect appropriate transmission distances [26].
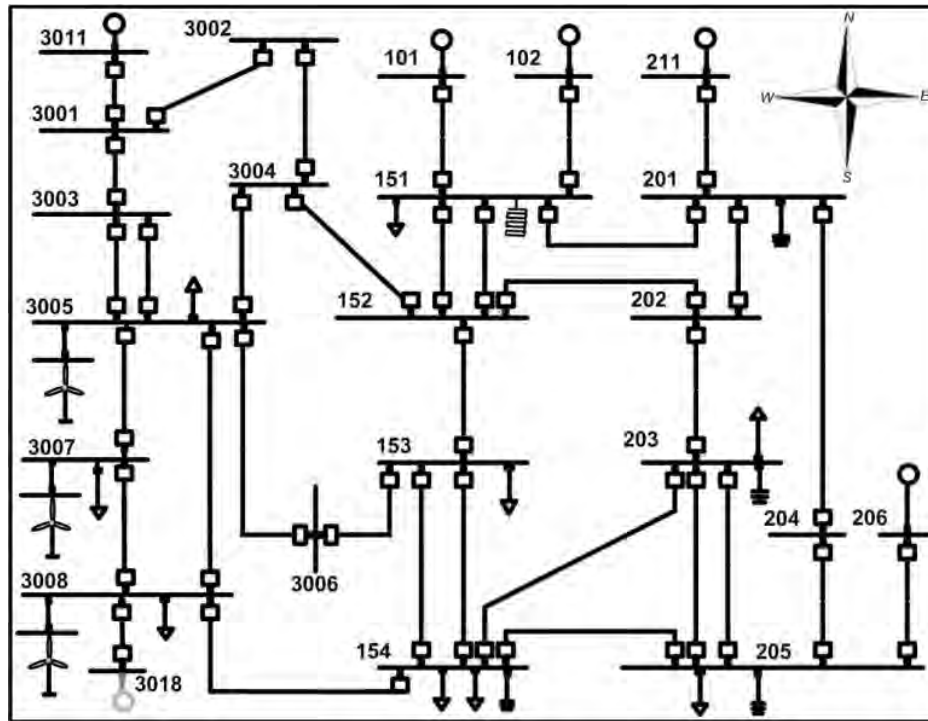
Figure 3.2 Simulated Power System with Park Interconnection at Bus 3008

In the base case the majority of generation is concentrated in the Northern region of the grid. The load centers are located in the South and South-East portion of the system with major concentration at buses 154 and 206. The South-West part of the network contains low load and low transmission capacity. Typical high wind regions have these characteristics and hence it is assumed a potential site for large scale wind facilities [27].

Since one of the underlying themes of this paper is to address the implementation of large DFIG penetration levels, unit 3018 has been taken off line. Installed in place of this unit

are 3 DFIG wind facilities strategically placed at buses 3005/ 7/ 8. The replacement of this unit was to simulate disbursed wind generation that would emphasize the impact of high DFIG penetration on system performance. To facilitate the transfer of energy from these high wind regions to the load centers the lines (3008 – 154), (3005 – 3007), and (3007 – 3008) are upgraded to have sufficient transmission capacity.

3.5.3 OPF Analysis Description

The OPF analysis described in section III is used to assess the impact of extended reactive capability on system operating costs. The central goal of using technique is to compare the system operation with restricted power factor versus the capability curve. The described system in figure 4 is studied with a load of 3340 MW and 1325 MVAr. At base case the depicted 5 conventional generators are online to satisfy this demand. The unit at bus 3011 is the slack bus and contains the most expensive generation. The production costs of all other generators are assumed to be the same. The wind parks are modeled to have a fixed production cost and are the least expensive generation. The units are modeled in the way to simulate the current practice of handling intermittent resources as price taking units, wherein all the available wind generation is purchased and no market is used to clear these bids. Due to the relative small scale of wind penetration in these markets their influence on setting the market price is considered negligible. [28-29]. In this study wind penetration is defined as the total capacity of wind generation compared to the total load.

$$Penetratio \quad n \quad Level = \frac{\sum Installed \quad wind \quad capacity}{\sum Load} \qquad 3.8$$

To analyze the impact of increased DFIG wind penetration, various penetration levels at 15, 20, 25, and 30% are simulated. At each penetration level the total wind generation is simulated at 2, 15, 50, and 100% output in order to consider various production conditions from cut-in to cut-out wind speeds. Since wind is not a constant resource this study aims to capture the effect of wind variability on system operating costs.

Table 3.2 Individual Plant Sizes at Different Penetration Levels

System Wind Penetration	Total Wind Capacity	Individual Plant Sizes
15 %	510	170
20 %	680	227
25 %	850	283
30 %	1020	340

In this analysis the total wind generation at each penetration level is assumed to be equally distributed between the DFIG wind parks located at buses 3005/7/8. The total system load is 3340 MW and by utilizing (18) the plant sizes are obtained. The total wind

capacity at the respective penetration levels are 510 MW, 680 MW, 850 MW and 1020 MW. At the described penetration levels the individual plant sizes are 170, 227, 283, and 340 MW. Table 3.2 summarizes the plant sizes at different penetration levels.

At 2% park output it is considered that the wind units have just cut-in and the real power output is at a minimum. When employing the capability curve, the reactive limits of the machines are the greatest at this output as compared the other output levels studied. As wind speeds increase the parks real output increases and consequently the reactive capability of the DFIG park reduces. In contrast, the FERC regulation allows wind units to increase their reactive capability as the real output is increased. Again referring to figure 2, at 100% real output the leading reactive capability of both strategies is approximately equal.

3.5.4 System Loss Reduction

At each penetration level the total system operating costs are computed for each output level. The system operating costs are comprised of both the cost of generation to meet the demand and generation cost to satisfy losses. When a unit is unable to meet its local reactive load, remote generation compensates this requirement, but the system incurs additional line losses. Since the demand is fixed the reactive dispatch of the DFIG parks results in reduced system losses due to DFIG generation being able to meet the local reactive requirements. In this study the cost of system losses are minute as compared to the cost of generation. Thus even a substantial reduction in losses will not reflect a significant savings in total operating costs. Hence the reduction in system losses is used as a metric of comparison between the reactive control strategies.

Table 3.3 Percent Reduction In Losses Using Capability Curve Over 0.95 Leading/Lagging Power Factor

Penetration Level / Plant Output	15%	20 %	25%	30%
2%	15.82	15.46	15.10	14.74
15%	8.54	7.17	6.54	7.06
50%	3.75	2.80	2.19	1.62
100%	0.34	0.35	0.11	0.02

Table 3.3 contains the percentage reduction in losses employing the capability curve as compared to an imposed 0.95 power factor limit. Observing the difference in the reactive capacity between the two control strategies from figure 2, it is evident that as the real

output of the wind park increases the additional reactive power available with the capability curve reduces. Correspondingly the percent reduction in system loss decreases with an increasing real power output.

DFIG wind parks implementing capability curve control may substantially reduce system losses especially at low plant output levels. This control strategy not only facilitates reductions in operating costs but avoids the necessity of additional reactive compensation required for secure operation of the power system. The combined savings in total system costs (losses+shunts) may help justify transmission investment for future wind installations [27].

3.5.5 Impact of Additional Reactive Power on Power Transfer Margin

The following analysis investigates the impact of the additional reactive power on power system transfer margin. The transfer margin is computed based on the minimum power transfer possible for various contingencies. For the above power system the contingencies considered are loss of transmission lines. Loss of generation is not considered in the analysis and hence generators and transformers connected to generators are not considered as contingencies. The base case load in the previous analysis does not provide a powerflow solution for all the contingencies. Hence the base case load level is reduced by 150 MVA to obtain the new base case for this analysis.

To compute the transfer margin the load and generation are increased in proportion to the base case load and generation dispatch. The base case generation dispatch is obtained based on the OPF formulation provided above. The penetration levels and output levels used in the previous analysis are again utilized to obtain the different transfer margins. Table 3.4 summarizes the increase in transfer margin for the various scenarios.

Table 3.4 Increase in Transfer Margin Using Capability Curve Over 0.95
Leading/Lagging Power Factor

Penetration Level / Plant Output	15%	20 %	25%	30%
2%	267.24	355.11	441.53	467.67
15%	238.19	320.98	375.44	427.00
50%	153.95	202.61	253.44	273.05
100%	20.33	23.24	28.32	29.05

The table demonstrates that with increasing system penetration of wind generation the increased power transfer margin increases. Given a base case load of 3200 MW the

percentage increase in power transfer margin over the base case loading varies from 8.4% to 14.6% with increasing system penetration from 15% to 30% at low wind speeds. At 50% output the percentage increase in transfer margin varies from 4.8% to 8.5% with increasing system penetration. At 100% plant output there is very little increase in reactive power available and this translates into a very marginal increase in transfer margin.

3.6 Dynamic Analysis Results

This section provides information regarding the results of dynamic simulations run on the test power system for a 25% DFIG wind penetration level. These simulations are to validate the installation of a large amount of DFIG units put in place of unit 3018 as found in the VSA methodology. These simulations not only test the validity of a 25% wind penetration, but also the performance of utilizing an extended reactive capability curve as described in the earlier Chapter 1. Section 3.6.1 explains the details behind the reactive capability comparison for the DFIG plants.

3.6.1 Voltage Control Application

There are two voltage control strategies that are implemented to demonstrate a comparison between DFIG park responses on system performance. The first strategy utilizes the +/- 0.95 power factor regulation set forth by FERC order 661-A, where the reactive limits are defined by the parks real output [11].

$$\left| Q_{\max} \right| = P_{output} \tan(\cos^{-1}(0.95)) \qquad\qquad 3.9$$

The second strategy utilizes the reactive capability that is detailed in the developed capability curve in figure 3.1. Both schemes use a proportional-integral (PI) controller that regulates the POI voltage as outlined in figure 3.3 [27].

The inputs to the controller are the set point voltage (V_{ref}) and the voltage measurement (V_{meas}) at the POI. The error signal between the voltages is used by the controller to compute the reactive power set point (Q_{ref}) of the DFIG. The range of control depends on the reactive limits of the DFIG (Q_{max}, Q_{min}). This voltage controller was incorporated into the existing DFIG control model available in PowerFactory. The controller design was developed using DIgSILENT Simulation Language (DSL) to compare the dynamic response of the strategies.

The main difference between the control strategies is the reactive power limitations (Q_{max}, Q_{min}) placed on the controller for a given real output. This variation in the limits will test the system response between the extended reactive limits of the capability curve over the regulated power factor limitations.
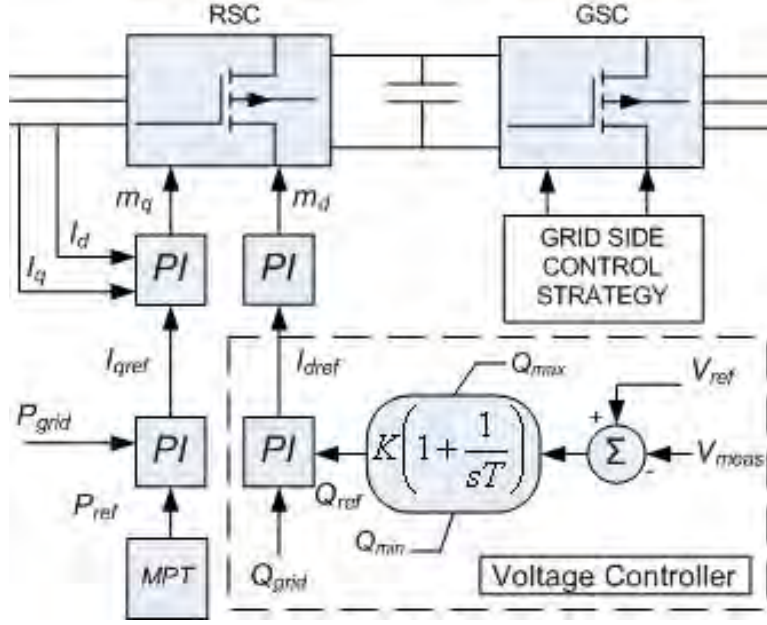
Figure 3.3 DFIG Wind Plant Voltage Controller Schematic

3.6.2 Dynamic Scenario Setup

At each penetration level the total wind generation is simulated at 2, 15, 50, and 100% output in order to consider various production conditions from cut-in to cut-out wind speeds. Since wind is not a constant resource this study aims to capture the effect of wind variability on system reliability.

At 2% park output it is considered that the wind units have just cut-in and the real power output is at a minimum. When employing the capability curve, the reactive limits of the machines are the greatest at this output as compared the other output levels studied. As wind speeds increase the parks real output increases and consequently the reactive capability of the DFIG park reduces. In contrast, the FERC regulation allows wind units to increase their reactive capability as the real output is increased. Again referring to figure 3.1, at 100% real output the leading reactive capability of both strategies is approximately equal.

Dynamic system data includes standard IEEE exciter and governor models imported from PSS/E for all synchronous machines. The motor loads are represented by standard induction machine models.

3.6.3 System Performance Validation

Given the static results gathered from the VSA analysis, dynamic simulation was carried out in DIgSILENT PowerFactory to analyze the transient response of the test system. Simulations were performed using RMS values (3rd order simulation models) that capture the electromechanical transients [30]. The inherent DFIG model in PowerFactory was modified to incorporate the designed voltage controller and derived converter ratings

24

from the previous sections. The parameters of the modified DFIG model are given in Appendix B.

Four power output scenarios are tested in order to assess the impact of the reactive control strategies with a high level of DFIG wind penetration. Wind park outputs of 2% (cut-in wind speed), 15%, 50%, and 100% generation are simulated on the previously described power system with a 20% penetration level of distributed DFIG wind generation.

The area around bus 3001 was identified as a critical fault location. A 3-phase short circuit was applied at this bus for a duration of 0.14 seconds to compare the responses between the voltage control strategies. It was determined in the VSA study that as penetration levels increase the reactive capability of the DFIG parks was insufficient for secure system operation. Hence, additional switched shunt capacitor banks of 150 MVAr were placed at buses 3005 and 3008 to ensure an accurate comparison of both strategies. For each control strategy the parks were initialized to 0.95 leading power factor. This ensured that pre-fault conditions of all machines are identical in each scenario for both control strategies. Before each simulation is performed the corresponding reactive limits are placed on the controller shown in Figure 3.3. As such, the (P, Q) coordinates are taken from the reactive power curve in Figure 3.1 and the regulated power factor limits are computed from (40) for the respective real outputs. The upper and lower reactive bounds, Q_{max} and Q_{max} in per units, are the limits for the voltage controller. The controller parameters are $K=1$ and $T=0.001$.

The following plots (Figures 3.4-3.7) detail the DFIG wind park responses to the disturbance near the fault at park 3005 and further away at park 3008. Each figure contains two sets of plots to compare the voltage control strategies. The three quantities of comparison are: voltage at load bus 153, reactive power output, and rotor current magnitudes through the PEC.

Bus 153 has been selected for monitoring its voltage performance due to the fact that it contains 42% of the system motor load. This bus voltage will be used as a metric of comparison between the voltage control strategies. Other quantities of interest are the total park reactive injections and rotor currents, which are integral in determining whether the wind plants electrical control is disabled.

The power electronic converter protection limitations were strictly taken into account with an over current setting of 600A (1.27 p.u.) given the 470A nominal current magnitude found from the converter sizing. Once triggered a resistive crowbar short-circuits the rotor windings for 0.15 seconds.

3.6.3.1 Scenario 1: 2% Output (Cut-in speed)

This scenario tests the system response for minimum wind levels when the turbines have just cut-in (4 m/s). The Q limits (p.u.) used in the controller based on the capability curve (CC) were (0.72,-0.92) and (0.0, 0.0) using the restricted power factor (RPF) mode. It can be observed from the bus 153 voltage in figure 3.4 that with the RPF control scheme the

system voltages are unable to recover post fault. In both strategies the PEC crowbar protection does not activate thus allows reactive injections through the fault. At fault clearance in the CC case the DFIG plants are able to dynamically compensate for the reactive burden placed on the synchronous generators by the induction motors. Thus, utilizing the extended reactive capability in the CC case stabilizes the system and prevents collapse.

Figure 3.4 Comparison of bus 153 voltage (p.u.), reactive power (MVAr) (parks: 3008/5 – red/black), and rotor current (kA) (parks: 3008/5 – pink/brown) from 20% penetration at cut-in speed with RPF (left) and with CC (right) control

3.6.3.2 Scenario 2: 15% Output

At 15% park output the corresponding Q limits for this study are (0.70, -0.90) for the CC case and (0.08, -0.08) for the RPF case. The PEC protection again does not activate at the fault initiation and over loading of the converters does not occur during the transient. Observing the bus voltage plots in figure 3.5 demonstrate that the CC control case provides enhanced post fault clearance voltage response. This is noticed in the reduced voltage overshoot as well as reduced ripple magnitudes. The improved post fault system

26

response in the CC case is mainly attributed to the increased reactive consumption at wind plant 3005 as viewed in the reactive plots.
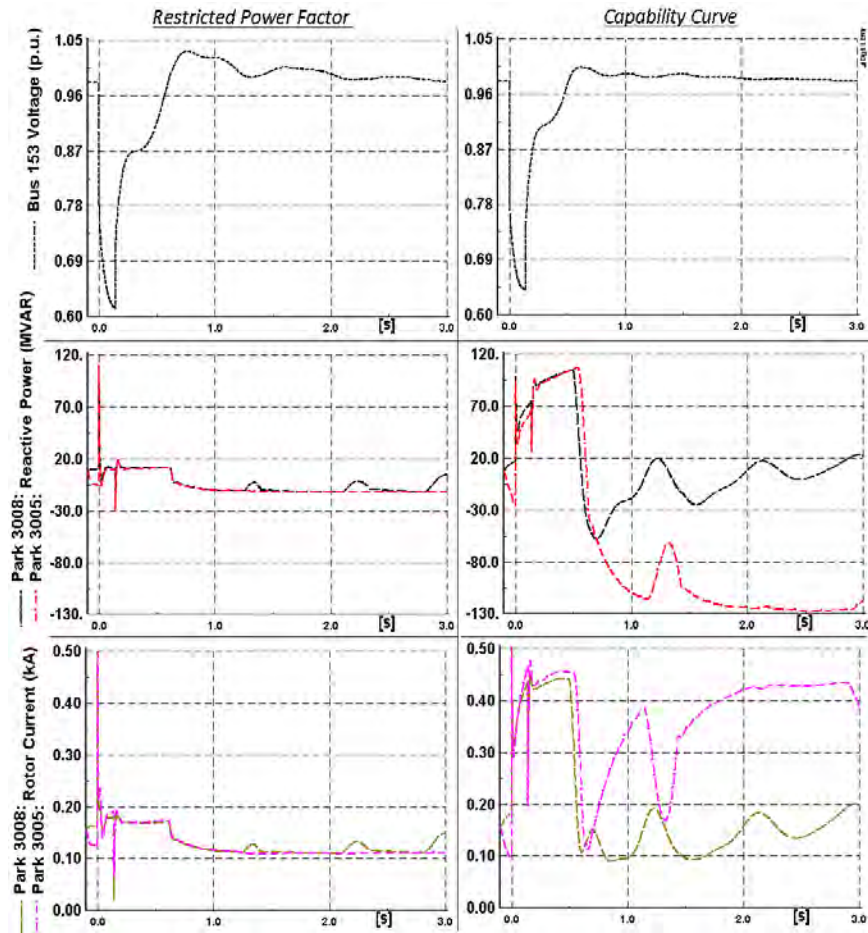
Figure 3.5 Comparison of bus 153 voltage (p.u.), reactive power (MVAr) (parks: 3008/5 – red/black), and rotor current (kA) (parks: 3008/5 – pink/brown) from 20% penetration at 15% output with RPF (left) and with CC (right) control

3.6.3.3 Scenario 3: 50% Output

At 50% park output the corresponding Q limits for this study are (0.60, -0.85) for the CC case and (0.18, -0.18) for the RPF case. The PEC protection trips at park 3005 at the fault initialization of the RPF case. This is depicted in the current plots of figure 3.6. Again the increased reactive consumption is very dominant in the CC case.
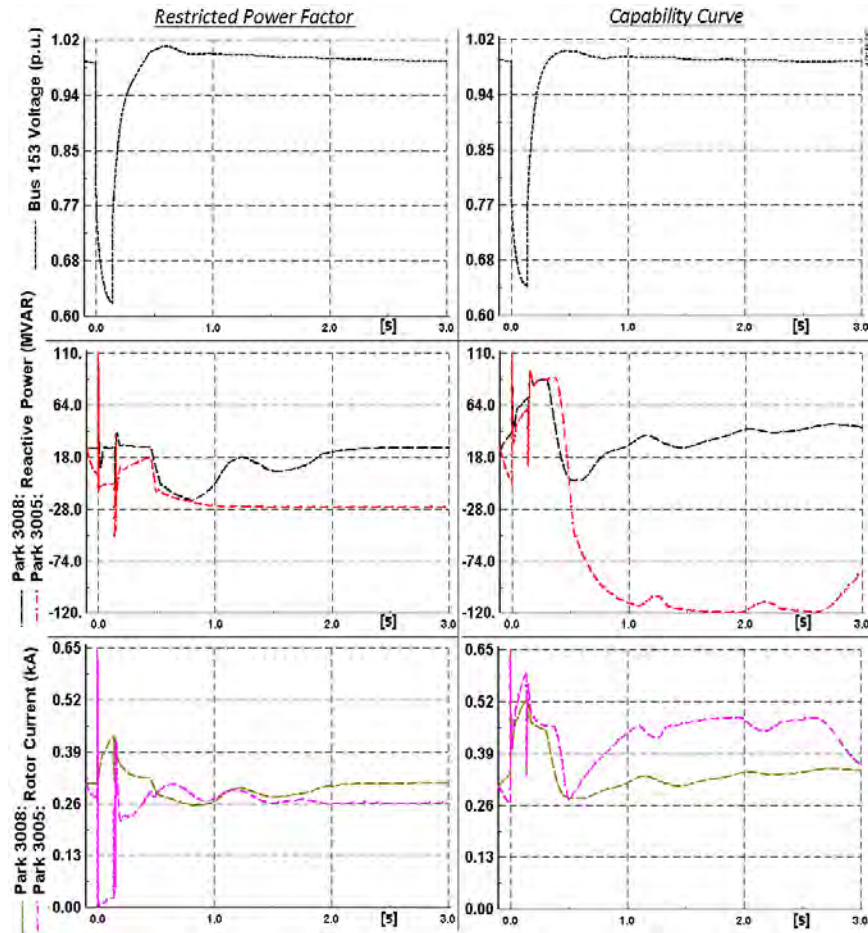
Figure 3.6 Comparison of bus 153 voltage (p.u.), reactive power (MVAr) (parks: 3008/5 – red/black), and rotor current (kA) (parks: 3008/5 – pink/brown) from 20% penetration at 50% output with RPF (left) and with CC (right) control

3.6.3.4 Scenario 4: 100% Output

The final study considers wind plant outputs to be at maximum capacity. The reactive limits placed on this study are (0.36, -0.69) for the CC and (0.34, -0.34) for the RPF modes of operation. It can be observed from the plots in figure 3.7, as the active power output of a park increases likewise does the current magnitude. The near nominal current at the initiation of the fault leads to tripping of the all wind parks (3005/7/8) PEC in both cases. At 0.15 seconds into both simulations the rotor protection clears, but due to large current transients the protection retriggers and none of the wind plants can regain power controllability until 0.30 seconds after the fault. In both cases the leading reactive limits are very similar hence the near identical reactive injections from wind farm 3008 and the voltage recovery at bus 153.

Although at 100% plant output the PEC protection triggers and all electrical control of the wind generation (20%) was not active for 0.30 seconds, the system appears relatively unaffected in the short term. In contrast the system experienced it's most dramatic recovery when wind resources were very low and the reactive capability was greatest

28

with the capability curve. Hence, restricting DFIG wind park operation to a fixed power factor range may introduce avoidable reliability risks.
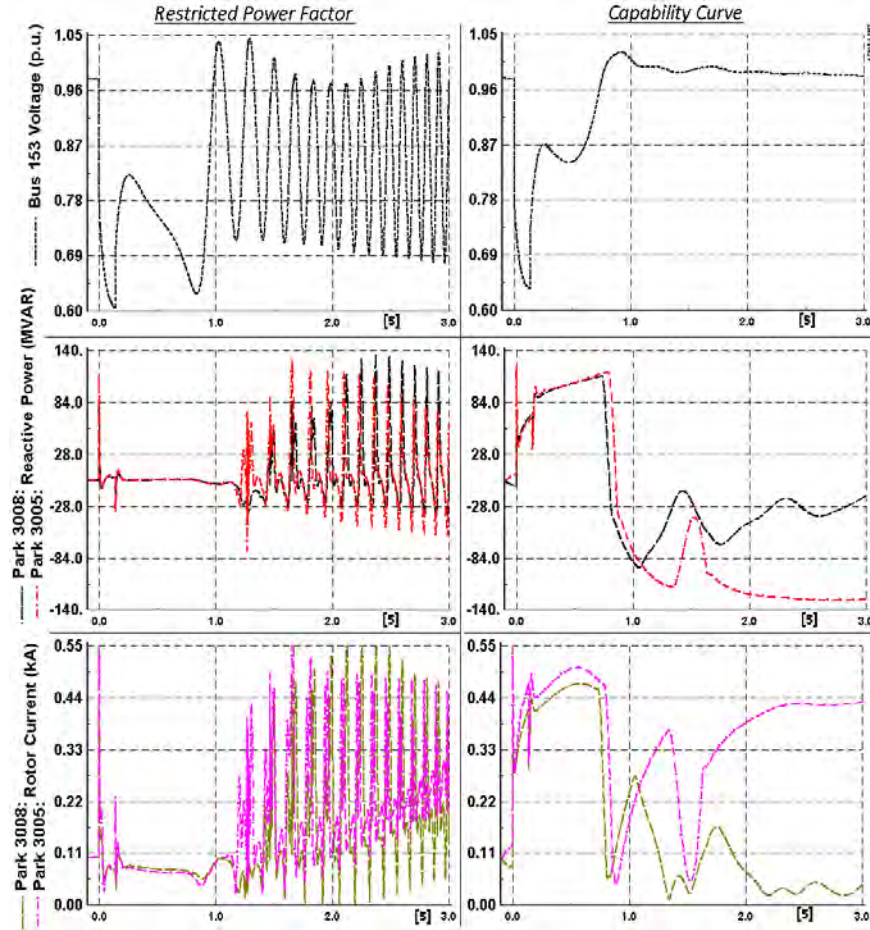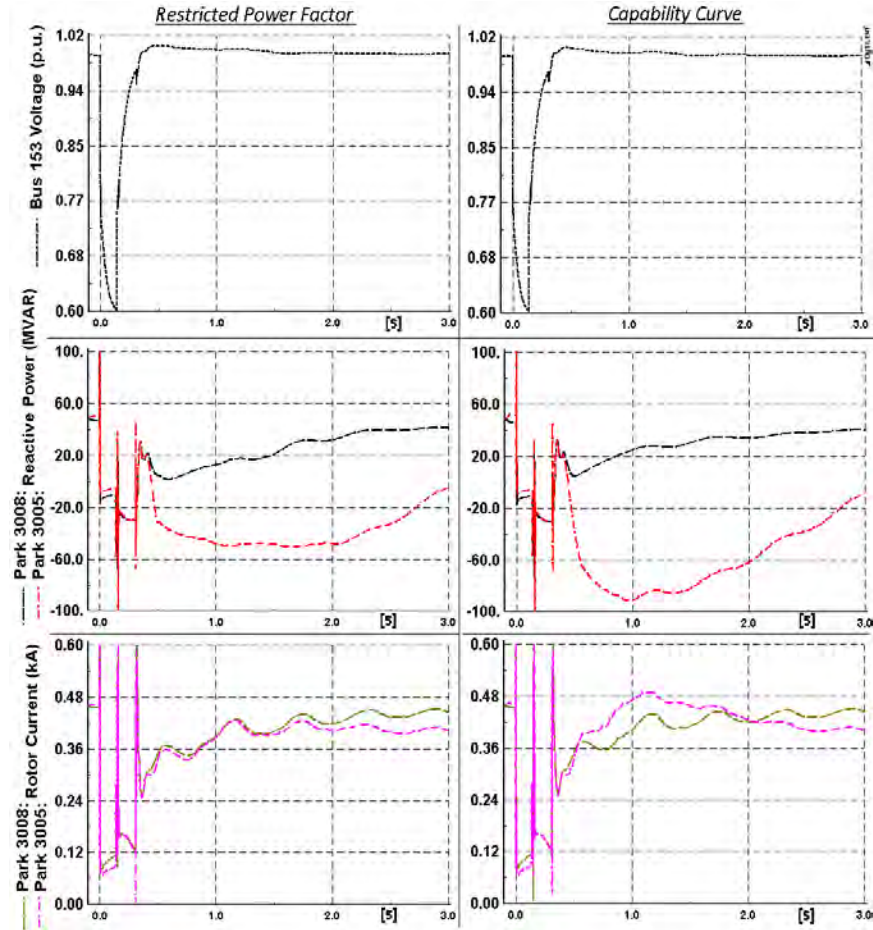

Figure 3.7 Comparison of bus 153 voltage (p.u.), reactive power (MVAr) (parks: 3008/5 – red/black), and rotor current (kA) (parks: 3008/5 – pink/brown) from 20% penetration at 100% output with RPF (left) and with CC (right) control

4. Incorporating Wind Variability into Voltage Security Analysis

The introduction of deregulated power system markets with the separation of generation, transmission and distribution has led to a stressed power system. The key characteristics of a stressed power system are depressed bus voltages, line flows reaching their rated limits and close proximity to voltage instability [31]. This is due to increased use of long distance transmission [31], and transmission investments not keeping up with natural load growth [32]. In the past three decades there have been a large number of voltage collapse incidents [33], which have led to the requirement of carrying out detailed voltage security assessment of the power system

The precise modeling of DFIG units is important for the voltage security assessment of the power system performance [1]. To accurately assess the stability of a system and to prevent voltage violations, computation of available reactive power in the system is essential [34]. The effect of wind speed variation and hence, park output variability becomes a critical factor when studying system performance with high penetration levels.

This section proposes a novel voltage security analysis tool that incorporates wind variability. The technique developed is general and is applicable for any type of wind generation technology. The voltage security assessment tool provides a Voltage Secure Region of Operation (VSROp). VSROp may be defined as the safe operating zone within a range of wind variability meeting voltage quality requirements. In previous sections it has been demonstrated that by implementing the full reactive capability of DFIG parks the excess available reactive power impacts system costs and may justify investment in DFIG generation.

4.1 Voltage Security Assessment Methodologies

According to [35], voltage stability refers to the ability of a power system to maintain steady voltages at all buses in the system after being subjected to a disturbance from a given initial operating condition. It depends on the ability to maintain/restore equilibrium between load demand and load supply from the power system. Any resulting instability occurs in the form of a progressive fall or rise of voltages of some buses. Major contributory factors to voltage instability are power system configuration, generation and load patterns [36-40]. A possible outcome of voltage instability is loss of load in an area, or tripping of transmission lines and other elements by their protective systems leading to cascading outages.

As mentioned in [41], the term voltage collapse is also often used. It is the process by which the sequence of events accompanying voltage instability leads to a blackout or abnormally low voltages in a significant part of the power system [38,41, 42].

Voltage problems typically occur in power systems which are heavily loaded faulted and/or have reactive power shortages [38]. Among the various factors which affect voltage stability issues, there is a special correlation between voltage instability problems and insufficient reactive power reserves [43]. Voltage collapse is related to reactive

power demands of loads not being met because of limitations on the available reactive power reserves and transmission of reactive power [44].

There are two general types of tools for voltage security assessment: dynamic and static. Dynamic analysis uses time-domain simulations to solve nonlinear system differential algebraic equations. Static analysis is based on the solution of conventional or modified powerflow equations.

Dynamic analysis provides the most accurate replication of the time responses of the power system [38, 45-47]. However, time-domain simulations are time consuming and computationally extensive. These limitations generally make dynamic analysis impractical for examination of a wide range of system conditions or for determining stability limits.

Static analysis [38, 48-53] involves only the solution of algebraic equations and therefore is computationally much more efficient than dynamic analysis. Voltage stability analysis often requires examination of lots of system states and many contingency scenarios. For this reason, the approach based on steady state analysis is more feasible.

For static voltage stability studies of a power system, the loading of the system is increased incrementally and slowly (in certain direction) to the point of voltage collapse. The MW-distance to this point is a good measure of system voltage stability limit. P-V analysis is a steady state-tool that develops a curve, which relates voltage at a bus (or buses) to load within an area. Bus voltages are monitored throughout a range of increased load.

The benefit of this methodology is that it provides an indication of proximity to voltage collapse throughout a range of load levels. Required input is standard load flow input data and the output is P-V curves for all specified buses. The voltage profile of the system is shown by the PV-curves which are plotted using power flow programs as the loading varies from the base values to the point of collapse.

Figure 4.1 demonstrates the P-V curves for a system. The three curves correspond to the base case (BC) and two contingencies (C1, C2). The PV margin reduces for contingencies (PV margin BC > PV margin C1 > PV margin C2), and hence including contingencies into voltage stability margin estimation is critical.
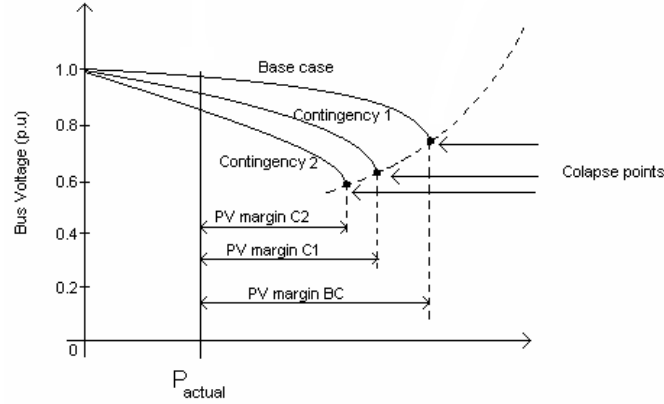
Figure 4.1 P-V Curve: Base Case and Contingencies

4.2 Incorporating Wind Variation into Maximum Power Estimation

Traditionally PV curves are drawn to study the nature of the voltage profiles of a particular load bus given an assumed direction of increase of conventional generation. Existing static Voltage Stability analysis assumes all generation to be dispatchable. Wind generation cannot be considered to be dispatchable [54] and hence a different approach is needed to understand the impact of wind variability on Voltage Stability Margin.

With increasing environmental concerns and political mandates, wind energy is becoming the preferred choice of renewable energy. Wind energy dispatch will play a pivotal role in order to meet the renewable portfolio standard to make wind generation comprise 20% of the whole power generation portfolio in the US by 2030 [55].

Electricity generated from wind power can be highly variable with several different timescales - hourly, daily, and seasonal periods are present in wind energy. Since instantaneous electrical generation and consumption must remain in balance to maintain grid stability, this variability can present substantial challenges to incorporating large amounts of wind power into a grid system. With wind power generation being increasingly incorporated into the existing power system, the traditional PV curves are unable to capture the stability margin for an integrated system which has high wind penetration (~20%). Intermittency and the non-dispatchable nature of wind energy production can raise various issues like increased regulation costs and operating reserves.

In order to include the wind variability, a P-V surface for secure operation is proposed. The developed surface is called the Voltage Secure Region of Operation (VSROp). The surface incorporates different levels of wind generation by representing different PV curves at different wind generation levels to obtain a three dimensional region of voltage secure operation. In the three dimensional region, the non-dispatchable wind generation (z axis) forms the additional axis along with the existing power generation, including losses of the system (x axis) and the per unit voltage (y axis).

Figure 4.2 below demonstrates a sample VSROp. The four PV curves corresponds to no wind and wind generations W1, W2 and W3 (W3>W2>W1). For each PV curve the amount of wind generation is kept constant and the load and generation is increased according to a set loading and generation increase scenario, which is kept constant for all PV curves. Another input to the PV surface calculation algorithm is the redispatch strategy for increase or decrease in wind generation.
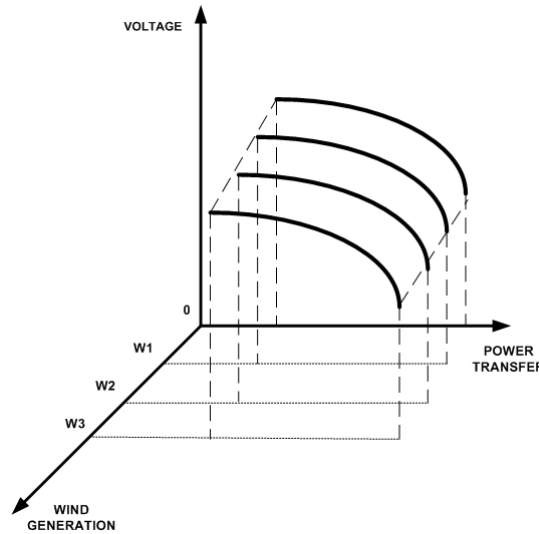
Figure 4.2 Voltage Secure Region of Operation (VSROp)

The flowchart for the proposed methodology is shown in figure 4.3. The proposed methodology includes the following steps:

4.2.1 Step 1: Obtain Input Data

This step basically involves obtaining the three inputs to the Voltage Security Assessment tool:
  a. The power flow data for the system under consideration.
  b. The assumed level of wind generation in the base case and wind variability that is to be studied.
  c. The redispatch strategy for increase or decrease in wind generation.

The power flow data includes the committed generations and their bid curves. It also includes the load increase direction and generation increase direction. The generation increase scenario is provided for all other generations except wind.

Historical wind speed data and load data is utilized to decide the amount of wind generation available in base case. The wind speed forecasts for maximum variability is utilized to decide at what values of wind variation PV curves are to be plotted.

The wind speed rate of variation along with the ramp rates of available generation is utilized to develop the generation redispatch strategy to compensate for variation in wind power in the system.

4.2.2 Step 2: Optimal Power Flow in the base case

The Optimal Power Flow formulation mentioned in section 3.5.1 is utilized at this stage. The Optimal Power Formulations allows the incorporation of the varying reactive capability with wind level variation.

4.2.3 Step 3: Full Contingency Based Margin Estimation

For a fixed wind energy dispatch, plot the PV curves using powerflow for all (n-1) contingencies. MATPOWER is used to obtain the PV curves. The contingency corresponding to the least power transfer margin is noted and the corresponding PV plot is stored. The set of all PV curves is plotted in the previously mentioned three dimensional space to obtain the Voltage secure PV surface.

The series of PV curves on different planes corresponding to a particular wind penetration level will constitute a hyperspace which will represent the stable voltage operating zone The base case dispatch is then utilized to estimate the least available margin in the PV surface.
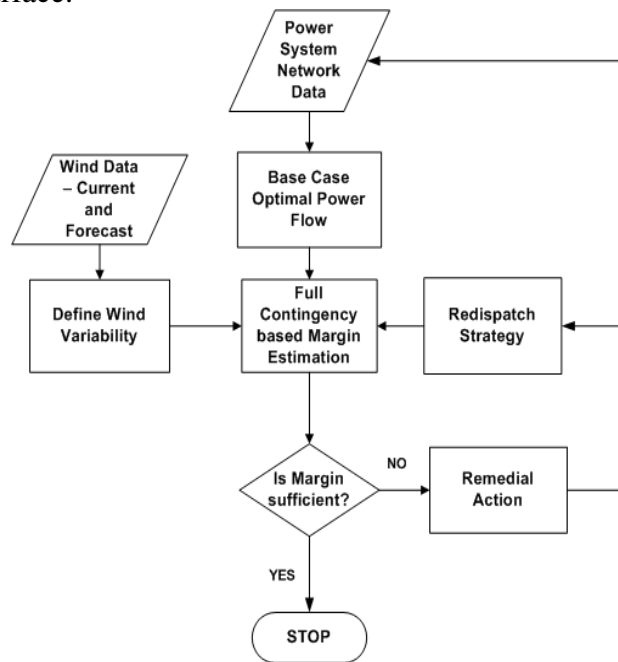
Figure 4.3 Flowchart for Voltage Security Assessment

4.2.4 Step 4: Margin Check and Remedial Action

The margin obtained in Step 3 is verified to meet the power margin requirements. If the margin requirements are not met then remedial actions are taken to increase the margin and the modified load flow data is fed into step 1 and the entire process is iteratively repeated until the desired margin is obtained.

The remedial actions that can be taken include but are not restricted to capacitor switching, commitment of additional generation units or load shedding. In the test case demonstrated we have only incorporated additional commitment of generation as a remedial action.

This hyperspace would give the power system operators a given region which might be too conservative, but is the perfectly safe operating zone. Also given current wind dispatch and estimated variability in the next hour, the operator would be able to quickly determine the amount of the margin that would be available for the system.

4.3 Case Study

4.3.1 Test System Description

The 23-bus test system used in section 3.5.4 is again considered. The generator at 3018 is taken offline. The 5 generators are assumend to have the same rating of 900 MW. Reactive limits on all generators are set to be 500 MVar and -150 MVar. Two locations are chosen for Wind Generation. One is located at bus 3008 and the second at bus 3002.The wind park of size 800 MW is chosen. Base case plant output is asumend to be 560 MW which is 20% of the base case load. The location at bus 3008 is not transmission constrained whereas the location 3002 is in a high generation low load area of the power system.

Two different redispatch strategies are assumed. One with the residual generation being picked up by Gen 3011 and Gen 101(marked in red). The second redispatch strategy assumes the generators at 211 and 206 to pe the pick up generators(marked in green). For each wind park location and redispatch strategy both Capability curve and FERC mandated restricted power factor is used to analyze the impact on transfer margin. For each maximum transfer margin obtained the most critical contingency is recorded.
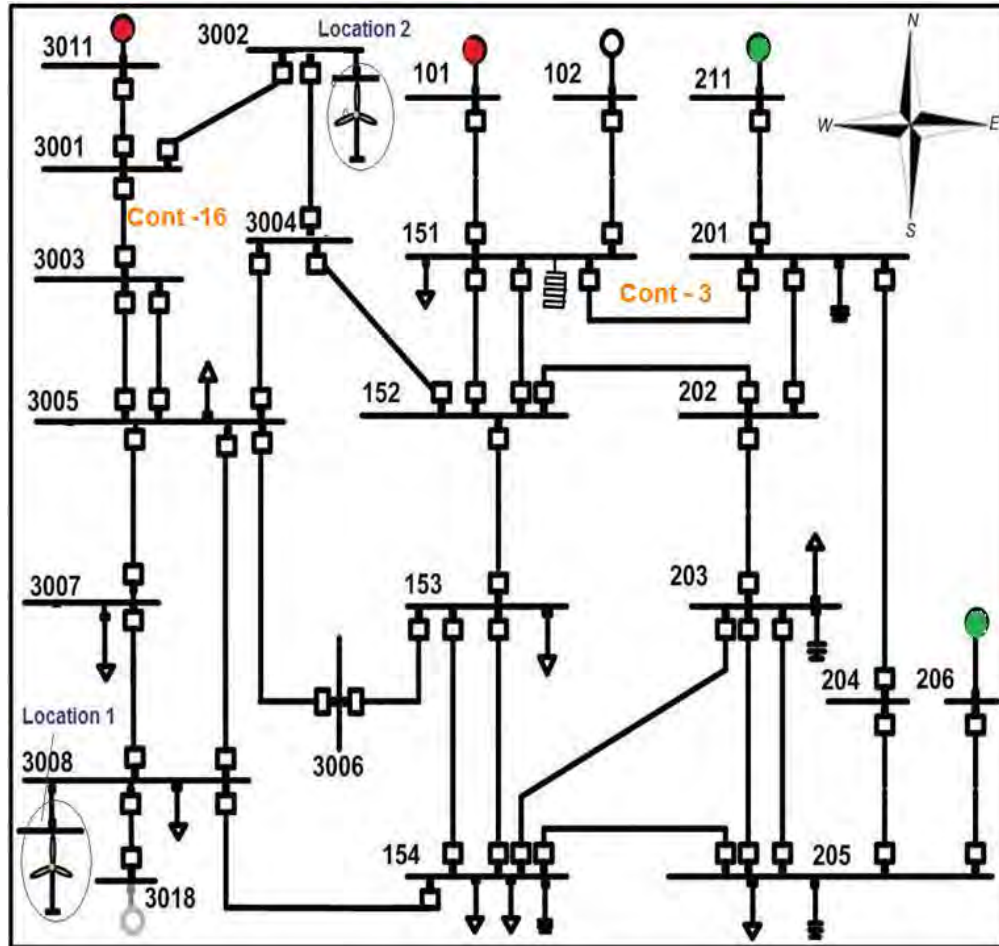
Figure 4.4 System Description for Case Study

4.3.2 Wind Farm at Location 1

The variation in power transfer margin as the wind level is varied from 0 to 800 MW is demonstrated in figures 4.5 and 4.6.
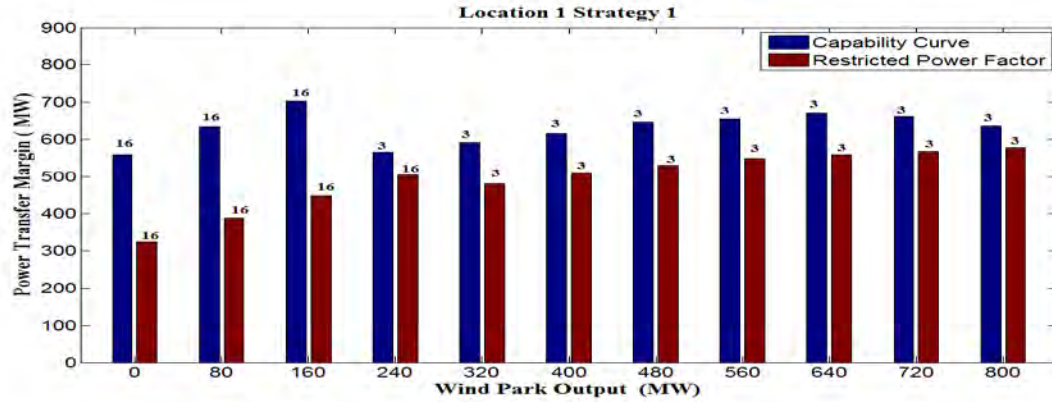
Figure 4.5 Power Transfer Margin Variation at Location 1 with Redispatch Strategy 1
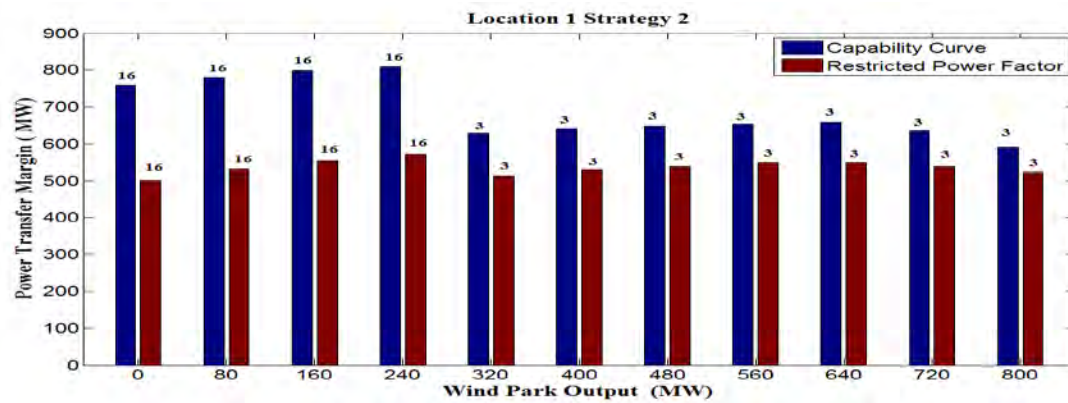
Figure 4.6 Power Transfer Margin Variation at Location 1 with Redispatch Strategy 2

At location 1 critical contingencies vary with varying wind levels. At lower wind levels the critical contingency is 16 whereas for higher wind speeds it s contingency 3. At location 1, the maximum margin for redispatch strategy 2 is obtained around 240 MW wind power output and for redispatch strategy 1 maximum margin is obtained at 160 MW plant output. At location 1, even though maximum transfer margin is less for redispatch strategy 1, the variation in transfer margin over the entire range of variability is lesser than strategy 2. The general trend at location 1 is that the power transfer peaks at between 160-240 MW and the next peak is at approximately 640 MW.

The variation in critical contingency at location 1 is attributed to the generator at bus 211 hitting its lower reactive power limit at higher wind levels for contingency 3.
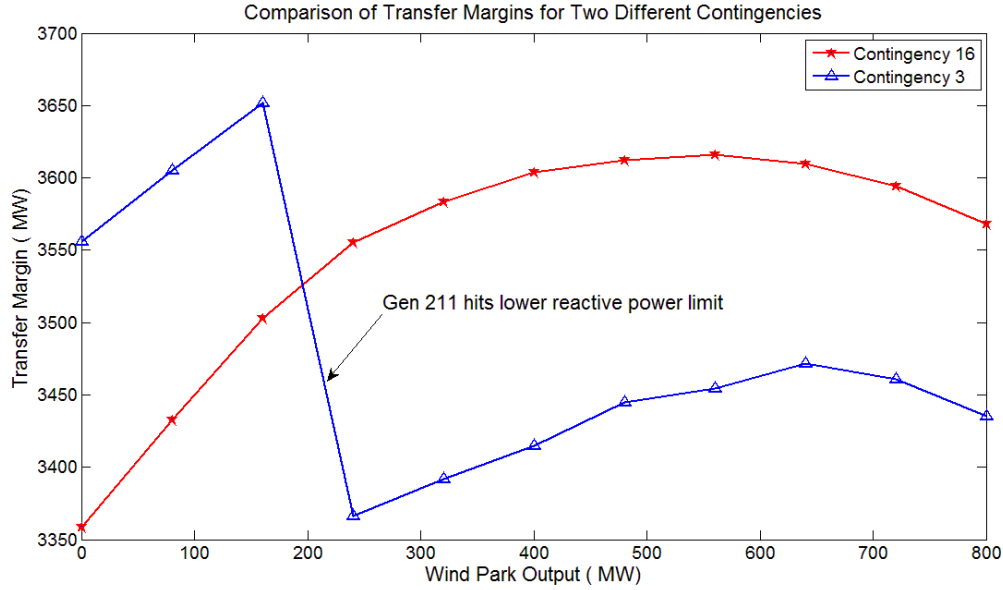
Figure 4.7 Transfer Margin Variations for contingencies 3 and 16 at Location 1
for Redispatch Strategy 1

4.3.3 Wind Farm at Location 2

The variation in power transfer margin as the wind level is varied at location 2 from 0 to 800 MW is demonstrated in figures 4.8 and 4.9. At location 2 there is no change in critical contingency over the entire range of variability. The general trend for the transfer margin at location 2 is that the transfer margin decreased with increasing wind levels. For redispatch strategy 1 it is observed that at higher wind levels capability curve provides convergence for all wind levels whereas with Restricted Power Factor no solution is obtained at 90% and 100% output. Comparing the two redispatch strategies, strategy 2 provides higher transfer margins at low wind levels. Both reactive power limits at 90% and 100% output, do not give convergence for all contingencies at base case.
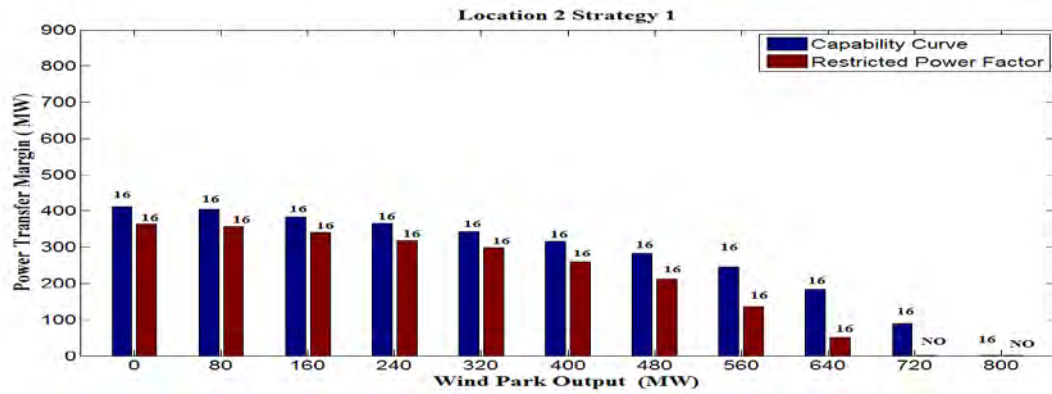
Figure 4.8 Power Transfer Margin Variation at Location 2 with Redispatch Strategy 1
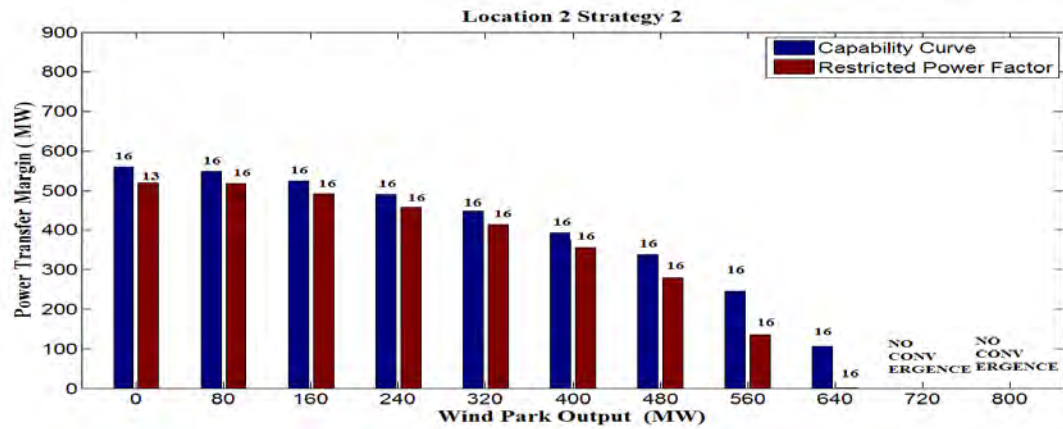
Figure 4.9 Power Transfer Margin Variation at Location 2 with Redispatch Strategy 2

4.3.4 Large System Implementation

A section of the Eastern Interconnection is used as the study area. The study area consists of 5600 buses with 11 areas. Two areas corresponding to MEC and ALTW are considered the 2 wind rich regions. The total base case load is 60179 MW with 3100 MW coming from wind in the considered wind rich area. The following table summarizes the generation and load in the areas considered.

Table 4.1: Generation and Load Summary for Areas Constituting the Study Region

Area	Generation	Load
130	2556	3579
331	5255	3271
356	11503	12473
357	3666	4283
363	23875	23401
540	1311	1701
635	5409	4158
640	2175	2356
645	1824	1924
652	5623	2333
680	1490	708

The system wind penetration is about 2.5% in the base case. The wind generation is increased by adding wind parks in the two wind rich areas and increasing load in the entire study area. This is done to simulate export of excess wind generation. The final study system has a load of 63,600 MW with 6500 MW coming from wind. With a given set of 50 critical contingencies we obtain this limit as the maximum wind that can be added in the system with a minimum power transfer margin of 300 MW at full wind potential. The penetration of wind in the study area is approximately 10 %. Now 3000 MW of wind is varied from 0 to 3000 and for this variance the VSROP is obtained. To compensate for reduced wind additional units are brought online to compensate for the loss of wind as compared to using the generators that are already online. The figure 4.10 below demonstrates the power transfer margins at different wind levels.

In this case also it is observed that utilizing the capability curve provides a significant increase in power transfer margin. It is also observed that the maximum power transfer margin is obtained neither at minimum wind nor at maximum wind. The critical contingency also varies with varying wind levels.
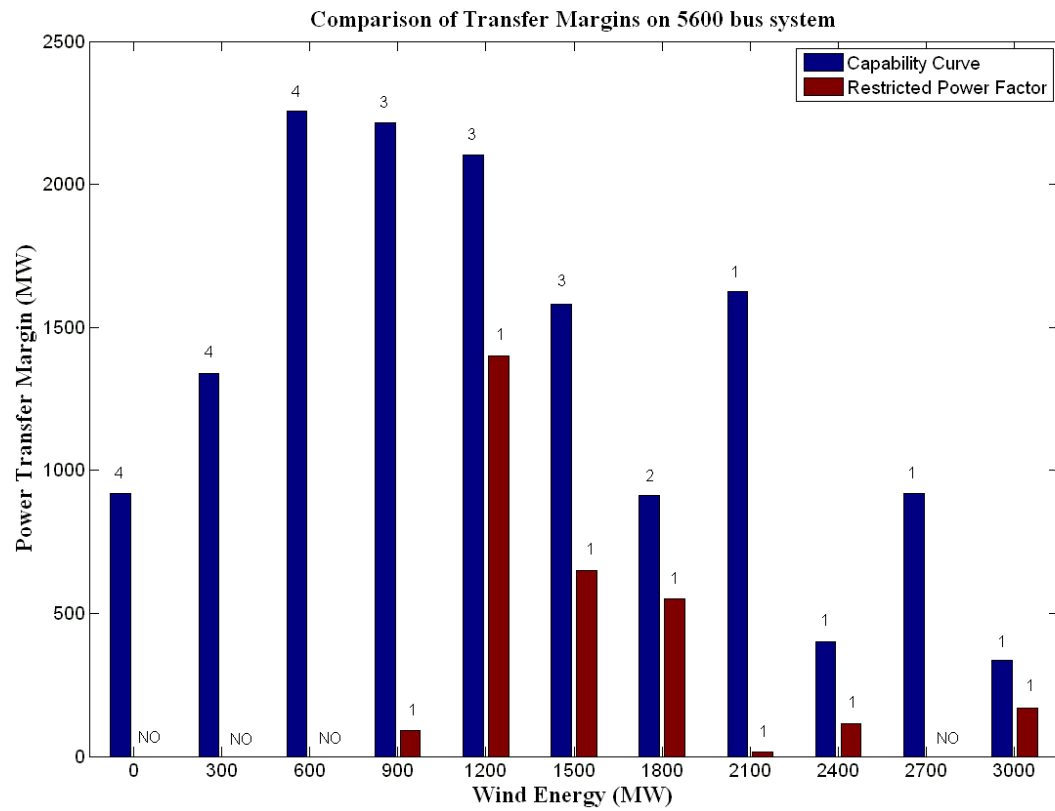
Figure 4.10 Power Transfer Margin Variation at Different Wind Levels
for the Large System

5. Conclusions

5.1 DFIG Control Enhancements

The control enhancements developed allow for better utilization of the DFIG machine for voltage control and reactive support. The additional control capabilities fully employ the available reactive power in the DFIG machine without harming the power electronics.

5.2 Impact of Additional Reactive Capability

The operation of DFIG wind parks implementing a capability curve paves the way for regulatory changes. The FERC order 661-A, gives general guidelines for interconnecting wind parks, but for specific parks employing DFIG units the restriction on power factor can be lifted. Fully utilizing the potential of a DFIG wind park may be obtained at no extra cost to the wind farm owner, which not only facilitates increase power transfer margins, but also improves the post fault voltage recovery following a disturbance. As levels of wind penetration continue to increase the responsibility of wind units to adequately substitute conventional machines becomes a critical issue. As demonstrated in this work, amending the fixed power factor regulation to bolster reactive support up to PEC limitations can drastically extend the plants reactive capability at partial loading.

5.3 Suggested Order 661-A Revisions

Given advanced SCADA systems and wind forecasting tools it is now possible to receive relatively accurate hour ahead wind generation predictions [56]. This technology is already being incorporated by the California Independent System Operators (CAISO) to schedule generation dispatch around intermittent resources [57]. Under these same principles, operators should also have access to timely information regarding the reactive capability of the plant. This would allow for a more accurate assessment of available reactive power reserves at high penetration levels. Therefore, a policy revision mandating wind park owners to submit plant capability curves to system operators may lend itself to not only more economic dispatch, but also increased stability during voltage emergencies [58].

At the plant level, the Irish grid code maintains a requirement where during a fault the wind park must provide the maximum possible amount of reactive current without violating generator limits [59]. By incorporating this rationale to include the capability curve, a revised U.S. grid code could implicitly define the exact injection to be commanded at the POI for a given operational point. As validated in the simulations, a system can be drastically improved from a farm that regulates its POI voltage. In all four scenarios the controller limits were defined by using the bounds of its capability curve.

The suggested amendments to the current FERC 661-A policy are based on the preceding results. Thus it was demonstrated that the presence of the additional reactive capacity in high penetration scenarios is crucial to enhancing system performance.

5.4 Incorporating Wind Variability into Voltage Security Assessment

A novel voltage stability assessment tool that incorporates wind variability and capability curve is developed. The developed tool calculates sets of PV curves plotted along parallel planes thus giving a three dimensional voltage secure region of operation (VSROp). This tool helps determine the wind level at which minimum power transfer margin is obtained. This power level need not be at minimum wind or maximum wind. The tool also provides the most restrictive contingency at each wind level.

The restricted power factor operation may lead to lower penetration levels. The redispatch strategy utilized for compensating increase/decrease in wind has an important impact on the transfer margin of a system. The most severe contingencies on a system depend on the level of wind generation.

References

[1] R. Zavadil, N. Miller, A. Ellis, and E. Muljadi, "Making connections," *IEEE Power & Energy Magazine*, pp. 26–37, November/December 2005.

[2] R. Doherty, "Establishing the role that wind generation may have in future generation portfolios," *IEEE T ransactions on Power Sy stems,* vol. 21, no. 3, pp. 1415–1422, August 2006.

[3] American Wind Energy Association : 2009: Another Record Year for Wind Energy Installations.

[4] Renewable Energy Policy Network for the 21st Century, Global Status Report: 2009.

[5] T. Berry, M. Jaccard, "The renewable portfolio standard: design considerations and an implementation survey", *Energy Policy,* vol. 29, no. 4, pp. 263-277, March 2001.

[6] L. Bird, M.Bolinger, T.Gagliano, R. Wiser, M. Brown, B. Parsons, "Policies and market factors driving wind power development in the United States", *Energy Policy*, vol. 33, no. 11,   pp. 1397-1407 , July 2005.

[7] American Wind Energy Association (AWEA), "Legislative Affairs", Retrieved on 17th July, 2008, from Available: http://www.awea.org/legislative/

[8] S.Muller, M.Deicke and Rik W. De Doncker, "Doubly Fed Induction Generator Systems for Wind Turbines," *IEEE I ndustry Applications M agazine,* pp. 26-33, May/June 2002.

[9] Website: *Institute of   E   nergy T   echnology-Aalborg U   niversity*: www.iet.aau.dk/education

[10] V. Akhmatov, "Variable-Speed Wind Turbines with Doubly-Fed Induction Generators Part IV: Uninterrupted Operation Features at Grid Faults with Converter Control Coordination", *Wind Engineering*, vol. 27, no.6, pp. 519-529, 2003.

[11] Federal Energy Regulatory Commission (FERC), Order No. 661A (Order on Rehearing) on interconnection for wind farms, December 12, 2005.

[12] A.D. Hansen, G. Michalke, "Fault Ride-Through Capability of DFIG Wind Turbines", *Renewable Energy*, vol. 32, pp. 1594-1610, 2007.

[13] R. Kemsley, G. Pannel, C. Barbier, "Cost Effective Improvements in DFIG Performance Under Fault Conditions for Offshore Applications", Econnect Ventures Ltd. [Online] *Available*: www.berr.gov.uk/files/file40640.pdf

[14] I. Erlich, H. Wrede, C. Feltes, "Dynamic Behavior of DFIG-Based Wind Turbines During Grid Faults", *Power Conversion Conference,* pp. 1195-1200*, April 2-5, 200*7.

[15] T. Lund, P. Sorensen, J. Eek, "Reactive Power Capability of a Wind Turbine with Doubly Fed Induction Generator", *Wind Engineering*, no. 10, pp. 379-394, 2007.

[16] E. Muljadi, S. Pasupulati, A. Ellis, D. Kosterov, "Method of equivalencing for a large wind power plant with multiple turbine representation," *Power and E nergy Society General Meeting - Conversion and Delivery of Electrical Energy in the 21st Century, 2008 IEEE*, vol., no., pp.1-9, 20-24 July 2008

[17] Electric Systems Consultancy, ABB Inc., Wind Farm Integration in British Columbia – Stages 3: Operation Impact, March 28, 2005.

[18] "Program Operation Manual", PSSE 30.3.2 Siemens Power Technologies Inc., 2005.

[19] *"*Program Application Guide", PSSE 30.3.2 Siemens Power Technologies Inc., 2005.

[20] DIgSILENT GmH, Manuals, DIgSILENT PowerFactory, Version 13.1., 2004.

[21] Peter Van Meirhaeghe, "Double fed induction machine: a EUROSTAG model", *Scientific P ublications-Eurostag*, November 2003[Online], Available: http://www.eurostag.be/frameset.htm

[22] Y. Lei, A. Mullane, G. Lightbody, R. Yacamini, "Modeling of the Wind Turbine With a Doubly Fed Induction Generator for Grid Integration Studies", *IEEE Trans. on Energy Conversion*, vol. 21, no. 1, pp. 257-64, March 2006.

[23] H.W. Dommel, W.F. Tinney, "Optimal Power Flow", *IEEE Transactions on Power Apparatus and Systems*, October 1968.

[24] H. Wang, C. E. Murillo-Sánchez, R. D. Zimmerman, R. J. Thomas, "On Computational Issues of Market-Based Optimal Power Flow", *IEEE Transactions on Power Systems*, Vol. 22, No. 3, Aug. 2007, pp. 1185-1193.

[25] "MATPOWER User's Manual", *MATPOWER 3 .2 s olver* [Online] Available: http://www.pserc.cornell.edu/matpower/

[26] P. Kundur, Power System Stability and Control. New York: McGraw-Hill, 1994.

[27] R.Piwko, R. DeMello, R. Gramlich, W. Lasher, D. Osborn, C. Dombek, K. Porter, "What Comes First?," *Power and E nergy Magazine, IEEE*, vol. 5, no. 6, pp.68-77, Nov.-Dec. 2007.

[28] P. Pinson, C. Chevallier, G.N. Kariniotakis, "Trading Wind Generation From Short-Term Probabilistic Forecasts of Wind Power," *Power Systems, I EEE T ransactions on* , vol.22, no.3, pp.1148-1156, Aug. 2007

[29] A.Fabbri, T.GomezSanRoman, J. RivierAbbad, V.H. MendezQuezada, "Assessment of the Cost Associated With Wind Generation Prediction Errors in a Liberalized Electricity Market," *Power Systems, IEEE Transactions on* , vol.20, no.3, pp. 1440-1446, Aug. 2005

[30] M. Poller, S. Achilles, "Aggregated wind park model for analyzing power system dynamics", DIgSILENT Publications, Retrieved on 17th July 2008, from http://www.digsilent.de/Consulting/Publications/

[31] Ming Ni, J.D. McCalley, V. Vittal, T. Tayyib, "Online risk-based security assessment," *Power Systems, IEEE Transactions on* , vol.18, no.1, pp. 258-265, Feb 2003

[32] M. Shahidehpour, "Investing in expansion: the many issues that cloud transmission planning," *Power and Energy Magazine, IEEE* , vol.2, no.1, pp. 14-18, Jan-Feb 2004

[33] H. Yoshida, K. Kawata, Y. Fukuyama, S. Takayama, Y. Nakanishi, "A particle swarm optimization for reactive power and voltage control considering voltage security assessment," *Power Systems, IEEE Transactions on* , vol.15, no.4, pp.1232-1239, Nov 2000

[34] Y. Chi; Y. Liu; W. Wang; H. Dai, "Voltage Stability Analysis of Wind Farm Integration into Transmission Network," *Power Sy stem T echnology, 2006. PowerCon 2006. International Conference on* , vol., no., pp.1-7, Oct. 2006

[35] P. Kundur, J. Paserba, V. Ajjarapu, G. Andersson,A. Bose, C. Canizares, N. Hatziargyriou, D. Hill, A. Stankovic, C. Taylor, T. Van Cutsem, V. Vittal, "Definition and classification of power system stability IEEE/CIGRE joint task force on stability terms and definitions," *Power Systems, IEEE Transactions on* , vol.19, no.3, pp. 1387-1401, Aug. 2004

[36] B. Gao, G. K. Morison, and P. Kundur, "Toward the development of a systematic approach for voltage stability assessment of large-scale power systems," IEEE Trans. Power Syst., vol. 11, no. 3, pp. 1314–1324,Aug. 1996.

[37] T. Nagao, K. Tanaka, and K. Takenaka, "Development of static and simulation programs for voltage stability studies of bulk power system," IEEE Trans. Power Syst., vol. 12, no. 1, pp. 273–281, Feb. 1997.

[38] P. Kundur, Power System Stability and Control. New York: McGraw-Hill, 1994.

[39] C. A. Canizares, A. C. Z. De Souza, and V. H. Quintana, "Comparison of performance indices for detection of proximity to voltage collapse," IEEE Trans. Power Syst., vol. 11, no. 3, pp. 1441–1447, Aug. 1996.

[40] A. Sode-Yome and N. Mithulananthan, "Comparison of shunt capacitor, SVC and STATCOM in static voltage stability margin enhancement," Int. J. Elect. Eng. Educ., vol. 41, no. 3, Jul. 2004.

[41] IEEE/PES Power System Stability Subcommittee, Voltage Stability Assessment: Concepts, Practices and Tools, special publication, final draft, Aug. 2003.

[42] C. W. Taylor, Power System Voltage Stability. New York: McGraw-Hill, 1994.

[43] A.M. Abed., "WSCC voltage stability criteria, undervoltage load shedding strategy, and reactive power reserve monitoring methodology," *Power Engineering Society Summer Meeting, 1999. IEEE* , vol.1, no., pp.191-197 vol.1, 18-22 Jul 1999

[44] L. Bao, Z. Huang, W. Xu, "Online voltage stability monitoring using VAr reserves," *Power Systems, IEEE Transactions on* , vol.18, no.4, pp. 1461-1469, Nov. 2003

[45] EPRI Final Report EL-461 0, "Extended Transient-Midterm Stability Package: Final Report", Prepared by Ontario Hydro, November 1992.

[46] J. Deuse and M. Stubbe, "Dynamic simulation of voltage collapses," *Power Systems, IEEE Transactions on* , vol.8, no.3, pp.894-904, Aug 1993

[47] W.W. Price, D.B. Klapper, N.W. Miller, A. Kurita, and H. Okubo, "A Multiple Faceted Approach to Power System Voltage Stability Analysis," *CIGRE,* paper 38-205, 1992.

[48] T. Van Cutsem, Y. Jacquemart, J.-N. Marquet, and P. Pruvot, "A Comprehensive Analysis of Mid-term Voltage Stability," paper 94 SM 51 1-6 PWRS, presented at IEEE/PES Summer Meeting, San Francisco, CA, July 24-28, 1994.

[49] B. Gao, G.K. Morison, and P. Kundur, "Voltage stability evaluation using modal analysis," *Power Systems, IEEE Transactions on* , vol.7, no.4, pp.1529-1542, Nov 1992

[50] T. Van Cutsem, "A method to compute reactive power margins with respect to voltage collapse," *Power Systems, IEEE Transactions on* , vol.6, no.1, pp.145-156, Feb 1991

[51] F. L. Alvarado and T. H. Jung, "Direct detection of voltage collapse conditions," in *Bulk Power System Voltage Phenomenon I\—Voltage Stability and Security* Potosi, MO, pp. 5.23-5.38.

[52] V. Ajjarapu and C. Christy, "The continuation power flow: a tool for steady state voltage stability analysis," *Power Systems, IEEE Transactions on* , vol.7, no.1, pp.416-423, Feb 1992.

[53] I. Dobson and L. Lu, "Using an Iterative Method to Compute a Closest Saddle Node Bifurcation in the Load Power Parameter Space of an Electric Power System," Bulk

Power System Voltage Phenomena, Voltage Stability and Security, NSF Workshop, Deep Creek Lake, MD, August 1991.

[54] A.A. Chowdhury and D.O. Koval, "Modeling Non-Dispatchable Wind Energy Sources in Generating Capacity Reliability Planning", Proceeding (442) European Power and Energy Systems - 2004, available online - http://www.actapress.com/PaperInfo.aspx?PaperID=17989&reason=500

[55] U.S. Department of Energy, Energy Efficiency and Renewable Energy, (2008, July). 20% Wind Energy by 2030: Increasing Wind Energy's Contribution to U.S. Electricity Supply

[56] V. Akhmatov, "Variable-Speed Wind Turbines with Doubly-Fed Induction Generators Part III: Model with the Back-to-back Converters", *Wind Engineering*, vol. 27, no.26, pp. 79-91, 2003

[57] S. Heier, *Grid Integration of Wind Conversion Systems*, John Wiley & Sons, Inc., 1998, p. 21-34

[58] A. Hansen, C. Jauch, P. Sørensen, F. Iov, F. Blaabjerg, "Initialisation of Grid-Connected Wind Turbine Models in Power-System Simulations", Wind Engineering, Vol. 27, No. 1, pp. 21-38, 2003

[59] A.D. Hansen, C. Jauch, P. Sorensen, F. Iov, F. Blaabjerg, "Dynamic Wind Turbine Models in System Simulation Tool DIgSILENT", Riso National Laboratory, Riso-R-1400(EN),[Online],Available:
www.digsilent.de/Software/Application_Examples/ris-r-1400.pdf

Project Publications

[1] Konopinski, R. J.; Vijayan, P.; Ajjarapu, V., "Extended Reactive Capability of DFIG Wind Parks for Enhanced System Performance," *Power Systems, IEEE Transactions on* , vol.24, no.3, pp.1346-1355, Aug. 2009

[2] P.Vijayan,S.Sarkar, V.Ajjarapu, "A Novel Voltage Stability Assessment Tool to Incorporate Wind Variability", *PES General Meeting 2009 , Calgary,* 26-30th July 2009

Appendix 1: Maximum Power Tracking Scheme

Doubly fed induction generator wind turbines control their machine's rotational speed to allow operation at maximum power based on the velocity of the wind. This can be accomplished using a power optimization strategy as discussed in [1]. A generic MPT characteristic, based on the GE 1.5 MW wind turbine, was developed for the DFIG wind turbine parks used in this system analysis. Figure A1 presents a graphic with various electrical outputs and generator rotational speeds versus the operational wind speeds with make up the MPT characteristic used in the simulations. The speed range of the machine was designed for a cut-in speed of 3.5 m/s to a cutout wind speed of 25 m/s.
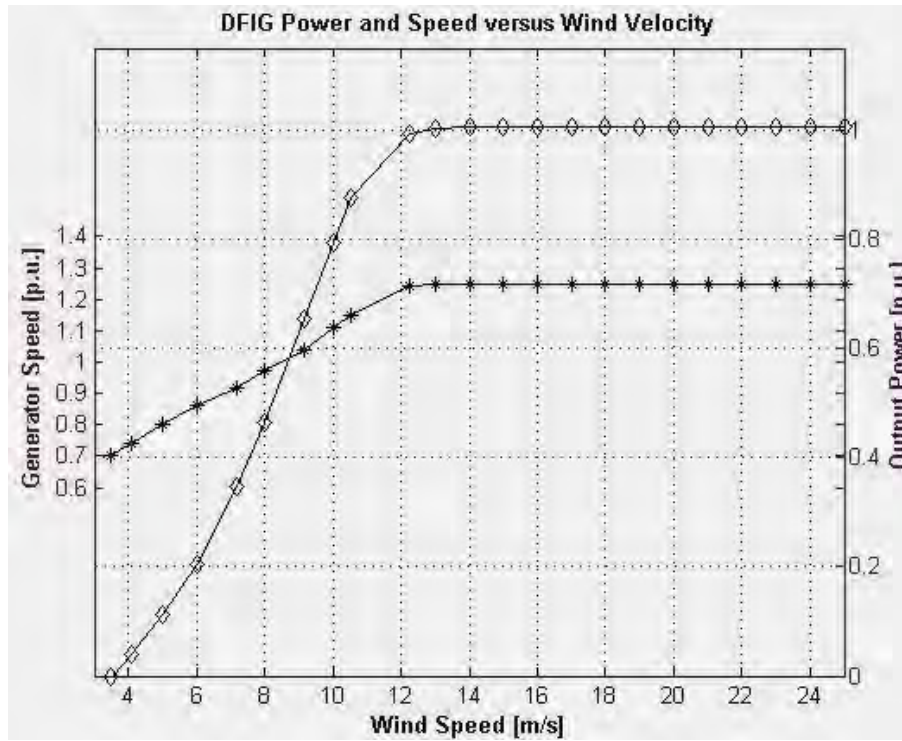
Figure A1: DFIG wind park electrical output (p.u.) and rotor speed (p.u.) versus wind velocity (m/s)

References:
[1] H. Li, Z. Chen, J.K. Pedersen, "Optimal Power Control Strategy of Maximizing Wind Energy Tracking and Conversion for VSCF Doubly Fed Induction Generator System", IEEE Power Electronics and Motion Control Conference 2006.

Appendix 2: Machine Parameters

The DFIG model developed for this study was comprised of information gathered from several sources. The model was based around, but not limited to the GE 1.5 MW production DFIG wind turbine. Since proprietary information regarding the exact operation of this machine was not available some inferences were made.

This paragraph explains the origin of the Table 7 simulation parameters and the performance characteristics. The generator electrical parameters were referenced from [1]. The rotor and generator mechanical parameters are defaults from DIgSILENT PowerFactory. The machine parameters (voltage & power ratings, gearbox ratio, etc.) were based on marketing documentation of the GE 1.5 MW wind turbine [2].

Table 7. DFIG Wind Park Machine Simulation Parameters

Rated electrical power	1.5 MW
Rated generator power	1.3 MW
Rated stator voltage	575 V
Rotor to stator turns ratio	3
Machine inertia	30 kgm^2
Rotor inertia	610000 kgm^2
Inductance: mutual, stator, rotor	4.7351, 0.1107, 0.1193 p.u.
Resistance: stator, rotor	0.0059, 0.0066 p.u.
Number of poles	3
Grid frequency	60 Hz
Gearbox ratio	1:72
Nominal rotor speed	16.67 rpm
Rotor radius	42 m
Maximum slip range	+/- 30%

References:
[1] T. Lund, P. Sorensen, J. Eek, "Reactive Power Capability of a Wind Turbine with Doubly Fed Induction Generator", *Wind Engineering*, no. 10, pp. 379-394, 2007.
[2] 1.5 MW Series Wind Turbine, GE Energy [Online] Available: http://www.gepower.com/prod_serv/products/wind_turbines/en/15mw/index.htm

PART 4

Impact of Increased DFIG Penetration on Market Mechanisms

Uday V. Shanbhag

Aswin Kannan

Harrison M. Kim

Arizona State University

Information about this project

Uday Shanbhag
Associate Professor
Dept. of Industrial & Enterprise Systems Engineering
117 Transportation Building
104 S. Mathews Ave.
Urbana, IL 61801
Tele: (217)244-4842
Fax: (217) 2445705
Email: udaybag@illinois.edu

Power Systems Engineering Research Center

The Power Systems Engineering Research Center (PSERC) is a multi-university Center conducting research on challenges facing the electric power industry and educating the next generation of power engineers. More information about PSERC can be found at the Center's website: http://www.pserc.org.

For additional information, contact:

Power Systems Engineering Research Center
Arizona State University
577 Engineering Research Center
Tempe, Arizona 85287-5706
Phone: 480-965-1643
Fax: 480-965-0745

Notice Concerning Copyright Material

Contents

List of Tables

List of Figures

Chapter 1

Introduction

As electricity markets gravitate towards a regimes where intermittent renewables such as windpower are an integral part of a firm's generation mix, multiple questions persist regarding how markets should evolve to accommodate such assets. Crucial to answering such questions is the development of a new generation of competitive models that can contend with the uncertainty in generation capacity, allow for a two-settlement networked structure and finally accommodate risk-aversion in the specification of agent preferences. Game-theoretic models have proved useful in analyzing a range of questions in the design and operation of markets. Early efforts employed Nash-Cournot models for capturing competitive interactions within a single-settlement electricity market [15, 16, 26]. Prompted by the knowledge that most markets incorporate a sequence of market clearings, single-settlement models have given way to multi-settlement frameworks for which the standard Nash-Cournot models prove inadequate. Inspired by work on spot-forward markets by Allaz [1], a host of formulations have been suggested for capturing two-settlement games and lead to multi-leader multi-follower games [4, 17, 34]. This class of games is characterized by generators competing in a Nash fashion in the forward market [34, 31, 18, 17] while being Stackelberg leaders with respect to the spot-market. The resulting equilibrium problem belongs to a class of equilibrium problem with equilibrium constraints (EPEC), a challenging class of equilibrium problems in which each agent is faced with solving a mathematical program with equilibrium constraints (MPECs). In a dominant class of the models, an arbitrage-free assumption remains central, with the work by Oren and his coauthors providing singular exceptions [21, 33]. In fact, Kamat and Oren in [21] present a model that permits arbitrage, and prescribe an independent price function in the forward market. Risk-aversion was considered in a single-agent setting in [7, 25, 24] but has been largely overlooked in the game-theoretic setting.

While extant research has laid the foundation for drawing insights pertaining to agent behavior in power markets, these models and the consequent solution concepts are inadequate from a variety of fronts, of which three are of interest in this paper: (1) First, much of the past efforts have presented a largely deterministic viewpoint, ignoring the uncertainty in fuel costs and demand. As markets, and the underlying grid infrastructure, evolve rapidly towards the envisaged smart grid, the accommodation of heterogeneous generation resources, such as windpower, becomes paramount. However, the variability inherent in such forms of generation implies that participants, particularly those with wind resources, are faced with significant risk. Unfortunately, existing game-theoretic models are largely aggregated around risk-neutral agents; (2) Second, the prescription of forward prices in two-period models is of relevance. A majority of past work in the realm of two-settlement

4

electricity market models has assumed an arbitrage-free setting where the forward prices are specified as expected spot prices. As first examined by Kamat and Oren [21] (termed in their work as the "market-clearing" model), an alternate model is obtained by assuming an price function dependent on forward positions, leading to possible deviations between forward and expected spot prices. While is simpler settings, quantitative statements regarding the resulting risk-premium can be made, in more general settings, the relationship has not been investigated closely; (3) Third, much remains unclear regarding the class of multi-leader multi-follower games. For instance, existence results are available under fairly strong assumptions, if at all [31, 18]. Further, even when equilibria are known to exist, there are no known convergent algorithms for computing these equilibria. Both shortcomings become even more pronounced when one considers the addition of risk and uncertainty.

The present work is principally motivated by analyzing a new class of game-theoretic models that can overcome the shortcomings specified in (1) and (2). Addressing (1) has gained increasing relevance as generation firms, particularly when characterized by a significant ownership in wind-based assets, face tremendous risk arising from uncertain generation resources. The success of integrating renewables into the next generation of electricity markets, as envisaged within the smart grid environment, relies on continued participation of generation firms with a high degree of windpower. Furthermore, it remains unclear as to whether higher participation comes at the cost of reliability. We propose a framework of stochastic games in which agents have heterogeneous risk preferences and agents employ a conditional value-at-risk metric to capture the risk associated with shortfall in capacity. Alternate models of forward pricing [21] point to the non-storability of electricity as being one reason for why the no-arbitrage condition may not hold. In accordance with Kamat and Oren [21], we use a Cournot-based price function in the forward market.

The equilibrium problem requires addressing (a) the inherently dynamic nature of competition, arising from the two-settlement structure, (b) the underlying uncertainty in the availability of windpower and other assets and finally (c) the possible risk-averseness of certain participants in their bidding decisions. To cope with the complexity of the setting, we consider a class of risk-averse stochastic Nash-Cournot models, in which agents make simultaneous bids in the forward market followed by *recourse* bids in the deviation markets that emerge in the real-time. The resulting class of games fall can be viewed as noncooperative generalization of S-adapted open-loop problems studied by Haurie and his coauthors [13, 14] for modeling multistage decision-making problems. The proposed adaptive game-theoretic framework incorporates the following:

Recourse-based structure: Competing in the forward or day-ahead market requires addressing the uncertainty in resource availability and costs. In an extension of stochastic programming [3], we employ an adaptive framework that incorprates the ability of agents to take recourse in the real-time market, contingent on the realization of uncertainty. Specifically, we allow agents to bid in the first-period and make simultanenous deviation bids for each possibility in the second-period.

Risk preferences : Past work on addressing uncertainty in competitive settings has ignored risk-averseness. Here, we use a conditional value-at-risk (CVaR) measure [27] to capture the risk associated with bidding with assets whose availability is uncertain in the real-time market.

Our framework can be viewed as a continuous-strategy Nash game in which agents make simultaneous bids in the forward and spot-market. Yet, such problems are well beyond the reach of existing theory for analyzing existence and uniqueness. This is primarily because of two reasons. First, the strategy sets across agents are coupled when one works within a regime of a

networked electricity market. Second, given that risk-averse agents employ CVaR measures, the resulting objectives are nonsmooth, making the analysis of equilibria more challenging. A majority of approaches for addressing continuous strategy games focus on the analysis of the corresponding equilibrium conditions, given compactly as a variational inequality [10]. Given that the constraints are coupled, a naive application of such ideas leads to a quasi-variational inequality, an object whose properties are less easy to provide. Further, the presence of a nonsmooth risk measure suggests that the resulting equilibrium conditions are given by a multivalued VI, again a problem that has tractable properties. Finally, the solution of such problems in practical settings is severely limited the massive complexity arising from the size of the network, the cardinality of the sample-space corresponding to the uncertainty and finally a possibly large number of agents. Motivated by all of these challenges, we provide a brief summary of our main contributions:

1. *Risk-based generalized Nash games:* We model a two-settlement risk-based Nash game as a generalized Nash game. By a suitable reformulation, we relate this game to a shared-constrained stochastic Nash game. Such an observation allows one to leverage the analytical tools for varitional inequalities for deriving properties of the generalized Nash games in both no-arbitrage as well as market-clearing settings.

2. *Analysis of equilibria:* The generalized Nash games discussed in [1.] generally lead to single-valued stochastic variational inequalities. The singular exception to this case is when the agents employ risk-measures that are parameterized by the decisions of their competitors (called the shared risk model). Here, the game leads to a multivalued stochastic variational inequality. In the absence of a compactness assumption on strategy sets, a possible avenue towards deriving existence statements is through an analysis of the coercivity properties of the variational inequality. Further, we show that the resulting variational inequalities in all but the shared risk model lead to monotone problems, implying that the $\epsilon-$Nash games admit unique equilibria.

3. *Convergent scalable schemes:* We present a hybrid projection-based cutting-plane scheme for addressing a regularized variant of the given class of problems. The overall convergence of the scheme is proved in both a dual as well as a primal-dual setting and error bounds are developed to contend with practical implementations. In particular, we analyze the error associated with premature termination of the dual scheme as well as with bounded complexity dual-based implementations where the underlying primal scheme is run for a finite number of steps. The uncertainty in the problem leads to massive projection problems which are solved via a cutting-plane method. Numerical results suggest that the schemes scale well with problem size.

4. *Insights for market design:* A numerical implementation on a 53-node model of Belgian network provided numerous insights for market design. For instance, we observe that higher levels of risk-aversion lead to lower participation in the forward markets while higher level of wind penetration leads to greater participation in the forward markets.

This report is organized into eight chapters and an appendix. Chapter 3 provides an overview of market design initiatives in the US insofar as they relate to accommodating windpower. Chapter 4 introduces the stochastic two-settlement electricity market model and derives the related stochastic variational inequalities. In chapter 5, we analyze the existence and uniqueness properties of the

equilibria arising in such games. A novel hybrid distributed scheme that combines projection methods with cutting-plane algorithms is presented in chapter 6 for obtaining equilibria in such games. In chapter 7, we obtain insights through a two-settlement networked electricity market model via a risk-based stochastic generalized Nash game. We conclude in chapter 8.

Chapter 2

Market design in the United States

An electricity market is a system for purchasing and selling electricity and consists of generating firms, the consumers and the independent system operator (ISO). The ISO is responsible for power allocation and dispatch. Most markets in the United States comprise of multiple settlements, where each settlement represents a clearing in a specific market (for instance, the day-ahead or real-time market). The forward market is generally a financial market and forward contracts are paid at the forward prices. The real-time market, expectedly, is physical in nature and real time imbalances are settled at the real time prices. Firms may also be penalized for deviating from their forward bids.

The installed wind power capacity in the U.S was approximately 1911 MW in 1990. It had grown to 4.4 GW by 2002 and subsequently grown to 6.7 GW by 2004. The energy produced from wind turbine generators was approximately 11.5 TWh in 2003. Wind power growth has been observed in two phases. The first phase was during the late 70's where rules such as long term contracts with private wind power producers were imposed. There were also federal and state tax incentives, which provided further incentives for wind power generation. The second phase was observed during the late 90's where federal and state tax incentives resulted in increases in penetration levels of renewable energy resources, of which wind constituted a major portion. The penalties laid for deviation have generally been low when compared to other forms of energy. In 2004, FERC (Federal Energy Regulatory Commission) proposed changes with respect to the market structure and rules. In particular, one such suggestion pertained to having reduced penalties for deviation to encourage participation [20]. Next, we provide an overview of the various parameters that have relevance as wind power penetration increases.

2.1 Market design Parameters

Bidding with windpower on the market rules and penalties. Higher the penalties for negative deviation, lesser the bidding in the forward or day ahead market. The various restrictions and constraints imposed on the market players are referred to as rules. We discuss the market design parameters in several markets in the United States in the forthcoming subsection [8, 20] where we discuss key design parameters pertaining to imbalance settlements, ancillary services, forecasting and scheduling.

2.1.1   Scheduling and imbalance settlements

Generally most markets fall within the realm of multi-settlement markets. In such settings, firms with wind-based assets are faced with bidding in the forward market while facing uncertainty in available capacity in the real-time market. For instance, the PJM system is a typical two settlement market, where firms are settled for their imbalances at the real time prices. The ISO-NE and NYISO systems are also two settlement markets, but it is not mandatory for wind to take part in the day ahead market and wind can be directly bid into the real-time market. The MISO system is strictly a two settlement market and if a resource is not designated as a capacity resource, it is not obliged to take part in the forward market. The CAISO, is also strictly a two settlement market. Shortfall may be greatly reduced with the presence of a forward market. Most notably [34] states the necessity of a two settlement market in bringing down the expected spot prices.

Imbalance refers to the deviation from the forward bids. In the instance of a positive deviation, the firms are paid for their deviations, at real time prices. When deviations are negative, the firms pay for deviations at the real time prices. Imbalances are generally settled at the respective spot prices in all the systems through the United States.

2.1.2   Deviation penalties

Other than imbalance settlements, the firms are penalized for deviations at a cost that is specific to the ISOs. Some system operators (such as PJM) do not impose penalties for deviation, particularly for windpower. New York ISO (NYISO), however, does not penalize wind generators, for deviations less than 1000 MW while other generators are charged for deviations. ISO-NE does not penalize wind-based generators for deviations while Midwest ISO (MISO) as well as the California ISO (CAISO) impose a penalty on deviation for any capacity resource. If wind generators are not designated as capacity resources, they are not imposed any penalties. The CAISO has a program called the participating intermittent resource program (PIRP) and firms taking part in this program generally obtain forecasts, that aid in schedules. Furthermore, PIRP-designated firms are not penalized for any deviations.

2.1.3   Forecasting

Forecasting techniques aid windpower generators in getting better estimates of availability and if the producers adhere to these estimates, the reliability of the market can be seen to improve. PJM and ISO- New England (ISO-NE) currently do not provide forecasts while NYISO uses persistence forecasting. Currently, most ISOs do not charge for forecasts, excepting CASIO that does indeed levy a fee. In the current setting, PIRP-designated firms taking part in the PIRP program, get hourly forecasts, and are not penalized for any deviations. Essentially this increases the participation of wind generators. If firms bid close to the forecasted power, lesser would be the expected shortfall. If, in contrast, they bid higher, the expected shortfall may be higher.

2.2   Insights for market design

From the earlier subsections, ISOs tend to use deviation penalties as a means of reducing possible shortfall in the real-time market. In addition, some ISOs provide forecasts at a fee and may subsequently relieve participants with intermittent resources from any deviation penalties. Deviation

penalties vary in their structure immensely. Some ISOs charge a penalty beyond a threshold while others have a smooth convex penalty applied. In all cases, the deviation costs are collected after the real-time market clears, providing no insights regarding the risk exposure prior to the real-time settlement. While deviation cost provides a measure of reliability, the measure is available primarily in an *ex-post* sense. We propose an alternate measure that is available prior to the real-time market clears; namely an *ex-ante* measure. Such a measure has significant utility since it provides the operator with a reliability metric, particularly from the standpoint of capacity shortfall. Yet, the well-posedness of the game and the resulting computation of equilibria is still open. We take the first step in presenting a two-settlement model and providing both a theoretical foundation as well as the computational framework for addressing it.

Chapter 3

A two-settlement market model

Consider a market comprising of g firms and an independent system operator competing over an electricity network. Let $\mathcal{N}$ denote the set of nodes of this network. Further, a firm may own generation at a set of multiple nodes, denoted by $\mathcal{N}_j$, for $j = 1, \ldots, g$. Multiple settlement markets are constructed around a sequence of clearings, each of which determines a price. Specifically, we focus primarily on a two-settlement market in which the first settlement specifies the forward price while the second is a consequence of physical transactions and determines the real-time price. We denote by x_{ij} the forward position at node i corresponding to firm j while the corresponding physical generation in scenario ω is denoted by y_{ij}^ω. Further, the nodal forward and real-time prices (in scenario ω) are denoted by p_i^f and p_i^ω, respectively. The independent system operator manages the injections and outflows at all the nodes, where the inflow at the ith node under scenario ω is denoted by r_i^ω where $i \in \mathcal{N}$. A positive value of r_i^ω marks an inflow and a negative value of the same marks an outflow. In effect, the generators and the ISO compete over a set of shared resources.

Our first model (section 4.1) captures a setting where agents compete within a risk-neutral setting (nodal forward price is equal to expected spot price) and are faced by deviation costs when their real-time generation levels differ from their forward bids. Such models may require modification in several ways. We consider two key changes in section 4.2. The first pertains to the cost of deviations. We consider a risk-based metric that modifies generation decisions. This risk measure, weighed by the risk-aversenenss levels, provides an ex-ante metric of risk exposure, in contrast with an ex-post cost. A second modification is introduced in the nature of forward price specification for which we prescribe a market-clearing model, as first suggested by Kamat and Oren [21]. The games in sections 4.1 and 4.2 lead to generalized Nash games, an extension of Nash games in which the strategy sets display an interaction. In section 4.3, we show that the generalized Nash game is equivalent to a Nash game with shared constraints.

3.1 Risk neutral deviation cost model

Our first model assumes that forward prices are specified by expected spot prices and departures from forward positions are discouraged through convex penalization costs. Given positive scalars (a_i^ω, b_i^ω), we define the nodal spot prices at scenario ω as an affine function of nodal consumption at that node which is given by the total generation by all firms at node i modified by the ISO's

injection, denoted by r_i^ω.

$$p_i^\omega(y^\omega, r_i^\omega) \triangleq a_i^\omega - b_i^\omega \left(\sum_{j \in \mathcal{J}} y_{ij}^\omega + r_i^\omega \right), \quad \forall i \in \mathcal{N}. \tag{3.1}$$

The arbitrage-free model requires that the nodal forward price is given by the expected nodal spot prices.

$$p_i^0 \triangleq \mathbb{E}p_i^\omega, \quad \forall i \in \mathcal{N}. \tag{3.2}$$

Furthermore, we denote the the cost of generation of firm j at node i during scenario ω by $\zeta_{ij}^\omega(y_{ij}^\omega)$ and the positive and negative deviation costs by $f_p(u_{ij}^\omega)$ and $f_n(v_{ij}^\omega)$, respectively where u_{ij}^ω and v_{ij}^ω are the positive and negative deviation levels from the forward positions x_{ij} while y_{ij}^ω, the real-time generation, is defined by

$$y_{ij}^\omega = x_{ij} + u_{ij}^\omega - v_{ij}^\omega.$$

In addition, the revenues accrued by the firms in the forward and real-time markets are given by $p_i^0 x_{ij} + \sum_{j \in \mathcal{J}} \mathbb{E}p_{ij}^\omega(y_{ij}^\omega - x_{ij})$. We begin by defining the profit of firm j and is given by the sum of forward and spot market revenues less generation and deviation costs:

$$\pi_j^a(z_j; z_{-j}) \triangleq \sum_{i \in \mathcal{N}_j} \left(p_i^0 x_{ij} + \mathbb{E}\left(p_i^\omega(y_{ij}^\omega - x_{ij}) - \zeta_{ij}^\omega(y_{ij}^\omega) - (f_p(u_{ij}^\omega) + f_n(v_{ij}^\omega)) \right) \right), \tag{3.3}$$

$$= \sum_{i \in \mathcal{N}} \underbrace{\mathbb{E}\left(p_i^\omega y_{ij}^\omega - \zeta_{ij}^\omega(y_{ij}^\omega) \right)}_{Mean\,Profit} - \underbrace{\mathbb{E}(f_p(u_{ij}^\omega) + f_n(v_{ij}^\omega))}_{Mean\,deviation\,costs}, \tag{3.4}$$

where z_j is defined as $z_j := \left(y_j, u_j, v_j, x_j \right)$ and y_j, u_j, v_j and x_j are given by

$$x_j = (x_{ij})_{i \in \mathcal{N}}, u_j = (u_{ij}^\omega)_{i \in \mathcal{N}, \omega \in \Omega}, v_j = (v_{ij}^\omega)_{i \in \mathcal{N}, \omega \in \Omega}, y_j = (y_{ij}^\omega)_{i \in \mathcal{N}, \omega \in \Omega}, \forall j \in \mathcal{J}.$$

The feasible region of the jth firm's problem is given by the point-to-set map $C_j(z_{-j})$ defined as

$$\mathcal{D}_j(z_{-j}) \triangleq \left\{ z_j : \begin{cases} y_{ij}^\omega = x_{ij} + u_{ij}^\omega - v_{ij}^\omega \\ y_{ij}^\omega \leq cap_{ij}^\omega \\ \sum_{j \in \mathcal{J}_i} y_{ij}^\omega + r_i^\omega \geq 0 \\ x_{ij}, u_{ij}^\omega, v_{ij}^\omega, y_{ij}^\omega \geq 0, \end{cases} \right\} \forall i \in \mathcal{N}, \forall \omega \in \Omega \right\}, \tag{3.5}$$

where $\mathcal{J}_i$ is the set of agents that have generation at node i. In the above set-valued mapping, the first constraint relates real-time generation to the forward positions through the deviation levels while the second constraint imposes a bound on real-time generation based on the random available capacity. The third constraint specifies that the net outflow at any node is nonnegative while the fourth set of constraints are merely the nonnegativity bounds. We are now ready to state the parameterized stochastic optimization problem faced by agent j where $j \in \mathcal{J}$:

$$\begin{array}{lll} \text{Ag}^a(z^{-j}) & \text{maximize} & \pi_j^a(z_j; z^{-j}) \\ & \text{subject to} & z_j \in \mathcal{D}_j(z^{-j}). \end{array}$$

12

The ISO maximizes expected social welfare in the spot market subject to network and flow constraints. By our sign convention, export(import) from any node is considered to be negative(positive). The network constraints are modeled by means of a DC approximation of Kirchhoff's laws. If Q denotes the power transfer distribution factors, then the feasible set faced by the ISO is given by the point-to-set valued map $\mathcal{D}_{g+1}$:

$$\mathcal{D}_{g+1}(z^{-(g+1)}) \triangleq \left\{ z_{g+1} : \left\{ \begin{array}{l} \sum_{i \in \mathcal{N}} r_i^\omega = 0 \\ \sum_{i \in \bar{\mathcal{N}}} Q_{l,i} r_i^\omega \leq K_l^\omega \\ \sum_{i \in \mathcal{N}} Q_{l,i} r_i^\omega \geq -K_l^\omega, \\ \sum_{j \in \mathcal{J}_i} y_{ij}^\omega + r_i^\omega \geq 0, \end{array} \right\} \quad \forall i \in \mathcal{N}, \forall l \in \mathcal{L}, \forall \omega \in \Omega \right\}.$$

where $\bar{\mathcal{N}} = (\mathcal{N} \backslash SL)$. Here, SL represents a slack node. Note that the first constraint is merely the power balance requirement, while the second and third represent the transmission capacity constraints. The fourth constraint ensures that the ISO cannot export more power than generated at a particular node. The ISO also cannot export power from a load node. The social welfare is given by the expectation of the spot-market revenue less generation cost or

$$\pi_{g+1}^a(z_{g+1}; z^{-(g+1)}) \triangleq \sum_{i \in \mathcal{N}} \mathbb{E} \left(\int_0^{\sum_{j \in \mathcal{J}} y_{ij}^\omega + r_i^\omega} p(\tau) d\tau - \sum_{j \in \mathcal{J}} \zeta_{ij}^\omega(y_{ij}^\omega) \right).$$

The resulting maximization problem faced by ISO is given by

$$\boxed{\begin{array}{lll} \text{Ag}^a(z^{-(g+1)}) & \text{maximize} & \pi_{g+1}^a(z_{g+1}; z^{-(g+1)}) \\ & \text{subject to} & z_{g+1} \in \mathcal{D}_{g+1}(z^{-(g+1)}). \end{array}}$$

We now define a risk-neutral deviation cost generalized Nash game as follows:

Definition 1 (Risk neutral deviation cost Nash game) *The risk-neutral deviation cost generalized Nash game is given by a collection of $g+1$ agents and denoted by the triple $(\Pi^a, \mathbf{C}, g)$. Furthermore, an equilibrium of this game is given by a tuple $\{z_1^*, \ldots, z_{g+1}^*\}$ where z_j^* solves the problem $Ag^A(z_{-j}^*)$ for all $j = 1, \ldots, g+1$ or*

$$z_j^* \in SOL(Ag^a(z_{-j}^*)), \forall j \in \mathcal{A}.$$

3.2   Risk averse market clearing model

Several questions emerge immediately as a consequence of the model suggested in section 4.1. The first of these pertains to reliability in electricity markets in the context of firms with uncertain generation assets. Shortfall in real-time generation capacity is penalized through a deviation cost, implying that the total cost of negative deviation arising for capacity shortfalls provides an estimate of the reliability of the market. For instance, if generators make low forward bids, then the likelihood of real-time shortfall is significantly lower. Unfortunately, such a measure of reliability is available upon the settlement of the real-time market, in effect an ex-post measure. Unfortunately, deivation cost models as specified in the earlier section are risk-neutral in that firms minimize the expected cost of deviation. In this section, we consider a modified model that replaces deviation costs

with a risk measure that incorporates the losses associated with shortfall in real-time generation. Such a modification has several benefits. First, it allows firms to compete with heterogeneous risk preferences where the risk corresponds to the losses associated with capacity shortfall in the real-time market. Second, the risk measure provides an ex-ante measure of reliability of the market.

The arbitrage-free model is built on the assumption that forward prices are given by expected spot prices. In practice, forward prices are a consequence of a market clearing and need not necessarily match expected spot prices. In fact, past work has related the forward prices to expected spot prices through volatility of demand and capacity. In this section, we consider a market clearing model for prescribing forward prices that is reflective of the true functionings of the market.

3.2.1 Shortfall risk measures

Current market models discourage deviations from forward positions through the imposition of convex costs on deviations. As a consequence, the firms minimize their expected revenue less their expected cost of generation and deviation. Specifically, if $X(\omega)$ represents the random loss under realization ω, then the the expected value problem is given by $\mathbb{E}X(\omega)$. However, such a model focuses on the *average* and does not consider the possibility that levels of real-time capacity may result in massive deviation costs. In effect, the expected-value approach does not allow for capturing risk-averseness.

Classical approaches to modeling risk preferences require the use of expected utility theory leading to agents maximizing their expected utility. In particular if $\mathbf{u} : \mathbb{R} \to \mathbb{R}$ is a concave utility function, then the ith firm would maximize $\mathbb{E}(\mathbf{u}(X(\omega)))$. Unfortunately, eliciting the utility functions of the agents remains rather challenging and often arbitrarily selected utility functions lead to solutions that are difficult to interpret. More recently, an approach for addressing risk aversion is through the use of risk measures. A classically studied risk functional is the variance, namely $\sigma^2(X(\omega))$, which has the obvious shortcoming that it treats upper deviations identical to lower deviations. This may be rectified by the use of upper and lower semideviations, of which the former is defined as

$$\sigma^+(X(\omega)) = (\mathbb{E}(X(\omega) - \bar{X})_+^2)^{1/2},$$

where $\bar{X} = \mathbb{E}X(\omega)$. Recently, the value-at-risk (VaR) measure has gained popularity in the financial industry is defined as

$$VaR_\alpha(X(\omega)) \triangleq H_X^{-1}(1 - \beta),$$

where $H_X(x) = \mathbb{P}(X(\omega) \leq x)$. Unfortunately, the VaR measure does not satisfy the properties of coherence. Additionally, the losses beyond the VaR$_\beta(X)$ can be arbitrarily large. The conditional value-at-risk or CvaR measure considers the expectation of the losses beyond the VaR level and is defined as

$$\text{CVaR}_\tau(X) \triangleq \min_{m \in \mathbb{R}} \left\{ m + \frac{1}{1 - \tau} \mathbb{E}(X - m)^+ \right\}. \tag{3.6}$$

Here, we consider two forms of loss functions $X(\omega)$ that are intended to replace the expected deviation costs from forward positions with measures that capture the *risk of shortfall*. These measures have a particular relevance when generation firms have significant variable capacity arising from wind. In determining the risk of shortfall, we consider two types of measures:

Non-shared measures: Such a risk measure would capture the risk arising from low real-time generation capacity. The resulting risk measure is given by

$$\text{CVaR}(cap_j; x_j) = \sum_{i \in \mathcal{N}} \left\{ m_{ij} + \frac{1}{1 - \tau} \mathbb{E}(\varrho_{ij}(cap_{ij}^\omega; x_{ij}) - m_{ij})^+ \right\},$$

. The function $\rho_{ij}(cap_{ij}^\omega, x_{ij})$ can be defined as any convex loss function which is greater than zero. In section 5 we prove the results for the functions of this type. In general one such loss function can take the form as follows:

$$\varrho_{ij}(cap_{ij}(\omega); x_{ij}) \triangleq \phi_j(x_{ij})(x_{ij} - cap_{ij}(\omega)), \tag{3.7}$$

where $\phi_j(.)$ is an increasing convex function. The implicit assumption in constructing such a measure is that the risk is a consequence of one's own decisions and is not affected by competitive decisions.

Shared risk measures: If the shortfall risk is at a nodal level then competitive decisions play a role in determining the risk exposure of a generating firm. If $\lambda_i(\omega)$ represents the random generation levels at node j in the spot market. We consider a loss function in which the expected shortfall in the spot market is given by $\sum_{j \in \mathcal{J}} x_{ij} - cap_i^\omega$. Each firm plays a role in this shortfall by means of its forward bid x_{ij} and the corresponding agent specific the loss function is given by

$$\varrho_{ij}(cap_i^\omega; x_i) \triangleq \varphi(x_{ij}) e^{\psi\left(\sum_{j \in \mathcal{J}_i} x_{ij} - cap_i^\omega\right)}. \tag{3.8}$$

3.2.2 Market clearing model for forward prices

In contrast with more standard arbitrage-free models in which the forward prices are given by expected spot prices, we assume a setting whether forward prices are determined via a market clearing, similar to the way in which spot prices are specified. Specifically, p_i^0 the forward price at node i is given by

$$p_i^0 = a_i^0 - b_i^0 \left(\sum_{j \in \mathcal{J}_i} x_{ij} \right), \tag{3.9}$$

where a_i^0 and b_i^0 are positive scalars for all $i \in \mathcal{N}$. The resulting profit function of firm $j = 1, \ldots, g$ is given by

$$\pi_j^b(z_j; z_{-j}) = \sum_{i \in \mathcal{N}} \underbrace{p_i^0 x_{ij} + \mathbb{E}\left(p_i^\omega(y_{ij}^\omega - x_{ij}) - \zeta_{ij}^\omega(y_{ij}^\omega)\right)}_{Mean\, profit} - \underbrace{\text{CVaR}_\tau(\varrho(\lambda_{ij}^\omega; x_{ij}))}_{Shortfall\, risk}. \tag{3.10}$$

Note that the profit function of the ISO remains unchanged implying that $\pi_{g+1}^b = \pi_{g+1}^a$.

Definition 2 (Generalized Nash game with nonshared and shared risk measures) *The generalized Nash game with nonshared risk $\mathcal{G}^b$ is denoted by the triple $(\Pi^b, \mathcal{D}, g)$ while the generalized Nash game with shared risk $\mathcal{G}^c$ is denoted by $(\Pi^c, \mathcal{D}, g)$. Furthermore, an equilibrium of $\mathcal{G}^b$ is given by a tuple $\{z_1^*, \ldots, z_{g+1}^*\}$ where z_j^* solves the problem $Ag^b(z_{-j}^*)$ for all $j = 1, \ldots, g + 1$ or*

$$z_j^* \in SOL(Ag^b(z_{-j}^*)), \forall j = 1, \ldots, g + 1.$$

3.3 Shared-constraint generalized Nash game

The classical Nash solution concept does not allow for interaction in the strategy sets. In our setting, we observe that the strategy sets are indeed coupled, leading to a generalized Nash game. In general, under suitable convexity and differentiability assumptions, the resulting equilibrium conditions of the shared-constraint Nash game are given by a quasi-variational inequality, an extension of the variational inequality [28, 12]. Recent work by Facchinei et al. [9] has shown that if the strategy sets are coupled through a shared constraint, an equilibrium of the game is given by the solution of an appropriately defined scalar variational inequality. In particular, if the firms and the ISO are coupled through

$$\sum_{j \in \mathcal{J}_i} y_{ij}^\omega + r_i^\omega \geq 0, \forall i \in \mathcal{N}, \forall \omega \in \Omega.$$

The analysis of generalized Nash equilibrium problems with a set of convex shared constraints has been studied by [9]. Consider a mapping $\mathbf{F}$ and a set $\mathbf{X}$ given by [1]

$$\mathbf{F}(z) \triangleq \left(\nabla_{z_j} \pi_j(z_j; z_{-j}) \right)_{j=1}^{g+1}, \mathbf{X} = \left(\prod_{j=1}^N \mathbf{X}_j \right) \cap \mathcal{D},$$

$$\mathbf{X}_j = \left\{ z_j : \begin{cases} y_{ij}^\omega = x_{ij} + u_{ij}^\omega - v_{ij}^\omega \\ y_{ij}^\omega \leq cap_{ij}^\omega \\ x_{ij}, u_{ij}^\omega, v_{ij}^\omega, y_{ij}^\omega \geq 0 \end{cases} \right\} \quad \forall i \in \mathcal{N}, \forall \omega \in \Omega \right\}$$

$$\mathbf{X}_{g+1} = \left\{ z_{g+1} : \begin{cases} \sum_{i \in \mathcal{N}} r_i^\omega = 0 \\ \sum_{i \in \bar{\mathcal{N}}} Q_{l,i} r_i^\omega \leq K_l^\omega \\ \sum_{i \in \bar{\mathcal{N}}} Q_{l,i} r_i^\omega \geq -K_l^\omega \end{cases} \right\} \quad \forall i \in \mathcal{N}, \forall l \in \mathcal{L}, \forall \omega \in \Omega \right\},$$

$$\mathcal{D} = \left\{ z : \sum_{j \in \mathcal{J}_i} y_{ij}^\omega + r_i^\omega \geq 0, \forall i \in \mathcal{N}, \forall \omega \in \Omega \right\}.$$

Then the key result of their work is that if VI$(\mathbf{X}, \mathbf{F})$ has a solution, then the original shared-constraint admits an equilibrium. The equilibrium corresponding to a solution of this variational problem is referred to as the normalized equilibrium [28] or the variational equilibrium [9] (VE). The formal result is given by the following.

Theorem 3 *Suppose the objective function $\pi_j(z_j; z_{-j})$ is convex in z_j for all z_{-j} for all $j \in \mathcal{J}$, π_j is differentiable in z and $\mathcal{D}$, $\mathbf{X}_1, \ldots, X_{g+1}$ are closed and convex sets. Then every solution to VI$(\mathbf{X}, \mathbf{F})$ is a solution to the shared-constraint game.*

In section 5, under suitable assumptions, we analyze whether a VE exists and can a uniqueness guarantee be provided.

---

[1] Note: $y_{ij}^\omega, u_{ij}^\omega, v_{ij}^\omega, s_{ij}^\omega, m_{ij}, x_{ij} \equiv 0, \forall i \in \mathcal{G}^c, \forall \omega \in \Omega, \forall j \in \mathcal{J}$. Also, the above holds $\forall i \in \mathcal{J}_i^c$.

Chapter 4

Analysis of equilibria

The analysis of the VE rests on the nature of the mapping $\mathbf{F}$ and the set $\mathbf{X}$. When $\mathbf{X}$ is closed and convex and $\mathbf{F}$ is continuous, compactness of $\mathbf{X}$ suffices for existence. Similarly, uniqueness follows if $\mathbf{F}$ is strongly monotone, which requires that there exists a $\nu > 0$ such that

$$(\mathbf{F}(x) - \mathbf{F}(y))^T (x - y) \geq \nu \|x - y\|^2, \quad \forall x, y \in \mathbf{X}.$$

Unfortunately, none of these requirements can be expected to hold in general. In particular, the compactness of $\mathbf{X}$ cannot be claimed given that forward positions are not bounded. Furthermore, the $\mathbf{F}$ mapping is not strongly monotone in practice. In fact, in risk-averse settings, $\mathbf{F}$ fails to even be single-valued. These complications motivate a deeper analysis of $\text{VI}(\mathbf{X}, \mathbf{F})$ and represent the core of this section.

In section 5.1, we focus on the risk-neutral deviation cost game and show that a unique variational equilibrium exists for such a game. While a similar existence result is shown for the risk-averse market-clearing model in section 5.2, a corresponding uniqueness result is shown for an appropriately defined ϵ-Nash equilibrium. Finally, the shared-risk extension leads to a nonsmooth Nash game whose equilibrium conditions are captured by a multivalued variational inequality. In section 5.3, we show that a solution to this variational inequality does indeed exist. The following assumptions hold for all the games of interest.

Assumption 4

(A1) *The cost of generation ζ_{ij}^ω is a convex twice-continuously differentiable function of y_{ij}^ω for all i and j and for all $\omega \in \Omega$.*

(A2) *The nodal spot-market price is defined by the affine price function (3.1) for all i and for all $\omega \in \Omega$.*

(A3) *The strategy sets $\mathbf{X}_j \subseteq \mathbb{R}^M$ are closed and convex for all $j = 1, \ldots, g + 1$.*

4.1 Risk-neutral deviation cost game

As mentioned earlier, the existence of a solution to a variational inequality is immediate when either the mapping is strongly monotone or the set is compact. However, existence of a solution may also be deduced by ensuring that a suitable coercivity requirement can be shown to hold. In particular, we have the following from [10]:

17

Theorem 5 *Let* $\mathbf{X}$ *be closed and convex and* $\mathbf{F} : \mathbf{X} \to \mathbb{R}^M$ *be a continuous mapping. If there exists a vector* $z^{ref} \in \mathbf{X}$ *such that*

$$\liminf_{z \in \mathbf{X}, \|z\| \to \infty} \mathbf{F}(z)^T (z - z^{ref}) > 0,$$

then the $VI(\mathbf{X}, \mathbf{F})$ *has a nonempty compact solution set.*

We begin our discussion by showing that for a feasible tuple of decisions, the ISO's decisions lie in a compact set.

Lemma 6 *Consider a tuple* $z_1, \ldots, z_{g+1}$ *such that* $z_j \in \mathbf{X}_j \cap \mathbf{C}$ *for all* $j \in \mathcal{J}$. *Then the import/export decisions* r_i^ω *are bounded for all* $i \in \mathcal{N}$.

Proof : Recall that from the feasibility of the tuple, we have $\sum_{i \in \mathcal{J}_i} y_{ij}^\omega + r_i^\omega \geq 0$ for all $i \in \mathcal{N}$. By the feasibility of the real-time generation, we have $y_{ij}^\omega \leq cap_{ij}^\omega$ for all $j \in \mathcal{J}_i, i \in \mathcal{N}$. This implies that, $r_i^\omega \geq -\sum_{j \in \mathcal{J}_i} cap_{ij}^\omega$ at all generation nodes, namely for all $i \in \mathcal{G}$. But

$$\sum_{i \in \mathcal{N}} r_i^\omega = 0 \text{ and } r_i^\omega \geq 0, \forall i \in \mathcal{G}^c \implies \sum_{i \in \mathcal{G}} r_i^\omega + \sum_{i \in \mathcal{G}^c} r_i^\omega = 0.$$

This implies that, $r_i^\omega + \sum_{k \in \mathcal{G}, k \neq i} r_k^\omega \leq 0, \forall i \in \mathcal{G}$. But, $r_k^\omega \geq -\sum_{j \in \mathcal{J}_k} cap_{kj}^\omega, \forall k \in \mathcal{G}$. It follows that

$$-\sum_{j \in \mathcal{J}_i} cap_{ij}^\omega \leq r_i^\omega \leq \sum_{k \in \mathcal{G}, k \neq i} \sum_{j \in \mathcal{F}} cap_{kj}^\omega, \qquad \forall i \in \mathcal{G}.$$

Since the total import at the load nodes cannot be greater than the total capacity and since no export is also possible at these nodes, it follows that $r_i^\omega \geq 0, \forall i \in \mathcal{G}^c$. It follows that

$$0 \leq r_i^\omega \leq \sum_{i \in \mathcal{G}^c} \sum_{j \in \mathcal{J}_i} cap_{ij}^\omega, \qquad \forall i \in \mathcal{G}^c.$$

The boundedness of r_i^ω for all $i \in \mathcal{N}$ can then be concluded. ∎

Using the boundedness of the r_i^ω and y_i^ω, we proceed to show that $\mathcal{G}^a$ admits an equilibrium by proving that $VI(\mathbf{X}, \mathbf{F})$ satisfies a coercivity property under the additional assumption on the deviation cost functions.

Assumption 7 *(A4) The deviation cost functions* $f_p^\omega(u_{ij}^\omega)$ *and* $f_n^\omega(v_{ij}^\omega)$ *are strictly convex, twice continuously differentiable and increasing in* u_{ij}^ω *and* v_{ij}^ω *for all* $\omega \in \Omega$

Proposition 8 (Existence of Nash equilibrium to $\mathcal{G}^a$) *Consider the game $\mathcal{G}^a$ and let assumptions (A1)–(A4) hold. Then $\mathcal{G}^a$ has a nonempty compact set of equilibria.*

Proof : Based on Theorem 3, it suffices to prove the existence of a solution to $VI(\mathbf{X}, \mathbf{F})$. By Lemma 5, this variational inequality is solvable if there exists a $z^{\mathrm{ref}} \in \mathbf{X}$ such that the expression in Theorem 5 is satisfied.

First, it is observed that $\mathbf{0} \in \mathbf{X}$ and z^{ref} is chosen to be $z^{\text{ref}} \triangleq \mathbf{0}$. It suffices to show that Theorem 5 holds. By our choice of z^{ref}, the term $\mathbf{F}(z)^T(z)$ can be written as

$$
\mathbf{F}(z)^T(z) \;=\; \underbrace{\sum_{\omega \in \Omega} \sum_{i \in N} \rho^{\omega}(-a_i^{\omega} + b_i^{\omega}(\sum_{j \in e\mathcal{J}_i} y_{ij}^{\omega} + r_i^{\omega}))r_i^{\omega}}_{term\,1\,(or)\,(\mathbf{F}_r(z))^T(r)} + \underbrace{\sum_{j \in \mathcal{J}} \sum_{\omega \in \Omega} \sum_{i \in \mathcal{N}_j} \rho^{\omega}(f_p'(u_{ij}^{\omega})u_{ij}^{\omega} + f_n'(v_{ij}^{\omega})v_{ij}^{\omega})}_{term\,2\,(or)\,\sum_{j \in \mathcal{J}} \mathbf{F}_{u_j}(z)^T(u_j) + \mathbf{F}_{v_j}(z)^T(v_j)}
$$

$$
+\; \underbrace{\sum_{j \in \mathcal{J}} \sum_{\omega \in \Omega} \sum_{i \in \mathcal{N}_j} \rho^{\omega}(-a_i^{\omega} + c_{ij}^{\omega} + (b_i^{\omega} + d_{ij}^{\omega})y_{ij}^{\omega} + b_i^{\omega}(\sum_{j \in \mathcal{J}} y_{ij}^{\omega} + r_i^{\omega}))y_{ij}^{\omega}}_{term\,3\,(or)\,\sum_{j \in \mathcal{J}} \mathbf{F}_{y_j}(z)^T(y_j)}.
$$

Consider any sequence $\{z^k\} \in \mathbf{X}$ such that $\lim_{k \to \infty} \|z^k\| = \infty$. Along any such sequence, the feasibility of y^k with respect to the capacity constraint implies that y^k stays bounded. By Lemma 6, $\{r^k\}$ stays bounded as well. It follows that one of x^k, u^k or v^k tend to infinity. It suffices to consider the following two cases.

Case 1: Suppose $x^k \to \infty$. Since y^k is bounded, either v_k or both v_k and u_k are growing to infinity. This ensures that term 2 tends to $+\infty$..

Case 2: Suppose the positive deviation u^k or the negative deviation v^k tends to infinity. It follows that term 2 tends to $+\infty$. This completes the proof. ∎

It remains to show that the VE corresponding to the solution of VI$(\mathbf{X}, \mathbf{F})$ is unique. Note that this does extend to claiming that the original generalized Nash game has a unique solution.

Proposition 9 (Uniqueness of Nash equilibrium to $\mathcal{G}^a$) *Consider the game $\mathcal{G}^a$ and let assumptions (A1)–(A3) hold. Then the VI$(\mathbf{X}, \mathbf{F})$ corresponding to $\mathcal{G}^a$ has a unique solution.*

Proof : We have proved that VI$(\mathbf{X}, \mathbf{F})$ is solvable. It suffices to show that the gradient mapping $\nabla \mathbf{F}$ is strictly monotone definite implying that the variational inequality has at most one solution. Since the player objectives are nodally decomposable, $\nabla \mathbf{F}$ and $\nabla_i \mathbf{F}_i$ are given by

$$
\nabla \mathbf{F} = \begin{pmatrix} \nabla_1 \mathbf{F}_1 & \mathbf{0} & \dots & \mathbf{0} \\ \mathbf{0} & \nabla_2 \mathbf{F}_2 & \ddots & \vdots \\ \vdots & \ddots & \ddots & \mathbf{0} \\ \mathbf{0} & \dots & \mathbf{0} & \nabla_N \mathbf{F}_N \end{pmatrix} \text{ and } \nabla \mathbf{F}_i = \begin{pmatrix} A_i^1 & \dots & 0 & C_i^1 & 0 \\ \vdots & \ddots & \vdots & \vdots & \vdots \\ 0 & \dots & A_i^n & C_i^n & 0 \\ B_i^1 & \dots & B_i^n & D_i & 0 \\ 0 & \dots & \dots & 0 & E_i \end{pmatrix},
$$

where $\nabla_i \mathbf{F}_i$ is the gradient of the $\mathbf{F}_i$ with respect to the variables corresponding to node i and the submatrices of $\nabla_i \mathbf{F}_i$ are specifed as follows:

$$
A_i^{\omega} = \begin{pmatrix} \rho^{\omega}(2b_i^{\omega} + d_{i1}^{\omega}) & \dots & \rho^{\omega}b_i^{\omega} \\ \vdots & \ddots & \vdots \\ \rho^{\omega}b_i^{\omega} & \dots & \rho^{\omega}(2b_i^{\omega} + d_{ig}^{\omega}) \end{pmatrix}, \forall \omega \in \Omega, C_i^1 = \begin{pmatrix} \rho^1 b_i^1 & \dots & 0 \\ \vdots & \ddots & \vdots \\ \rho^1 b_i^1 & \dots & 0 \end{pmatrix},
$$

$$
C_i^n = \begin{pmatrix} 0 & \dots & \rho^n b_i^n \\ \vdots & \ddots & \vdots \\ 0 & \dots & \rho^n b_i^n \end{pmatrix},
$$

19

$$
E_i = \begin{pmatrix} E_i^1 & \cdots & 0 \\ \vdots & \ddots & \vdots \\ 0 & \cdots & E_i^J \end{pmatrix}, E_i^j = \begin{pmatrix} f_p''(u_{ij}^1) & 0 & \cdots & \cdots & 0 \\ 0 & f_n''(v_{ij}^1) & \ddots & & \vdots \\ \vdots & & \ddots & \ddots & \ddots & \vdots \\ \vdots & & & \ddots & f_p''(u_{ij}^n) & 0 \\ 0 & \cdots & \cdots & 0 & f_n''(v_{ij}^n) \end{pmatrix}, \forall j \in \mathcal{J}
$$

$$
B_i^1 = \begin{pmatrix} \rho^1 b_i^1 & \cdots & \rho^1 b_i^1 \\ \vdots & \ddots & \vdots \\ 0 & \cdots & 0 \end{pmatrix}, B_i^n = \begin{pmatrix} 0 & \cdots & 0 \\ \vdots & \ddots & \vdots \\ \rho^n b_i^n & \cdots & \rho^n b_i^n \end{pmatrix}, \text{and } D_i = \begin{pmatrix} \rho^1 b_i^1 & \cdots & 0 \\ \vdots & \ddots & \vdots \\ 0 & \cdots & \rho^n b_i^n \end{pmatrix}.
$$

The gradient map $\nabla_f \mathbf{F}_i$ is defined in the order y, r, u and u respectively. From the strict convexity of the deviation penalties, the matrix H is positive definite. It suffices to show that the submatrix

$$
\bar{F}_i = \begin{pmatrix} A_i^1 & \cdots & 0 & C_i^1 \\ \vdots & \ddots & \vdots & \vdots \\ 0 & \cdots & A_i^n & C_i^n \\ B_i^1 & \cdots & B_i^n & D_i \end{pmatrix}
$$

is positive definite which follows if $\forall i \in \mathcal{G}$,

$$
\begin{aligned}
s^T \bar{F}_i s &= \sum_{\omega=1}^n \rho^\omega b_i^\omega \left(\sum_{k=1}^g s_{(\omega-1)g+k} \right)^2 + \sum_{\omega=1}^n \rho^\omega \sum_{k=1}^g (b_i^\omega + d_{ik}^\omega) s_{(\omega-1)g+k}^2 \\
&+ \sum_{\omega=1}^n \rho^\omega b_i^\omega s_{ng+\omega} \sum_{k=1}^g s_{(\omega-1)g+k} + \sum_{\omega=1}^n \rho^\omega b_i^\omega s_{ng+\omega} \sum_{k=1}^J s_{(\omega-1)g+k} + \sum_{\omega=1}^n b_i^\omega s_{ng+\omega}^2 \\
&= \sum_{\omega=1}^n \rho^\omega b_i^\omega \left(\left(\sum_{k=1}^g s_{(\omega-1)g+k} \right) + s_{ng+\omega} \right)^2 + \sum_{\omega=1}^n \rho^\omega \sum_{k=1}^g (b_i^\omega + d_{ik}^\omega) s_{(\omega-1)g+k}^2 > 0.
\end{aligned}
$$

It follows that $\nabla \mathbf{F}$ is positive definite completing the proof. But this implies that $\mathbf{F}$ is a strictly monotone mapping and at most one VE exists. The required uniqueness result can be concluded by the earlier existence result. ∎

4.2 Risk-based market-clearing Nash game

Next, we consider the game denoted by $\mathcal{G}^b$. Invoking the definition of the conditional value at risk, we can reformulate the nonsmooth firm problem as a smooth convex program by the addition of a set of convex constraints, each corresponding to one realization of uncertainty. Effectively the

problem for agent $j \in \mathcal{F}$, we have

$$
\begin{array}{lll}
Ag^{RA}(z^{-j}) & \text{maximize} & \displaystyle\sum_{i \in \mathcal{G}} \left(\pi_{ij}(x_{ij}) + \mathbb{E}(\pi_{ij}^\omega(y_{ij}^\omega; r_i^\omega)) - (m_{ij} + \sum_{\omega \in \Omega} \rho^\omega \frac{s_{ij}^\omega}{1-\tau}) \right) \\[2em]
& \text{subject to} & \left\{ \begin{array}{l} y_{ij}^\omega = x_{ij} + u_{ij}^\omega - v_{ij}^\omega \\ y_{ij}^\omega \le cap_{ij}^\omega \\ s_{ij}^\omega \ge \varrho(x_{ij}, \lambda_{ij}^\omega) - m_{ij} \\ \sum_{j \in \mathcal{J}_i} y_{ij}^\omega + r_i^\omega \ge 0 \\ x_{ij}, u_{ij}^\omega, v_{ij}^\omega, y_{ij}^\omega, s_{ij}^\omega, m_{ij} \ge 0 \end{array} \right\}, \forall i \in \mathcal{N} \quad \forall \omega \in \Omega.
\end{array}
$$

In constructing a variational inequality, the convexity of the objectives is essential. The following result shows that this is indeed so in the context of the risk-based Nash game, under a mild assumption on the specification of forward price function.

Lemma 10 *Suppose assumption (A4) holds and suppose $\mathbb{E}(b_i^\omega) \le 4b_i^0$ for all i. Then the objective functions of the firms and the ISO are concave.*

Proof : It suffices to prove the convexity of the expectation term of every agent's objective, given by $\eta_{ij}(x_{ij}, y_{ij}; y_{i,-j})$, defined as

$$
\eta_{ij}(x_{ij}, y_{ij}; x_{i,-j}, y_{i,-j}) = -(a_i^0 - b_i^0 \sum_{j \in \mathcal{J}} x_{ij}) x_{ij} - \sum_{\omega \in \Omega} \rho^\omega (a_i^\omega - b_i^\omega (\sum_{j \in \mathcal{J}} y_{ij}^\omega + r_i^\omega))(y_{ij}^\omega - x_{ij}).
$$

The gradient and Hessian of this function are given by

$$
\nabla \eta_{ij} = \begin{pmatrix} b_i^0 x_{ij} + b_i^0 \sum_{j \in \mathcal{J}} x_{ij} - a_i^0 + \sum_{\omega \in \Omega} \rho^\omega a_i^\omega - \sum_{\omega \in \Omega} \rho^\omega b_i^\omega (\sum_{j \in \mathcal{J}} y_{ij}^\omega + r_i^\omega) \\ \rho^\omega(-a_i^1 + b_i^1(y_{ij}^1 + \sum_{j \in \mathcal{J}} y_{ij}^1) + b_i^1 r_i^1 - b_i^1 x_{ij}) \\ \vdots \\ \rho^n(-a_i^n + b_i^n(y_{ij}^n + \sum_{j \in \mathcal{J}} y_{ij}^n) + b_i^n r_i^n - b_i^n x_{ij}) \end{pmatrix},
$$

and $\nabla^2 \eta_{ij} = \begin{pmatrix} 2b_i^0 & -\rho^1 b_i^1 & \cdots & -\rho^n b_i^n \\ -\rho^1 b_i^1 & 2\rho^1 b_i^1 & \cdots & 0 \\ \vdots & \vdots & \ddots & \vdots \\ -\rho^n b_i^n & 0 & \cdots & 2\rho^n b_i^n \end{pmatrix}$, respectively.

Let s be an arbitrary nonzero vector. Then,

$$
\begin{aligned}
s^T \nabla^2 \eta_{ij} s &= 2b_i^0 s_1^2 - 2s_1 \sum_{\omega=1}^n \rho^\omega b_i^\omega s_{\omega+1} + 2 \sum_{\omega=1}^n \rho^\omega b_i^\omega s_{\omega+1}^2 \\
&= (2b_i^0 - \sum_{\omega=1}^n \rho^\omega \frac{b_i^\omega}{2}) s_1^2 + \sum_{\omega=1}^n \rho^\omega \frac{b_i^\omega}{2} s_1^2 - 2s_1 \sum_{\omega=1}^n \rho^\omega b_i^\omega s_{\omega+1} + 2 \sum_{\omega=1}^n \rho^\omega b_i^\omega s_{\omega+1}^2 \\
&= (2b_i^0 - \sum_{\omega=1}^n \rho^\omega \frac{b_i^\omega}{2}) s_1^2 + \sum_{\omega=1}^n \rho^\omega b_i^\omega \left(\frac{s_1}{\sqrt{2}} - \sqrt{2} s_{\omega+1} \right)^2.
\end{aligned}
$$

By assumption $\mathbb{E}(b_i^\omega) \le 4b_i^0$ implying that $s^T \nabla^2 \eta_{ij} s > 0$ for all nonzero s and $\eta_{ij}(x_{ij}, y_{ij}; y_{i,-j})$ is a strictly convex function in x_{ij} and y_{ij} for all $x_{i,-j}$ and $y_{i,-j}$. The convexity of π_j in z_j follows from recalling that the generation costs and the conditional value at risk (CVaR) measure are known to be convex. ∎

Proposition 11 (Existence of a Nash equilibrium to $\mathcal{G}^b$) *Consider the nonshared risk-based game $\mathcal{G}^b$ and let assumptions (A1)–(A4) hold. Then $\mathcal{G}^b$ admits a nonempty compact set of equilibria.*

Proof : Based on Theorem 3, it suffices to prove the existence of a solution to VI$(\mathbf{X}, \mathbf{F})$. By Theorem 5, this variational inequality is solvable if there exists a $z^{\mathrm{ref}} \in \mathbf{X}$ such that the expression in Theorem 5 holds. If we set $(s_{ij}^\omega)^{\mathrm{ref}} \triangleq \varrho(0, \lambda_{ij}^\omega)$, and $x^{\mathrm{ref}}, y^{\mathrm{ref}}, r^{\mathrm{ref}}, m^{\mathrm{ref}} \triangleq 0$, then $z^{\mathrm{ref}} \in \mathbf{X}$. By our choice of z^{ref}, the term $\mathbf{F}(z)^T(z)$ can be written as:

$$
\begin{aligned}
\mathbf{F}(z)^T(z) = & \underbrace{\sum_{\omega\in\Omega}\sum_{i\in N}\rho^\omega(-a_i^\omega + b_i^\omega(\sum_{j\in\mathcal{J}}y_{ij}^\omega + r_i^\omega))r_i^\omega}_{(\mathbf{F}_r(z))^T(r)} + \sum_{j\in\mathcal{J}}\kappa_j\underbrace{\sum_{i\in\mathcal{N}_j}\sum_{\omega\in\Omega}\rho^\omega(\frac{s_{ij}^\omega - (s_{ij}^\omega)^{ref}}{1-\tau} + m_{ij})}_{(\mathbf{F}_{s_j}(z))^T(s_j) + (\mathbf{F}_{m_j}(z))^T(m_j)} . \\
& + \underbrace{\sum_{j\in\mathcal{J}}\sum_{\omega\in\Omega}\sum_{i\in\mathcal{N}_j}\rho^\omega(-a_i^\omega + c_{ij}^\omega + (b_i^\omega + d_{ij}^\omega)y_{ij}^\omega + b_i^\omega(\sum_{j\in\mathcal{J}}y_{ij}^\omega + r_i^\omega) - b_i^\omega x_{ij})y_{ij}^\omega}_{\mathbf{F}_{y_j}(z)^T(y_j)} \\
& + \underbrace{\sum_{j\in\mathcal{J}}\sum_{i\in\mathcal{N}_j}b_i^0 x_{ij} + b_i^0\sum_{j\in\mathcal{J}}x_{ij} - a_i^0 + \sum_{\omega\in\Omega}\rho^\omega a_i^\omega - \sum_{\omega\in\Omega}\rho^\omega b_i^\omega(\sum_{j\in\mathcal{J}}y_{ij}^\omega + r_i^\omega)x_{ij}}_{\mathbf{F}_{x_j}(z)^T(x_j)} .
\end{aligned}
$$

The term $\mathbf{F}(z)^T z$ may be rewritten as

$$
\begin{aligned}
\mathbf{F}(z)^T(z) = & \underbrace{\sum_{j\in\mathcal{J}}\sum_{\omega\in\Omega}\sum_{i\in\mathcal{N}_j}\rho^\omega(-a_i^\omega + c_{ij}^\omega + (b_i^\omega + 2d_{ij}^\omega)y_{ij}^\omega + b_i^\omega(\sum_{j\in\mathcal{J}}y_{ij}^\omega + r_i^\omega))y_{ij}^\omega}_{term\,1} \\
& + \underbrace{\sum_{j\in\mathcal{J}}(\sum_{i\in\mathcal{N}_j}b_i^0 x_{ij} + b_i^0\sum_{j\in\mathcal{J}}x_{ij} - a_i^0 + \sum_{\omega\in\Omega}\rho^\omega a_i^\omega - \sum_{\omega\in\Omega}\rho^\omega b_i^\omega(\sum_{j\in\mathcal{J}}2y_{ij}^\omega + r_i^\omega))x_{ij}}_{term\,2} \\
& + \underbrace{\sum_{\omega\in\Omega}\sum_{i\in N}\rho^\omega(-a_i^\omega + b_i^\omega(\sum_{j\in\mathcal{J}}y_{ij}^\omega + r_i^\omega))r_i^\omega}_{term\,3} \\
& + \underbrace{\sum_{j\in\mathcal{J}}\kappa_j\sum_{i\in\mathcal{N}_j}\sum_{\omega\in\Omega}\rho^\omega(\frac{s_{ij}^\omega - (s_{ij}^\omega)^{\mathrm{ref}}}{1-\tau} + m_{ij})}_{term\,4} . \quad\quad (4.1)
\end{aligned}
$$

From Lemma 6, we may conclude that terms 1 and 2 are bounded for any sequence, $\{z_k\}$, such that $\|z_k\| \to \infty$. It follows that one of the sequences $\{\|x_k\|\}, \{\|s_k\|\}$ and $\{|m_k|\}$ are tending to $+\infty$.[1]

Case 1: Suppose the forward generation bid x^k tends to infinity implying that term 2 tends to $+\infty$ at a quadratic rate.

---

[1]In this model we do not consider deviation penalties and terms u and v are automatically dropped.

Case 2: Suppose either (or both) s^k or $|m^k|$ tend to $+\infty$. $s^k \in \mathbf{X}$, $m^k \in \mathbf{X}$, $s^k \geq 0$ and $s^k + m^k$ is bounded from below. If, m^k tends to $-\infty$, then s^k tends to $+\infty$. Hence, term 4 grows to $+\infty$. If m^k or s^k tend to $+\infty$, then term 4 tends to $+\infty$. [2]

Case 3: Suppose x^k tends to $+\infty$ and any combination of s^k, and $|m^k|$ tends to $+\infty$. If m^k alone tends to $-\infty$, then term 4 tends to $-\infty$ and term 2 tends to $+\infty$ at a quadratic rate. Consequently, the entire sum tends to $+\infty$. If s^k tends to $+\infty$, m^k reduces to $-\infty$ and x^k tends to $+\infty$ then Cases 1 and 3 can be used in conjunction. The other possibilities lead to immediate results of the limit tending to $+\infty$.

Consider any sequence $\{z^k\} \in \mathbf{X}$ such that $\lim_{k \to \infty} \|z^k\| = \infty$. Since none of the terms converge to $-\infty$ and at least one of the terms converge to ∞, it follows that

$$\liminf_{z \in \mathbf{X}, \|z\| \longrightarrow \infty} \mathbf{F}(z)^T(z) = \infty.$$

This completes the proof. ■

A uniqueness result rests on being able to show that the mapping is strictly monotone. However, in the current setting, the mapping arising from the nonshared risk-based game can only be shown to be monotone, as the next result shows.

Proposition 12 (Uniqueness of $\epsilon-$ Nash game $\mathcal{G}^b$) *Consider the nonshared risk-based game $\mathcal{G}^b$ and let assumptions (A1)–(A4) hold. Then the resulting mapping $\mathbf{F}$ is monotone over $\mathbf{X}$.*

Proof : To show that $\mathbf{F}$ is monotone, it suffices to show that the gradient mapping $\nabla \mathbf{F}$ is positive semidefinite. The gradient mapping may be defined as,

$$\nabla \mathbf{F} = \begin{pmatrix} \nabla_1 \mathbf{F}_1 & \mathbf{0} & \dots & \mathbf{0} \\ \mathbf{0} & \nabla_2 \mathbf{F}_2 & \ddots & \vdots \\ \vdots & \ddots & \ddots & \mathbf{0} \\ \mathbf{0} & \dots & \mathbf{0} & \nabla_N \mathbf{F}_N \end{pmatrix},$$

where $\nabla_i F_i$ represents the gradient mapping with respect to the nodal variables corresponding to node i. The matrix $\nabla F_i, \forall i \in \mathcal{G}$ is given by

$$\nabla \mathbf{F}_i = \begin{pmatrix} P_i^0 & P_i^1 & \dots & P_i^n & H_i & 0 \\ R_i^1 & S_i^1 & \dots & 0 & F_i^1 & 0 \\ \vdots & \vdots & \ddots & \vdots & \vdots & \vdots \\ R_i^n & 0 & \dots & S_i^n & F_i^n & 0 \\ 0 & T_i^1 & \dots & T_i^n & G_i & 0 \\ 0 & 0 & \dots & \dots & 0 & V_i \end{pmatrix}, \text{ where}$$

$$P_i^\omega = \begin{pmatrix} -\rho^\omega b_i^\omega & \dots & -\rho^\omega b_i^\omega \\ \vdots & \ddots & \vdots \\ -\rho^\omega b_i^\omega & \dots & -\rho^\omega b_i^\omega \end{pmatrix}, R_i^\omega = \begin{pmatrix} -\rho^\omega b_i^\omega & \dots & 0 \\ \vdots & \ddots & \vdots \\ 0 & \dots & -\rho^\omega b_i^\omega \end{pmatrix},$$

$$S_i^\omega = \begin{pmatrix} \rho^\omega (2b_i^\omega + d_{i1}^\omega) & \dots & \rho^\omega b_i^\omega \\ \vdots & \ddots & \vdots \\ \rho^\omega b_i^\omega & \dots & \rho^\omega (2b_i^\omega + d_{ig}^\omega) \end{pmatrix}, \forall \omega \in \Omega$$

---

[2] Here s^{ref} is finite because λ is finite and $\varrho(0, \lambda_{ij}^\omega)$ is also finite.

$$
P_i^0 = \begin{pmatrix} 2b_i^0 & \cdots & b_i^0 \\ \vdots & \ddots & \vdots \\ b_i^0 & \cdots & 2b_i^0 \end{pmatrix}, H_i = \begin{pmatrix} -\rho^1 b_i^1 & \cdots & -\rho^n b_i^n \\ \vdots & \ddots & \vdots \\ -\rho^1 b_i^1 & \cdots & -\rho^n b_i^n \end{pmatrix},
$$

$$
G_i = \begin{pmatrix} \rho^1 b_i^1 & \cdots & 0 \\ \vdots & \ddots & \vdots \\ 0 & \cdots & \rho^n b_i^n \end{pmatrix}, V_i = \begin{pmatrix} 0 & \cdots & 0 \\ \vdots & \ddots & \vdots \\ 0 & \cdots & 0 \end{pmatrix}.
$$

$$
F_i^1 = \begin{pmatrix} \rho^1 b_i^1 & \cdots & 0 \\ \vdots & \ddots & \vdots \\ \rho^1 b_i^1 & \cdots & 0 \end{pmatrix}, F_i^n = \begin{pmatrix} 0 & \cdots & \rho^n b_i^n \\ \vdots & \ddots & \vdots \\ 0 & \cdots & \rho^n b_i^n \end{pmatrix},
$$

$$
T_i^1 = \begin{pmatrix} \rho^1 b_i^1 & \cdots & \rho^1 b_i^1 \\ \vdots & \ddots & \vdots \\ 0 & \cdots & 0 \end{pmatrix}, T_i^n = \begin{pmatrix} 0 & \cdots & 0 \\ \vdots & \ddots & \vdots \\ \rho^n b_i^n & \cdots & \rho^n b_i^n \end{pmatrix}.
$$

The mapping is represented in the order x_i, y_i, r_i, s_i and m_i. M_i refers to the zero matrix representing the second order derivatives with respect to s and m. Since, the matrix M_i is a zero matrix, it suffices to show that the mapping with the last row and column with respect to M_i being removed is positive semi-definite. Let $\hat{\mathbf{F}}_i$ represent such a mapping. Let s refer to an arbitrary vector. Then,

$$
\begin{aligned}
s^T \nabla \hat{\mathbf{F}}_i s &= b_i^0 \sum_{k=1}^{g} s_k^2 + b_i^0 \left(\sum_{k=1}^{g} s_k \right)^2 - \sum_{\omega=1}^{n} \rho^\omega b_i^\omega \sum_{k=1}^{g} s_k s_{\omega g + k} \\
&- \sum_{\omega=1}^{n} \rho^\omega b_i^\omega \sum_{k=1}^{g} s_k \sum_{k=1}^{g} s_{\omega g + k} + \sum_{\omega=1}^{n} \rho^\omega b_i^\omega \left(\sum_{k=1}^{g} s_{\omega g + k}^2 + \left(\sum_{k=1}^{g} s_{\omega g + k} \right)^2 \right) \\
&+ \sum_{\omega=1}^{n} \rho^\omega \left(\sum_{k=1}^{g} d_{ik}^\omega s_{\omega g + k}^2 \right) + \sum_{\omega=1}^{n} \rho^\omega b_i^\omega \left(s_{(n+1)g + \omega} \sum_{k=1}^{g} s_{\omega g + k} \right) \\
&- \sum_{\omega=1}^{n} \rho^\omega b_i^\omega \left(s_{(n+1)g + \omega} \sum_{k=1}^{g} s_k \right) \\
&+ \sum_{\omega=1}^{n} \rho^\omega b_i^\omega \left(s_{(n+1)g + \omega} \sum_{k=1}^{g} s_{\omega g + k} \right) + \sum_{\omega=1}^{n} \rho^\omega b_i^\omega \left(s_{(n+1)g + \omega} \right)^2
\end{aligned}
$$

Adding and subtracting terms, this can be given by

$$
\begin{aligned}
s^T \nabla \hat{\mathbf{F}}_i s &= (b_i^0 - \sum_{\omega=1}^{n} \frac{\rho^\omega b_i^\omega}{4}) \sum_{k=1}^{g} s_k^2 + (b_i^0 - \sum_{\omega=1}^{n} \frac{\rho^\omega b_i^\omega}{4})(\sum_{k=1}^{g} s_k)^2 - \sum_{\omega=1}^{n} \rho^\omega b_i^\omega \sum_{k=1}^{g} s_k s_{\omega g + k} \\
&+ \sum_{\omega=1}^{n} \frac{\rho^\omega b_i^\omega}{4} \sum_{k=1}^{g} s_k^2 + \sum_{\omega=1}^{n} \frac{\rho^\omega b_i^\omega}{4}(\sum_{k=1}^{g} s_k)^2 - \sum_{\omega=1}^{n} \rho^\omega b_i^\omega \sum_{k=1}^{g} s_k \sum_{k=1}^{g} s_{\omega g + k} \\
&+ \sum_{\omega=1}^{n} \rho^\omega b_i^\omega (\sum_{k=1}^{g} s_{\omega g + k}^2 + (\sum_{k=1}^{g} s_{\omega g + k})^2) + \sum_{\omega=1}^{n} \rho^\omega (\sum_{k=1}^{g} d_{ik}^\omega s_{\omega g + k}^2) \\
&+ 2 \sum_{\omega=1}^{n} \rho^\omega b_i^\omega \left(s_{(n+1)g + \omega} \sum_{k=1}^{g} s_{\omega g + k} \right) - \sum_{\omega=1}^{n} \rho^\omega b_i^\omega \left(s_{(n+1)g + \omega} \sum_{k=1}^{g} s_k \right) \\
&+ \sum_{\omega=1}^{n} \rho^\omega b_i^\omega \left(s_{(n+1)g + \omega} \right)^2 .
\end{aligned}
$$

On rearranging, $s^T \nabla \hat{\mathbf{F}}_i s$ is given by

$$
\begin{aligned}
&(b_i^0 - \sum_{\omega=1}^{n} \frac{\rho^\omega b_i^\omega}{4}) \sum_{k=1}^{g} s_k^2 + (b_i^0 - \sum_{\omega=1}^{n} \frac{\rho^\omega b_i^\omega}{4})(\sum_{k=1}^{g} s_k)^2 + \sum_{\omega=1}^{n} \left(\rho^\omega b_i^\omega \sum_{k=1}^{g} \left(\frac{s_k}{2} - s_{\omega g + k} \right)^2 \right) \\
&+ \sum_{\omega=1}^{n} \rho^\omega (\sum_{k=1}^{g} d_{ik}^\omega s_{\omega g + k}^2) \\
&+ \sum_{\omega=1}^{n} \rho^\omega b_i^\omega \left(s_{(n+1)g + \omega} + \sum_{k=1}^{g} s_{\omega g + k} - \sum_{k=1}^{g} \frac{s_k}{2} \right)^2 .
\end{aligned}
$$

By assumption $4 b_i^0 \geq \mathbb{E} b_i^\omega$, it follows that $s^T \nabla \hat{\mathbf{F}}_i s \geq 0$ for all $i \in \mathcal{G}$ implying that ∇F_i is also positive semidefinite for all $i \in \mathcal{G}$. The gradient mapping for a load node for all $i \in \mathcal{G}^c$ is given by

$$
\nabla \mathbf{F}_i = \begin{pmatrix} \rho^1 b_i^1 & \dots & 0 \\ \vdots & \ddots & \vdots \\ 0 & \dots & \rho^n b_i^n \end{pmatrix} .
$$

Since the gradient mappings corresponding to the load nodes are positive definite, the positive semidefiniteness of the entire gradient mapping $\nabla \mathbf{F}$ follows. Consequently, $\mathbf{F}$ is a monotone mapping and its regularization, namely $\mathbf{F}_\epsilon = \mathbf{F} + \epsilon \mathbf{I}$, is a strongly monotone mapping. It follows that a unique solution to $VI(\mathbf{X}, \mathbf{F}_\epsilon)$ exists, allowing us to conclude a unique ϵ-Nash equilibrium exists. ∎

Before proceeding to discuss a more general class of risk-based games, it is worth commenting on whether the uniqueness result may be strengthened. It must be emphasized that the monotonicity of the mapping itself is not the main barrier in obtaining a global uniqueness certificate. In fact, the monotonicity of the mapping can be utilized in some settings to derive precisely such a result. For instance, by leveraging [10, Prop. 3.6.6] when $\mathbf{F}(z)$ is a monotone mapping, then the local uniqueness of a solution to VI$\mathbf{X}, \mathbf{F}$) is a sufficient condition for global uniqueness. Proving local uniqueness of a solution to $VI(\mathbf{X}, \mathbf{F})$ requires the definition of the critical cone using the tangent cone and the orthogonal complement to $\mathbf{F}(z)$ at z, denoted by $\mathbf{F}(z)^\perp$.

Definition 13 *The tangent cone of* $\mathbf{X}$ *at* $x \in \mathbf{X}$ *is denoted by* $\mathcal{T}(z; \mathbf{X})$ *and consists of all vectors* $d \in \mathbb{R}^n$, *called tangent vectors to* $\mathbf{X}$ *at* z, *for which there exist a sequence of vectors* $\{y^k\} \subset \mathbf{X}$ *and a sequence of scalars* $\{\tau^k\}$ *such that*

$$\lim_{k \to \infty} y^k = z, \quad \lim_{k \to \infty} \tau^k = 0, \quad and \quad \lim_{k \to \infty} \frac{y_k - z}{\tau^k} = d.$$

The critical cone, denoted by $\mathcal{C}(z; \mathbf{X})$, *is defined as*

$$\mathcal{C}(z; \mathbf{X}, \mathbf{F}) \equiv \mathcal{T}(z; \mathbf{X}) \cap \mathbf{F}(z)^{\perp}.$$

However, from [10, Prop.3.3.4], the local uniqueness of a solution to $\mathrm{VI}(\mathbf{X}, \mathbf{F})$ follows if $\nabla \mathbf{F}(z)$ is strictly copositive over the critical cone $\mathcal{C}(z; \mathbf{X}, \mathbf{F})$. Unfortunately, such a result cannot be seen to hold since ∇F_i has a zero block (as denoted by V_i) implying that it cannot be strictly copositive, in any reduced space.

4.3   Risk-based market clearing game with shared risk

When the risk measure is parameterized by competitive decisions, the approach employed in the previous section cannot be employed. This is a direct consequence of the nature of the coupling between the strategy sets; it ceases to have the attractive shared property preventing us from using a variational inequality with a single-valued mapping for purposes of analysis. Instead, we retain the nonsmooth risk measure in the objective and attempt to show that the resulting multivalued variational inequality is solvable. We begin by noting that the risk-measure represents the minimal value of the optimization problem

$$\mathrm{CVaR}_{\tau_i}(\varrho_{ij}) \triangleq \min_{m_{ij} \in \mathbb{R}} \left\{ m_{ij} + \frac{1}{1 - \tau_i} \max(\varrho_{ij}^{\omega} - m_{ij}, 0) \right\},$$

where the dependence of ϱ_{ij} on x_i is suppressed. We may then consider the game as being one over the larger space given by $\mathbf{X} \times \mathbb{R}^g$ and the corresponding multivalued variational inequality arising from the equilibrium conditions of the nonsmooth game is given by

$$\partial_z \Pi^c(z^*, m^*)^T(z - z^*) + \partial_m \Pi^c(z^*, m^*)^T(m - m^*) \geq 0 \quad \forall(z \times m) \in \mathbf{X} \times \mathbb{R}^g, \tag{4.2}$$

where $\partial_z \Pi^c(z, m)$ and $\partial_m \Pi^c(z, m)$ are given by

$$\partial_z \Pi^c(z, m) \triangleq \prod_{j=1}^{g+1} \partial_{z_j} \pi_j^c(z_j, m_j; z_{-i}) \text{ and } \partial_m \Pi^c(z, m) \triangleq \prod_{j=1}^{g} \partial_{m_j} \pi_j^c(z_j, m_j; z_{-j}),$$

respectively. Furthermore, we have that $\partial_{ij} \pi_j = \partial_{z_{ij}} \pi_j \times \partial_{m_{ij}} \pi_j$. The generalized Clarke gradient $\partial_{ij} \pi_i$ is defined as

$$\partial_{ij} \pi_j^c(z_j, m_j; z_{-j}) = \partial_{ij}(p_i^0 x_{ij} + \mathbb{E}\left(p_i^\omega(y_{ij}^\omega - x_{ij}) - \zeta_{ij}^\omega(y_{ij}^\omega)\right))$$

$$- \left(\kappa_i \mathbb{E} \left(\underbrace{m_{ij} + \frac{1}{1 - \tau} \max(\varrho_{ij}^\omega - m_{ij}, 0)}_{\upsilon_{ij}^\omega} \right) \right)$$

$$= \nabla_{ij} \left(p_i^0 x_{ij} + \mathbb{E}\left(p_i^\omega(y_{ij}^\omega - x_{ij}) - \zeta_{ij}^\omega(y_{ij}^\omega)\right) \right) - \kappa_i \mathbb{E} \partial_{ij} \upsilon_{ij}^\omega$$

26

where the interchange of the expectation and derivative follows immediately since the sample-space is finite and the summation is finite. Note that the equality holds in the second expression since all the terms except one are continuously differentiable. Finally, it is recalled from nonsmooth Clarke calculus [6] that

$$\partial_{x_{ij}} \upsilon_{ij}^{\omega} = \partial_{x_{ij}} \left(\max(\varrho_{ij}^{\omega} - m_{ij}, 0) \right) = \begin{cases} (\varrho_{ij}^{\omega})', & \text{if } \varrho_{ij}^{\omega} - m_{ij} > 0, \\ \operatorname{conv}\{(\varrho_{ij}^{\omega})', 0\} & \text{if } \varrho_{ij}^{\omega} - m_{ij} = 0, \\ 0, & \text{if } \varrho_{ij}^{\omega} - m_{ij} < 0, \end{cases}$$

Based on (3.8), we have

$$(\varrho_{ij}^{\omega})' = (\varphi'(x_{ij}) + \varphi(x_{ij}))e^{(\sum_{j \in \mathcal{J}} x_{ij} - cap_i^{\omega})}.$$

Similarly, the generalized Clarke gradient of the risk measure with respect to m_{ij} is given by

$$\partial_{m_{ij}} \upsilon_{ij}^{\omega} = \partial_{m_{ij}} \left(m_{ij} + \frac{1}{1-\tau} \max(\varrho_{ij}^{\omega} - m_{ij}, 0) \right) = 1 + \frac{1}{1-\tau} \partial_{m_{ij}} \operatorname{conv}\{(\varrho_{ij}^{\omega} - m_{ij}), 0\}$$

$$= \begin{cases} 1 - \frac{1}{1-\tau_i}, & \text{if } \varrho_{ij}^{\omega} - m_{ij} > 0, \\ 1 + \frac{1}{1-\tau_i} \operatorname{conv}\{-1, 0\}, & \text{if } \varrho_{ij}^{\omega} - m_{ij} = 0, \\ 1, & \text{if } \varrho_{ij}^{\omega} - m_{ij} < 0. \end{cases}$$

It follows that if $\vartheta_{ij}^{\omega} \in \partial_{ij} \upsilon_{ij}^{\omega}$, then its component ϑ_{ij}^{ω} is defined as

$$\vartheta_{ij}^{\omega} \triangleq \begin{pmatrix} \vartheta_{ij}^{z,\omega} \\ \vartheta_{ij}^{m,\omega} \end{pmatrix} = \begin{pmatrix} \alpha_{ij}^{z,\omega} \varrho_{z_{ij}}' \\ 1 - \frac{\alpha_{ij}^{m,\omega}}{1-\tau_i} \end{pmatrix} \quad \text{where } (\alpha_{ij}^{z,\omega}, \alpha_{ij}^{m,\omega}) \text{ is given by}$$

$$\begin{cases} (\alpha_{ij}^{z,\omega}, \alpha_{ij}^{m,\omega}) = (1, 1) & \varrho_{ij}^{\omega} - m_{ij} > 0, \\ (\alpha_{ij}^{z,\omega}, \alpha_{ij}^{m,\omega}) \in [0, 1] \times [0, 1] & \varrho_{ij}^{\omega} - m_{ij} = 0, \\ (\alpha_{ij}^{z,\omega}, \alpha_{ij}^{m,\omega}) = (0, 0) & \varrho_{ij}^{\omega} - m_{ij} < 0. \end{cases} \tag{4.3}$$

We prove the existence of a shared-constraint Nash equilibrium in the nonsmooth settings by showing that the following sufficiency condition from [11] is satisfied.

Theorem 14 *Consider the generalized Nash game denoted by $\mathcal{G} = (\Pi, \mathcal{D}, g)$. Suppose assumptions (A1)–(A4) hold. If there exists a bounded open set D and a vector $z^{ref} \in D \cap \mathbf{X}$ such that $L_< \cap bd(D) = \emptyset$, where*

$$L_< \triangleq \left\{ z \in \mathbf{X} : \exists \vartheta \in \partial \pi(z), (z - z^{ref})^T \vartheta < 0 \right\},$$

then $\mathcal{G}$ admits a nonsmooth Nash equilibrium in $\mathbf{X}$.

It can be seen that $L_<$, defined above, is nonempty, if the following holds:

$$\liminf_{\substack{\|z\| \to \infty, z \in \mathbf{X} \\ \vartheta \in \partial \pi(z)}} \vartheta^T (z - z^{\mathrm{ref}}) > 0.$$

We prove that precisely such a condition holds in showing that the nonsmooth shared-risk generalized Nash game admits an equilibrium. We first make an assumption on the loss function.

Assumption 15 *(A5) The function $\varphi(x_{ij})$ is an increasing convex twice-continuously differentiable function. Moreover, the function is strictly increasing and positive for all $x_{ij} \geq 0$. That is, $\varphi'(x_{ij}) > 0$ and $\varphi(x_{ij}) \geq 0$.*

Theorem 16 (Existence: nonsmooth shared-constraint Nash game) *Consider $\mathcal{G}^c$ denoted by $(\Pi^c, \mathcal{D}, g)$ and suppose assumptions (A1)–(A5) hold. Then $\mathcal{G}^c$ admits an equilibrium.*

Proof : We define a vector $w^{\mathrm{ref}} \triangleq \mathbf{0} \in \mathbf{X}$ and proceed to show

$$\lim_{\substack{\|w\| \to \infty, w \in \mathbf{X} \\ \vartheta \in \partial\pi(z)}} w^T \vartheta = \infty$$

where the components of ϑ, namely ϑ_{ij} are defined in (4.3). The expression $w^T \vartheta$ can be written as the sum of the following terms:

$$term\,1 + term\,2 + term\,3 + \underbrace{\sum_{j \in \mathcal{F}} \left(\sum_{i \in \mathcal{N}_j} \sum_{\omega \in \Omega} \rho^\omega \vartheta_{ij}^{m,\omega} m_{ij} \right)}_{term\,4} + \underbrace{\sum_{j \in \mathcal{F}} \left(\sum_{i \in \mathcal{N}_j} \sum_{\omega \in \Omega} \rho^\omega \vartheta_{ij}^{z,\omega} x_{ij} \right)}_{term\,5},$$

where terms 1 to 3 are defined in (4.1). Since $\varphi(x_{ij})$ is positive and an increasing function of x_{ij}. Then $\varphi(x_{ij}) > 0$ and $\varphi'(x_{ij}) \geq 0$. Consider the following cases:

Case 1 : Suppose $x_{ij} \to \infty$ implying that $\vartheta_{ij}^{z,\omega} \to \infty$. Consequently, terms 2 and 5 tend to $+\infty$.

Case 2 : Suppose $m_{ij} \to \infty$. Then, $\vartheta_{ij}^{m,\omega} = 1$. Consequently, Term 4 tends to $+\infty$. Consider instead a sequence along which $m_{ij} \to -\infty$. Then, $\vartheta_{ij}^{m,\omega} = \frac{-\tau_i}{1-\tau_i}$. Consequently term 4 tends to $+\infty$.

Case 3 : Suppose $x_{ij} \to \infty$ and $|m_{ij}| \to \infty$. Then ϱ_{ij}^ω and $(\varrho_{ij}^\omega)'$ tend to infinity at an exponential rate. Then, $\vartheta_{ij}^{z,\omega} \to \infty$ and $\vartheta_{ij}^{m,\omega} \to \frac{-\tau}{1-\tau}$. Then, term 2 tends to $+\infty$ at a quadratic rate. It follows that term 5 grows to $+\infty$ at an exponential rate and term 4 $\to \pm\infty$ linearly. As a consequence, the sum tends to positive infinity.

Case 4 : Suppose $x_{ik} \to \infty, k \neq j, \exists k \in \mathcal{J}$ and $|m_{ij}| \to \infty$. It follows that ϱ_{ij}^ω and $(\varrho_{ij}^\omega)'$ tend to $+\infty$ at an exponential rate. Moreover, $\vartheta_{ij}^{z,\omega} \to \infty$ and $\vartheta_{ij}^{m,\omega} \to \frac{-\tau_i}{1-\tau_i}$. Then, term 2 tends to $+\infty$ at a quadratic rate and term 5 grows to $+\infty$ at an exponential rate. Furthemore, term 4 $\to \pm\infty$ at a linear rate. It can then be concluded that the sum tends to $+\infty$.

Consider any sequence $\{z^k\}$ such that $\lim \|z^k\| = \infty$ and $z_k \in \mathbf{Y}$. From the above cases, either (i) at least one of the terms converges to ∞ or (ii) one term converges to $-\infty$ linearly while at least one converges to $+\infty$ at a quadratic rate. The required result follows. $\blacksquare$

As we emphasized earlier in this section, the nonsmooth game leads to a multivalued variational inequality that is less easy to solve in practice. However, the smoothed problem leads to a variational inequality for which a solution can be shown to exist. Often, the solvability of the smoothed problem can be directly concluded through a degree-theoretic approach (see [10]). Instead, we use the avenue

that has been followed through this paper in claiming the existence of a solution to the smoothed problem, which relies on the following approximation of the max-function. Let,

$$q_{ij}^\omega = \varphi(x_{ij})e^{(\sum_{j\in\mathcal{J}} x_{ij}-\lambda_i^\omega)} - m_{ij}.$$

Consider a function $f(q_{ij}^\omega) = \max(q_{ij}^\omega, 0)$ which can be can be written as,

$$f(q_{ij}^\omega) = \frac{q_{ij}^\omega + |q_{ij}^\omega|}{2},$$

where $|q_{ij}^\omega|$ represents the absolute value of q_{ij}^ω. The absolute value function as known is not differentiable at zero and can be approximated by a globally smooth function described as follows:

$$|q_{ij}^\omega| \approx \sqrt{(q_{ij}^\omega)^2 + \epsilon},$$

implying that the smooth approximation $f_\epsilon(q_{ij}^\omega)$ and its first and second derivatives are given by,

$$f_\epsilon(q_{ij}^\omega) = \frac{q_{ij}^\omega + \sqrt{(q_{ij}^\omega)^2 + \epsilon}}{2}, f_\epsilon'(q_{ij}^\omega) = \frac{1}{2}\left(1 + \frac{q_{ij}^\omega}{\sqrt{(q_{ij}^\omega)^2 + \epsilon}}\right), f_\epsilon''(q_{ij}^\omega) = \frac{\epsilon}{2((q_{ij}^\omega)^2 + \epsilon)^{\frac{3}{2}}}.$$

As seen from the above expressions, the function lies in C^∞ and is clearly convex. Using this function, we approximate v_{ij}^ω by

$$v_{ij,\epsilon}^\omega = \left(m_{ij} + \frac{f_\epsilon(q_{ij}^\omega)}{1 - \tau_i}\right).$$

It follows that the

$$\nabla_{x_{ij}} v_{ij,\epsilon}^\omega = \frac{f'(q_{ij}^\omega)}{1 - \tau}\left((\varphi'(x_{ij}) + \varphi(x_{ij}))e^{(\sum_{j\in\mathcal{J}} x_{ij}-\lambda_i^\omega)}\right), \nabla_{m_{ij}} v_{ij,\epsilon}^\omega = \left(1 - \frac{f_\epsilon'(q_{ij}^\omega)}{1 - \tau_i}\right).$$

This allows us to define a smoothed mapping, denoted by $\mathbf{F}_\epsilon$, that corresponds to the equilibrium conditions of a smoothed game.

Proposition 17 *Suppose assumptions (A1)–(A5) hold. Then VI$(\mathbf{X}, \mathbf{F}^\epsilon)$ has a compact nonempty solution set.*

Proof : Consider an $z^{\text{ref}} \equiv 0 \in \mathbf{X}$. So, it suffices to show that,

$$\liminf_{z\in\mathbf{X}, \|z\|\longrightarrow\infty} \mathbf{F}^\epsilon(z)^T(z) > 0,$$

where $\mathbf{F}^\epsilon(z)^T(z)$ is given by

$$term\,1 + term\,2 + term\,3 + \underbrace{\sum_{j\in\mathcal{J}}\sum_{i\in\mathcal{N}_j}\sum_{\omega\in\Omega}\rho^\omega \nabla_{m_{ij}} v_{ij,\epsilon}^\omega(m_{ij})}_{term\,4} + \underbrace{\sum_{j\in\mathcal{J}}\sum_{i\in\mathcal{N}_j}\sum_{\omega\in\Omega}\rho^\omega \nabla_{x_{ij}} v_{ij,\epsilon}^\omega(x_{ij})}_{term\,5},$$

where terms 1–3 are defined in (4.1). Consider the following cases and recall that φ is positive and an increasing function:

Case 1 : Suppose $x_{ij} \to \infty$ and $q_{ij}^\omega \to \infty$. Consequently, terms 2 and 5 tend to $+\infty$.

Case 2 : Suppose $m_{ij} \to \infty$. Then, $q_{ij}^\omega \to -\infty$ implying that term 4 tends to $+\infty$. Consider $m_{ij} \to -\infty$. Then, $q_{ij}^\omega \to \infty$ and term 4 tends to $+\infty$.

Case 3 : Suppose $x_{ij} \to \infty$ and $|m_{ij}| \to \infty$. Then, $q_{ij}^\omega \to \infty$ and term 2 tends to $+\infty$ at a quadratic rate. Furthermore, term 5 tends to $+\infty$ at an exponential rate while term 4 $\to \pm\infty$ linearly. It follows that the sum tends to $+\infty$.

Case 4 : Suppose $x_{ik} \to \infty, k \neq j, \exists k \in \mathcal{J}$ and $|m_{ij}| \to \infty$. Then, $q_{ij}^\omega \to \infty$ and term 2 tends to $+\infty$ at a quadratic rate. Furthermore, term 5 tends to $+\infty$ at an exponential rate and term 4 $\to \pm\infty$ linearly. We may then conclude that the sum tends to $+\infty$.

Consider any sequence $\{z^k\}$ such that $\lim \|z^k\| = \infty$ and $z_k \in \mathbf{X}$. In this case, either (i) one of the terms converges to ∞ or (ii) one term converges to $-\infty$ linearly and the other converges to ∞ at a quadratic rate. This concludes the proof. ∎

Chapter 5

A hybrid cutting-plane projection method

The game-theoretic problems, denoted by $\mathcal{G}^a$ and $\mathcal{G}^b$, introduced in the section 4 lead to stochastic variational problems that are shown to be monotone. While significant theory exists for solving monotone variational inequalities [10, 22], unfortunately most schemes can neither be implemented in a distributed setting (since the constraint sets are coupled) nor do they possess the scalability required to address this class of problems since our class of problems can be arbitrarily large in terms of the number of agents, the size of the network and the cardinality of the sample-space. Accordingly, our focus is on developing convergent algorithms with suitable error bounds, for addressing this class of problems. We place an emphasis on the construction of distributed schemes that scale with the cardinality of the sample-space, namely $|\Omega|$, the number of agents $|\mathcal{J}|$ and the size of the network $|\mathcal{N}|$. To address these needs, we develop a *distributed projection-based method* that employs a *cutting-plane method* for solving the agent-specific projection problems.

In section 6.1, we describe a dual and a primal-dual projection method for the solution of shared-constraint stochastic Nash games. At the heart of these schemes is a projection step that leads to a stochastic convex program. In section 6.2, we describe a cutting-plane method for the solution of such problems that scales with $|\Omega|$. Convergence theory and error bounds for the projection-based primal-dual and dual schemes are developed in section 6.3. Finally, in section 6.4, we examine the numerical behavior of the schemes.

5.1   Distributed primal-dual and dual projection methods

Consider an $N-$player deterministic Nash game in which the jth agent solves the parameterized convex optimization problem given by

$$
\begin{array}{lll}
\mathrm{A}(z_{-j}) & \text{maximize} & \pi_j(z_j; z_{-j}) \\
& \text{subject to} & z_j \in \mathbf{Z}_j,
\end{array}
$$

where $\pi_j(z_j; z_{-j})$ is a convex function of z_j for all z_{-j} and $\mathbf{Z}_j$ is a closed and convex set. Then a standard distributed projection scheme is given by

$$
z_j^{k+1} := \Pi_{\mathbf{Z}_j}(z_j^k + \gamma \nabla \pi_j(z_j^k; z_{-j}^k)), \ \text{ for all } j = 1, \dots, N,
$$

where γ is a fixed steplength. Yet, such a scheme relies on two properties: First, the gradient mapping given by $F(z)$ needs to satisfy strict monotonicity, strong monotonicity or co-coercivity property [10] over a set $\mathbf{Z}$ where $F(z)$ and $\mathbf{Z}$ are defined as

$$F(z) := -\left(\nabla_{z_1}\pi_1^T, \quad \ldots, \quad \nabla_{z_N}\pi_N^T\right)^T \text{ and } \mathbf{Z} \triangleq \prod_{j=1}^{N} \mathbf{Z}_j.$$

Second, the strategy sets across agents cannot be coupled. In our setting, neither assumption holds and therefore a direct application of the primal approach cannot be employed.

Instead, we observe that the shared-constraint game can be cast as a monotone complementarity problem in the primal-dual space. By solving a sequence of regularized (and therefore strongly monotone) complementarity problems through a Tikhonov regularization scheme [10], we obtain a solution to the original problem. This avenue allows us to leverage fixed steplength projection schemes for the solution of each regularized complementarity problem. Importantly, each subproblem can be massive, with a size proportional to $|\Omega| \times |\mathcal{J}| \times |\mathcal{N}|$, and a direct solution of such problems is only possible in modest settings. To cope with such a challenge, we develop a distributed framework that relies on decomposition methods that scale well with all three sources of complexity.

We now proceed to describe the distributed projection framework. If the Lagrange multipliers corresponding to the shared constraint are denoted by λ, then it follows that (z^*, λ^*) is an equilibrium of shared-constraint Nash game if and only if (z^*, λ^*) is a solution of set of coupled fixed-point problems:

$$z = \Pi_{\mathbf{Z}}(z - \gamma\mathbf{F}_z(z, \lambda)) \tag{5.1}$$

$$\lambda = \Pi_{\mathbb{R}_m^+}(\lambda - \gamma\mathbf{F}_\lambda(z, \lambda)), \tag{5.2}$$

where

$$\mathbf{F}_z(z, \lambda) = \begin{pmatrix} -\nabla_{z_1}\pi_1 - \nabla_{z_1}d(z)^T\lambda \\ \vdots \\ -\nabla_{z_N}\pi_N - \nabla_{z_N}d(z)^T\lambda \end{pmatrix} \text{ and } \mathbf{F}_\lambda(z, \lambda) = d(z). \tag{5.3}$$

The fixed-point representations motivate a *primal-dual* method that requires constructing a primal and dual method on the same timescale with a fixed steplength γ_{pd} in a regularized setting. Specifically, this entails the following set of regularized primal and dual steps for $k \geq 0$:

$$z_j^{k+1} = \Pi_{\mathbf{Z}_j}(z_j^k - \gamma_{pd}(\mathbf{F}_z(z_j^k; z_{-j}^k, \lambda^k) + \epsilon^\ell z_j^k)), \text{ for all } j \tag{5.4}$$

$$\lambda^{k+1} = \Pi_{\mathbb{R}_m^+}(\lambda^k - \gamma_{pd}(\mathbf{F}_\lambda(z^k, \lambda^k) + \epsilon^\ell\lambda^k)), \tag{5.5}$$

where ϵ^ℓ is the regularization parameter at the ℓth iteration of the outer Tikhonov scheme. In the regularized primal-dual approach, the steplength γ_{pd} has to be chosen in accordance with the monotonicity and Lipschitz constant of the appropriate mappings in *both* the primal and dual spaces (see section 6.3 for more details). In effect, if the mappings in one of the spaces has a large Lipschitz constant (or alternately a low monotonicity constant), the progress of the entire algorithm may be hampered.

A dual method for solving the monotone complementarity problem does not tie these two steplengths together and can be employed instead. This requires that for every update in the dual space, an *exact* primal solution is required. In particular, for $k \geq 0$, this leads to a set of iterations given by

$$z_j^k = \Pi_{\mathbf{Z}_j}(z_j^k - \gamma_d(\mathbf{F}_z(z_j^k; z_{-j}^k, \lambda^k) + \epsilon^\ell z_j^k)), \text{ for all } j \tag{5.6}$$

$$\lambda^{k+1} = \Pi_{\mathbb{R}_m^+}(\lambda^k - \gamma_p(\mathbf{F}_\lambda(z^k, \lambda^k) + \epsilon^\ell \lambda^k)), \tag{5.7}$$

where γ_p and γ_d are the primal and dual steplengths, respectively. The termination of the inner scheme occurs when the error in the fixed-point problem falls within a threshold and is ensured by the following for the primal-dual scheme

$$\left\| \left(\frac{\|z^{k+1} - z^k\|}{1 + \|z^k\|}, \frac{\|\lambda^{k+1} - \lambda^k\|}{1 + \|\lambda^k\|} \right) \right\| \leq \epsilon^{inner}, \tag{5.8}$$

and the dual scheme

$$\frac{\|\lambda^{k+1} - \lambda^k\|}{1 + \|\lambda^k\|} \leq \epsilon^{inner}, \tag{5.9}$$

Note that the primal iteration really refers to the solution of the fixed-point problem in the primal space. Naturally, the exact solution of such a problem may prove difficult, suggesting instead that we may need to employ inexact or approximate solutions. Expectedly, this would lead to errors that would require quantification. This analysis is provided, along with suitable convergence results, in section 6.3.

Algorithm 1: Distributed Primal-dual and Dual Projection Methods

0 initialization $k = 0, \ell = 0$;
   choose constants $\epsilon^0, \epsilon^{inner}, \epsilon^{outer} > 0$ and γ_{pd}, γ_p and γ_d, initial solution (z^0, λ^0), $\bar{\gamma} < 1$;
   while $\epsilon^\ell > \epsilon^{outer}$ **do**
       while conditions (5.8) or (5.9) are not satisfied do
1   Let λ^{k+1} be given by (5.5) (Primal-dual) or (5.7) (Dual) ;
2   Let z^{k+1} be given by (5.4) (Primal-dual) or the solution of (5.6) (Dual) ;
3 $k := k + 1$;
       end
4   Update regularization $\epsilon^{\ell+1} := \bar{\gamma}\epsilon^\ell$;
5 $\ell := \ell + 1$;
   end

5.2 A scalable cutting-plane method for the projection problem

A question that has been taken for granted is the solution to the primal projection problem, denoted by (5.4) and (5.6). In the current setting, $\mathbf{Z}_j$ is a polyhedral set implying that this problem is a strongly convex quadratic program. In the past, this problem has been solved by a variety of schemes (such as interior-point methods, active-set methods and others). All of these schemes are necessarily direct approaches in that they make no obvious effort to utilize the structure of the problem. However, in this instance, the problems belong to a fairly well-understood class of problems, namely *recourse-based stochastic quadratic programs*, a class of problems that grow with

$|\Omega|$ and may be solved efficiently via cutting-plane methods [2, 32], as we describe next. Solving the projection step in the primal space (5.6),(5.4), requires solving a stochastic convex program given by

$$
\begin{aligned}
\text{minimize} \quad & \tfrac{1}{2}(\widehat{z}_j - \bar{z}_j^k)^T(\widehat{z}_j - \bar{z}_j^k) \\
\text{subject to} \quad & \widehat{z}_j \in \mathbf{Z}_j,
\end{aligned}
$$

where

$$
\bar{z}_j^k = (z_j^k - \gamma F_{z_j}(z_j; z_{-j}^k, \lambda^k)), \widehat{z}_j = \begin{pmatrix} \widehat{x}_j \\ (\widehat{y}_j^\omega)_{\omega \in \Omega} \end{pmatrix}, \widehat{x}_j = \begin{pmatrix} x_j \\ m_j \end{pmatrix}, \widehat{y}_j^\omega = \begin{pmatrix} u_j^\omega \\ v_j^\omega \\ y_j^\omega \\ s_j^\omega \end{pmatrix}., \forall j \in \mathcal{J},
$$

$$
\bar{z}_j^k = (z_j^k - \gamma F_{z_j}(z_j; z_{-j}^k, \lambda^k)), \widehat{z}_j = \begin{pmatrix} \widehat{x}_j \\ (\widehat{y}_j^\omega)_{\omega \in \Omega} \end{pmatrix}, \widehat{x}_j = (0), \widehat{y}_j^\omega = \begin{pmatrix} r_1^\omega \\ \vdots \\ r_N^\omega \end{pmatrix}, j = g + 1.
$$

In settings where the loss function in the risk measure is affine (or in the risk-neutral deviation cost setting), the projection problem reduces to a stochastic quadratic program given by [1]

$$
\begin{aligned}
\text{minimize} \quad & \tfrac{1}{2}\widehat{x}_j^T \widehat{x}_j + \widehat{x}_j^T \bar{x}_j + \sum_{\omega \in \Omega} \left(\tfrac{1}{2}(\widehat{y}_j^\omega)^T(\widehat{y}_j^\omega) - (\widehat{y}_j^\omega)^T \bar{y}_j^\omega \right) \\
\text{subject to} \quad & (\widehat{x}_j, \widehat{y}_j^\omega) \in \mathbf{Z}_j = \left\{ (\widehat{x}_j, \widehat{y}_j^\omega) : \left\{ \begin{array}{c} A_1 \widehat{x}_j + A_2 \widehat{y}_j^\omega = \widehat{b}_j^\omega \\ A_3 \widehat{y}_j^\omega \leq cap_{ij}^\omega, \\ A_4 \widehat{x}_j \geq 0, \\ \widehat{y}^\omega \geq 0, \end{array} \right\} \forall \omega \in \Omega \right\},
\end{aligned}
$$

where $A_1, A_2, A_3,$ and A_4 are defined appropriately. As Ω grows in cardinality, a direct solution of the quadratic program becomes challenging. Instead, we pursue a stochastic programming avenue by noting that the constraint structure allows one to cast the problem as a recourse-based stochastic program. Specifically, we have

$$
\begin{aligned}
\text{minimize} \quad & \tfrac{1}{2}\widehat{x}_j^T \widehat{x}_j + \widehat{x}_j^T \bar{x}_j + \mathcal{Q}(\widehat{x}_j) \\
\text{subject to} \quad & A_4 \widehat{x}_j \geq 0
\end{aligned}
$$

where $\mathcal{Q}(\widehat{x}_j) = \mathbb{E}Q(\widehat{x}_j; \omega)$ and $Q(\widehat{x}_j; \omega)$ is the optimal value of the scenario-specific quadratic program:

$$
\text{Sub}(\widehat{x}_j; \omega) \qquad
\begin{aligned}
\text{minimize} \quad & \left(\tfrac{1}{2}(\widehat{y}_j^\omega)^T(\widehat{y}_j^\omega) - (\widehat{y}_j^\omega)^T \bar{y}_j^\omega \right) \\
\text{subject to} \quad & y_j^\omega \in \mathbf{Y}_j^\omega(\widehat{x}_j)
\end{aligned}
$$

and

$$
\mathbf{Y}^\omega(\widehat{x}_j) = \left\{ \widehat{y}_j^\omega : \left\{ \begin{array}{c} A_2 \widehat{y}_j^\omega = \widehat{b}_j^\omega - A_1 \widehat{x}_j \\ A_3 \widehat{y}_j^\omega \leq cap_{ij}^\omega, \\ \widehat{y}^\omega \geq 0 \end{array} \right\} \right\}.
$$

Algorithm 2: L–shaped method
---
0 initialization $k = 1, j \in \mathcal{J}, U_j^k = \infty, L_j^k = -\infty$;
    choose $\epsilon_1, \tau, u > 1$;
    while $|U_j^k - L_j^k| > \tau$ **do**
1   Solve (Master$_k$) to get $\left(\widehat{x}_j^k, \theta_j^k \right)$;
2   Update lower bound L_j^k;
3   Solve Sub$(\widehat{x}_j^k; \omega)$ for all $\omega \in \Omega$;
4   Construct (G_I^k, g_I^k);
5   Update upper bound U_j^k and add optimality cut (G_I^k, g_I^k) to (Master$_k$);
6 $k = k + 1$
    end

The key challenge in solving recourse-based stochastic optimiztion problems lies in ensuring that scenario-specific second-stage problems are solved in parallel. In 1969, based on a decomposition scheme suggested by Benders [2], Van-Slyke and Wets [32] suggested a cutting-plane method for the solution of recourse-based stochastic linear programs (LPs) that allows for such a parallelization. While much has been done on the solution of stochastic LPs (cf. [19, 3]), stochastic convex programming has been less studied in general. Parallel schemes for the solution of stochastic QPs via splitting and projection methods were discussed by Womersley and Chen [5] while extensions to the L-shaped cutting-plane method have been suggested by Zakeri et al. [35], Shanbhag [30], amongst others. We employ a similar scheme for solving the stochastic quadratic program arising from the projection problem. It should be emphasized that in general, a first-stage decision $\widehat{x}$ might render the $\mathbf{Y}^\omega(\widehat{x})$ empty. However, in this particular case, the nonnegative deviation levels u^ω and v^ω can be made arbitrarily large to ensure that the second-stage problem is *always feasible* and the resulting problem is said to possess complete recourse.

The L-shaped method for the solution of stochastic QPs requires solving a sequence of increasingly constrained (QPs) (called the master problem) where the additional constraints, termed as cuts, arise from the solution of the set of scenario-specific second-stage problems. The master problem is given by

$$
\begin{array}{ll}
\text{Master}_k \qquad \underset{\widehat{x}_j, \theta_j}{\text{minimize}} & \frac{1}{2}\widehat{x}_j^T \widehat{x}_j + \widehat{x}_j^T \bar{x}_j \\[2mm]
\text{subject to} & A_4 \widehat{x}_j \geq 0 \\
& \theta - G_{j,i}^T \widehat{x}_j \geq g_{j,i}, \quad i = 1, \dots, k.
\end{array}
$$

where $(G_{j,i}, g_{j,i})$ is the ith cut added to the jth agent's projection problem and is defined in [30]. Note that the ith cut associated with the jth agent requires the solution of Sub$(\widehat{x}_j^i)$. It is worth reiterating that the complexity arising from a massive sample-space is addressed by decomposing what is a potentially massive QP into a set a set of smaller QPs. In the L-shaped method, the termination is contingent on the upper and lower bounds beings sufficiently close. These bounds are defined as

$$
L_j^k \equiv \tfrac{1}{2}(\widehat{x}_j^k)^T (\widehat{x}_j^k) + (\widehat{x}_j^k)^T \bar{x}_j^k + \theta_j^k \text{ and } U_j^k \equiv \min\{U_j^{k-1}, \tfrac{1}{2}(\widehat{x}_j^k)^T (\widehat{x}_j^k) + (\widehat{x}_j^k)^T \bar{x}_j^k + \mathcal{Q}(\widehat{x}_j^k)\},
$$

---

[1]In our computational results we define the loss function to be of the form: $\rho_{ij}^\omega = \chi(x_{ij} - cap_{ij}^\omega)$, where $\chi = 0$, for $x_{ij} \leq cap_{ij}^\omega$. So, in addition to the earlier set of constraints we have another constraint $s_{ij}^\omega \geq -m_{ij}$.

respectively. Notice that $\{L_k^I\}$ is a monotonically increasing sequence while $\{U_k^I\}$ is a monotonically decreasing sequence. The L-shaped method with inexact cuts (Algorithm 2) proceeds as given below [30]. The convergence of the scheme is easily proved and can be found in [3, 29]. Next, we discuss the convergence properties of the overall projection scheme.

5.3 Convergence and error analysis of projection methods

Convergence of projection schemes is reliant on the underlying mappings satisfy a strict or strong property. The absence of such a property is addressed through a Tikhonov-based regularization scheme. Each iterate of the Tikhonov scheme may be solved efficiently and in this subsection, we provide the convergence theory for the suggested dual and primal-dual schemes for solving precisely such problems.

In this section, we present three sets of results. First, our convergence statements require a precise specification of the Lipschitz and monotonicity constants of the relevant mapping and represents our first result. Second, we present a convergence result for the dual scheme in a regularized setting and further equip this result with error bounds on the suboptimality and infeasibility (with respect to the shared constraint) if the dual scheme terminates prematurely. The *exact* form of the dual scheme requires exact primal iterates for a given dual solution. In a regime where a bound on the primal strategy sets is assumed to be available, we relax this requirement in constructing an *inexact dual method* and allow for *inexact* primal solutions. The third set of results focus on developing error bounds for the dual scheme in this setting along with suitable bounds on the suboptimality and infeasibility when the dual scheme terminates prematurely.

By recalling the definitions of $\mathbf{F}_z$ and $\mathbf{F}_\lambda$ in (5.3), we further define $\mathbf{F}_z^\epsilon, \mathbf{F}_\lambda^\epsilon, \mathbf{F}_f^\epsilon$ and $\mathbf{F}_d$ as

$$\mathbf{F}_z^\epsilon := \mathbf{F}_z + \epsilon z, \mathbf{F}_\lambda^\epsilon := \mathbf{F}_\lambda + \epsilon \lambda, \mathbf{F}_f^\epsilon := \begin{pmatrix} \nabla_{z_1} \pi_1 + \epsilon z_1 \\ \vdots \\ \nabla_{z_N} \pi_N + \epsilon z_N \end{pmatrix}, \tag{5.10}$$

$$\mathbf{F}_d := \begin{pmatrix} \nabla_{z_1} d^T \lambda \\ \vdots \\ \nabla_{z_N} d^T \lambda \end{pmatrix}, \mathbf{F}_z^\epsilon := \mathbf{F}_f^\epsilon - \mathbf{F}_d. \tag{5.11}$$

Furthermore, we define $z, z_i, l_i^\omega, l_i \ u_i, v_i, s_i, m_i$ and x_i as follows:

$$z = \begin{pmatrix} z_1 \\ \vdots \\ z_N \end{pmatrix}, z_i = \begin{pmatrix} l_i \\ u_i \\ v_i \\ s_i \\ m_i \\ x_i \end{pmatrix}, l_i^\omega = \begin{pmatrix} y_{i1}^\omega \\ \vdots \\ y_{iJ}^\omega \\ r_i^\omega \end{pmatrix}, l_i = \begin{pmatrix} l_i^1 \\ \vdots \\ l_i^n \end{pmatrix},$$

$$u_i = \begin{pmatrix} u_{i1}^1 \\ \vdots \\ u_{iJ}^n \end{pmatrix}, v_i = \begin{pmatrix} v_{i1}^1 \\ \vdots \\ v_{iJ}^n \end{pmatrix}, s_i = \begin{pmatrix} s_{i1}^1 \\ \vdots \\ s_{iJ}^n \end{pmatrix}, m_i = \begin{pmatrix} m_{i1} \\ \vdots \\ m_{iJ} \end{pmatrix}, x_i = \begin{pmatrix} x_{i1} \\ \vdots \\ x_{iJ} \end{pmatrix}$$

Using these definitions, the Lipschitz and strong monotonicity constants of $\mathbf{F}_\epsilon$ can be derived.

Lemma 18 *Consider the mapping* $\mathbf{F}_\epsilon(z, \lambda)$ *as defined in (5.10) and arising from the generalized Nash games* $\mathcal{G}^a$ *and* $\mathcal{G}^b$*. Then this mapping is strongly monotone and Lipschitz continuous.*

Proof :   We first derive the Lipschitz constant for $\mathbf{F}_\epsilon$. This requires analyzing each of the three terms.

$$\|\mathbf{F}^\epsilon(z^1, \lambda^1) - \mathbf{F}^\epsilon(z^2, \lambda^2)\| = \left\| \begin{pmatrix} \mathbf{F}_f^\epsilon(z^1, \lambda^1) - \mathbf{F}_f^\epsilon(z^2, \lambda^2) + \mathbf{F}_d(z^1, \lambda^1) - \mathbf{F}_d(z^2, \lambda^2) \\ \mathbf{F}_\lambda(z^1, \lambda^1) - \mathbf{F}_\lambda(z^2, \lambda^2) \end{pmatrix} \right\|$$

$$\leq \underbrace{\|\mathbf{F}_f^\epsilon(z^1, \lambda^1) - \mathbf{F}_f^\epsilon(z^2, \lambda^2)\|}_{\textbf{Term 1}} + \underbrace{\|\mathbf{F}_d(z^1, \lambda^1) - \mathbf{F}_d(z^2, \lambda^2)\|}_{\textbf{Term 2}} + \underbrace{\|\mathbf{F}_\lambda^\epsilon(z^1, \lambda^1) - \mathbf{F}_\lambda^\epsilon(z^2, \lambda^2)\|}_{\textbf{Term 3}}.$$

We bound each of the three terms as follows:

Term 1:   Given two vectors z^1 and z^2, we may decompose $\mathbf{F}$ into $H + B$ allowing term 1 to be expressed as

$$\mathbf{F}_i(z^1) - \mathbf{F}_i(z^2) = \begin{pmatrix} F_i^l(z^1) - F_i^l(z^2) \\ F_i^u(z^1) - F_i^u(z^2) \\ F_i^v(z^1) - F_i^v(z^2) \\ F_i^s(z^1) - F_i^s(z^2) \\ F_i^m(z^1) - F_i^m(z^2) \\ F_i^x(z^1) - F_i^x(z^2) \end{pmatrix} = \underbrace{\begin{pmatrix} H_i^l(z^1) - H_i^l(z^2) \\ H_i^u(z^1) - H_i^u(z^2) \\ H_i^v(z^1) - H_i^v(z^2) \\ H_i^s(z^1) - H_i^s(z^2) \\ H_i^m(z^1) - H_i^m(z^2) \\ H_i^x(z^1) - H_i^x(z^2) \end{pmatrix}}_{\textbf{term 4}} + \underbrace{\begin{pmatrix} B_i^l(z^1) - B_i^l(z^2) \\ B_i^u(z^1) - B_i^u(z^2) \\ B_i^v(z^1) - B_i^v(z^2) \\ B_i^s(z^1) - B_i^s(z^2) \\ B_i^m(z^1) - B_i^m(z^2) \\ B_i^x(z^1) - B_i^x(z^2) \end{pmatrix}}_{\textbf{term 5}}.$$

The nonzero components of terms 4 and 5 are defined as follows:

$$\left(H_i^l(z^1) - H_i^l(z^2)\right)_\omega = \begin{pmatrix} \rho^\omega (2b_i^\omega + d_{i1}^\omega)(y_{i1,\omega}^1 - y_{i1,\omega}^2) \\ \vdots \\ \rho^\omega (2b_i^\omega + d_{iJ}^\omega)(y_{iJ,\omega}^1 - y_{iJ,\omega}^2) \\ \rho^1 b_i^\omega (r_{i,\omega}^1 - r_{i,\omega}^2) \end{pmatrix}$$

$$\left(B_i^l(z^1) - B_i^l(z^2)\right)_\omega = \begin{pmatrix} \rho^\omega \left(b_i^\omega (\sum_{j \in \mathcal{J}, j \neq 1}(y_{ij,\omega}^1 - y_{ij,\omega}^2)) + b_i^\omega (r_{i,\omega}^1 - r_{i,\omega}^2) - b_i^\omega (x_{i1}^1 - x_{i1}^2)\right) \\ \vdots \\ \rho^1 \left(b_i^\omega (\sum_{j \in \mathcal{J}, j \neq J}(y_{ij,\omega}^1 - y_{ij,\omega}^2)) + b_i^1 (r_{i,\omega}^1 - r_{i,\omega}^2) - b_i^\omega (x_{iJ}^1 - x_{iJ}^2)\right) \\ \rho^1 \left(b_i^\omega (\sum_{j \in \mathcal{J}}(y_{ij,\omega}^1 - y_{ij,\omega}^2))\right) \end{pmatrix}$$

$$H_i^u(z^1) - H_i^u(z^2) = \begin{pmatrix} \rho^1 e_{i1}^1 (u_{i1,1}^1 - u_{i1,1}^2) \\ \vdots \\ \rho^n e_{iJ}^n (u_{iJ,n}^1 - u_{iJ,n}^2) \end{pmatrix}, H_i^v(z^1) - H_i^v(z^2) = \begin{pmatrix} \rho^1 o_{i1}^1 (v_{i1,1}^1 - v_{i1,1}^2) \\ \vdots \\ \rho^n o_{iJ}^n (v_{iJ,n}^1 - v_{iJ,n}^2) \end{pmatrix}$$

$$H_i^x(z^1) - H_i^x(z^2) = \begin{pmatrix} 2b_i^0 (x_{i1}^1 - x_{i1}^2) \\ \vdots \\ 2b_i^0 (x_{iJ}^1 - x_{iJ}^2) \end{pmatrix}$$

$$+ \begin{pmatrix} b_i^0 \sum_{j \in \mathcal{J}, j \neq 1}(x_{ij}^1 - x_{ij}^2) - \sum_{\omega \in \Omega} \rho^\omega b_i^\omega (\sum_{j \in \mathcal{J}}(y_{ij,\omega}^1 - y_{ij,\omega}^2) + r_{i,\omega}^1 - r_{i,\omega}^2) \\ \vdots \\ b_i^0 \sum_{j \in \mathcal{J}, j \neq J}(x_{ij}^1 - x_{ij}^2) - \sum_{\omega \in \Omega} \rho^\omega b_i^\omega (\sum_{j \in \mathcal{J}}(y_{ij,\omega}^1 - y_{ij,\omega}^2) + r_{i,\omega}^1 - r_{i,\omega}^2) \end{pmatrix}.$$

37

Let the Lipschitz constants for terms 4 and 5 be denoted by M_4 and M_5, respectively. Then M_4 and M_5 are bounded as

$$M_4^i = \begin{cases} \max_{\omega \in \Omega, j \in \mathcal{J}} \left(\rho^\omega (2b_i^\omega + d_{ij}^\omega), \rho^\omega e_{ij}^\omega, \rho^\omega o_{ij}^\omega \right), & i \in \mathcal{G} \\ \max_{\omega \in \Omega} \rho^\omega b_i^\omega, & i \in \mathcal{G}^c \end{cases}$$

$$\text{and} \quad M_5^i = \begin{cases} \sum_{\omega \in \Omega} b_i^\omega (1 + J\sqrt{J+1}) + J\left(\sqrt{(J-1)(b_i^0)^2 + \sum_{\omega \in \Omega}(\rho^\omega b_i^\omega)^2(J+1)} \right), & i \in \mathcal{G} \\ 0, & i \in \mathcal{G}^c \end{cases}$$

respectively. The Lipschitz constant for the mapping $\mathbf{F}$ is given by

$$M = \max_{i \in \mathcal{N}} (M_i), \quad \text{where} \quad M_i = \sqrt{(M_4^i)^2 + (M_5^i)^2} \quad \forall i.$$

Term 2: Term 2 may be bounded as

$$\begin{aligned} \|\mathbf{F}_d(z^1, \lambda^1) - \mathbf{F}_d(z^2, \lambda^2)\| &= \|\nabla d(z^1)^T \lambda_1 - \nabla d(z^2)^T \lambda^2\| \\ &\leq \|\nabla d(z^1)^T \lambda_1 - \nabla d(z^2)^T \lambda^1\| + \|\nabla d(z_2)^T(\lambda^1 - \lambda^2)\| \\ &\leq \|\nabla d(z^1) - \nabla d(z^2)\|\|\lambda^1\| + \|\nabla d(z^2)\|\|\lambda^1 - \lambda^2\|, \end{aligned}$$

where the inequalities follows from the application of the triangle inequality and the Cauchy-Schwartz inequality. Furthermore, $\nabla d(z)$ is a constant since $d(z)$ is a polyhedral constraint given by $d(z) = Bz$ implying that $\|\nabla d(z^1) - \nabla d(z^2)\| = 0$, allowing us to conclude that

$$\|\mathbf{F}_d(z^1, \lambda^1) - \mathbf{F}_d(z^2, \lambda^2)\| \leq \|B\|\|\lambda^1 - \lambda^2\|.$$

Term 3: Term 3 may be bounded by recalling that $d(z)$ is polyhedral, allowing us to proceed as follows

$$\begin{aligned} \|\mathbf{F}_\lambda(z_1, \lambda_1) - \mathbf{F}_\lambda(z_2, \lambda_2)\| &\leq \|d(z^1) - d(z^2)\| + \epsilon\|\lambda^1 - \lambda^2\| \\ &\leq \|B\|\|z^1 - z^2\| + \epsilon\|\lambda^1 - \lambda^2\|, \end{aligned}$$

where the inequalities follow again from the triangle inequality, the Cauchy-Schwartz inequality and the functional form of $d(z)$. It follows that the Lipschitz constant for the overall mapping is given by $(M + \|B\| + \epsilon)$.

The strong monotonicity of the mapping $\mathbf{F}^\epsilon$ with monotonicity constant ϵ can be deduced by noting that $\nabla \mathbf{F}^\epsilon$, given by

$$\nabla \mathbf{F}^\epsilon = \begin{pmatrix} \nabla_z \mathbf{F}_z + \epsilon \mathbf{I} & -\nabla d^T \\ \nabla d & \epsilon \mathbf{I} \end{pmatrix},$$

is positive definite since $\nabla_z \mathbf{F}_z$ is positive semidefinite for all z. ∎

The convergence of the primal-dual method is contingent on the mapping $\mathbf{F}_\epsilon(z, \lambda)$ being Lipschitz and strongly monotone. Convergence under weaker conditions such as strict monotonicity can also be guaranteed while mere monotonicity requires alternate schemes (such as two-step methods) (See [10, Ch. 12]). From Lemma 18, the mapping $\mathbf{F}^\epsilon$ is strongly monotone and Lipschitz continuous and the convergence of the primal-dual scheme may be directly concluded.

Proposition 19 (Convergence of primal-dual scheme [10]) *Consider the primal-dual scheme given by (5.4) and (5.5). If $\mathbf{F}^\epsilon$ is strongly monotone with constant ϵ and Lipschitz continuous with constant L and $\gamma^{pd} \leq \frac{2}{L+\epsilon}$, then the sequence $\{z^k\}$ converges to z^*_ϵ.*

5.3.1 Exact and inexact dual schemes

In this subsection, we consider the dual scheme in both its exact and inexact forms. While a proof for the convergence of the original dual scheme is provided in [22], we present a different argument in a regularized setting. Crucial to this result is the supporting requirement on co-coercivity of $d(z(\lambda))$. We provide a proof that uses the mapping $\mathbf{F}^\epsilon_z, \mathbf{F}^\epsilon_f$ and $\mathbf{F}_d$ as defined in (5.10), adapted from a result in [22]. It must be emphasized that the inexact dual has been studied recently by the second author in an optimization setting [23] and our results, while couched in the game-theoretic setting, are closely related. Yet, given that they have never been proved for equilibrium problems, we see the results here being of relevance. Furthermore, the polyhedral nature of $d(z)$ simplifies some of the proofs are often simpler and allows for somewhat different yet more refined bounds. Additionally, the bounds allow for articulating a direct relationship with the complexity in the game.

Lemma 20 *Consider the function $d(z(\lambda))$ where $z(\lambda)$ is a solution to the primal problem (5.1). Then $d(z(\lambda)) \equiv Bz$ is co-coercive with constant $\epsilon/\|B\|^2$ or*

$$(\lambda_2 - \lambda_1)^T(d(z(\lambda_1)) - d(z(\lambda_2))) \geq \frac{\epsilon}{\|B\|^2}\|d(z(\lambda_2)) - d(z(\lambda_1))\|^2 \qquad \text{for all} \quad \lambda_1, \lambda_2 \in \mathbb{R}^+_m.$$

Furthermore, we have

$$\|z(\lambda_1) - z(\lambda_1)\| \leq \frac{\|B\|}{\epsilon}\|\lambda_1 - \lambda_2\| \qquad \text{for all} \quad \lambda_1, \lambda_2 \in \mathbb{R}^+_m.$$

Proof: Let $z_1 \equiv z(\lambda_1)$ and $z_2 \equiv z(\lambda_2)$ represent solutions to VI($\mathbf{Z}, \mathbf{F}^\epsilon_z(z; \lambda_1)$) and VI($\mathbf{Z}, \mathbf{F}^\epsilon_z(z; \lambda_2)$), respectively. Then, we have

$$(z_2 - z_1)^T\mathbf{F}^\epsilon_f(z_1, \lambda_1) \geq 0 \quad \text{and} \quad (z_1 - z_2)^T\mathbf{F}^\epsilon_f(z_2, \lambda_2) \geq 0.$$

By recalling from (5.3), we have that

$$(z_2 - z_1)^T(\mathbf{F}_d(z_1, \lambda_1) - \mathbf{F}_d(z_2, \lambda_2)) \geq (z_2 - z_1)^T(\mathbf{F}_d(z_2) - \mathbf{F}_d(z_1)) \geq \epsilon\|z_2 - z_1\|^2. \qquad (5.12)$$

It follows from the definition of $d(z)$ that

$$(z_2 - z_1)^T(\mathbf{F}_d(z_1, \lambda_1) - \mathbf{F}_d(z_2, \lambda_2)) = (z_2 - z_1)^T(-B^T\lambda_1 + B^T\lambda_2)$$
$$= (Bz_2 - Bz_1)^T(-\lambda_1 + \lambda_2) = (d(z_2) - d(z_1))^T(\lambda_2 - \lambda_1)$$
$$\geq \epsilon\|z_2 - z_1\|^2 \geq \frac{\epsilon}{\|B\|^2}\|d(z_1) - d(z_2)\|^2,$$

where the last two inequalities follow from (5.12) and the Lipschitz continuity of $d(z)$ with constant $\|B\|$. Finally by applying the Cauchy-Schwartz inequality to the first inequality above, we have

$$\|z_2 - z_1\|^2 \leq \frac{1}{\epsilon}(d(z_2) - d(z_1))^T(\lambda_2 - \lambda_1) \leq \frac{1}{\epsilon}\|B\|\|z_2 - z_1\|\|\lambda_2 - \lambda_1\|$$

giving us $\quad \|z_2 - z_1\| \leq \frac{\|B\|}{\epsilon}\|\lambda_2 - \lambda_1\|. \quad \blacksquare$

39

Using the co-coercivity of $d(z(\lambda))$, the convergence of the iterates constructed from regularized dual scheme can be shown to converge to λ_ϵ^*, a dual solution to the regularized problem.

Proposition 21 (Convergence of exact dual scheme) *Consider the dual scheme given by* (5.6) *and* (5.7). *If $d(z(\lambda))$ is co-coercive with constant $\eta_{cc} = \frac{\epsilon}{\|B\|^2}$ and γ^d satisfies*

$$\gamma_d < \min\left\{\frac{1}{\epsilon}, \frac{2\eta_{cc}}{1 + 2\eta_{cc}\epsilon}\right\}, \tag{5.13}$$

then the sequence $\{\lambda^k\}$ converges to λ_ϵ^*.

Proof : By invoking the definition of λ^{k+1}, noting that λ^* is a fixed-point of (5.2) and the non-expansivity of the Euclidean projector, we have

$$
\begin{aligned}
\|\lambda^{k+1} - \lambda_\epsilon^*\| &= \left\|\Pi_{\mathbb{R}_m^+}(\lambda^k - \gamma_d d(z^k) - \gamma_d\epsilon\lambda^k) - \lambda_\epsilon^*\right\| \\
&= \left\|\Pi_{\mathbb{R}_m^+}(\lambda^k - \gamma_d d(z^k) - \gamma_d\epsilon\lambda^k) - \Pi_{\mathbb{R}_m^+}(\lambda_\epsilon^* - \gamma_d d(z_\epsilon^*) - \gamma_d\epsilon\lambda_\epsilon^*)\right\| \\
&\leq \left\|(\lambda^k - \gamma_d d(z^k) - \gamma_d\epsilon\lambda^k) - (\lambda_\epsilon^* - \gamma_d d(z_\epsilon^*) - \gamma_d\epsilon\lambda^*)\right\| \\
&= \left\|(1 - \gamma_d\epsilon)(\lambda^k - \lambda_\epsilon^*) - \gamma_d(d(z^k) - d(z_\epsilon^*))\right\|.
\end{aligned}
$$

Then, by expanding the square of the expression on the right hand side and by leveraging the co-coercivity of $d(\lambda(z))$ with respect to z, we have the following inequality:

$$
\begin{aligned}
\|\lambda^{k+1} - \lambda_\epsilon^*\|^2 &\leq (1 - \gamma_d\epsilon)^2\|\lambda^k - \lambda_\epsilon^*\|^2 + (\gamma_d)^2\|d(z^k) - d(z_\epsilon^*)\|^2 \\
&\quad - 2\gamma_d(1 - \gamma_d\epsilon)(\lambda^k - \lambda_\epsilon^*)^T(d(z^k) - d(z_\epsilon^*)) \\
&\leq (1 - \gamma_d\epsilon)^2\|\lambda^k - \lambda_\epsilon^*\|^2 + (\gamma_d^2 - 2\gamma_d\eta_{cc}(1 - \gamma_d\epsilon))\|d(z^k) - d(z_\epsilon^*)\|^2,
\end{aligned}
$$

where the second inequality follows from the co-coercivity of $d(z(\lambda))$ with a constant η_{cc}. Convergence of the scheme follows if γ_d is chosen in accordance with

$$\gamma_d < \min\left\{\frac{1}{\epsilon}, \frac{2\eta_{cc}}{1 + 2\eta_{cc}\epsilon}\right\}, \quad \text{where} \quad \eta_{cc} = \frac{\epsilon}{\|B\|^2}. \qquad \blacksquare$$

The convergence of λ^k to λ_ϵ^* suggests that if the dual scheme terminates prematurely, a simple bound on the suboptimality of z^k and the infeasibility $\max(0, d(z^k))$ can be provided.

Lemma 22 *Consider the dual scheme given by* (5.6) *and* (5.7) *and suppose $d(z(\lambda))$ is co-coercive with constant $\epsilon/\|B\|^2$. Then for any $k \geq 0$ we have*

$$\|z^k - z^*\| \leq \frac{\|B\|}{\epsilon}\|\lambda^k - \lambda_\epsilon^*\| \quad and \quad \max(0, -d(z^k)) \leq \frac{\|B\|^2}{\epsilon}\|\lambda^k - \lambda_\epsilon^*\|.$$

Proof : A bound on the suboptimality may be directly obtained from Lemma 20. The infeasibility in the constraint $d(z) \geq 0$, namely $\max(0, -d(z))$, is bounded as shown through the

40

following sequence of relationships, that use the Cauchy-Schwartz inequality and the bound on the suboptimality of z^k:

$$\max(0, -d(z^k)) \leq -Bz^k = -B(z^k + z_\epsilon^* - z_\epsilon^*) \leq B(z_\epsilon^* - z^k)$$

$$\leq \|B\| \|z_\epsilon^* - z^k\| \leq \frac{\|B\|^2}{\epsilon} \|\lambda_\epsilon^* - \lambda^k\|. \quad \blacksquare$$

A shortcoming of the dual scheme is the need for exact primal solutions for every dual solution. Since this requires iteratively solving a fixed-point problem, it can prove to be an inordinately expensive component of the algorithm. Our intent is in constructing a *bounded complexity* variant. This can be directly attained by requiring that only K iterations of the primal scheme be employed for a given value of the dual iterates as given by

$$z_j^{t+1} = \Pi_{\mathbf{Z}_j}(z_j^t - \gamma_d(\mathbf{F}_z(z_j^t; z_{-j}^t, \lambda^k) + \epsilon^\ell z_j^t)), \text{ for all } j, t = 0, \dots, K-1. \tag{5.14}$$

However, in obtaining error bounds, we require that the primal strategy sets be bounded. It is worth remarking that in general this bound may be difficult to obtain in closed-form but we assume that such a bound is available for purposes of this analysis. Specifically, we assume that $\|z\| \leq M_z$ throughout the remainder of this section. Finally, the strong monotonicity of the primal problem implies that $\|z^t - z^*\| \leq q_p^{t/2}\|z^0 - z^*\|$, where $q_p < 1$.

Proposition 23 *Consider the inexact dual scheme given by (5.14) and (5.7). If $d(z(\lambda))$ is co-coercive with constant $\epsilon/\|B\|^2$, $\|z\| \leq M_z$ and γ^d satisfies*

$$\gamma_d < \min\left(\frac{1+\epsilon^2}{2\epsilon}, \frac{2\eta_{cc}}{1+2\eta_{cc}\epsilon}\right)$$

then we have

$$\|\lambda^k - \lambda_\epsilon^*\| \leq q_d^k\|\lambda^0 - \lambda_\epsilon^*\|^k + \left(\frac{1-q_d^k}{1-q_d}\right)\left((\frac{2}{\epsilon^2}+4)\|B\|q_p^{K/2}M_z^2(1+\|B\|q_p^{K/2})\right).$$

Proof : As earlier, the definition of λ^{k+1} and the fixed-point property of λ_ϵ^*, we have the following inequality:

$$\|\lambda^{k+1} - \lambda_\epsilon^*\| = \|\Pi_{\mathbb{R}_m^+}(\lambda^k - \gamma_d(d(z_K^k) + \epsilon_k\lambda^k)) - \Pi_{\mathbb{R}_m^+}(\lambda_\epsilon^* - \gamma_d(d(z^*) + \epsilon_k\lambda_\epsilon^*))\|$$

$$\leq \|(\lambda^k - \gamma_d(d(z_K^k) + \epsilon_k\lambda^k)) - (\lambda_\epsilon^* - \gamma_d(d(z^*) + \epsilon_k\lambda_\epsilon^*))\|$$

By adding and subtracting terms and by using the triangle inequality, the right-hand side can be shown to be

$$\|(\lambda^k - \gamma_d(d(z_K^k) + \epsilon\lambda^k)) - (\lambda^* - \gamma_d(d(z^*) + \epsilon_k\lambda_\epsilon^*))\|^2$$

$$= \|(1-\gamma_d\epsilon)(\lambda^k - \lambda_\epsilon^*) - \gamma_d(d(z_K^k) - d(z_\epsilon^*))\|^2$$

$$= (1-\gamma_d\epsilon)^2\|\lambda^k - \lambda_\epsilon^*\|^2 + \gamma_d^2 \underbrace{\|d(z_K^k) - d(z_\epsilon^*)\|^2}_{\textbf{term 1}} \underbrace{-2\gamma_d(1-\gamma_d\epsilon)(\lambda^k - \lambda_\epsilon^*)^T(d(z_K^k) - d(z_\epsilon^*))}_{\textbf{term 2}}.$$

41

By noting that $d(z_k)$ is given by $Bz_k \geq 0$ for some matrix B, it follows that term 1 can be bounded by

$$\|d(z_K^k) - d(z_\epsilon^*)\|^2 \leq \|d(z_K^k) - d(z^k)\|^2 + \|d(z^k) - d(z_\epsilon^*)\|^2 + 2\|d(z^k) - d(z_K^k)\|\|d(z^k) - d(z_\epsilon^*)\|.$$

Furthermore, by using the co-coercivity of $d(x(\lambda))$, term 2 may be bounded in the following fashion:

$$
\begin{aligned}
&- 2\gamma_d(1 - \gamma_d\epsilon)(\lambda^k - \lambda_\epsilon^*)^T(d(z_K^k) - d(z_\epsilon^*)) \\
&= -2\gamma_d(1 - \gamma_d\epsilon)(\lambda^k - \lambda_\epsilon^*)^T(d(z^k) - d(z_\epsilon^*)) - 2\gamma_d(1 - \gamma_d\epsilon)(\lambda^k - \lambda_\epsilon^*)^T(d(z_K^k) - d(z^k)) \\
&\leq -2\gamma_d(1 - \gamma_d\epsilon)\frac{\epsilon}{\|B\|^2}\|d(z^k) - d(z_\epsilon^*)\|^2 + \gamma_d^2\|\lambda^k - \lambda_\epsilon^*\|^2 + (1 - \gamma_d\epsilon)^2\|d(z_K^k) - d(z^k)\|^2.
\end{aligned}
$$

Using the bounds on terms 1 and 2, we have the following:

$$
\begin{aligned}
&(1 - \gamma_d\epsilon)^2\|\lambda^k - \lambda_\epsilon^*\|^2 + \gamma_d^2\|d(z_K^k) - d(z_\epsilon^*)\|^2 - 2\gamma_d(1 - \gamma_d\epsilon)(\lambda^k - \lambda_\epsilon^*)^T(d(z_K^k) - d(z_\epsilon^*)) \\
&\leq (1 - \gamma_d\epsilon)^2\|\lambda^k - \lambda_\epsilon^*\|^2 \\
&+ \gamma_d^2\left(\|d(z_K^k) - d(z^k)\|^2 + \|d(z^k) - d(z_\epsilon^*)\|^2 + 2\|d(z^k) - d(z_K^k)\|\|d(z^k) - d(z_\epsilon^*)\|\right) \\
&- 2\gamma_d(1 - \gamma_d\epsilon)\frac{\epsilon}{\|B\|^2}\|d(z^k) - d(z_\epsilon^*)\|^2 + \gamma_d^2\|\lambda^k - \lambda_\epsilon^*\|^2 + (1 - \gamma_d\epsilon)^2\|d(z_K^k) - d(z^k)\|^2 \\
&= \underbrace{\left((1 - \gamma_d\epsilon)^2 + \gamma_d^2\right)\|\lambda^k - \lambda_\epsilon^*\|^2 + \left(\gamma_d^2 - 2\gamma_d\frac{\epsilon}{\|B\|^2}(1 - \gamma_d\epsilon)\right)\|d(z_k) - d(z_\epsilon^*)\|^2}_{\textbf{term 3}} \\
&+ \underbrace{(\gamma_d^2 + (1 - \gamma_d\epsilon)^2)\|d(z_K^k) - d(z^k)\|^2 + 2\gamma_d^2\|d(z^k) - d(z_K^k)\|\|d(z^k) - d(z_\epsilon^*)\|}_{\textbf{term 4}}.
\end{aligned}
$$

If $\eta_{cc} = \epsilon/\|B\|^2$ and γ_d is chosen in accordance with

$$
\begin{array}{lll}
\left((1 - \gamma_d\epsilon)^2 + \gamma_d^2\right) & < 1, & \gamma_d < \frac{1+\epsilon^2}{2\epsilon} \\
\left(\gamma_d^2 - 2\gamma_d\eta_{cc}(1 - \gamma_d\epsilon)\right) & < 0, & \gamma_d < \frac{2\eta_{cc}}{1+2\eta_{cc}\epsilon},
\end{array}
\quad \implies \quad \gamma_d < \min\left(\frac{1+\epsilon^2}{2\epsilon}, \frac{2\eta_{cc}}{1+2\eta_{cc}\epsilon}\right).
$$

then term 3 would lead to a contraction. In fact, if γ_d satisfies $\gamma_d < \frac{1+\epsilon^2}{2\epsilon}$, then it follows that

$$\gamma_d \leq \frac{1+\epsilon^2}{2\epsilon} \leq \frac{1}{2\epsilon} \leq \frac{1}{\epsilon},$$

implying that $(1 - \gamma_d\epsilon) > 0$. Note that the error arising from term 4 may be bounded by recalling that $d(z) = Bz$ is a Lipschitz continuous mapping implying that

$$
\begin{aligned}
&(\gamma_d^2 + (1 - \gamma_d\epsilon)^2)\|d(z_K^k) - d(z^k)\|^2 + 2\gamma_d^2\|d(z^k) - d(z_K^k)\|\|d(z^k) - d(z_\epsilon^*)\| \\
&\leq (\gamma_d^2 + (1 - \gamma_d\epsilon)^2)\|B\|^2\|z_K^k - z^k\|^2 + 2\gamma_d^2\|B\|\|z^k - z_K^k\|M_z
\end{aligned}
$$

Then by observing that $\|z^k - z_K^k\| \leq \|z^k - z_0^k\|q_p^{K/2} \leq M_z q_p^{K/2}$, where the first inequality follows from geometric convergence of the sequence $\{z_K^k\}$ to z^k as $K \to \infty$ and the second follows from the boundedness of the primal space with bound M_z. It follows that

$$
\begin{aligned}
&(\gamma_d^2 + (1 - \gamma_d\epsilon)^2)\|B\|^2\|z_K^k - z^k\|^2 + 2\gamma_d^2\|B\|\|z^k - z_K^k\|M_z \\
&\leq (\gamma_d^2 + (1 - \gamma_d\epsilon)^2)\|B\|q_p^K M_z^2 + 2\gamma_d^2\|B\|^2 q_p^{K/2} M_z^2.
\end{aligned}
$$

Finally, by observing that $(\gamma_d^2 + (1 - \gamma_d\epsilon)^2) \le (\gamma_d^2 + (1 + \gamma_d\epsilon)^2)$ which is further bounded by $(\frac{1}{\epsilon^2} + 4)$ and $\gamma_d^2 \le \frac{1}{\epsilon^2}$, we have

$$(\gamma_d^2 + (1 - \gamma_d\epsilon)^2)\|B\|q_p^K M_z^2 + 2\gamma_d^2\|B\|^2 q_p^{K/2} M_z^2 \le (\frac{1}{\epsilon^2} + 4)\|B\|q_p^K M_z^2 + \frac{2}{\epsilon^2}\|B\|q_p^{K/2} M_z^2$$

$$\le (\frac{2}{\epsilon^2} + 4)\|B\|q_p^{K/2} M_z^2 (1 + \|B\|q_p^{K/2}).$$

Then given a starting point λ^0, we have

$$\|\lambda^k - \lambda_\epsilon^*\| \le q_d^k\|\lambda^0 - \lambda_\epsilon^*\|^k + \underbrace{\left(\frac{1 - q_d^k}{1 - q_d}\right)\left((\frac{2}{\epsilon^2} + 4)\|B\|q_p^{K/2} M_z^2 (1 + \|B\|q_p^{K/2})\right)}_{\textbf{Error from inexact solution of primal}}. \quad \blacksquare$$

It can be seen that the error term arising from inexact primal solutions converges to zero as $K \to \infty$. We conclude this section with a bound on the suboptimality of z^k and infeasibility associated with $d(z^k)$ if the dual scheme terminates prematurely.

Lemma 24 *Consider the inexact dual scheme given by (5.14) and (5.7). If $d(z(\lambda))$ is co-coercive with constant $\epsilon/\|B\|^2$, $\|z\| \le M_z$ and γ^d satisfies*

$$\gamma_d < \min\left(\frac{1 + \epsilon^2}{2\epsilon}, \frac{2\eta_{cc}}{1 + 2\eta_{cc}\epsilon}\right)$$

Then for any nonnegative integers $k, K \ge 0$, we have

$$\|z_K^k - z_\epsilon^*\| \le q_p^{K/2} M_z + \frac{\|B\|}{\epsilon}\|\lambda^k - \lambda_\epsilon^*\|,$$

$$\max(0, -d(z_K^k)) \le \|B\|\left(q_p^{K/2} M_z + \frac{\|B\|^2}{\epsilon}\|\lambda^k - \lambda_\epsilon^*\|\right).$$

Proof : The first result follows easily by using the triangle inequality and employing the earlier result.

$$\|z_K^k - z_\epsilon^*\| \le \|z_K^k - z^k\| + \|z^k - z_\epsilon^*\|$$

$$\le q_p^{K/2} M_z + \frac{\|B\|}{\epsilon}\|\lambda^k - \lambda_\epsilon^*\|.$$

Similarly, the bound on the infeasibility at a point z_K^k is provided by adding and subtracting $d(z_\epsilon^*)$, applying the triangle and Cauchy-Schwartz inequality:

$$\max(0, -d(z_K^k)) \le -d(z_K^k) = -d(z_K^k) + d(z_\epsilon^*) - d(z_\epsilon^*)$$

$$\le -B(z_K^k - z_\epsilon^*) \le \|B\|\|z_K^k - z^k\| + \|B\|\|z^k - z_\epsilon^*\|$$

$$\le \|B\|q_p^{K/2} M_z + \frac{\|B\|^2}{\epsilon}\|\lambda^k - \lambda_\epsilon^*\|. \quad \blacksquare$$

5.4 Numerical performance

In this section, we examine the performance of our hybrid projection-based cutting-plane scheme with a focus on several questions. First, we consider whether the scheme scales with $|\Omega|$, $|\mathcal{J}|$ and $|\mathcal{G}|$. Second, we examine the relative performance of the primal-dual versus the dual scheme. Finally, we examine the benefits arising from inexact solutions of the primal problem.

We confine our discussion to the game $\mathcal{G}^b$ and examine the behavior of the scheme on a strongly monotone problem where the regularization parameter ϵ is $1e^{-3}$. The algorithm was implemented on a Matlab environment in SUSE-Linux on a processor with a clockspeed of 2.39 GHZ and a memory of 16 GB.
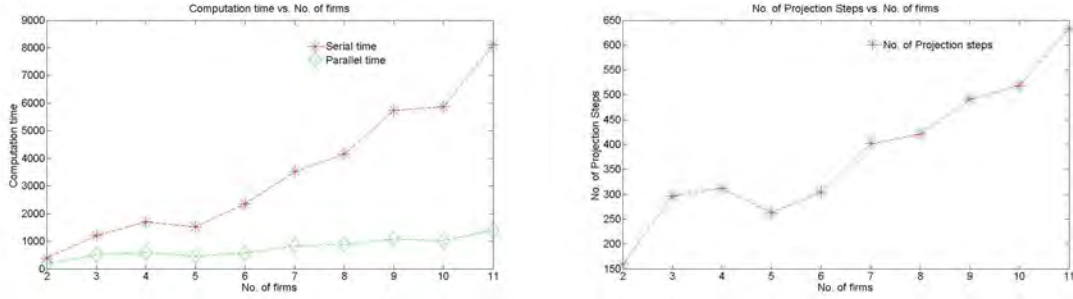

Figure 5.1: Scalability in number of firms

Scalability: The algorithm is implemented in a distributed fashion with each agent solving his projection problem independently. As a consequence, we expect that the effort should scale with the number of agents. In fact, when the number of firms is raised from 2 to 11, the variation of serial and parallel times are shown in Figure 5.1. The variation in the number of overall projection steps with increase in the number of firms is also shown in Figure 5.1. The projection scheme is terminated when $\epsilon^{inner} = 5e^{-3}$. Both graphs show that the effort, both in terms of CPU time and projection steps, grows slowly with the number of firms.

If an analogous question is studied when the number of generating nodes is varied, we observe similar results, as shown in Figure 5.2. Note that the the nodal problems decompose at the firm level implying that large networks, while computationally expensive, will not lead to rapid growth in effort. Instead, such settings will necessitate the solution of a larger number of separable nodal problems.

Perhaps the most challenging source of complexity is the uncertainty. This leads to arbitrarily large projection problems which are addressed through a cutting-plane method. If the number of scenarios from 30 to 240, then the variation of serial and parallel times are as seen in Figure 5.3. Additionally, the variation in the number of overall projection steps is also shown in Figure 5.3. It is seen that the effort grows slowly with an increase in the size of the sample-space, suggesting that the decomposition scheme for solving the projection problem proves efficient.

Comparison between primal-dual, exact dual and inexact-dual schemes: For a two firm problem, with one generating node and thirty scenarios, we employed the primal-dual, exact dual
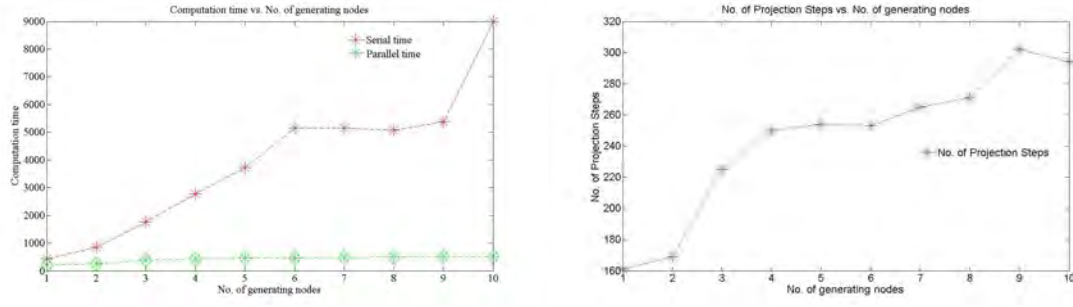
Figure 5.2: Scalability in number of generating nodes
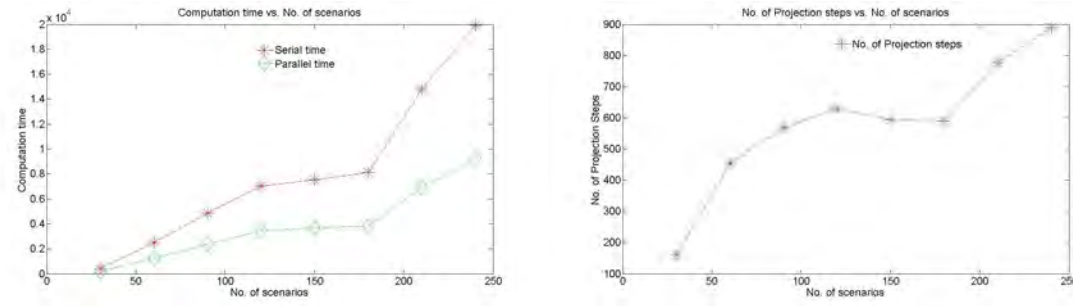
Figure 5.3: Increasing Number of scenarios- Scalability

and inexact dual schemes. It was observed that the primal-dual scheme required 160 iterations. The performance of the dual scheme for different levels of primal computation is shown in Table 5.1. Note that total effort refers to the sum of both primal and dual steps. It can be seen that the primal-dual step tends to be more efficient than the dual scheme while the fewer primal steps lead to far more efficient schemes in the context of inexact-dual methods.

Table 5.1: Inexact-dual scheme: Total effort vs. no of primal steps

Total no. of Iterations	No. of Primal steps
180	3
198	6
207	9
228	12
225	15
234	18

Chapter 6

Insights for market design

In this section we provide some insights on the proposed set of models by examing the strategic behavior of agents in the setting of a 53-node network, referred to as the Belgian grid and shown in Figure 8.1. This network has provided the basis for a variety of prior studies [34] and the line impedances and capacities are listed in Table 8.1. We assume that nodes 7, 9, 10, 11, 14, 22, and 24 house generation facilities. We assume that the generation mix at each of these nodes is identical and is specified by Table 6.1. Here, the generation capacities and costs are assumed to be normally distributed with specified parameters. Demand at all the nodes is articulated through affine functions. In the forward-clearing model, the intercepts in the forward and spot markets are taken to be fixed at 1500 at all nodes while the slopes in the spot market are assumed to vary normally with a mean of 1 and a variance of 0.02. The coefficient in the loss function is taken to be, $\chi = 40$. As specified earlier, $\chi = 0$, for $x_{ij} \leq cap_{ij}^{\omega}$.

Table 6.1: Generator details

Generator type	Capacity	Linear cost	Quadratic cost
Oil 1	$\mathcal{N} \sim (2000,10)$	N(10,1)	$\mathcal{N} \sim (0.3,0.01)$
Oil 2	$\mathcal{N} \sim (2000,10)$	$\mathcal{N} \sim (10,1)$	$\mathcal{N} \sim (0.3,0.01)$
Wind 3	$\mathcal{N} \sim (650,270)$	$\mathcal{N} \sim (0,0)$	$\mathcal{N} \sim (0,0)$
Wind 4	$\mathcal{N} \sim (730,320)$	$\mathcal{N} \sim (0,0)$	$\mathcal{N} \sim (0,0)$
Coal 5	$\mathcal{N} \sim (1400,10)$	$\mathcal{N} \sim (12,1)$	$\mathcal{N} \sim (0.25,0.01)$
Coal 6	$\mathcal{N} \sim (1400,10)$	$\mathcal{N} \sim (12,1)$	$\mathcal{N} \sim (0.25,0.01)$

Our intent lies in ascertaining the relationship of a variety of parameetrs, such as risk-aversion, uncertainty and demand levels, on market outcomes such as forward market participation and penetration levels of wind resources. Throughout, we employ our projection-based cutting-plane method for obtaining solutions, the sole exception being the shared-risk problems that lead to possibly nonmonotone games.

Risk aversion: In this setting, we vary risk aversion parameter κ_i for all the firms from 0–3 in steps of 0.5. As shown in Figure 6.1, we find that the forward bids drop for the wind generators and increase for the coal and oil generators. This behavior suggests that as generators become risk-averse, firms with a larger number of wind-based assets tend to be conservative in forward market bidding. This is primarily because firms with uncertain generation face much higher risk of shortfall.

As they are penalized higher amounts for exposing the market to such risk, firms tend to bid lower, reducing their risk exposure. This is manifested through lower participation in the forward market by wind-based generators. Figure 6.1 also shows the increasing risk premium with increasing risk aversion. This states that the firms bag higher incentives with increasing risk. The increasing risk in the forward market for the wind generators, make way for better profits and incentives for the other generators. In a model that allows for a separate settlement for determining forward prices, we observe that the risk premium grows with risk-aversion. Note that the risk premium is given by the difference between the forward price and the expected spot price at a particular node.
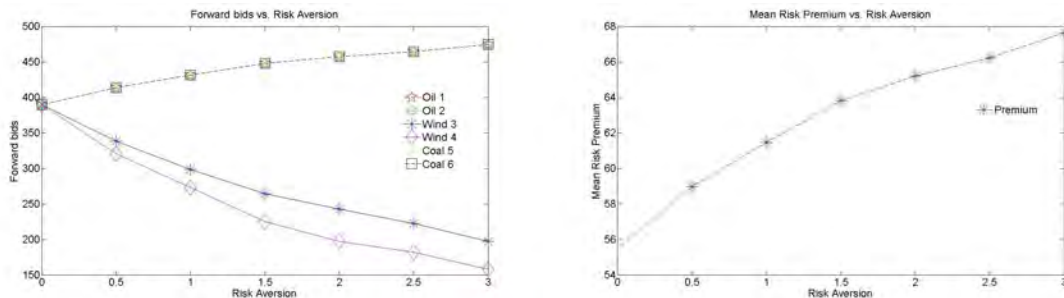

Figure 6.1: Increasing risk aversion

Uncertainty in generation capacity: If the generators are assumed to have constant risk aversion parameter (fixed at 1 for all firms), we examine how uncertainty impacts risk exposure and level of forward participation. While coal and oil generators are expected to be close to deterministic in their availability, we assume that wind generators are faced with far greater uncertainty. In our numerical experiments, we vary the standard deviation of the wind generators (Wind 3 and Wind 4) from 10 to 885 in steps of 175. Expectedly, the risk exposure increases as the variability in wind assets grows (Figure 6.2). Moreover, while the general belief would be that participation in the forward markets would aid in hedging spot-market uncertainty, the introduction of risk measures suggests that wind-based generators are less inclined to participate. It should be emphasized that the deviation costs tend to have a similar impact on behavior. Note that drops in forward market participation lead to higher prices in the forward market with respect to the spot and are are captured by an increase in risk-premium with higher uncertainty in wind assets.

Demand functions: A crucial question is how the choice of forward price function influences the results. In no-arbitrage models, this problem does not appear since the forward price function is not explicitly defined. In our market clearing models, we expect that our assumption on forward price function have significant impact on the results that emerge. Yet, it appears that for sufficiently low forward price intercepts, there is no forward market participation since the revenues garnered through participation are not sufficient. However, beyond a certain level, forward market participation becomes positive. Therefore, while the precise level of the forward market intercept is not as relevant, if the prices are set too low (a consequence of low intercepts), then this adversely affects bidding in this market. In our experiments, we fix the spot intercepts, slopes and forward slopes and vary the forward intercepts from 150 to 1800 in steps of 150. We find that there are
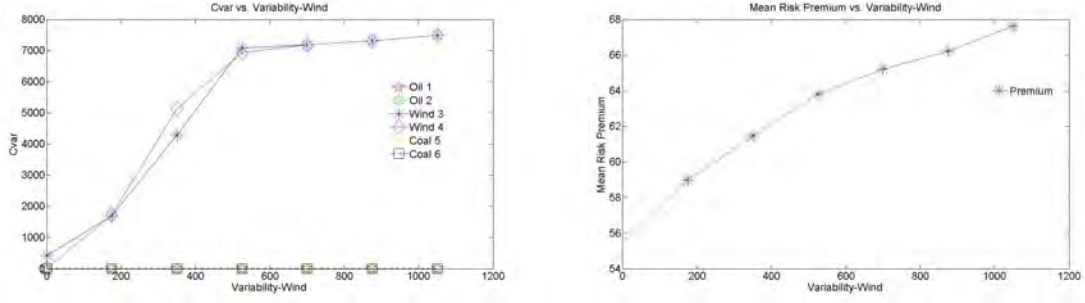
Figure 6.2: Increasing Variability-Wind

no forward bids till a particular value of the forward intercept. We also find that the forward bids and the premium increase as the forward intercept increases. Table 6.2 shows the variation of the forward bids and premium across node 11. We find that the forward bids are zero when there is no risk premium (when the expected spot prices are greater than the forward prices). When the risk premium is positive, the forward bidding at a node is non-zero. This clearly states that the firms do not bid in the forward market, unless they see an incentive. Similar behavior is observed across all the generating nodes.

Table 6.2: Increasing forward intercepts-variation of premium and forward bids at node 10

Intercept	Total Bids	Risk premium
450	0	*
600	0	*
750	0	*
900	0	*
1050	0	*
1200	52.73	8.52
1350	178.06	35.55
1500	303.77	62.19
1650	434.17	84.24

Increasing penetration of wind: As the role of renewables in the nation's fuel mix grows, a question that remains is whether forward markets will continue attract participation. We investigate this question by increasing the mean of the capacity of the wind generators from 300 to 2050 in steps of 350 and also raise the standard deviations in availability from 150 to 1025 in steps of 175. We observe that for a fixed level of risk aversion, the forward bids of all the firms increase with increasing wind power penetration. This is in response to the volatility in the spot market with wind power penetration (Figure 6.3). We also observe that with increasing wind power penetration, there is a significant increase in profits of wind generators at the expense of the profits of firms with no wind assets as shown in Figure 6.3.
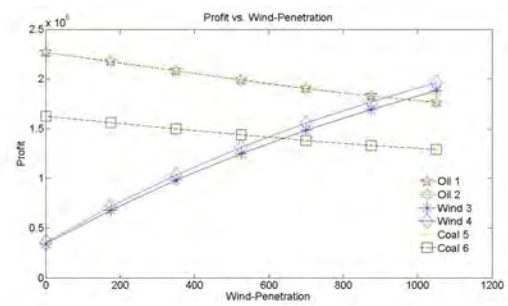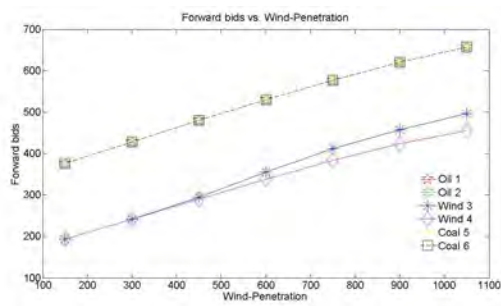
Figure 6.3: Increasing Penetration-Wind

Chapter 7

Summary

Motivated by increasing penetration of wind resources in power markets, we construct a two-period game-theoretic model in which agents are possibly risk averse and contend with uncertainty in the spot-market. The resulting Nash game is complicated by uncertainty, nonsmoothness and shared constraints. Through an analysis of the variational conditions, we prove that equilibria exist and the $\epsilon-$game admits a unique equilibrium. Furthermore, the variational inequalities in all but the shared risk model are found to be monotone. Scalable computation of equilibria is generally challenging when faced by shared constraints and uncertainty. We present a distributed projection-based method that uses a cutting-plane scheme for solving the stochastic projection problems. Error bounds are presented for generalizations of the scheme that allow for inexact computations and premature termination. Preliminary numerical results suggest that the scheme scales slowly with problem size. The algorithms were applied to an equilibrium problem arising in the Belgian network and allowed us to draw a range of insights that are expected to aid in market design.

Chapter 8

Appendix

8.1   The complementarity problem

Under the assumptions of regularity, the variational inequality can be written in the form of a complementarity problem. The solution to the complementarity problem is the same as that of the VI and in turn a solution for the original GNP. For computation, we solve the complementarity problem to get the solution of the VI and in turn a solution to the original GNP.

Non-Shared Risk

For our computation, we assume the loss function to be linear. Let us assign the multipliers $\alpha_{ij}^{\omega}, \beta_{ij}^{\omega}$ to equality and capacity constraints respectively.Let $\gamma_{ij}^{\omega}, \delta_{ij}^{\omega}$ refer to the constraints with respect to s_{ij}^{ω}. Let, $\mu^{\omega}, \sigma_l^{\omega}, \eta_l^{\omega}$ be the multipliers assigned to the power balance/ equality and transmission constraints of the Independent System Operator. Let ϕ_i^{ω} represent the multiplier for the shared constraint. Then, the complementarity problem can be represented as follows:

$$0 \leq x_{ij} \perp b_i^0 x_{ij} + b_i^0 \sum_{j \in \mathcal{J}} x_{ij} - a_i^0 + \sum_{\omega \in \Omega} \rho^\omega a_i^\omega - \sum_{\omega \in \Omega} \rho^\omega b_i^\omega (\sum_{j \in \mathcal{J}} y_{ij}^\omega + r_i^\omega) - \sum_{\omega \in \Omega} \alpha_{ij}^\omega + \xi \sum_{\omega \in \Omega} \delta_{ij}^\omega \geq 0$$

$$0 \leq y_{ij}^\omega \perp \rho^\omega(-a_i^\omega + c_i^\omega + (b_i^\omega + d_{ij}^\omega) y_{ij}^\omega + b_i^\omega(\sum_{j \in \mathcal{J}} y_{ij}^\omega) + b_i^\omega r_i^\omega - b_i^\omega x_{ij}) + \alpha_{ij}^\omega + \beta_{ij}^\omega - \phi_i^\omega \geq 0$$

$$0 \leq u_{ij}^\omega \perp f_p'(u_{ij}^\omega) - \alpha_{ij}^\omega \geq 0$$

$$0 \leq v_{ij}^\omega \perp f_n'(v_{ij}^\omega) + \alpha_{ij}^\omega \geq 0$$

$$0 \leq s_{ij}^\omega \perp \frac{\kappa_j \rho^\omega}{1 - \tau} - \gamma_{ij}^\omega - \delta_{ij}^\omega \geq 0$$

$$free \perp \kappa_j - \sum_{j \in \mathcal{J}} \gamma_{ij}^\omega - \sum_{j \in \mathcal{J}} \delta_{ij}^\omega = 0$$

$$0 \leq \beta_{ij}^\omega \perp cap_{ij}^\omega - y_{ij}^\omega \geq 0$$

$$0 \leq \gamma_{ij}^\omega \perp s_{ij}^\omega + m_{ij} \geq 0$$

$$0 \leq \delta_{ij}^\omega \perp s_{ij}^\omega + m_{ij} - \chi(x_{ij} - \lambda_{ij}^\omega) \geq 0$$

$$free \perp y_{ij}^\omega - x_{ij} + u_{ij}^\omega - v_{ij}^\omega = 0$$

$$0 \leq \phi_i^\omega \perp \sum_{j \in \mathcal{J}} y_{ij}^\omega + r_i^\omega \geq 0$$

$$free \perp -\rho^\omega a_i^\omega + \rho^\omega b_i^\omega(\sum_{j \in \mathcal{J}} y_{ij}^\omega + r_i^\omega) + \mu^\omega + \sum_{l \in \mathcal{L}} Q_{l,i}(\sigma_l^\omega - \eta_l^\omega) - \phi_i^\omega = 0, \qquad i \in \mathcal{G}$$

$$r_i^\omega \perp -\rho^\omega a_i^\omega + \rho^\omega b_i^\omega r_i^\omega + \mu^\omega + \sum_{l \in \mathcal{L}} Q_{l,i}(\sigma_l^\omega - \eta_l^\omega) \geq 0, \qquad i \in (\mathcal{G}^c - \{51\})$$

$$r_i^\omega \perp -\rho^\omega a_i^\omega + \rho^\omega b_i^\omega r_i^\omega + \mu^\omega \geq 0, \qquad \text{slack node-51}$$

$$free \perp \sum_{i \in \mathcal{N}} r_i^\omega = 0$$

$$\sigma_l^\omega \perp K_l^\omega - \sum_{i \in \mathcal{N}} Q_{l,i} r_i^\omega \geq 0$$

$$\eta_l^\omega \perp K_l^\omega + \sum_{i \in \mathcal{N}} Q_{l,i} r_i^\omega \geq 0.$$

8.1.1 Network details

Details on the Belgian grid are listed as follows.

8.1.2 Variable and parameter definitions

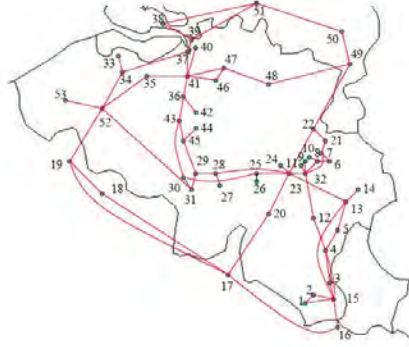Table 1 states the notation for the variables and parameters and sets.

Figure 8.1: The Belgian grid

Table 8.1: Network details

Line	Imp. (Ohm)	Cap.(MW)	Line	Imp. (Ohm)	Cap.(MW)	Line	Imp. (Ohm)	Cap.(MW)
1-2	23716	345	16-17	2633	5154	34-37	7048	1350
1-15	6269	345	17-18	4236	1715	34-52	12234	1350
2-15	8534	345	17-19	1939	5140	35-41	14204	1350
3-4	5339	240	17-20	8071	1179	35-52	9026	1420
3-15	11686	240	18-19	1465	13170	36-41	15777	2770
4-5	6994	510	19-52	11321	1179	36-42	11186	2840
4-12	5887	405	20-23	13165	1316	36-43	15408	2770
4-15	3644	240	21-22	47621	1420	37-39	66471	1420
5-13	6462	510	22-23	11391	1350	37-41	21295	1350
6-7	23987	300	22-49	9138	1350	38-39	10931	1650
6-8	9138	400	23-24	41559	5540	38-51	17168	946
7-21	14885	541	23-25	16982	1420	39-51	8596	1650
7-32	5963	410	23-28	8610	1350	40-41	11113	2770
8-9	45360	400	23-32	33255	1350	41-46	11509	2840
8-10	26541	800	25-26	134987	1420	41-47	13797	1420
8-32	11467	400	25-30	11991	1420	43-45	34468	1350
9-11	20157	410	27-28	64753	1420	44-45	47128	1420
9-32	10012	375	28-29	38569	1350	46-47	34441	1420
11-32	18398	375	29-31	284443	1350	47-48	14942	1420
12-32	4567	405	29-45	14534	1350	48-49	6998	1420
13-14	121410	2700	30-31	269973	1420	49-50	5943	3784
13-15	5094	790	30-43	10268	1420	50-51	2746	5676
13-23	5481	2770	31-52	1453	400	52-53	1279	2840
15-16	8839	400	33-34	40429	1420			

Table 8.2: Definition of variables and parameters and sets

x_{ij}	Forward decision of generation from firm j at node i
$u_{ij}^{\omega}, v_{ij}^{\omega}$	Positive and negative deviations respectively at scenario ω from firm j at node i
$y_{ij}^{\omega}, cap_{ij}^{\omega}$	Total spot generation decision and total generation capacity at scenario ω for firm j at node i
r_i^{ω}	ISO's spot decision at scenario ω at node i
n, Ω, ρ^{ω}	Number of scenarios, set of all scenarios and probability of scenario ω
p_i^{ω}	Nodal demand function or price at scenario ω at node i
$c_{ij}^{\omega}, d_{ij}^{\omega}$	Coefficient of linear and quadratic terms in the cost function at scenario ω for firm j at node i
f_p, f_n	Penalty functions for positive and negative deviations
$\mathrm{VaR}_{\tau}(\cdot), \mathrm{CVaR}_{\tau}(\cdot)$	Value at risk and Conditional value at risk measures
N_g, N	Number of generating nodes and total nodes in the network
a_i^0, b_i^0	Intercept and Slope respectively at node i in the forward market
$a_i^{\omega}, b_i^{\omega}$	Intercept and Slope respectively at node i at scenario ω
$g + 1$	Number of agents including g firms and the ISO - $(g+1)^{th}$ agent
$Q_{l,i}$	Power flowing across line l due to unit injection/withdrawal of power at node i
$\kappa_j, \forall j \in \mathcal{F}$	Risk factor or risk aversion parameter for firm j
$\varphi(x_{ij})$	Increasing function with respect to x_{ij}
χ	Coefficient of losses used in the loss function
$\mathcal{N}_j, \mathcal{N}_j^c$	Set of all generating nodes and non-generating nodes for firm j respectively
$\mathcal{L}, \mathcal{N}$	Set of all transmission lines and set of all nodes respectively
$\mathcal{G}, \mathcal{G}^c$	Set of all generating nodes and load nodes respectively
$\mathcal{J}, \mathcal{A}$	Set of all generating firms and set of all agents (firms and the ISO) respectively

Bibliography

[1] B. Allaz. Oligopoly, uncertainty and strategic forward transactions. *Journal of Industrial Organization*, 10:297–308, 1992.

[2] J. F. Benders. Partitioning procedures for solving mixed-variables programming problems. *Numer. Math.*, 4:238–252, 1962.

[3] J. R. Birge and F. Louveaux. *Introduction to Stochastic Programming: Springer Series in Operations Research.* Springer, 1997.

[4] J. Cardell, C. Hitt, and W. Hogan. Market power and strategic interaction in electricity networks. *Resource and Energy Economics*, 19(1):109–137, 1997.

[5] X. Chen and R. S. Womersley. Random test problems and parallel methods for quadratic programs and quadratic stochastic programs. *Optim. Methods Softw.*, 13(4):275–306, 2000.

[6] F. H. Clarke. *Optimization and nonsmooth analysis*, volume 5 of *Classics in Applied Mathematics*. Society for Industrial and Applied Mathematics (SIAM), Philadelphia, PA, second edition, 1990.

[7] A. J. Conejo, F. J. Nogales, and J. M. Arroyo. Risk-constrained self-scheduling of a thermal power producer. *IEEE Transactions on Power Systems*, 19(3):1569–1574, 2004.

[8] E. DeMeo, K. Porter, and C. Smith. *S*-wind power and electricity markets. *Utility Wind Integration Group*, 2007.

[9] F. Facchinei, A. Fischer, and V. Piccialli. On generalized Nash games and variational inequalities. *Oper. Res. Lett.*, 35(2):159–164, 2007.

[10] F. Facchinei and J.-S. Pang. *Finite Dimensional Variational Inequalities and Complementarity Problems: Vols I and II.* Springer-Verlag, NY, Inc., 2003.

[11] F. Facchinei and J.-S. Pang. *Nash-Equilibria:The Variational Approach.* In progress, 2009.

[12] P. T. Harker. A variational inequality approach for the determination of oligopolistic market equilibrium. *Math. Programming*, 30(1):105–111, 1984.

[13] A. Haurie and F. Moresino. Computation of *S*-adapted equilibria in piecewise deterministic games via stochastic programming methods. In *Advances in dynamic games and applications (Maastricht, 1998)*, volume 6 of *Ann. Internat. Soc. Dynam. Games*, pages 225–252. Birkhäuser Boston, Boston, MA, 2001.

[14] A. Haurie and G. Zaccour. *S*-adapted equilibrium in games played over event trees: an overview. In *Advances in dynamic games*, volume 7 of *Ann. Internat. Soc. Dynam. Games*, pages 417–444. Birkhäuser Boston, Boston, MA, 2005.

[15] B. Hobbs. Linear complementarity models of nash-cournot competition in bilateral and poolco power markets. *IEEE Transactions on Power Systems*, 16(2):194–202, 2001.

[16] B. Hobbs and C. Metzler. Nash-cournot equilibria in power markets on a linearized dc network with arbitrage: formulations and properties. *Networks and Spatial Economics*, 3:123–150, 2003.

[17] B. F. Hobbs, C. B. Metzler, and J.-S. Pang. Strategic gaming analysis for electric power systems: An MPEC approach. *IEEE Transactions on Power Systems*, 15:638–645, 2000.

[18] X. Hu and D. Ralph. Using epecs to model bilevel games in restructured electricity markets with locational prices. *Working Paper*, 2006.

[19] G. Infanger. *Planning Under Uncertainty*. Boyd and Fraser Publishing Co., 1994.

[20] D. Justus. *S*-case study 5: Wind power integration into electricity systems. *OECD Environment Directorate International Energy Agency*, 2005. International Energy Technology Collaboration and Climate Mitigation.

[21] R. Kamat and S. S. Oren. Two-settlement systems for electricity markets under network uncertainty and market power*. *Journal of regulatory economics*, 25(1):5–37, 2004.

[22] I. V. Konnov. *Equilibrium Models and Variational Inequalities*. Elsevier, 2007.

[23] J. Koshal, A. Nedić, and U. V. Shanbhag. Distributed multiuser optimization: Algorithms and error analysis. *To appear in the Conference proceedings of the IEEE Conference on Decision and Control (CDC), 2009*.

[24] T. Li and M. Shahidehpour. Risk-constrained generation asset arbitrage in power systems. *IEEE Transactions on Power Systems*, 22(3):1330–1339, 2007.

[25] T. Li, M. Shahidehpour, and Z. Li. Risk-constrained bidding strategy with stochastic unit commitment. *IEEE Transactions on Power Systems*, 22(1):449–458, 2007.

[26] C. Metzler, B. Hobbs, and J.-S. Pang. Nash-cournot equilibria in power markets on a linearized dc network with arbitrage: Formulations and properties. *Networks and Spatial Theory*, 3(2):123–150, 2003.

[27] R. Rockfellar and S. Uryasev. Optimization of conditional value-at-risk. *Journal of risk*, 2:21 – 41, 2000.

[28] J. B. Rosen. Existence and uniqueness of equilibrium points for concave n-person games. *Econometrica*, 33(3):520–534, July 1965.

[29] A. Ruszczynski. Decomposition methods. In *Handbook in Operations Research and Management Science*, volume 10, pages 141–212. Elsevier Science, Amsterdam, 2003.

[30] U. V. Shanbhag. *Decomposition and Sampling Methods for Stochastic Equilibrium Problems.* PhD thesis, Department of Management Science and Engineering (Operations Research), Stanford University, 2006.

[31] U. V. Shanbhag, G. Infanger, and P. W. Glynn. A complementarity framework for forward contracting under uncertainty. *Under review*, 2007.

[32] R. M. Van Slyke and R. Wets. L-shaped linear programs with applications to optimal control and stochastic programming. *SIAM J. Appl. Math.*, 17:638–663, 1969.

[33] D. J. Veit, A. Weidlich, J. Yao, and S. S. Oren. Simulating the dynamics in two-settlement electricity markets via an agent-based approach. *International Journal of Management Science*, 1(2):83–97, 2006.

[34] J. Yao, I. Adler, and S. S. Oren. Modeling and computing two-settlement oligopolistic equilibrium in a congested electricity network. *Operations Research*, 56(1):34–47, 2008.

[35] G. Zakeri, A. B. Philpott, and D. M. Ryan. Inexact cuts in Benders decomposition. *SIAM J. Optim.*, 10(3):643–657, 2000.